Polycyclic aromatic hydrocarbons

Laboratory infrared signatures of astrochemical evolution

Lemmens, A.K.

Publication date
2022

Document Version
Final published version

Polycyclic aromatic hydrocarbons

Alexander Karel Lemmens

POLYCYCLIC AROMATIC HYDROCARBONS

Laboratory infrared signatures of astrochemical evolution

Alexander Karel Lemmens

Polycyclic aromatic hydrocarbons: laboratory infrared signatures of astrochemical evolution

ACADEMISCH PROEFSCHRIFT

ter verkrijging van de graad doctor
aan de Universiteit van Amsterdam
op gezag van de Rector Magnificus
prof. dr. ir. K.I.J. Maex
ten overstaan van een door het College voor Promoties ingestelde commissie,
in het openbaar te verdedigen in de Agnietenkapel
op donderdag 10 maart 2022, te 13.00 uur

door

Alexander Karel Lemmens

geboren te Margraten

Promotiecommissie

Promotores:	prof. dr. W.J. Buma	Universiteit van Amsterdam
	prof. dr. A.M. Rijs	Vrije Universiteit Amsterdam
Overige leden:	prof. dr. H.J. Bakker	Universiteit van Amsterdam
	prof. dr. A.M. Brouwer	Universiteit van Amsterdam
	dr. S. Brünken	Radboud University
	prof. dr. H.M. Cuppen	Universiteit van Amsterdam
	dr. T.J. Lee	NASA Ames Research Center
	prof. dr. H.V.J. Linnartz	Universiteit Leiden
	prof. dr. M.S. de Vries	University of California, Santa Barbara

Faculteit der Natuurwetenschappen, Wiskunde en Informatica

“The answer, my friend, is blowin' in the wind” - Bob Dylan

Cover: “There is no second”

4 cyclones across the Western Hemisphere on the 4th of September 2019, all with sustained winds of over 40 knots. The individual hexagons are covers of PhD theses defended at the University of Amsterdam: “One is All, and by it All, and for it All’
Credits original image: NASA Earth Observatory/Joshua Stevens; NOAA National Environmental Satellite, Data, and Information Service.

ISBN: 978-94-6419-448-7

The research covered in this thesis was conducted in the Molecular Photonics group at the Van 't Hoff Institute for Molecular Sciences, University of Amsterdam and in the FELIX Laboratory, Radboud University. The work was financially supported by the Netherlands Organisation for Scientific Research (NWO, Dutch Astrochemistry Network-II).

Contents

Chapter 1

Introduction

1.1 The structure of carbon

The ouroboros returns

This thesis is about polycyclic aromatic hydrocarbons (PAHs). Although it originates in first instance from the importance of these compounds in astrochemical research, the topic by itself would definitely have appealed quite a lot to the organic chemists in the mid- and late 19th century as well. In fact, one could very well say that present astronomers are taking the interest in the structure of carbon that organic chemists had in the 19th century. The detection of over 200 abundant and widespread molecules in space nowadays with most of the larger molecules containing carbon has prompted astronomers to look at matter and space between stars on a molecular level. At the same time, the interpretation of such astronomical observations heavily relies on knowledge acquired here on earth in the laboratory, thereby giving molecular physicists a leading role in elucidating the complexities of carbon evolution in space and providing an excuse to perform laboratory experiments.

One of the first scientists, and certainly one of the most influential, to represent an organic molecule using a ball-and-stick model is Friedrich August Kekulé. While this particular schematic view of molecules consisting of atoms linked together by bonds is nowadays trivial for most people (think of the Atomium in Brussel), this so-called atomistic view of molecules was at that time only just being accepted. It is remarkable that with the limited experimental tools chemists had then and there, they were able to deduce the microscopic atomic architecture of molecules. Before that, chemists had concluded that the composition and sequence of atoms in a molecule relates to the physical properties of the bulk material, such as boiling point, melting point etc. However, the observation of molecules with the same composition but with varying physical properties, isomers, incited chemists to expand their molecular models. It became the major drive in discovering the structure of molecules: the desire to explain the number of possible isomers or derivatives of a molecule.

Kekulé linked the physical properties of bulk chemicals to the three-dimensional arrangement of atoms within a molecule. Specifically, he suggested the use of tetravalence and the tetrahedral structure of carbon. With this suggestion, he laid the groundwork for his students (of which three were given the Nobel prize in chemistry!) and many other organic chemists. One of the organic molecules that Kekulé is particularly known for is benzene, belonging to the class of aromatic molecules, characterized by their pleasant odor. He writes about these aromatic compounds: “when one performs forceful reactions on aromatic substances, often a part of the compound is eliminated, but the major product consist of at least six carbon atoms that can bind six other atoms”.[1,2] The major product of six carbon atoms, called benzene, is now indeed known to be stabilized by

aromaticity (a different meaning of the word), and therefore survives the forceful reactions. Only one isomer was found for every mono-substituted benzene and three isomers for every disubstituted benzene, implying an equivalence of the six carbon atoms. Kekulé wanted to explain, in light of the tetravalence of carbon, which structure of six equivalent carbon atoms could bind six other atoms. The most obvious, a chain of six carbon atoms with alternating single and double bonds would be able to bind more than six atoms, so would not be a workable solution. After what must have been a horrifying dream about a snake biting its own tail, he concluded the following: "if the two carbon atoms at the end of the chain are connected to each other by a bond, so that one has a closed chain, one arrives at a core of six carbon atoms that still has six free bonds". Kekulé hypothesized further that the six carbon atoms form a symmetric ring so that they occupy analogous places in the molecule and are therefore truly equivalent. Benzene, he says, could be represented by a hexagon (Figure 1.1). The symbol of a snake biting its own tail, the ouroboros, intentionally or ironically, is one of the oldest symbols in alchemy, representing the eternity and endless return of matter.

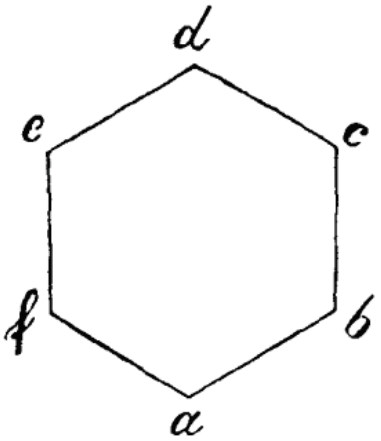

Figure 1.1: The hexagonal structure of benzene drawn by Kekulé[2]

1.2 Molecular structure and light

The third dimension

Jacobus Henricus van 't Hoff, a theoretical physical chemist, was a student of Kekulé. Less than ten years after Kekulé's proposal of the hexagonal structure of benzene, van 't Hoff

published his “Voorstel tot uitbreiding der tegenwoordig in de scheikunde gebruikte structuur-formules in de ruimte; benevens een daarmee samenhangende opmerking omtrent het verband tussen optisch actief vermogen en chemische constitutie van organische verbindingen”.[3] With this publication, van ’t Hoff introduced the idea of the asymmetric carbon atom. He wanted to account for some cases of substances where more isomers were found than models at that time could account for. He realized that if a carbon atom is saturated with four different groups, two tetrahedrons can be constructed that are each other’s mirror image, and that they can never be superimposed: one has two isomeric structures. With this hypothesis he was able to systematically account for all observed isomers, but equally important, he was able to make a connection between the three-dimensional structure of a molecule and its optical activity. Van ‘t Hoff concluded that every organic solution that rotates the polarization of light must contain such a three-dimensional asymmetric carbon atom. The work of van ‘t Hoff established a new paradigm in all areas of chemistry, where understanding the three dimensional structure of a molecule is key to explaining its properties. In a way, the theory of Van ‘t Hoff added one extra dimension to chemistry: where Kekulé and others represented molecules mostly in two dimensions, the new paradigm made chemists use a three-dimensional arrangement of atoms to explain molecular properties (Figure 1.2). Later, van ‘t Hoff was allowed to set up his own laboratory in Amsterdam and received the first Nobel Prize in Chemistry for his work in physical chemistry on dilute solutions and osmosis. The direct connection between the three-dimensional structure of a molecule and its optical -that is, in the case of the present thesis, spectroscopic- properties is used throughout the presented studies; it is no exaggeration to say that one could not do without.

Figure 1.2: Tetrahedrons used by van ‘t Hoff as models for the structure of tetravalent carbon. The double tetrahedrons are used as model for structures containing a carbon-carbon double bond. Credit: Rijksmuseum Boerhaave

Not much later, in the beginning of the 20th century, a technique was developed that gave unprecedented insight into the structure of matter, x-ray crystallography. After pioneering work by von Laue and William Henry and William Lawrence Bragg, it became possible to determine atomic positions within a crystal. In 1914, father and son Bragg applied the new method of x-ray crystallography to diamond and found an 'extremely simple' structure.[4] They confirmed the tetrahedral arrangement of carbon that was already being used by chemists such as van 't Hoff. Hypotheses made by chemists were thus being confirmed by physicists. One further example of interest comes from 1917. In that year, Peter Debye and Paul Scherrer used the recently discovered method of crystal powder x-ray diffraction to investigate the structure of graphite. They concluded that the carbon atoms in graphite were arranged in plane hexagons and that benzene itself might be of a similar form. X-ray work on liquid benzene suggested they were dealing with a very flat molecule.[5] In 1929, Kathleen Lonsdale confirmed that the benzene ring in hexamethylbenzene is indeed hexagonal and planar, similar to the structure and size of the carbon arrangement in graphite.[6] As yet, we have primarily focused on explaining optical properties as a result of the three-dimensional arrangement of atoms. It is clear that the other way around, namely to use light to investigate the structure of molecules, is highly rewarding and one of the points of focus of current research.

1.3 Quantization of energy

"An act of desperation" – M. Planck

Concurrent with the development of the atomistic model of molecules was the discussion on the relation between mechanics and thermodynamics. Max Karl Ernst Ludwig Planck was fascinated by the second law of thermodynamics that the entropy of an isolated system can only increase or remain constant: the law that gives an arrow of time to natural processes. At around the same time, a major challenge in physics was to describe the radiation emitted by a black body, a concept introduced in 1860 by Kirchhoff, professor of physics in Berlin prior to Planck. A black body is an object that absorbs all incident electromagnetic radiation and although an ideal black body does not exist, it proved to be crucial in the development of quantum theory. A black body emits radiation depending on its temperature: a hot body emits more radiation and radiation with a shorter wavelength than a colder body. Think of an iron nail in a flame which first becomes red and then bright white as it gets hotter. To explain these properties, physicists made successive comparisons between theoretical and experimental spectra of black-body radiation, which led to new insights (Figure 1.3). Such a practice can in fact also be recognized all throughout the present thesis.

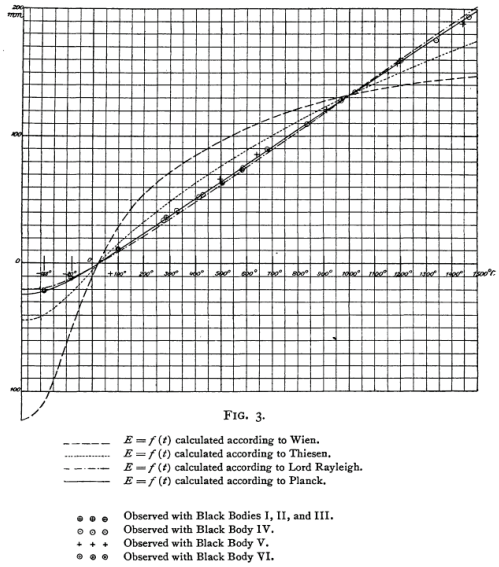

Figure 1.3: The successive comparison of different theoretical models of black body radiation to experiments led to the concept of energy quantization (extracted from [7])

In first instance, Planck used Wien's empirical radiation law, which was in good agreement with measurements performed in Berlin, and gave it a theoretical foundation. In 1899 he established a true physical character of Wien's law based on the entropy of an ideal oscillator.[8] However, new results from Berlin showed a disagreement between the experiment and Wien's law at low frequencies and this prompted Planck to go back to the drawing board. Planck was reluctant to use Boltzmann's ideas about the connection between entropy and probability which were based on an atomistic concept of molecules. But in what he recalls as 'an act of desperation', he obtained a fundamental basis of a new law that agreed perfectly with all measurements using Boltzmann's theory on probabilistic entropy.[9] The latter theory established a direct relation between entropy and disorder as expressed in what is now known as the Boltzmann equation. To quantify disorder, Planck distributed the total energy of a black body amongst oscillators that have finite 'energy elements', the number of possible ways a distribution can be realized yields the entropy.

One would say that with the introduction of 'energy elements' and Planck's constant, quantum theory is born, but the essential role *and* consequences of energy quantization were only realized later by, in particular, Einstein. By introducing the quantization of light he consolidated quantum theory. After all, both Planck and Einstein received the Nobel prize for their contribution to quantum physics. Other creative scientists further

developed the new description of atoms, molecules and their properties known as quantum mechanics: Niels Bohr added the atomic model accounting for the stability of atoms, Louis de Broglie postulated that matter had wave-like properties, Werner Heisenberg formulated the uncertainty principle for wave-like systems, Erwin Schrödinger postulated the Schrödinger equation that governs the evolution of a quantum mechanical system. Together with Paul Dirac, Max Born, Wolfgang Pauli and other scientists they conceived the quantum mechanics which forms the foundation on which we rely nowadays for interpreting experiments. The quantized particles of light, photons, still offer us the most direct experimental probe into the structure and quantum mechanical nature of atoms and molecules.

1.4 Carbon in the universe

Molecular physics comes to life

The scientific discipline that focusses on the interaction between light and matter is called spectroscopy. As will become clear below, quantization of energy is key in this respect, because quantum mechanics tells us that atoms and molecules have discrete energy levels. Transitions between these levels -as occurring when light interacts with matter- are thus only possible for particular frequencies of light. In other words, the uniqueness of atoms or molecules is imprinted into its electromagnetic spectrum. Thus, we can use light not only as a probe to examine quantum mechanical properties, but also to identify atoms and molecules.

The latter feature makes spectroscopy come to life in astronomy, since the most practical way to study distant astrophysical objects is by studying the light that is absorbed or emitted by these objects and that reaches our 'eyes' by means of ground- or space-based telescopes. Fraunhofer was the first to detect a number of dark lines in the emission spectrum of the sun, mostly in the visible region of the electromagnetic spectrum. Already in the early 19th century, he concluded that the dark lines contain information on the source of the light. Sadly, only after his death, Kirchhoff (Planck's predecessor in Berlin) assigned the lines to atomic absorptions, because they coincided with emission lines in the spectra of specific heated elements.[10] Fraunhofer thus was correct in saying that the dark lines contained information about the source, and more specifically, about the chemical elements present in the star's atmosphere.

The first molecule to be detected in space was the carbon-containing diatomic CH, by means of its strong electronic transition in the visible region of the spectrum.[11] A true revolution in astrochemistry came with the development of radio astronomy in the 1960s that enabled scientists to detect a vast amount of new molecules in the interstellar

medium (ISM) or circumstellar medium (CSM). One major shortcoming, however, is that radio astronomy is 'blind' to (highly) symmetric molecules. The reason for this is that the strength of a rotational transition of a molecule (occurring at radio frequencies) is proportional to the square of the permanent electric dipole moment. Symmetric molecules are often non-polar and therefore pure rotational transitions are not allowed. Moreover, as molecules increase in size, the number of accessible energy levels increases at a given temperature. This results in substantial decrease of the chance that molecules in an ensemble absorb or emit at the same frequency. The technique thus has a bias towards smaller molecules. Nowadays, the two largest molecules detected in space are the fullerenes C_{60} and C_{70}, specifically in a young planetary nebula[12]. These highly symmetric, large molecules were not identified using electronic or rotational transitions, but based on vibrational emission spectra in the infrared region. Later, the C_{60}^+ ion was assigned using two electronic transitions in the near-infrared.[13,14]

Despite the vast number of smaller molecules identified and the detection of fullerenes, many spectral features remain unidentified. An old mystery, discovered almost a hundred years ago in 1922 by Mary Lea Heger, concerns spectral features caused by the absorption of light by the interstellar medium and now referred to as the diffuse interstellar bands (DIBs).[15] These are sharp features observed from the near-infrared to the UV part of the spectrum and have remained nearly completely unassigned (an exception being C_{60}^+). Moreover, in the mid- and far-infrared region, distinct emission features are observed towards many different phases of the ISM, including planet-forming disks, surfaces of dark clouds, star-forming regions, carbon-rich stars in their last stage, and the general diffuse ISM. Airborne, ground- and space-based telescopes observe the infrared emission in these different regions referred to as the unidentified infrared bands (UIRs).

In 1984 Léger and Puget hypothesized that polycyclic aromatic hydrocarbons (PAHs) are the carriers of the UIR bands (Figure 1.4).[16] They based their hypothesis on the thermodynamic properties and the chemical stability of PAHs. PAH molecules, temporarily heated by absorption of a UV photon, would lose their energy through radiative transitions between vibrational levels that occur in the infrared. One year later, Allamandola *et al.* presented the first spectroscopic indications of the presence of PAHs in the ISM by comparing nothing less than Raman spectra of car exhaust (PAHs are major constituents in soot particles) to the UIR spectra of the Orion Nebula.[17] The hypothesis that PAHs are responsible for the UIR bands is now widely recognized and the UIR bands are now often termed the aromatic infrared bands (AIBs).[18] Some intensity of the UIRs may be the result of aliphatic hydrocarbons, but the dominating contribution is from aromatic species. PAHs can not only explain the UIR bands, but also form a link between the smaller organic molecules identified by radio astronomy and fullerenes. Moreover, there are strong indications that electronic transitions of molecules such as PAHs are responsible for the DIBs. PAHs are thus key species to understand the organic inventory in space and are

quite probably the stepping stone for assigning and understanding many, still unidentified spectral features in astronomical observations.

Although there is a diverse distribution of PAHs, there are indications that this distribution is dominated by a limited set of PAHs. One such an indication is that there is a remarkable spectroscopic similarity up to the smallest details between observed spectra of photodissociation regions (PDRs) in different reflection nebulae.[19] Moreover, it has been shown that a preference for a small set of theoretical spectra of large and compact PAHs exists to fit particular spectral features (the 15-20 μm band patterns).[20] Additionally, only a small number of PAHs are able to account for the strong absorption at one particular wavelength (the 11.3 μm band). The subtle variations that do exist between the observed spectra can be explained by slight variations in the distribution of such a small set of PAHs.[19,21] This set of larger PAHs thought to be stable enough to survive the harsh conditions of the ISM have been branded grandPAHs.

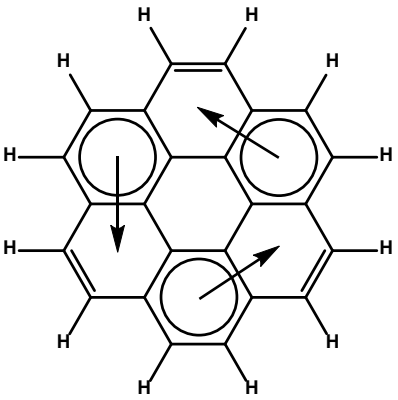

Fizure 1.4: Molecular structure of the PAH coronene ($C_{24}H_{12}$) described by Clar's aromatic π-sextet model

The term polycyclic aromatic hydrocarbon (PAH) is autological and refers to molecules composed of multiple, often fused, rings (polycyclic), consisting of hydrogen and carbon (hydrocarbon), stabilized by aromaticity (aromatic). Although one may not realize, we are constantly surrounded by PAHs in our daily life. They are a major constituent in soot in almost all natural and anthropogenic combustion processes, they are present in burned food, and even mothballs are made of PAHs. Derivatives of PAHs are already used in electronic devices because of their tunable photophysical properties[22,23], but also their stability holds great promise and will most likely make them much more common in future technological applications. PAHs are stabilized due to aromaticity, where the term aromaticity is no longer used for referring to their odor, but to aromatic stability as will be explained later in this paragraph. As a result, this particular form of hydrocarbons is more fit to withstand the hostile environment of the ISM, and this is the reason that much

carbon in space is locked up in PAH molecules. Kekulé described benzene as rapidly interconverting between two structures with alternating single and double bonds.[24] However, it was Erich Hückel working with Peter Debye in Zürich who used a number of approximations to describe the electronic structure of polyenes - fully utilizing the symmetry of the molecules and breaking free from the classical chemical bond- thereby uncovering the quantum mechanical origin of aromatic stability.[25] One approximation was that all carbon atoms are identical and having equal bonds to all its neighbors, resulting in the delocalization of electrons. Another Erich -Erich Clar- worked on extending the theory of aromatic systems to larger benzenoid species. Based on many experiments, he described in *The Aromatic Sextet* how a myriad of properties of PAHs can, at least qualitatively, be explained by the number and location of aromatic π-sextets, that is to say, benzene moieties.[26] He formulated a rule stating that the resonance structure of a PAH with the largest number of aromatic π-sextets (or a superposition of equals) contributes most to the electronic characteristics of the molecule. The other rings are generally more reactive. Moreover, he stated that isomers containing more aromatic π-sextets are more stable than isomers with less aromatic π-sextets and that the non-π-sextets in the dominant resonance structure are most reactive. Using Clar's insights, spectroscopic properties such as the HOMO-LUMO gap, the ionization potential, and others can amazingly well be understood.

In the previous, PAHs and their properties have been considered from a more historically oriented perspective. This is important because it has set the stage for starting to explore the unknowns that the studies in this thesis aim to put light on. To this purpose, the remainder of this chapter will focus in more detail on the spectroscopic properties of PAHs and their role in the universe.

1.5 Spectroscopy of cosmic PAHs

Molecular probes to follow the evolution of the universe

Besides fullerenes, PAHs are the largest molecules found in space. They are the result of combustion-like chemistry in stellar ejecta and continue being processed in the ISM, but also influence the very same chemical processes and physical environment. Thereby, they catalyze other chemical reactions and even influence star and planet formation. PAH emission features are detected across all phases of galactic evolution, from star forming regions to proto-planetary disks and even in meteorites. Depending on their environment, they can interact with other atoms or molecules and are subjected to energetic particles and photons. They can act as a nucleation site (also in the earth's atmosphere)

for grain formation and thereby affect the condensation in dense molecular clouds. In these molecular clouds they also influence the temperature and charge balance, and can function as a radiation shield for the clouds interior.[27] It is therefore clear that understanding the composition and evolution of molecules -and PAHs in particular- in space is key to comprehend the evolution of the universe.

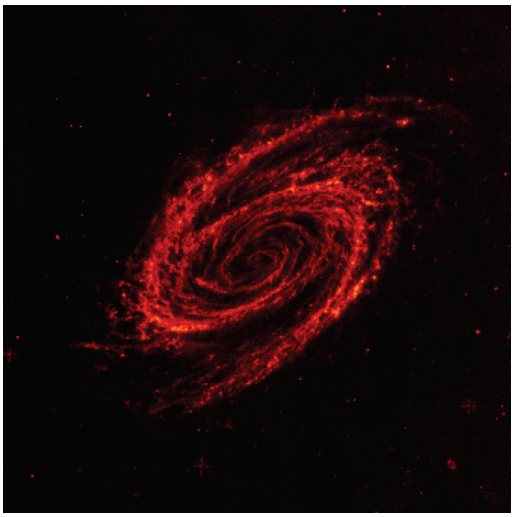

Figure 1.5: PAHs are valuable tracers for following the evolution of galaxies. This observation shows the spiral arms of the nearby galaxy Messier 81 located in the constellation of Ursa Major made by the Spitzer Space Telescope at 8 μm (red, PAH emission, processed). Credit: NASA/JPL-Caltech

The widespread presence and involvement of PAHs in the universe makes them valuable tracers for star and planetary formation. Most ultraviolet (UV) and optical light emitted by young stars is absorbed by dust and PAHs and re-emitted in the infrared. This makes the PAH emission dependent on the radiation intensity of a star and thereby its formation rate. In star-forming regions, this IR emission even dominates over the stellar emission beyond about 5 μm.[28] Observing and interpreting the IR emission provides us with a solid basis for understanding the interstellar environment and setting up astronomical models for its chemical evolution, as well as the formation of stars and planets.[29] With this recognition, it should be said that the infrared space observatories revolutionized PAH research. The Infrared Space Observatory and subsequently NASA's Spitzer Space Telescope provided us with both images and spectra of emission by PAHs associated with star formation in our own galaxy or in the distant universe (Figure 1.5). The Spitzer Space Telescope was named after Lyman Spitzer, who suggested the use of space telescopes to avoid the limitations that arise by looking through the earth's atmosphere. The capabilities of the upcoming James Webb Space Telescope will bring this research to an entirely

new level by providing higher sensitivity and spatial resolution and covering a broad wavelength range.[30] The interpretation of the wealth of observations that will be unleashed relies on a profound understanding of the photophysical properties and chemistry of molecules in space and PAHs in particular. For spectroscopists the task is here to support such understanding by laboratory experiments and theory. A major challenge and yearning objective that this task accompanies is to investigate the infrared spectra of grandPAHs under cold and isolated conditions.

In order for a PAH to make a vibrational transition and absorb or emit infrared light, the electric dipole must change during the vibration. The vibrational motion of molecules consisting of N atoms can (in the harmonic approximation) be described by a set of (3N-6) orthogonal vibrations called normal modes that can be excited independently. Within this approximation one can associate each normal motion with a specific harmonic potential energy surface on which the vibration takes place. The shape of the potential energy surface determines the vibrational energy levels between which transitions can take place. The extent to which the dipole is affected and the spacing between energy levels in vibrational modes determines the resulting intensity and frequency of IR bands, respectively. Since the structure of PAHs is very similar, many modes of different PAH species will have similar potential energy surfaces, and thus coinciding IR transitions. Hence, spectral identification using IR emission of a single PAH species from a mixture is fairly complicated. The strong CH stretch mode in the mid-IR, for example, is a localized vibration involving the C-H bonds and is only marginally affected by the global PAH structure. Delocalized vibrations such as the drumhead motion, on the other hand, are much more dependent on the full structure of the molecule. Transitions of such vibrations occur at longer wavelengths, making the far-IR a promising diagnostic region. A link between the mathematical question: '*can one hear the shape of a drum*' is suited here, teaching us that, indeed, the shape of a drum can be estimated using a finite number of frequencies.[31] For PAHs, however, also observational limitations by the dust background emission and the intrinsic weak transitions make the far-IR a challenging region.

Interstellar PAH emission originates from PAHs that relax to the ground state after absorbing a (F)UV photon from, for example, nearby stars.[32] The absorption of a UV photon brings a PAH into an electronically excited state and via internal conversion and intersystem crossing, the photon energy is converted into vibrational energy. Due to the low density in the ISM, PAH molecules do not lose their vibrational energy through collisions with other molecules, as collisions occurs on the order of a day. As a result, they are not in thermal equilibrium with their environment. Instead, PAHs lose the energy they receive roughly yearly by the emission of infrared photons through a vibrational cascade on the timescale of seconds.[33] The observed infrared emission spectrum is an average over different relaxation pathways of different PAHs. Because the laboratory reproduction of spectra of a large number of (grand)PAHs under a wide variety of directly relevant

interstellar conditions is extremely demanding and difficult, interpretation relies on theoretical modeling of such emission cascades. Then again, in the construction of these emission models, experimental validation of the intrinsic infrared spectra of PAHs -that is under cold and isolated conditions-is of fundamental importance.

In recent years, such experimental validation of calculated IR spectra has revealed the much larger than expected limitations of the harmonic approximation in the CH stretch region[34]. Especially in this higher-energy region with a high density of vibrational states, anharmonic effects play an important if not dominant role in determining the appearance of the IR spectrum[35]. In this thesis we therefore heavily rely on amending the insufficiencies of the harmonic approximations by using what will be called an 'anharmonic treatment'. This treatment firstly includes an improved asymmetric shape of the potential, that can lead to a shift in transition frequencies. Secondly, in the anharmonic framework modes can interact with each other, allowing for energy redistribution and causing shifts in band positions of vibrationally excited molecules. Furthermore, if two vibrational energy levels are close in energy, they can interact and typically push each other apart in energy. Finally, anharmonic perturbations do not only affect the energies of vibrational levels but can also influence the intensity of transitions between them. Although the above might seem to imply that anharmonicity rules the entire vibrational spectrum, this is certainly not the case. In fact, one of the surprising conclusions of our studies is that low-frequency modes -that a priori always were deemed to be anharmonic- are in fact well described by the harmonic approximation.

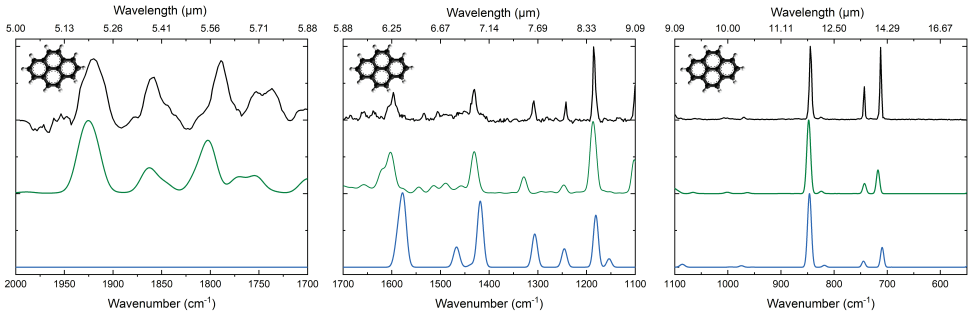

Figure 1.6: Comparison between calculated and experimental spectra of pyrene indicated in top left corner. Top, black: absorption spectrum obtained using IR-UV ion dip spectroscopy. Middle, green: anharmonic predicted spectrum, taking into account resonances and combination bands (no frequency scaling). Bottom, blue: prediction with the harmonic approximation (NASA Ames Database, with linear frequency scaling).

1.6 Chemistry of cosmic PAHs

"A tale of cold black giant clouds and warm red giant stars" – H. Kroto

The ability to form complex species such as PAHs makes carbon a major player in the evolution of the universe. Although the abundance of carbon is much lower than hydrogen or helium, its capacity to form multiple bonds makes it chemically much more interesting and results in the fact that most detected molecules contain at least one carbon atom.

The formation of organic molecules, including PAHs, starts with the formation of carbon. Carbon begins its cycle in the interior of stars, where it is produced by nuclear fusion. Asymptotic giant branch (AGB) stars are important contributors in the formation of carbon. Convective processes drive elemental carbon or oxygen to the surface and around the exterior CO is formed. If carbon is more abundant than oxygen, it is not captured in CO. Especially towards the end of a star's life, much of the interior of the star is ejected into the interstellar medium (ISM). In a way, the ISM can be considered as a repository of matter, as it contains ashes from previous stars that at some point can form new stellar systems. In the ISM, material circulates in about hundred million years between more diffuse and dense regions, while being processed by cosmic radiation. At a certain point, dense (molecular) clouds collapse and form new stars and planets, taking up the carbon that was ejected by previous stars.[36] One such cycle takes a few billion years and considering that the universe is 13 billion years old, most stellar systems are now from second or third generation. In fact, our sun is a third-generation star meaning that most of the carbon on our planet and in our bodies has also been through such a stellar cycle.

The formation mechanisms of larger molecules, PAHs and grandPAHs in particular, are of great interest to astrochemists. They are expected to form the connection between small organic molecules -of which many have been identified- and large fullerenes. But also for the production of carbon-based technology that includes fullerenes, carbon nanotubes or graphene, the chemistry of aromatic carbon is important. Also not to forget is the chemistry leading to soot, which is emitted into the atmosphere in large quantities by human combustion. However, current formation models are inadequate in accounting for the observed production rates and abundance of PAHs in the ISM.[37,38] The shortcoming is a consequence of an incomplete picture of the complexity of the network of reactions.[39]

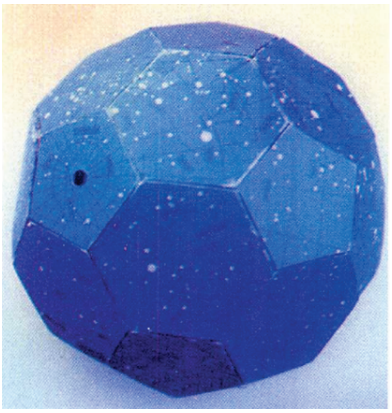

Figure 1.7: A card model of a truncated icosahedron with a map of the night sky that played a key role in the discovery of C_{60} Buckminster fullerene[40]

It is up to laboratory experiments to discover yet unknown reaction pathways, especially towards larger PAHs and fullerenes. The key role that laboratory astrochemistry plays here is best exemplified by the story of Buckminsterfullerene discovered by Harold Kroto.[41] In experiments aimed to reveal the chemistry of carbon molecules that are formed in interstellar space, Kroto and coworkers discovered a remarkably stable cluster consisting of 60 carbon atoms. The cluster was formed in a laser-induced plasma of carbon from a graphite surface. With little to go on, Kroto suggested that the C_{60} molecules should have a truncated icosahedral structure (like a football). He named it Buckminsterfullerene after consulting the studies of Richard Buckminster Fuller, living in Carbondale, of all places! Received with skepticism in the beginning, the discovery of the so called fullerenes, a new allotrope of carbon, was crowned with the Nobel Prize in Chemistry in 1996. The success story does not end there, turning full circle back to astrochemistry. The very same molecule discovered in 1985 in the laboratory has quite recently been detected in the young planetary nebula Tc 1 by the Spitzer Space Telescope[12].

To date, fundamentally new bimolecular reactions are continuously being revealed and as for the complexity of the reaction network involving PAHs, laboratory astrochemistry has just scratched the surface. In this thesis, the reaction network of relatively simple aromatic hydrocarbons in a discharge is revealed by mass selective IR spectroscopy. The experiments are complementary to other gas-phase complex mixture analyses such as microwave spectroscopy, as a wealth of new, non-polar molecules such as PAHs -not observed by microwave spectroscopy- are identified to be formed here. In constructing astrochemical models that describe the chemical evolution of the interstellar or circumstellar medium, the intermediate and product species that we identify serve as key ingredient. Combined with quantum chemical calculations on reaction surfaces, one can start to build quantitative models, where the polar intermediate abundancies can be

benchmarked against the microwave studies. But because PAHs are expected to play a major role the interstellar carbon chemistry, the identification of their specific configuration and place within a reaction network in gas-phase conditions will be a pillar in constructing reliable astrochemical models.

1.7 In this thesis

In this thesis, infrared light is used to probe the potential energy surface and intrinsic spectroscopic properties of large PAHs and PAH complexes. Using a cold molecular beam in combination with narrow-band lasers, the experiments in this thesis provide detailed insights into the spectroscopic properties of PAHs, from the near- to the far-IR. Experimental spectra are compared to theory with special attention given to the astrophysical implications of the interpretation of the AIBs. Such comparisons allow us to come to a true understanding of the fundamentals governing these spectra, and this in turn is -and must be- the basis for advancing the state-of-the-art of models interpreting astronomical observations. At the same time, infrared spectroscopy is applied to explore gas-phase chemistry of PAHs in controlled conditions aimed at understanding the formation mechanisms of PAHs in interstellar space, the other key element for advancing the state-of-the-art of these models.

In the experiments reported on in this thesis, rather than examining the effect of the molecules on light by absorption spectroscopy, the effect of light on molecules is probed indirectly using action spectroscopy. The reason for this is that the attenuation of light by a dilute molecular beam is very small. Instead, the ions that are created by laser light via Resonance Enhanced Multi-Photon Ionization (REMPI) are monitored by a time-of-flight mass spectrometer. If the laser light is resonant with an electronic transition in a molecule, an increase in ion yield at the corresponding mass is detected, which can be translated to an electronic absorption spectrum. IR spectra are also recorded using action spectroscopy, via the IR-UV ion dip scheme. This scheme relies on the change of the vibrational population in the electronic ground state after IR absorption. Resonant IR excitation results in a decrease of the ion signal (ion dip) produced by the REMPI process. Knowing the exact mechanism of IR-UV ion dip is essential to relate the magnitude of ion dips to absolute absorption cross sections. In Chapter 2, REMPI spectra recorded after far- and mid-IR absorption provide unique insights in the mechanism of IR-UV ion dip in the far-IR, but also in the properties of delocalized modes of PAHs. The delocalized character of far-IR vibrational modes generally makes them more dependent on the complete structure of a PAH and therefore valuable for astronomical identification of specific molecules. So far, this region has been relatively unexplored under relevant conditions in the laboratory, that is, under isolated conditions and at low temperatures. The far-IR region

is covered by the free-electron-laser FELIX located in Nijmegen, where most experiments have taken place.

The successful comparison between high-resolution gas-phase experimental and theoretical spectra in previous studies involved relatively small PAHs in the CH-stretch region. It is not clear at all to what extent the currently employed models need to be adapted for larger molecules such as the ones classified as grandPAHs, but this clearly is crucial for assessing astronomical observations in which gransPAHs are thought to play a prominent role. Producing a sufficient amount of gas-phase grandPAHs to seed into a molecular beam has so far restricted many experiments to smaller species. Generally, the transition to the gas phase is achieved by resistive heating but at temperatures that in practice can still be reached, the vapor pressure of grandPAHs is insufficient. In order to meet this challenge, grandPAHs are brought into the gas phase by laser desorption and subsequently entrained and cooled in an expansion of a noble gas. Laser desorption is routinely used to bring large biomolecules that cannot be heated without fragmentation into the gas phase. The desorption laser is mildly focused on a graphite sample bar on which the sample is deposited. The laser pulse instantly heats a small portion of fresh sample, which desorbs nearly without fragmentation. For grandPAHs, the fast and extreme heating is more than sufficient to bring ample amount of molecules into the gas phase. In Chapter 3, the gas-phase mid-IR spectra of the polyacene series from naphthalene to pentacene are characterized, thereby expanding the comparative studies to longer wavelengths. Considering that the mid-IR is potentially a more diagnostic region for identifying certain classes of PAHs in the ISM, an accurate description of this spectral region is quite important to astronomers. Using the free electron laser FELIX, a broad wavelength range is covered that is used to evaluate (anharmonic) theoretical methods. We show that a significant fraction of intensity is associated with combination bands in the 5-6 μm region that cannot be ignored. At longer wavelengths, the anharmonically predicted spectra are in good agreement with experimental results. Laser desorption made it possible to extend studies to the larger, involatile pentacene species, opening a route to investigate even larger PAHs under suitable conditions.

Motivated by the hypothesis that a small set of most stable PAHs could dominate the population, the laser desorption route to larger PAHs is pursued in Chapter 4. The infrared spectra of coronene, ovalene, hexa(peri)benzocoronene and peropyrene under cold and isolated conditions are reported and compared to harmonic and, where available, anharmonic calculations. The grandPAHs are investigated in both in the mid- and far-IR, from 3 to 100 μm (3150 to 100 cm^{-1}) thus covering the entire relevant wavelength region. The different regions of the infrared spectra all have their advantages and disadvantages. Whereas the 3 μm CH-stretch region is accessible by ground-based telescopes, our studies show that this region is dominated by resonances and anharmonic shifts, complicating the analysis. Furthermore, the dependence on large-scale structure is considerably

less at shorter wavelengths where moreover interstellar emission is broad. This changes when moving to longer wavelengths. However, in the CH out-of-plane region, which is more dependent on size and topology, we find that the anharmonic treatment of grand-PAH spectra -in contrast to the same treatment applied to smaller PAHs- leads to unrealistic results that impede the comparison between experiment and theory. The holy grail, therefore, seems to be found in the far-IR where the delocalized modes are most diagnostic for specific molecules and the emission is more narrow. Here, however, the major drawback arises from the observational side as the bands in this region have a low intensity, which, together with the dust background emission, impedes identification of spectroscopic signatures of PAHs. Evidently, the most promising way forward is to use a combination of all regions to determine the composition of the PAH population, which is one of the incentives for the full-spectrum approach taken in Chapter 4.

The chapters 2, 3 and 4 elucidate mainly on the mechanical potential energy surface of vibrational motions. In Chapter 5 the focus is on the electric potential and oscillator strength of transitions in the infrared. By combining data from several theoretical and experimental sources, predicted oscillator strengths of the CH out-of-plane and CH stretch vibrations are examined. The ratio between these bands is commonly used to determine the size distribution of PAHs in the ISM and appears to have been underestimated. Chapter 5 gives an impression of the implications of this underestimation on the determination of the size distribution of PAHs in the universe.

Until now, we only considered covalent interactions between carbon atoms. More and more, however, it is realized that non-covalent, long-distance interactions can play a major role in supramolecular chemistry, the properties of materials, the function of biomolecules and many more fields. Chapters 6 and 7 concern homo- and hetero complexes of PAHs that exist by the grace of the weak intermolecular forces, collectively called van der Waals forces, named after a colleague of van 't Hoff, Johannes Diderik van der Waals. Non-covalent complexes of PAHs are of particular relevance to astrochemistry, or combustion chemistry for that matter, as they embody the initial steps of condensation and soot formation. They bridge the gap between gas phase and solid-state configurations of carbon. Moreover, the condensation of small molecules such as water on the surface of aerosols is at the core of cloud formation. Soot particles consisting of PAHs can form a major fraction of aerosols in polluted areas. A detailed understanding of the non-covalent interactions is essential to determine and understand the structure of such molecular complexes and their (spectral) characteristics. Chapter 6 focusses on the far-IR and UV spectral signatures that result from the interactions between PAHs and water.

A special type of non-covalent interactions, π-π stacking, manifests itself in stacked aromatic units. The π-π stacking effect, can be viewed as the energy difference between stacked aromatic rings and saturated rings of the same size. It is not common knowledge

that the π-π stacking effect solely occurs in parallel oriented aromatic molecules and does not originate from π-orbital overlap or electrostatic forces. Instead, theory indicates that the π-π stacking effect results from non-local electron correlation from systems with spatially close π-orbitals. Moreover, for small aromatic units, such as the ones often present in biomolecular systems, the π-π stacking effect is calculated to be less important than other non-covalent interactions. In fact, the benzene dimer is found to adopt a T-shaped rather than a parallel configuration. For large aromatic systems, on the other hand, it is well established that the strong adhesive force between monomers is due to a significant π-π stacking effect. In Chapter 7, infrared spectroscopy is used to probe the weak interactions that exist between systems consisting of two aromatic rings. The experiments provide strong indications for the geometry of the dimers and thereby contribute to insights in the peculiar π-π stacking interactions between aromatic molecules.

It is remarkable that in the dilute conditions of the interstellar medium, large organic molecules such as PAHs or even grandPAHs are formed. Now, more than ever, it is of interest to elucidate the formation pathways because both polycyclic species (1- and 2-cyanonaphthalene, fullerenes) and small aromatic molecules (benzene, benzonitrile) have been detected. So far, most models describing gas-phase bottom-up formation pathways have proven insufficient to reproduce the observed abundancies of PAHs or their derivatives. It appears that either the existing reactions proceed more efficiently than expected or that additional routes, which have not been considered yet, play a significant role in the formation process. In recent years, multiple new and efficient reaction routes have been identified in crossed molecular beam experiments or in the pyrolysis of dilute gases. The pathways to polycyclic species discovered in the laboratory are supported by quantum chemical reaction surface calculations and often appear to be efficient at low-temperature conditions.

Despite these major advances in uncovering possible reaction routes, it is likely that quite a number of other routes still need to be discovered, especially when larger PAHs are concerned. Laboratory experiments play in this respect a key role. A complicating factor is the simultaneous operation of multiple, possibly entangled, pathways. Disentangling this complex network requires systematic identification of intermediates, products and abundances of reaction of PAHs under controlled conditions. Whereas in stellar outflows or the ISM photons ionize atoms or molecules and induce gas-phase reactions leading to larger species, the experiments reported here use an electrical discharge to make ions and/or radicals and initiate gas-phase reactions. Multiple spectroscopic techniques are complementary here to identify species in the complex reaction mixture. Microwave spectroscopy allows for the identification of the structure of a large number of molecules and to determine the relative abundances of different products. A major drawback is that the method is only sensitive to polar molecules and that species with larger masses are

harder to detect. It is expected that many polycyclic species are symmetric and do not have a permanent dipole moment. Since these species would be 'invisible', obtaining a complete picture of the reaction routes would become quite complicated. Mass-selective infrared spectroscopy in combination with quantum chemical calculations, on the other hand, is ideally suited for identifying non-polar, larger molecules. In Chapters 8 and 9, using naphthalene or benzene as precursor, many new species resulting from the complex network of PAH formation pathways are identified. The products reveal that multiple reactions leading to PAH growth occur simultaneously and competitively, findings that serve as a key ingredient for constructing reliable models of the carbon chemistry in the universe.

References

1 A. Kekulé, *Bull. la Société Chim. Paris*, 1865, **3**, 98–110.
2 A. Kekulé, *Ann. der Chemie*, 1866, **137**, 129–196.
3 J. H. Van 't Hoff, *Voorstel tot uitbreiding der tegenwoordig in de scheikunde gebruikte structuur-formules in de ruimte; benevens een daarmee samenhangende opmerking omtrent het verband tussen optisch actief vermogen en chemische constitutie van organische verbindingen*, Utrecht, 1874.
4 W. H. Bragg and W. L. Bragg, *Nature*, 1913, **91**, 557.
5 P. Debye and P. Scherrer, *Gött. Nachr.*, 1916, 16.
6 K. Lonsdale, *Proc. R. Soc. L.*, 1929, **123**, 494–515.
7 H. Rubens and F. Kurlbaum, *Astrophys. J.*, 1901, **14**, 335–348.
8 H. Kragh, Max Planck: the reluctant revolutionary, physicsworld.com, (accessed 23 April 2021).
9 M. Planck, *Ann. Phys.*, 1901, **309**, 553–563.
10 G. Kirchhoff, *Verhandlungen des naturhistorisch-medizinischen Vereins zu Heidelb.*, 1859, **1**, 251–255.
11 W. S. Adams, *Astrophys. J.*, 1941, **93**, 11–23.
12 J. Cami, J. Bernard-Salas, E. Peeters and S. E. Malek, *Science*, 2010, **329**, 1180–1182.
13 B. H. Foing and P. Ehrenfreund, *Nature*, 1994, **369**, 296–298.
14 E. K. Campbell, M. Holz, D. Gerlich and J. P. Maier, *Nature*, 2015, **523**, 322–323.
15 M. L. Heger, *Lick Obs. Bull.*, 1922, **10**, 141–145.
16 A. Leger and J. L. Puget, *Astron. Astrophys.*, 1984, **137**, L5–L8.
17 L. J. Allamondola, A. G. G. M. Tielens and J. R. Barker, *Astrophys. J.*, 1985, **290**, L25–L28.

18 A. G. G. M. Tielens, *Molecular Astrophysics*, Cambridge University Press, Cambridge, 2021.
19 H. Andrews, C. Boersma, M. W. Werner, J. Livingston, L. J. Allamandola and A. G. G. M. Tielens, *Astrophys. J.*, 2015, 807, 24pp.
20 C. W. Bauschlicher, A. Ricca, C. Boersma and L. J. Allamandola, *Astrophys. J. Suppl. Ser.*, 2018, **234**, 32.
21 B. A. Croiset, A. Candian, O. Berné and A. G. G. M. Tielens, *Astron. Astrophys.*, 2016, **590**, A26.
22 J.-H. Lee, C.-H. Chen, P.-H. Lee, H.-Y. Lin, M. Leung, T.-L. Chiu and C.-F. Lin, *J. Mater. Chem. C*, 2019, **7**, 5874.
23 D. Zhang and L. Duan, *J. Phys. Chem. Lett.*, 2019, **10**, 2528–2537.
24 A. Gero, *J. Chem. Educ.*, 1954, **31**, 201–202.
25 E. Hückel, *Zeitschrift für Phys.*, 1931, **70**, 204–286.
26 E. Clar, *The Aromatic Sextet*, Wiley, London, 1972.
27 A. G. G. M. Tielens, *Rev. Mod. Phys.*, 2013, **85**, 1021–1081.
28 D. Calzetti, *Nat. Astron.*, 2020, **4**, 437–439.
29 E. Herbst and E. F. Van Dishoeck, *Annu. Rev. Astron. Astrophys.*, 2009, **47**, 427–480.
30 M. Clampin, *Adv. Sp. Res.*, 2008, **41**, 1983–1991.
31 M. Kac, *Am. Math. Mon.*, 1966, **73**, 1–23.
32 E. Peeters, C. Mackie, A. Candian and A. G. G. M. Tielens, *Acc. Chem. Res.*, 2021, **54**, 1921–1933.
33 C. J. Mackie, T. Chen, A. Candian, T. J. Lee and A. G. G. M. Tielens, *J. Chem. Phys.*, 2018, 149, 134302.
34 A. Candian and C. J. Mackie, *Int. J. Quantum Chem.*, 2017, **117**, 146–150.
35 T. Chen, *Astrophys. J. Suppl. Ser.*, 2018, **238**, 18.
36 T. Henning and F. Salama, *Science*, 1998, **282**, 2204–2211.
37 A. M. Burkhardt, R. A. Loomis, C. N. Shingledecker, K. Long, K. Lee, A. J. Remijan, M. C. Mccarthy and B. A. Mcguire, *Nat. Astron.*, 2021, **5**, 181–187.
38 I. Cherchneff, J. R. Barker and A. G. G. M. Tielens, *Astrophys. J.*, 1992, **401**, 269–287.
39 R. I. Kaiser and N. Hansen, *J. Phys. Chem. A*, 2021, **125**, 3826–3840.
40 H. W. Kroto, *Nobel Lect.*, 1996, 44–79.
41 H. W. Kroto, J. R. Heath, S. C. O'Brien, R. F. Curl and R. E. Smalley, *Nature*, 1985, **318**, 162–163.

Chapter 2

Far-infrared absorption of neutral polycyclic aromatic hydrocarbons

This chapter is published as:
Alexander K. Lemmens, Daniël B. Rap, Johannes M. M. Thunnissen, Sébastien Gruet, Amanda L. Steber, Sanjana Panchagnula, Alexander G. G. M. Tielens, Melanie Schnell, Wybren Jan Buma, and Anouk M. Rijs*, The Journal of Physical Chemistry Letters*, **11**, 21, 2020.

2.1 Abstract

Gas-phase IR–UV double-resonance laser spectroscopy is an IR absorption technique that bridges the gap between experimental IR spectroscopy and theory. The IR experiments are used to directly evaluate predicted frequencies and potential energy surfaces as well as to probe the structure of isolated molecules. However, a detailed understanding of the underlying mechanisms is, especially in the far-IR regime, still far from complete, even though this is crucial for properly interpreting the recorded IR absorption spectra. Here, events occurring upon excitation to vibrational levels of polycyclic aromatic hydrocarbons by far-IR radiation from the FELIX free electron laser are followed using resonance-enhanced multiphoton ionization spectroscopy. These studies provide detailed insight into how ladder climbing and anharmonicity influence IR–UV spectroscopy and therefore the resulting IR signatures in the far-IR region. Moreover, the potential energy surfaces of these low-frequency delocalized modes are investigated and shown to have a strong harmonic character.

2.2 Introduction

Infrared absorption spectroscopy has proven to be a powerful technique for characterizing and monitoring the physical and chemical properties of molecules. The technique provides vibrational fingerprints that give direct access to their electronic and conformational structure. At the same time, they are also essential for obtaining insight into their thermochemistry and reaction dynamics. At the core of these applications is a full and detailed understanding of vibrations in terms of nuclear motions and the characteristics of the multidimensional electronic potential energy surface on which these motions take place. This is most effectively realized by comparing experimentally measured quantities with theoretical predictions. Such comparisons provide on one hand the means to assign an experimental spectrum but, equally importantly, are also key to assessing theoretical methods. High-resolution spectroscopy on isolated molecules plays in this respect an important role as it is the most direct means for making such comparisons. IR–UV ion dip spectroscopy is the ideal method for obtaining high-resolution, mass- and conformer-selective IR spectra.[1] In an astronomical context, IR–UV spectroscopy has proven to be indispensable for providing accurate band positions for relevant molecules such as polycyclic aromatic hydrocarbons (PAHs) and for evaluating various theoretical methods that aim to incorporate anharmonicity.[2–8] More widely, it is being used for the structural characterization of neutral and isolated molecules that range from peptides and DNA bases to molecular machines.[1,9–13]

The comparison between experiment and theory relies on not only the band positions but also their intensities. The latter are of particular importance within the framework of astrophysics where relative and absolute cross sections are used to determine the composition and abundance of molecular species in the universe.[14] To relate IR–UV ion dips to absolute absorption cross sections, a detailed understanding of the IR–UV ion dip mechanism is essential. Although the general principles of the method are well understood, detailed insight into the underlying processes is to a large extent lacking. The far-IR region is of special interest because it is less congested[15,16] than the mid- or near-IR regions, and the emission from interstellar space in the far-IR region is inherently less broad.[17] Moreover, the low-frequency modes of PAHs involve their global structure and thereby provide diagnostic fingerprints of their size and topology.

IR–UV ion dip spectroscopy is based on the change of the vibrational population in the electronic ground state of a molecule by IR absorption, which is probed by resonance-enhanced multiphoton ionization (REMPI) spectroscopy. Resonant IR excitation leads to a decrease in the magnitude of the REMPI signal due to the difference in vibrational frequencies in the electronic ground and excited state, and/or the change in the overlap of the vibrational wave functions.[18] Often, a decrease of >50% is observed, which implies that the IR absorption step cannot simply be described with a two-level model consisting of the vibrationally ground and excited state. Instead, different processes involving more than two states, such as IR-induced fragmentation or intramolecular vibrational energy redistribution (IVR), must occur within the time scale of these experiments.[19,20] More insight into the IR–UV depletion mechanism can be obtained by probing the molecule after IR absorption and determining the vibrational state(s) that is populated. This can in principle be done by recording REMPI excitation spectra after IR excitation.[18,21–24] Such an approach is especially attractive for far-IR vibrational modes where excitation localizes the population in a few eigenstates, whereas in the case of near-IR excitation, statistical inhomogeneous broadening by IVR impedes a straightforward interpretation of the UV excitation spectrum.[18]

Here we report far-IR studies on naphthalene, anthracene, phenanthrene, acenaphthene, acenaphthene-d_{10}, chrysene, pyrene, and benzo[*ghi*]perylene, all of which are prototypical PAHs that feature various topological aspects of importance. The far-IR region has so far remained out of reach for PAHs under astronomically relevant conditions, that is, as isolated gas-phase molecules and at low temperatures. Table 2.1 summarizes the experimental IR frequencies found for each molecule in the region of 80–250 cm^{-1} together with the calculated frequencies in this region.

Generally, delocalized, low-frequency vibrational modes of aromatic rings, such as ring puckering and other large-amplitude motions, are being termed anharmonic,[25–29] but from an experimental point of view, this is far from clear. In our experiments, we probe not only the depopulation of the vibrational ground state but also the population

of distinct low-energy vibrationally excited states. Our studies, therefore, enable us to obtain insight into the mechanism of IR–UV ion dip spectroscopy and to determine the (an)harmonic character of delocalized low-frequency vibrational modes of PAHs.

2.3 Methods

Acenaphthene, acenaphthene-d10, chrysene, phenanthrene, naphthalene, anthracene, pyrene, and benzo[ghi]perylene were injected into a molecular beam by resistively heating the samples around their melting point just in front of a Series 9 pulsed valve from General Valve. The source was operated at 20 Hz with argon as carrier gas and a backing pressure of around 2.5 bar. The gas was expanded into vacuum, passed through a skimmer and delivered vibrationally and rotationally cold to the interaction region. In the interaction region, the molecular beam was probed with a perpendicular UV laser beam of about 1 mJ/pulse provided by a Nd:YAG laser pumped dye laser, a ±100 μJ/pulse UV beam of 193 nm from an ArF excimer laser, and the far-IR radiation of FELIX (10 μs pulse)[30]. To record the far-IR absorption bands, the molecular species were ionized via Resonance Enhanced Multi-Photon ionization (REMPI) preceded by the FELIX laser beam with a few μs which was scanned over the range of approximately 85-250 cm-1, performing IR-UV ion dip spectroscopy.[31] The precise far-IR band positions were obtained by scanning the IR laser with steps of 0.25 cm-1 and fitting the observed band with a Gaussian function. The laser beam was propagating colinearly with the molecular beam, ensuring full use of the 10 μs, 2.5-30 mJ laser radiation. FELIX has a bandwidth of approximately 1% of the photon frequency. In order to record the far-IR ion gain REMPI spectra, the IR laser FELIX was positioned on a resonant transition and the UV dye laser was scanned in the indicated range. In both cases, the IR beam was set to alternate between on and off to simultaneously obtain a background signal, directly correcting for fluctuations in the ion signal. The assignments are supported by harmonic IR frequency calculations performed using density functional theory at the B3LYP/6-31G* level of theory in the Gaussian16 program package.[32,33] Anharmonic frequency calculations are performed using the same package at the B3LYP/N07D level of theory.

2.4 Results and discussion

The black traces in Figure 2.1 show the UV excitation spectrum near the 0_0^0 origin band of acenaphthene-d_{10}, while the red traces correspond to REMPI spectra taken after resonant IR excitation of a mid-IR band at 1604 cm^{-1} (CC in-plane vibration) and a far-IR band

at 189 cm^{-1} (drumhead motion). Excitation in the mid-IR region causes depopulation of the ground state and leads to statistical inhomogeneous broadening of the origin band due to the high density of states at this energy.[18] IR absorption in this region thus results in depletion at the band origin frequency and a smoothly varying IR ion gain (IRIG)[23,24] at frequencies other than the band origin. In contrast, in the far-IR excitation experiment, a low-frequency vibrational state is populated at an energy where the density of states is much lower. As a result, IR excitation produces a vibrational population distribution over only a few eigenstates, leading to resolved features in the UV excitation spectrum that probes this distribution. In the following, we will first assign these resolvable IRIG bands and then discuss the implications of these assignments on the mechanism of far-IR–UV ion dip spectroscopy. Finally, we will evaluate the (an)harmonic properties of the low-frequency modes of the studied PAHs on the basis of the observed spectral features.

Table 2.1: Overview of predicted and experimentally determined far-IR modes in the 80-250 cm^{-1} region for indicated PAHs.

molecule	**experimental cm^{-1}**	**harmonic NASA Ames cm^{-1}**	**anharmonic (B3LYP/NO7D) cm^{-1}**
anthracene	88.2 ± 0.13	90.7	88.1
phenanthrene	97.2 ± 0.10	99.7	97.1
benzo[ghi]perylene	127.4 ± 0.22	130.2	126.05
acenaphthene-d_{10}	143.5 ± 0.06	--	147.7
acenaphthene	157.4 ± 0.06	--	160.6
naphthalene	166.8 ± 0.14	171.5	170.8
acenaphthene-d_{10}	189.1 ± 0.02	--	192.7
benzo[ghi]perylene	197.0 ± 0.24	199.9	194.757
pyrene	207.1 ± 0.17	209.4	211
acenaphthene-d_{10}	208.9 ± 0.56	--	--
acenaphthene	212.5 ± 0.05	--	217.7
phenanthrene	223.0 ± 0.08	226.2	224.2
chrysene	230.3 ± 0.28	232.8	231.1
anthracene	232.0 ± 0.08	230.3	232
phenanthrene	244.5 ± 0.27	244.2	243

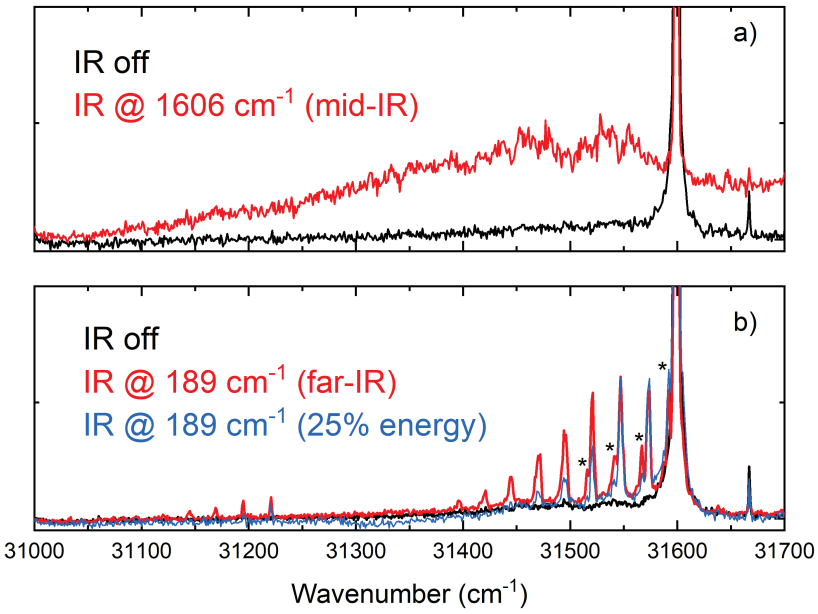

Figure 2.1: Experimental REMPI excitation spectrum (black traces) of the origin band of acenaphthene-d_{10} at 31599 cm^{-1} recorded in the absence of IR excitation. The colored traces show spectra with the IR laser FELIX preceding the REMPI process at a resonant frequency of (a) 1606 cm^{-1} (pulse energy of 13 mJ, red) or (b) 189 cm^{-1} [6 mJ (red) and 1.5 mJ (blue), red and blue traces scaled such that the $(\nu_3)_{v''=2}^{v'}$=2 bands have the same intensity]. In both cases, there is a decrease [ion dip (see [34])] at the origin transition and an increase (ion gain) at frequencies other than the origin after IR absorption. The unresolved gain in panel a reflects the outcome of statistical inhomogeneous broadening, while panel b shows distinct bands indicating that vibrational excitation is restricted to only a few eigenstates.

The appearance of resonant transitions in the ion gain spectrum (Figure 2.1b) at frequencies lower than the origin band, after excitation of ν_3 at 189 cm^{-1}, indicates that distinct vibrational levels in the electronic ground state are populated after far-IR excitation. The ion gain bands show a regular spacing of 25.5 cm^{-1}, which necessarily must be associated with $(\nu_3)_{v''=n}^{v'=n}$ transitions because 25.5 cm^{-1} is lower than the lowest-frequency vibrational mode of acenaphthene-d_{10}. Such a regular spacing is possible only if the potential energy surface in the electronic ground and excited state along the normal mode ν_i is highly harmonic. Indeed, we find from the variation in band spacings an anharmonicity of ~0.1%.

A schematic energy diagram with the possible IR and UV excitation routes is shown in Figure 2.2. The ladder-climbing pathway displayed in Figure 2.2a results in the population of higher vibrational levels of the harmonic vibrational mode at the IR frequency

for which the fundamental transition is excited (possible deviation of 1% resulting from the full width at half-maximum of FELIX). Vibrational overlap considerations dictate that UV transitions will predominantly take place between vibrational levels with the same vibrational quantum number in the electronic ground and excited state. Because the frequencies of vibrational modes in these two states are different, with typically lower frequencies in the excited state, the $(\nu_3)_{v''=n}^{v'=n}$ transitions are observed as a regular red-shifted progression with a spacing corresponding to the difference in the vibrational energy of mode ν_i in the two electronic states. Such a ladder-climbing pathway was considered in the far-IR study of tryptamine, but the presence of multiple conformers precluded an unambiguous assignment of the observed transitions, unlike what is possible in the study presented here.[22]

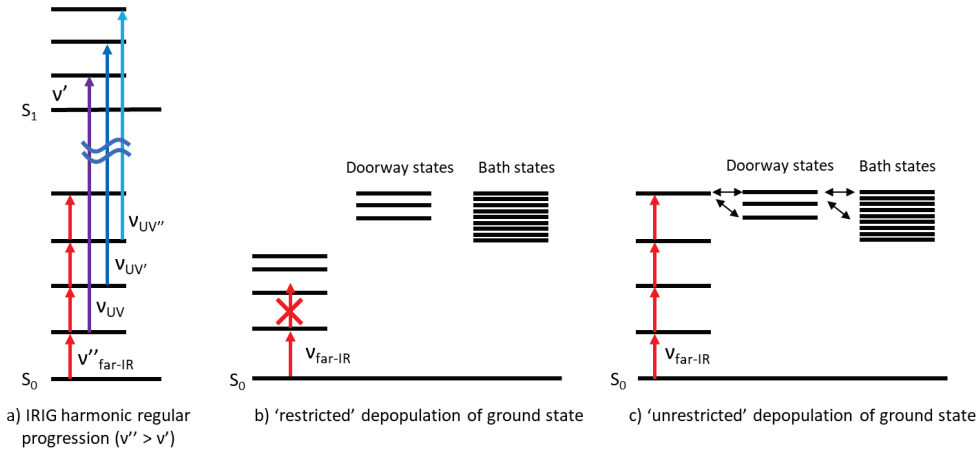

Figure 2.2: (a) Schematic representation of ladder climbing leading to a regular red-shifted progression in IRIG spectra. (b) "Restricted" absorption in an anharmonic potential with nonequidistant vibrational levels, which results in IVR for low-frequency vibrational modes being largely inhibited. (c) "Unrestricted" depopulation of the ground state in a harmonic potential with equidistant vibrational levels where ladder climbing in low-frequency vibrational modes allows access to otherwise nonaccessible IVR pathways.

Figure 2.1 shows that the IR pulse energy has a marked influence on the REMPI spectrum. First, we observe that with a lower pulse energy (blue trace) higher vibrational quanta levels are not reached. Second, the red trace taken at higher pulse energies shows bands marked with an asterisk that are not (or hardly) present in the blue trace. These bands are associated with transitions involving the $(\nu_2)_{v''=1}^{v'=1}$ transition. Their presence implies a redistribution of vibrational energy to the $(\nu_2)_{v''=1}$ level that clearly occurs only if levels of ν_3 are reached with sufficiently high quantum numbers. Similar redistributions are observed at other IR frequencies and for the other molecules we have studied (see Figure 2.4). Generally, we find that at very low IR frequencies, we can still assign

quite reliably transitions occurring upon IVR, but for higher-frequency transitions, the number of possibilities becomes too large for unambiguous assignment.

Ladder climbing in harmonic vibrational modes has important consequences for the interpretation of IR ion dip intensities. In the case of anharmonic modes, only one photon can be absorbed (Figure 2.2b). For low-frequency modes, the density of states at the accessed vibrational energy is so low that IVR is not possible, resulting in a maximum depopulation of 50% of the ground state. Ladder climbing followed by IVR from higher vibrational levels (Figure 2.2c) allows for multiple IR photon absorption and depopulation of the ground state by >50%. The (an)harmonic character of a vibrational mode thus strongly determines the amount of depopulation of the ground state and, thereby, the observed IR ion dip intensity.

The pathways described above imply that REMPI spectra obtained after far-IR excitation should depend critically on the IR laser pulse energy. On one hand, the harmonic ladder is climbed to relatively low vibrational quantum numbers at low energies and IVR is restricted. At higher pulse energies, on the other hand, vibrational levels with higher quantum numbers are accessed and IVR is enhanced. Our experiments confirm this: at a low IR laser pulse energy (Figure 2.3d, red trace), distinct, narrow transitions are observed and IVR-induced broadening is limited. As we move to higher pulse energies, these features disappear as an IVR threshold is reached and only a broadened IR-induced REMPI feature remains (Figure 2.3a, purple trace).

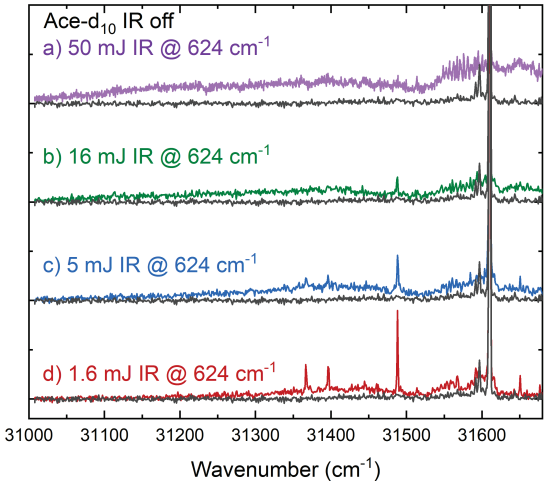

Figure 2.3: REMPI spectra near the origin region of acenaphthene-d_{10} at an IR excitation frequency of 624 cm^{-1}. The IR laser pulse energies used were approximately (a) 50 mJ (purple), (b) 16 mJ (green), (c) 5 mJ (blue), and (d) 1.6 mJ (red). The black trace in each plot shows the REMPI excitation spectrum without IR excitation and serves as a reference. Unscaled REMPI spectra are provided in [34].

Another important consequence of this power dependence is that one should be cautious when interpreting signal intensities in IRIG spectra because a lower IR pulse energy might very well result in a stronger IRIG signal at particular UV probe frequencies. IRIG signals are, thus, not necessarily related to IR cross sections in a 1:1 manner. Moreover, normally an exponential relation between laser power and IR depletion is assumed, but this model is based on the assumption of a fast irreversible IVR process without a threshold. This may clearly fail under conditions such as those used in our experiments.

Figure 2.4 displays an overview of REMPI spectra measured near the origin transition to the lowest electronically excited singlet state of selected PAHs with (color) and without (black) IR pre-excitation. The IR frequencies range from the far-IR to mid-IR. For IR excitation up to 600 cm^{-1}, regular progressions are observed, while excitation at higher frequencies leads to broadened spectra. The vibrational modes are either out-of-plane butterfly or drumhead motions, except for those of acenaphthene-d_{10} (383 cm^{-1}) and anthracene (232 cm^{-1}), which are in-plane scissoring modes. A full overview of the transitions that have been assigned on the basis of quantum chemical calculations in the electronic ground and excited states of the pertinent compound is provided in [34]. Secondary progressions associated with transitions involving a decrease in the vibrational quantum number are visible for acenaphthene-d_{10} upon excitation with IR frequencies of 189 and 383 cm^{-1}. In the case of 189 cm^{-1} excitation, a second progression is shifted by exactly twice the fundamental frequency, while for the 383 cm^{-1} excitation, the second progression is shifted by exactly the fundamental frequency. The assignment of the progression of naphthalene to a transition between two different vibrational mode numbers is justified by the fact that these modes are the same normal modes and, therefore, have the largest vibrational overlap. A similar situation exists for the 232 cm^{-1} IR-pumped REMPI spectrum of anthracene. In some IR ion gain spectra, the red-shifted bands consist of a doublet or series of bands, e.g., for acenaphthene-d_{10} with 189 cm^{-1} and acenaphthene with 210 cm^{-1} IR excitation. We tentatively assign these bands to result from lower-frequency $(\nu_i)_{\nu''=1}^{\nu'=1}$ transitions that become observable after IVR to a lower-frequency mode ν_i.

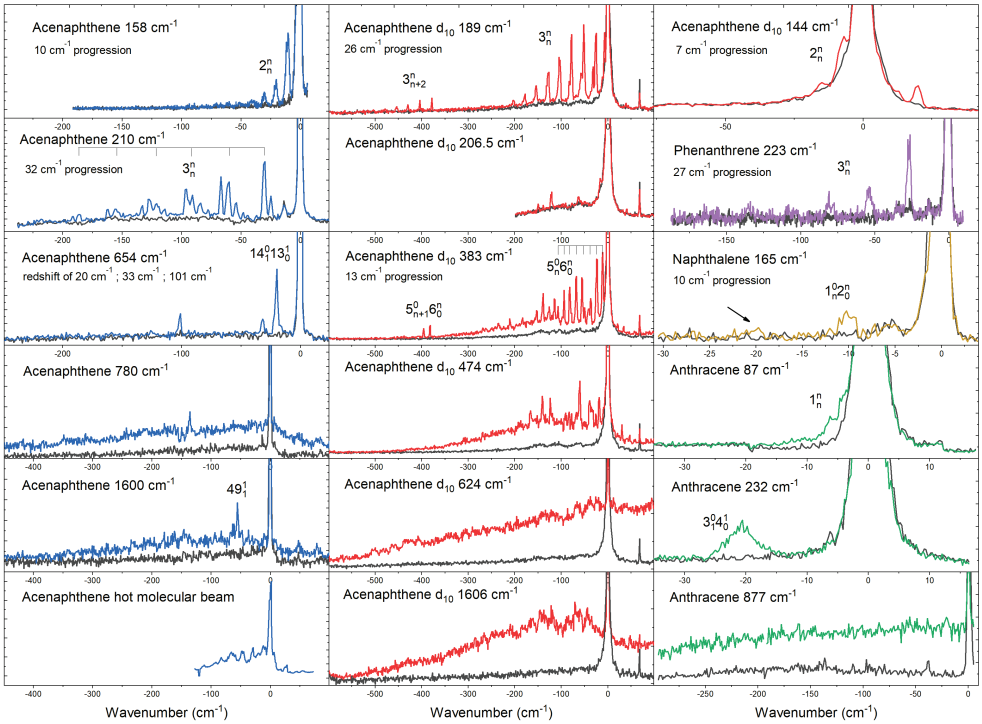

Figure 2.4. Experimental REMPI spectra of naphthalene, acenaphthene, acenaphthene-d_{10}, anthracene, and phenanthrene (black traces) near the origin bands (set to zero). The colored traces show REMPI excitation spectra with the IR laser at the resonant IR frequency indicated within each subplot preceding REMPI probing. Full unscaled spectra are provided in [34].

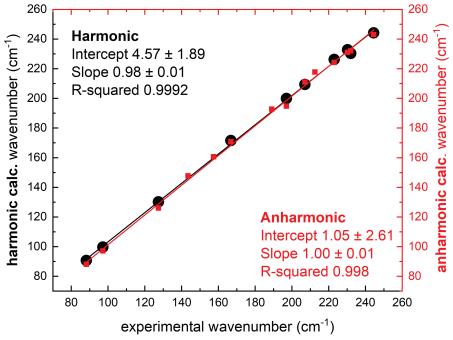

Figure 2.5: Calculated harmonic[14] (black) and anharmonic (red) frequencies as a function of the experimentally determined frequencies. Scaled harmonic calculations are at least as accurate as anharmonic calculations.

Figure 2.4 (bottom, left) also displays a "hot" molecular beam REMPI spectrum of acenaphthene that illustrates the difference between the population of vibrational states at a higher temperature[35] and the population of vibrational states due to resonant IR excitation. A clear difference in structure is observed between the hot bands in the "hot" spectrum and the IR ion gain features in the REMPI spectra obtained with 1600 or 780 cm^{-1} excitation. Compared to the 1600 cm^{-1} IRIG spectrum, there is relatively more intensity close to the band origin in the "hot" spectrum. The 780 cm^{-1} gain spectrum shows a broadening of the band origin to both the red and blue side of the band origin, whereas the "hot" spectrum shows the most intensity on the red side. Resonant vibrational excitation cannot simply be seen as creating a Boltzmann distribution of vibrational energy. Even well within the mid-IR range, a notable difference in structure is observed in the IR ion gain, which becomes clear when the 624 and 1606 cm^{-1} excitation REMPI spectra of acenaphthene-d_{10} are compared. Similarly, this can be seen in the 780 and 1600 cm^{-1} excitation REMPI spectra of acenaphthene. These observations indicate that the redistribution of vibrational energy follows quite different pathways after excitation at 780 or 1600 cm^{-1}.

An interesting case arises when the vibrational frequencies of the ground and electronically excited states are very similar; the normally observed red-shift in the ion gain REMPI spectra is no longer resolvable. This occurs partly in the case of the IR excitation of acenaphthene-d_{10} at 144 cm^{-1}. REMPI spectra taken after IR excitation show a red shift of ~7 cm^{-1}, partly falling within the width of the origin transition and impeding optimal detection of depletion. This observation is in particular important in the context of studies of large PAHs as these PAHs undergo only a small structural change upon electronic excitation and have similar vibrational energies in the electronic ground and excited state. To be able to probe the effect of IR absorption, one relies on a change in Franck–Condon factors upon excitation or of the ionization cross section from the electronically excited state.

2.5 Conclusions

REMPI spectra obtained after IR excitation of specific vibrational levels in the far-IR and mid-IR regions have provided unique insight into the mechanisms of IR–UV ion dip spectroscopy in the different frequency regimes. At low IR frequencies, vibronic transitions from distinct vibrational levels have been observed that unambiguously prove ladder climbing occurs. This is an important conclusion as it means that many more transitions can contribute to the depletion of the vibration-less ground state than what has been assumed to date. Moreover, vibrational energy redistribution pathways become available that previously were not taken into account. The IVR threshold that, depending on

the IR photon energy, can or cannot be reached can introduce nonlinearity into the intensity of IR ion dip absorption bands. This conclusion provides a gratifying explanation for puzzling observations from the past, in which low-frequency modes appeared with a much higher intensity in IR–UV ion dip spectra than predicted by theoretical calculations. At higher frequencies, vibrational energy redistribution readily occurs, which, in combination with differences in vibrational frequencies in the electronic ground and excited states, leads to a reasonably smooth ion gain feature.

The observation of ladder climbing in low-frequency vibrational modes is surprising because it has been assumed that these modes would be quite anharmonic as calculated anharmonic force constants are relatively large. To calibrate (an)harmonic theory for the PAHs in the far-IR range, we have compared experimental IR frequencies obtained in this work with theoretical predictions of harmonic and anharmonic frequencies (Figure 2.5). As expected from the IRIG results, the scaled harmonic frequency predictions are at least as accurate as anharmonic frequencies. Contrary to *a priori* expectations, the low-frequency modes are very harmonic (some with a deviation of only 0.1%), which is, from an astronomical point of view, positive news because harmonic models are often used to interpret interstellar infrared emission features. They can thus be used to accurately predict far-IR frequencies.

References

1 K. Schwing and M. Gerhards, *Int. Rev. Phys. Chem.*, 2016, **35**, 569–677.
2 E. Maltseva, C. J. Mackie, A. Candian, A. Petrignani, X. Huang, T. J. Lee, A. G. G. M. Tielens, J. Oomens and W. J. Buma, *Astron. Astrophys.*, 2018, **610**, 1–13.
3 H. Piest, G. Von, Helden and G. Meijer, *Astrophys. J.*, 1999, **520**, L75–L78.
4 J. Roithová, J. Jašík, J. J. Del Pozo Mellado and D. Gerlich, *Faraday Discuss.*, 2019, **217**, 98–113.
5 M. Basire, P. Parneix and F. Calvo, *J. Phys. Chem. A*, 2010, **114**, 3139–3146.
6 A. Candian and C. J. Mackie, *Int. J. Quantum Chem.*, 2017, **117**, 146–150.
7 J. Oomens, a. G. G. M. Tielens, B. G. Sartakov, G. von Helden and G. Meijer, *Astrophys. J.*, 2003, **591**, 968–985.
8 J. Bloino, *J. Phys. Chem. A*, 2015, **119**, 5269–5287.
9 E. Gloaguen and M. Mons, *Top. Curr. Chem.*, 2015, **364**, 225–270.
10 M. S. de Vries and P. Hobza, *Annu. Rev. Phys. Chem.*, 2007, **58**, 585–612.
11 S. Bakels, M. P. Gaigeot and A. M. Rijs, *Chem. Rev.*, 2020, **120**, 3233–3260.
12 S. I. Ishiuchi, K. Yamada, H. Oba, H. Wako and M. Fujii, *Phys. Chem. Chem. Phys.*, 2016, **18**, 23277–23284.
13 R. N. Pribble and T. S. Zwier, *Science*, 1994, **265**, 75–79.

14 C. W. Bauschlicher, A. Ricca, C. Boersma and L. J. Allamandola, *Astrophys. J. Suppl. Ser.*, 2018, **234**, 32.
15 G. Mulas, G. Malloci, C. Joblin and D. Toublanc, *Astron. Astrophys.*, 2006, **456**, 161–169.
16 C. Boersma, C. W. Bauschlicher, L. J. Allamandola, A. Ricca, E. Peeters and A. G. G. M. Tielens, *Astron. Astrophys.*, 2010, **511**, A32.
17 C. J. Mackie, T. Chen, A. Candian, T. J. Lee and A. G. G. M. Tielens, *J. Chem. Phys.*, 2018, 149, 134302.
18 N. S. Nagornova, T. R. Rizzo and O. V. Boyarkin, *Angew. Chemie - Int. Ed.*, 2013, **52**, 6002–6005.
19 R. A. Coveleskie, D. A. Dolson and C. S. Parmenter, *J. Chem. Phys.*, 1980, **72**, 5774–5775.
20 J. Oomens, B. G. Sartakov, G. Meijer and G. von Helden, *Int. J. Mass Spectrom.*, 2006, **254**, 1–19.
21 Y. Yamada, N. Mikami and T. Ebata, *J. Chem. Phys.*, 2004, **121**, 11530–11534.
22 M. Schmitt, F. Spiering, V. Zhaunerchyk, R. T. Jongma, S. Jaeqx, A. M. Rijs and W. J. Van Der Zande, *Phys. Chem. Chem. Phys.*, 2016, **18**, 32116–32124.
23 J. C. Dean, E. G. Buchanan, W. H. James, A. Gutberlet, B. Biswas, P. V. Ramachandran and T. S. Zwier, *J. Phys. Chem. A*, 2011, **115**, 8464–8478.
24 E. G. Buchanan, W. H. James, A. Gutberlet, J. C. Dean, L. Guo, S. H. Gellman and T. S. Zwier, *Faraday Discuss.*, 2011, **150**, 209–226.
25 A. G. Császár, *Wiley Interdiscip. Rev. Comput. Mol. Sci.*, 2012, **2**, 273–289.
26 J. Laane and R. C. Lord, *J. Chem. Phys.*, 1967, **47**, 4941–4945.
27 J. Mahé, S. Jaeqx, A. M. Rijs and M.-P. Gaigeot, *Phys. Chem. Chem. Phys.*, 2015, **17**, 25905–25914.
28 V. Yatsyna, D. J. Bakker, R. Feifel, A. M. Rijs and V. Zhaunerchyk, *Phys. Chem. Chem. Phys.*, 2016, **18**, 6275–6283.
29 D. J. Bakker, A. Peters, V. Yatsyna, V. Zhaunerchyk and A. M. Rijs, *J. Phys. Chem. Lett.*, 2016, **7**, 1238–1243.
30 D. Oepts, A. F. G. Van, D. Meer and P. W. Van Amersfoort, *Infrared Phys. Technol.*, 1995, **36**, 297–308.
31 A. M. Rijs, E. R. Kay, D. A. Leigh and W. J. Buma, *J. Phys. Chem. A*, 2011, **115**, 9669–9675.
32 M. J. Frisch, G. W. Trucks, H. B. Schlegel, G. E. Scuseria, M. A. Robb, J. R. Cheeseman, G. Scalmani, V. Barone, G. A. Petersson, H. Nakatsuji, X. Li, M. Caricato, A. V. Marenich, J. Bloino, B. G. Janesko, R. Gomperts, B. Mennucci, H. P. Hratchian, J. V. Ortiz, A. F. Izmaylov, J. L. Sonnenberg, D. Williams-Young, F. Ding, F. Lipparini, F. Egidi, J. Goings, B. Peng, A. Petrone, T. Henderson, D. Ranasinghe, V. G. Zakrzewski, J. Gao, N. Rega, G. Zheng, W. Liang, M. Hada, M. Ehara, K. Toyota,

R. Fukuda, J. Hasegawa, M. Ishida, T. Nakajima, Y. Honda, O. Kitao, H. Nakai, T. Vreven, K. Throssell, J. Montgomery, J. A., J. E. Peralta, F. Ogliaro, M. J. Bearpark, J. J. Heyd, E. N. Brothers, K. N. Kudin, V. N. Staroverov, T. A. Keith, R. Kobayashi, J. Normand, K. Raghavachari, A. P. Rendell, J. C. Burant, S. S. Iyengar, J. Tomasi, M. Cossi, J. M. Millam, M. Klene, C. Adamo, R. Cammi, J. W. Ochterski, R. L. Martin, K. Morokuma, O. Farkas, J. B. Foresman and D. J. Fox, *Gaussian, Inc., Wallingford CT*.

33 A. D. Becke, *J. Chem. Phys.*, 1993, **98**, 5648–5652.

34 A. K. Lemmens, D. B. Rap, J. M. M. Thunnissen, S. Gruet, A. L. Steber, S. Panchagnula, A. G. G. M. Tielens, M. Schnell, W. J. Buma and A. M. Rijs, *J. Phys. Chem. Lett.*, 2020, **11**, 8997–9002.

35 O. Pirali, M. Vervloet, G. Mulas, G. Malloci and C. Joblin, *Phys. Chem. Chem. Phys.*, 2009, **11**, 3443.

Chapter 3

Anharmonicity in the mid-infrared spectra of polycyclic aromatic hydrocarbons

This chapter is published as:
Alexander K. Lemmens, Daniël B. Rap, Johannes M. M. Thunnissen, Cameron J. Mackie, Alessandra Candian, Alexander G. G. M. Tielens, Anouk M. Rijs and Wybren Jan Buma, *Astronomy & Astrophysics,* 628, A130, 2019

3.1 Abstract

In this work we determine the effects of anharmonicity on the mid-infrared spectra of the linear polycyclic aromatic hydrocarbons (PAHs) naphthalene, anthracene, tetracene and pentacene recorded using the free electron laser FELIX. Comparison of experimental spectra obtained under supersonic jet conditions with theoretically predicted spectra was used to show if anharmonicity explicitly needs to be taken into account. Anharmonic spectra obtained using second-order vibrational perturbation theory agree on average within 0.5% of the experimental frequencies. Importantly, they confirm the presence of combination bands with appreciable intensity in the 5–6 μm region. These combination bands contain a significant fraction of the IR absorption, which scales linearly with the size of the PAH. Detection and assignment of the combination bands are a preliminary indication of the accuracy of far-IR modes in our anharmonic theoretical spectra. Detailed analysis of the periphery-sensitive CH out-of-plane band of naphthalene reveals that there is still room for improvement of the VPT2 approach. In addition, the implications of our findings for the analysis of the aromatic infrared bands are discussed.

3.2 Introduction

Currently, the generally accepted hypothesis for the origin of the aromatic infrared bands (AIBs) is the IR emission of UV-pumped polycyclic aromatic hydrocarbons (PAHs).[1–3] Because of their ubiquity, PAHs can have major effects on heating and ionization processes in the interstellar medium (ISM), and thereby on the chemistry occurring in molecular clouds.[4] Vice versa, the spectral features of these compounds are in principle sensitive probes for the physical environment of particular regions in the ISM and their chemical evolution. The relative strength of the observed AIBs implies that astronomically relevant PAHs have sizes of the order of 50 carbon atoms.[5–8] Our knowledge on the photophysical properties of such large PAHs is as yet far from complete, but is key to advancing the interpretation of astronomical observations.[9] Laboratory spectroscopy is therefore needed to gain more insight into these properties.[10] Such experiments should preferably be carried out under astronomically relevant conditions, that is, under low-temperature and isolated conditions such that spectral shifts and/or intensity variations by the environment can be excluded.[11]

In recent years we have pioneered an approach in which we employ mass-selective ion detection in combination with high-resolution laser spectroscopy to obtain mass- and conformation-selective IR absorption spectra with a resolution and sensitivity that by far exceed what was hitherto possible.[12–14] This work has primarily focused on the

3 μm near-IR region associated with aromatic and aliphatic CH stretch vibrations, and has shown how extensive the influence of anharmonicity[15] is on the appearance of the spectra.[13,16] State-of-the-art anharmonic calculations were shown to be able to accurately reproduce the experimental spectra.[17–19] This conclusion is important as it provided strong and unambiguous support for the use of theoretical spectra calculated with such a methodology in cases where experimental spectra are not available.

The studies on the near-IR region were used to determine the presence of specific classes of PAHs based on the overall shape of the near-IR emission. A more detailed characterization – and potentially a probe for identifying individual PAHs – is in principle available by considering the mid- and far-infrared spectral features.[6] The mid-IR part of the spectrum of neutral gas-phase PAHs has so far, however, remained largely unexplored, with the exception of individual emission bands of naphthalene.[20] Mid-IR studies have been performed employing matrix isolation spectroscopy (MIS)[21], but these spectra are subject to spectral shifts, intensity distortions[14] and sample impurities.[11] A further aspect impeding gas-phase mid-IR studies is the availability of appropriate light sources. Here, we resort to molecular beams and use a Free Electron Laser to obtain cold, gas-phase IR absorption spectra of isolated molecules that can be used without further modification to validate theory. The far-IR (below ±660 cm^{-1}) is another spectral regime containing signatures that can be directly related to the identity of specific PAHs.[6,8,22] The interpretation of the spectral features in this region heavily relies on properly taking anharmonic effects into account and validation of calculated far-IR frequencies of PAHs is therefore necessary. Anharmonic bands in the mid-IR can be associated with combination bands built upon one or more far-IR fundamentals. Mid-infrared spectra may therefore aid in the validation of both mid-IR and far-IR calculated vibrational frequencies.

In the present study we obtained the mid-IR spectra of the full range of polyacenes from naphthalene to pentacene. This series gives us the possibility to assess the effect of molecular size on photophysical properties and to extrapolate these results to larger species. It will be shown that anharmonic calculations lead to theoretically predicted spectra that are in good (0.5% deviation) agreement with the experimental ones. Combined, these experimental and theoretical studies underpin the importance of anharmonicity in this region of the spectrum, and provide key handles for furthering the development of astronomical models.

3.3 Methods

Experiments have been performed at the FELIX laboratory[23] using the molecular beam setup described in bu Rijs et al.[24] Samples of naphthalene, anthracene, and tetracene were heated close to their melting point in a glass container and expanded into vacuum

with a Series 9 pulsed valve from General Valve using argon as a carrier gas. The backing pressure was typically around 2.5 bar. The low vapor pressure of pentacene at our maximum heating temperature required the use of laser desorption[25,26] to get sufficient molecules into the gas-phase. The sample was mixed with graphite powder and applied on a solid graphite bar. A pulsed 1064 nm laser beam (Polaris Pulsed Nd:YAG Laser, New Wave Research) with a typical energy of 1 mJ/pulse was used to desorb the pentacene molecules. Subsequently they were picked up by a jet of argon (4 bar backing pressure) created with a Jordan pulsed valve. The skimmed molecular beam was crossed by a UV excitation laser beam with typical pulse energies of a few millijoules that was provided by a Nd:YAG laser pumped UV dye laser (Spectra-Physics/Radiant Dye), an ionization laser beam of 193 nm provided by an ArF excimer laser (Neweks) and an IR laser beam provided by the free electron laser (FEL) FELIX. The ions were mass-separated using a time-of-flight spectrometer and detected with a multichannel plate detector. A delay generator (SRS DG645) was used for synchronization and triggering of the equipment. Infrared spectra were acquired by IR-UV ion dip spectroscopy, tuning the UV excitation laser beam to the $S_1 \leftarrow S_0$ transition[13,27] of the investigated compound and scanning the IR wavelength. The bandwidth of the IR source FELIX is about 1% of the photon frequency produced.

Experimental spectra have been compared to simulated spectra on the anharmonic[28,29] B3LYP[30]/N07D[19,31] level of theory – hereafter referred to as anharmonic – and the harmonic B3LYP/4-31G level of theory – hereafter referred to as harmonic. The anharmonic spectra were calculated using the Gaussian16 suite of programs using default thresholds[32], whereas the harmonic spectra were downloaded from the NASA Ames PAH database and scaled with multiple scaling factors as described in by Bauschlicher et al.[33] For comparison with the experimental spectra, theoretical spectra have been convolved with a Gaussian line shape with a full width at half maximum (FWHM) of 0.3% of the photon frequency (slightly narrower than the FEL bandwidth of 1% for clarity).

3.4 Results and discussion

Figures 3.1a–d report the mid-IR spectra of jet-cooled naphthalene, anthracene, tetracene, and pentacene, respectively, in the 5–18 μm region. The linewidths are determined by the bandwidth of FELIX, which is approximately 1% of the photon frequency. This means that a narrower linewidth is obtained in the far-IR part of the spectrum (about 3 cm^{-1} FWHM) than in the 5 μm region. The experimental spectra are compared to both harmonically calculated spectra obtained from the NASA Ames PAH spectral database[8,33] (Figures 3.1a–d in blue) that are conventionally used, and spectra obtained from high-level anharmonic calculations (Figures 3.1a–d in green, present work).

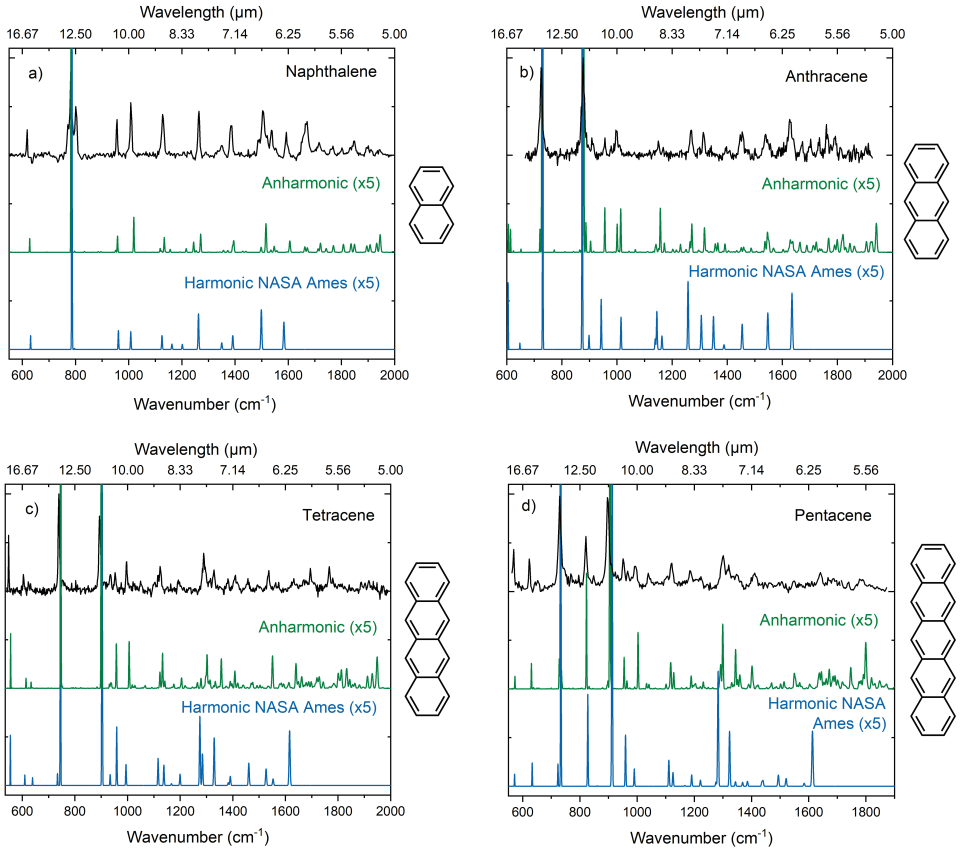

Figure 3.1: Molecular beam gas-phase IR absorption spectra of (*a*) naphthalene, (*b*) anthracene, (*c*) tetracene and (*d*) pentacene (black). Predicted IR spectra using the harmonic and anharmonic approximation are given as blueand green traces, respectively. The harmonic spectra have been obtained from the NASA Ames PAH spectral database.[33] The predicted spectra are multiplied by a factor five, truncating the strongest bands to enable a better visualization of the low-intensity bands (normalized spectra can be found in [34]).

The spectral features with a large absorption match reasonably well with the spectra predicted using the harmonic approximation. The strongest band by far in the experimental spectrum of naphthalene (Figures 3.1a) is at 783 cm^{-1} and can be assigned to a CH out-of-plane (OOP) bending mode involving all CH bonds. The experimental spectra of longer polyacenes (anthracene, tetracene and pentacene, Figures 3.1b–d) display in this frequency region two intense bands with comparable intensities. The lower-energy band corresponds to the CH OOP bending mode of the four adjacent hydrogens on the outer aromatic rings (quartets), while the band on the blue side corresponds to the CH OOP bending mode of the solo hydrogens on the inner aromatic rings. Since naphthalene does not possess enclosed rings, it displays only one single band. The spectra show that

the intensity of the solo CH OOP modes increases upon elongation of the polyacene chain. This observation confirms that the CH OOP frequency region is sensitive to the periphery of the molecule considered.[35]

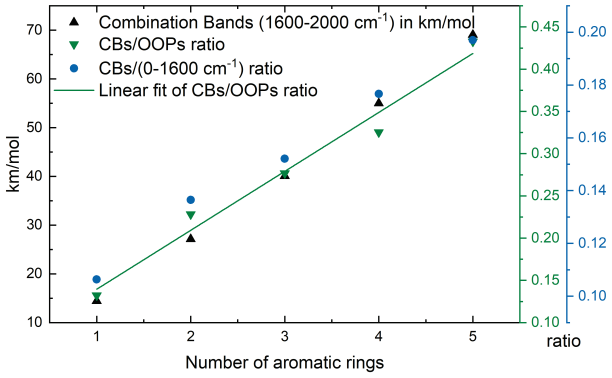

Figure 3.2: Cumulative intensity of the combination band (CB) region (1600–2000 cm^{-1}, black) and the ratio to the 0–1600 cm^{-1} region (blue) as well as to the CH out-of-plane (OOPs) bands (green) as a function of the number of aromatic rings in polyacenes (and benzene for the single ring species). The green trace corresponds to a linear fit to the CBs/OOPs ratio data with a slope of 0.0698 ± 0.0062 and an intercept of 0.070 ± 0.021.

The most striking difference between the harmonic and anharmonic spectra is the activity in the 1600–2000 cm^{-1} region. Below 1600 cm^{-1}, high-intensity bands are predicted reasonably well within the harmonic approximation, but at higher frequencies the activity observed in the experimental spectra can only be reproduced by calculations that account for anharmonicity (green traces). Such calculations show that these bands originate from combination bands built upon CH OOP bending modes. This assignment is in line with studies on substituted PAHs (see e.g., Bellamy 1975[35] and references therein). In the case of pentacene, these bands contain a cumulative intensity of 69 km mol^{-1}, compared to a cumulative intensity of 350.5 km mol^{-1} of the region below 1600 cm^{-1} according to the anharmonic calculations. Thus a significant amount of absorption (20%) in the region between 1600 and 2000 cm^{-1} is not predicted when using the harmonic approximation. The resolution of our experiments is limited by the laser bandwidth and thus does not allow us to fully resolve all combination bands in the 5–6 μm region. The larger polyacenes in particular show a high density of states in this region. However, based on the features that are resolved, standard deviations in frequencies of 0.4, 0.7, 0.5, and 0.4% are found for naphthalene, anthracene, tetracene, and pentacene, respectively. A table containing the assigned transitions is provided in the Appendix (Table 3.1).

The agreement between theory and experiment is very good for naphthalene, both with respect to band position as well as shape. However, anthracene and tetracene show more differences between experiment and theory in the “combination band” region. For

anthracene, various distinct bands are measured between 1650 and 1800 cm^{-1} whereas theory predicts an absorption feature that is more spread out. Another example is the rather strong band at 1767 cm^{-1} in the experimental spectrum of tetracene whereas the calculated spectrum predicts a broader feature with less peak intensity. The spectrum of pentacene is overall in good agreement with theory. Particularly, the region between 1250 and 1400 cm^{-1} changes significantly when anharmonicity is accounted for.

The excellent agreement between experiment and theory allows us to use the theoretical calculations with confidence to investigate how the size of the polyacene correlates with the ratio of the integrated intensity in the 1600–2000 cm^{-1} combination band region and the integrated intensity of fundamental bands (see Figure 3.2). Figure 3.2 shows that upon increasing the size of the PAH, combination bands acquire a larger absolute and fractional part of the total IR absorption intensity, which is in line with the higher density of vibrational states in larger PAHs. The fractional increase is observed both relative to the CH OOP bands as well as the integrated intensity of the bands below 1600 cm^{-1}. These ratios could thus provide a sensitive means to determine the size of (linear) PAHs in interstellar clouds. Remarkable in this respect is that the relation found by Boersma et al.[36] for a larger ensemble of PAHs is opposite to the trend found in this study for polyacenes: for a larger number of carbon atoms, the combination bands/CH OOP ratio decreases. This may simply be explained by the fact that in this study a particular subset of PAHs is taken into account rather than a diverse ensemble. Another interesting observation that can be made concerns the general appearance of the 5–6 μm region. Only two distinct bands belonging to the AIBs appear in this region, at 5.25 and 5.7 μm[36]. The present study shows that this region is largely built upon combination bands involving the CH OOP modes which, as discussed in the beginning of this section, are very sensitive to the periphery of the molecule in question. The presence of only two features in the AIB bands therefore strongly suggests a large similarity in the periphery of the PAHs present in these regions since a variety of peripheries would lead to a more uniform absorption in the combination band region.

Another region that is key to finding signatures directly related to the size of PAHs is the far-IR region.[6,8,22] This region is prone to be susceptible to the effects of anharmonicity, but has so far proven to be difficult to study, certainly under conditions relevant for astronomical observations. In the far-IR region, large-amplitude vibrations such as the anharmonic ring puckering motion of PAHs are active. Particularly for such large-amplitude modes, the anharmonic VPT2 calculations may lead to inaccurate results since the truncation of the Taylor expansion of the potential energy curve in VPT2 is an oversimplification and higher-order terms need to be taken into account.[37] Moreover, extreme caution must be taken when applying VPT2 to modes where the harmonic term does not dominate the shape of the potential energy curve.[29,38] For example, in the case of the hetero-PAH aminophenol it was shown previously that ring puckering is poorly described

by the VPT2 treatment.[39,40] The anharmonic bands in the mid-IR provide such a way to assess the low-energy part of the potential energy surface as they involve combination bands built upon one or more fundamentals from the far-IR. For example, in the case of naphthalene, a broader band is present at 1351 cm^{-1} in both experiment and anharmonic calculations. This band has contributions from an IR-active fundamental band at 1372 cm^{-1} and a combination band of the IR-inactive 387 and 970 cm^{-1} modes. The good agreement between experiment and theory thus indicates that the calculated mode at 387 cm^{-1} is well described. Similarly, we find for tetracene that several bands between 996 and 1123 cm^{-1} involving far-IR fundamentals are well predicted in the anharmonic calculations. On the other hand, in naphthalene a 479 and 772 cm^{-1} combination band is predicted at 1244 cm^{-1} but is not observed in the experimental spectrum. Also for anthracene, some predicted bands are not present in the experiment: the predicted band at 614 cm^{-1} is missing in the anthracene MIS spectrum[41] and several combination bands are not present in our gas phase spectrum around 1700 cm^{-1}. Although the present study provides some insight into the validity of calculations of the far-IR region, it is clear that further far-IR studies – and in particular experimental studies in the region itself – are needed for a more detailed characterization. Such studies will indeed shortly be performed in our laboratories.

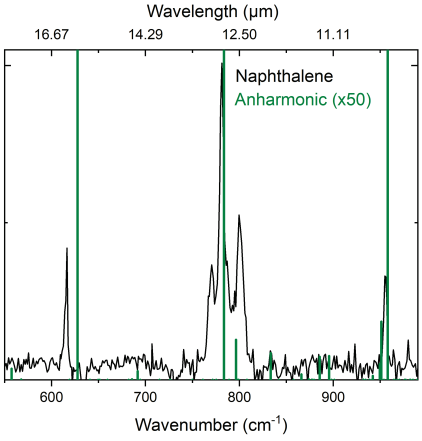

Figure 3.3: Zoom-in of the gas-phase IR absorption spectrum of jet-cooled naphthalene (black). The predicted absorption spectrum using the anharmonic approximation is shown in green. The simulation is multiplied by a factor 50 for better visualization of low-intensity bands.

Our studies have shown for the larger part excellent agreement between experimental and anharmonic theoretical spectra. However, they also show that higher-order perturbations in the Taylor expansion of the PES or dipole moment surface, which are as yet not incorporated into the theory, do play a role. This is most evident from the intense absorption feature at 783 cm^{-1} in the spectrum of naphthalene. Previously, this feature

was observed as a doublet in both matrix isolation[21] and in cationic form in supersonically cooled gas phase[42]. With the present resolution it becomes clear that this feature actually consists of three well-resolved bands at 770.8, 782.7, and 800.5 cm^{-1} (Figure 3.3). In a study at higher temperatures[20], the triplet band structure is not observed, but clear rotational structure is shown. The side bands in our observation cannot be rotational contours, since the rotational temperature in our experiments is much lower than would be required for the given splitting. Our present anharmonic calculations that only take double combination bands into account do not reproduce this splitting. One could therefore hypothesize that triple combination bands might be the origin of the splitting. This appears to be contradicted by the studies reported by Bloino[43] where transitions with three quanta in the final state are calculated. These calculations do not show intense transitions at 770.8 and 800.5 cm^{-1} but rather in the near-IR region. Inspection of the vibrational levels at this energy shows that the state density is high enough to support the presence of three bands. At the same time we have to conclude that the calculation of their intensities is apparently still far from what it should be. A contributing factor might be that for the involved motions the dipole moment surface is not well described by the calculations. Studies focusing on this dipole moment surface are therefore of interest and are being pursued.

3.5 Astrophysical implications

The present study confirms the far-reaching consequences of anharmonicity in the mid-IR spectra of linear PAHs. Firstly, it demonstrates how anharmonic calculations are a sine qua non condition to simulate the 5–6 μm region. The combination bands that underlie the observed activity in this region contain a significant amount of IR absorption intensity, and this fraction increases with the size of the polyacene. In fact, the PAHs studied here suggest a linear relationship between the length of the polyacene and the intensity ratio of combination bands to fundamentals. A surprising aspect of the measured spectra is that, while there are only one or two strong CH OOP modes, the 1600–2000 cm^{-1} region is rich in spectral detail. The strong CH OOP modes couple to more than one IR inactive mode, leading to this rich spectrum. Interestingly, the interstellar spectra are dominated by only two bands. From this it is clear that further study of the relative intensities of larger PAHs is important, since deviating intensities in calculations can lead to misinterpretation of astronomical data. Secondly, in addition to the combination bands, the length of the polyacene also has a profound influence on the overall appearance of the IR spectrum: the OOP CH bending modes are a sensitive probe for the periphery of the molecule and since the combination bands are mostly comprised of at least one CH OOP mode, this also holds for the combination bands. Thirdly,

anharmonic effects well below 1000 cm^{-1} have been observed – and naphthalene provides in this respect a most prominent example – that cannot be neglected since bands with a very strong absorption are involved. The present theoretical approach is not capable of providing a consistent explanation for the observed activity, and we thus conclude that higher-order perturbations associated with both the potential energy surface and the dipole moment surface are more important than previously assumed. The resulting intensity discrepancies can have important consequences in the context of the analysis of astronomical observations and lead to an incorrect interpretation in terms of relative abundances of charged or neutral species. Finally, the observations of combination bands built upon far-IR modes give a preliminary indication of the accuracy of the anharmonic calculations in predicting far-IR modes which are important as they have the potential to be sensitive probes of PAH size.[6] Our results suggest that the far-IR frequencies are accurately predicted within a few wavenumbers, but their coupling and intensities still need further improvement.

3.6 Conclusions

High-resolution mid-IR absorption spectra of the polyacenes naphthalene, anthracene, tetracene, and pentacene were obtained using IR-UV double resonance laser spectroscopy under astronomically relevant conditions. Comparison of these spectra with theoretical spectra predicted by harmonic and anharmonic calculations unambiguously shows the necessity to incorporate anharmonicity into astronomical models. Our anharmonically predicted spectra have a frequency deviation of 0.5% without the use of a scaling factor. We show that the 5–6 μm region contains a significant fraction of intensity associated with combination bands that should not be ignored in the analysis of astronomical spectra. For the polyacenes series studied here, the fraction of combination band intensity scales linearly with the length of the polyacene. This underlines the importance of incorporating anharmonicity in spectral analyses since PAHs in the interstellar medium are generally thought to be much larger than pentacene. The assignment of several combination bands has also provided a preliminary indication of the accuracy of current computational methodologies for calculating frequencies of far-IR bands. These far-IR bands are of interest since they could serve as a "label" for the substructure of PAHs, and are currently being pursued in our laboratories.

Overall, the present anharmonic calculations lead to very good agreement with experimental results. However, detailed analyses of, for example, the out-of-plane CH bending region of naphthalene show that in particular regions considerable differences still occur. Since these regions are often leading in astronomical analyses, further studies are required to determine the cause of these differences. One of the aspects which in that

respect needs further attention is the dipole moment surface, which so far has been assumed to be constant near the equilibrium geometry.

In the present study, pentacene needed to be studied using laser desorption instead of heating which up until now could be used to seed molecules into the molecular beam. Our IR absorption studies show that spectra obtained with laser desorption compare favorably with spectra obtained under heating conditions. This opens up a route to investigate the spectral signatures of large PAHs at the same level of detail as has been shown possible for smaller PAHs. Preliminary experiments performed in our laboratories on much larger PAHs indeed support this conclusion.

References

1 L. J. Allamandola, A. G. G. M. Tielens and J. R. Barker, *Astrophys. J. Suppl. Ser.*, 1989, **71**, 733–775.

2 K. Sellgren, *Astrophys. J.*, 1984, **277**, 623–633.

3 A. G. G. M. Tielens, *Annu. Rev. Astron. Astrophys*, 2008, **46**, 289–337.

4 E. Herbst, *Chem. Soc. Rev.*, 2001, **30**, 168–176.

5 H. Andrews, C. Boersma, M. W. Werner, J. Livingston, L. J. Allamandola and A. G. G. M. Tielens, *Astrophys. J.*, 2015, 807, 24pp.

6 C. Boersma, C. W. Bauschlicher, L. J. Allamandola, A. Ricca, E. Peeters and A. G. G. M. Tielens, *Astron. Astrophys.*, 2010, **511**, A32.

7 B. A. Croiset, A. Candian, O. Berné and A. G. G. M. Tielens, *Astron. Astrophys.*, 2016, **590**, A26.

8 A. Ricca, C. W. Bauschlicher, A. L. Mattioda, C. Boersma and L. J. Allamandola, *Astrophys. J.*, 2010, **709**, 42–52.

9 A. G. G. M. Tielens, *Astrochem. Astrobiol.*, 2013, **85**, 35–72.

10 J. Oomens, in *PAHs and the Universe*, EDP Sciences, 2011, vol. 46, pp. 61–73.

11 C. Joblin, L. D'Hendecourt, A. Leger and D. Defourneau, *Astron. Astrophys.*, 1994, **281**, 923–936.

12 E. Maltseva, A. Petrignani, A. Candian, C. J. Mackie, X. Huang, T. J. Lee, A. G. G. M. Tielens, J. Oomens and W. J. Buma, *Astrophys. J.*, 2015, **814**, 6pp.

13 E. Maltseva, A. Petrignani, A. Candian, C. J. Mackie, X. Huang, T. J. Lee, A. G. G. M. Tielens, J. Oomens and W. J. Buma, *Astrophys. J.*, 2016, **831**, 11pp.

14 E. Maltseva, C. J. Mackie, A. Candian, A. Petrignani, X. Huang, T. J. Lee, A. G. G. M. Tielens, J. Oomens and W. J. Buma, *Astron. Astrophys.*, 2018, **610**, 1–13.

15 A. Candian and C. J. Mackie, *Int. J. Quantum Chem.*, 2017, **117**, 146–150.

16 A. J. Huneycutt, R. N. Casaes, B. J. McCall, C. Y. Chung, Y. P. Lee and R. J. Saykally, *ChemPhysChem*, 2004, **5**, 321–326.

17 C. J. Mackie, A. Candian, X. Huang, E. Maltseva, A. Petrignani, J. Oomens, W. J. Buma, T. J. Lee and A. G. G. M. Tielens, *J. Chem. Phys.*, 2015, **143**, 1–15.
18 C. J. Mackie, A. Candian, X. Huang, E. Maltseva, A. Petrignani, J. Oomens, A. L. Mattioda, W. J. Buma, T. J. Lee and A. G. G. M. Tielens, *J. Chem. Phys.*, 2016, **145**, 84313.
19 C. J. Mackie, A. Candian, X. Huang, E. Maltseva, A. Petrignani, J. Oomens, W. J. Buma, T. J. Lee and A. G. G. M. Tielens, *Phys. Chem. Chem. Phys.*, 2018, **20**, 1189–1197.
20 O. Pirali, A. M. Vervloet, G. Mulas, G. Malloci and C. Joblin De, *Phys. Chem. Chem. Phys.*, 2009, **11**, 3443–3454.
21 D. M. Hudgins and S. A. Sandford, *J. Phys. Chem. A*, 1998, **102**, 329–343.
22 K. Zhang, B. Guo, P. Colarusso and P. F. Bernath, *Science*, 1996, **274**, 582–3.
23 D. Oepts, A. F. G. Van, D. Meer and P. W. Van Amersfoort, *Infrared Phys. Technol.*, 1995, **36**, 297–308.
24 A. M. Rijs, E. R. Kay, D. A. Leigh and W. J. Buma, *J. Phys. Chem. A*, 2011, **115**, 9669–9675.
25 G. Meijer, M. S. de Vries, H. E. Hunziker and H. R. Wendt, *Appl. Phys. B*, 1990, **51**, 395–403.
26 A. M. Rijs and J. Oomens, *Top. Curr. Chem.*, 2015, **364**, 1–42.
27 A. Amirav, U. Even and J. Jortner, *Opt. Commun.*, 1980, **32**, 266–268.
28 V. Barone, *J. Chem. Phys.*, 2005, **1221**, 14108–1007.
29 V. Barone, M. Biczysko and J. Bloino, *Phys. Chem. Chem. Phys.*, 2014, **16**, 1759–1787.
30 A. D. Becke, *J. Chem. Phys.*, 1993, **98**, 5648–5652.
31 V. Barone, P. Cimino and E. Stendardo, *J. Chem. Theory Comput.*, 2008, **4**, 751–764.
32 M. J. Frisch, G. W. Trucks, H. B. Schlegel, G. E. Scuseria, M. A. Robb, J. R. Cheeseman, G. Scalmani, V. Barone, G. A. Petersson, H. Nakatsuji, X. Li, M. Caricato, A. V. Marenich, J. Bloino, B. G. Janesko, R. Gomperts, B. Mennucci, H. P. Hratchian, J. V. Ortiz, A. F. Izmaylov, J. L. Sonnenberg, D. Williams-Young, F. Ding, F. Lipparini, F. Egidi, J. Goings, B. Peng, A. Petrone, T. Henderson, D. Ranasinghe, V. G. Zakrzewski, J. Gao, N. Rega, G. Zheng, W. Liang, M. Hada, M. Ehara, K. Toyota, R. Fukuda, J. Hasegawa, M. Ishida, T. Nakajima, Y. Honda, O. Kitao, H. Nakai, T. Vreven, K. Throssell, J. Montgomery, J. A., J. E. Peralta, F. Ogliaro, M. J. Bearpark, J. J. Heyd, E. N. Brothers, K. N. Kudin, V. N. Staroverov, T. A. Keith, R. Kobayashi, J. Normand, K. Raghavachari, A. P. Rendell, J. C. Burant, S. S. Iyengar, J. Tomasi, M. Cossi, J. M. Millam, M. Klene, C. Adamo, R. Cammi, J. W. Ochterski, R. L. Martin, K. Morokuma, O. Farkas, J. B. Foresman and D. J. Fox, *Gaussian, Inc., Wallingford CT*.

33 C. W. Bauschlicher, A. Ricca, C. Boersma and L. J. Allamandola, *Astrophys. J. Suppl. Ser.*, 2018, **234**, 32.
34 A. K. Lemmens, D. B. Rap, J. M. M. Thunnissen, C. J. Mackie, A. Candian, A. G. G. M. Tielens, A. M. Rijs and W. J. Buma, *Astron. Astrophys.*, 2019, **628**, A130.
35 L. J. Bellamy, *The Infra-red Spectra of Complex Molecules*, Chapman and Hall, London, 1975.
36 C. Boersma, A. L. Mattioda, C. W. Bauschlicher, E. Peeters, A. G. G. M. Tielens and L. J. Allamandola, *Astrophys. J.*, 2009, **690**, 1208–1221.
37 A. G. Császár, *Wiley Interdiscip. Rev. Comput. Mol. Sci.*, 2012, **2**, 273–289.
38 J. Mahé, S. Jaeqx, A. M. Rijs and M.-P. Gaigeot, *Phys. Chem. Chem. Phys.*, 2015, **17**, 25905–25914.
39 J. Laane and R. C. Lord, *J. Chem. Phys.*, 1967, **47**, 4941–4945.
40 V. Yatsyna, D. J. Bakker, R. Feifel, A. M. Rijs and V. Zhaunerchyk, *Phys. Chem. Chem. Phys.*, 2016, **18**, 6275–6283.
41 D. M. Hudgins and S. A. Sandford, *J. Phys. Chem. A*, 1998, **102**, 344–352.
42 H. Piest, G. Von, Helden and G. Meijer, *Astrophys. J.*, 1999, **520**, L75–L78.
43 J. Bloino, *J. Phys. Chem. A*, 2015, **119**, 5269–5287.

Appendix

Table 3.1: Measured and calculated (anharmonic) bands of naphthalene, anthracene, tetracene and pentacene with frequencies in (cm^{-1}) and normalized intensities.

Naphthalene				**Anthracene**			
Exp (cm^{-1})	**rel. intensity**	**calc. cm^{-1}**	**rel. intensity**	**Exp (cm^{-1})**	**rel. intensity**	**calc. cm^{-1}**	**rel. intensity**
618.24	0.11	627.4	0.05	724.8	0.84	727.6	1.00
770.8	0.30	…	…	877.6	1.00	879.0	0.60
782.7	1.00	784.6	1.00	908.8	0.25	904.2	0.03
800.5	0.54	795.9	0.00	956.3	0.03	955.8	0.09
956.0	0.24	958.5	0.02	979.0	0.15	1000.0	0.04
1007.7	0.53	1018.0	0.04	996.2	0.49	1013.0	0.02
1127.4	0.56	1133.2	0.03	1149.0	0.20	1157.2	0.02
1264.0	0.41	1269.0	0.02	1167.4	0.09	1171.9	0.02
1351.2	0.20	1350.0	0.01	1233.0	0.05	1230.0	0.01
1387.9	0.41	1388.0	0.02	1270.0	0.04	1271.0	0.02
1491.1	0.17	1496.0	0.00	1299.6	0.10	1300.9	0.00
1503.6	0.91	1503.0	0.00	1313.1	0.33	1317.4	0.07
1536.5	0.40	1537.0	0.03	1328.0		1327.0	
1595.0	0.22	1606.0	0.01	1342.1	0.09	1356.5	0.02
1671.1	0.87	1673.0	0.01	…	…	1365.9	0.01
1717.0	0.34	1722.0	0.01	1397.4	0.08	1391.9	0.00
1768.1	0.14	1766.0	0.00	1409.6	0.04	1405.0	0.00
1802.1	0.10	1808.0	0.01	1447.1	0.24	1451.1	0.00
1849.3	0.33	1850.0	0.01	1454.5	0.30	1459.3	0.01

1898.0	0.18	1896.0	0.01	1538.9	0.60	1543.0	0.01
1944.7	0.11	1947.0	0.03	1626.0	0.98	1633.0	0.02
				1673.0	0.14	1664.0	0.03
				1703.0	0.19	1689.0	0.01
Pentacene				1735.0	0.18	1723.0	0.00
Exp (cm^{-1})	**rel. intensity**	**calc. cm^{-1}**	**rel. intensity**	1760.0	0.41	1768.0	0.00
574.5	0.02	573.0	0.02	1775.0	0.14	1789.0	0.00
621.2	0.04	630.0	0.04	1792.0	0.34	1799.0	0.00
730.2	0.36	732.0	0.71	1812.0	0.06	1815.0	0.02
823.3	0.22	823.0	0.22				
897.9	1.00	905.0	1.00				
948.9	…	955.0	…	**Tetracene**			
967.0	0.41	964.0	0.09	**Exp (cm^{-1})**	**rel. intensity**	**calc. cm^{-1}**	**rel. intensity**
993.5	0.32	1003.0	0.13	548.0	0.19	555.6	0.11
1017.4	…	…	…	604.0	0.11	614.1	0.02
1039.4	0.22	1033.0	0.03	623.0	0.05	624.6	0.00
1103.0	0.12	1116.0	0.02	631.3	0.04	633.4	0.01
1122.3	0.26	1128.0	0.11	738.7	1.00	746.3	1.00
1155.6	0.11	…	…	892.9	0.96	900.0	0.81
1176.8	0.30	1189.0	0.05	934.4	0.21	938.7	0.01
1183.9	0.18	…	…	952.4	0.18	957.4	0.09
1204.0	0.16	1204.0	0.03	975.8	0.06	…	…
1218.0	0.10	…	…	996.6	0.29	1006.0	0.09
1232.8	…	…	…	1049.4	0.10	1067.3	0.01
1265.6	…	…	…	1123.8	0.35	1133.0	0.07
1288.0	0.67	1292.0	0.28	1081.3	0.11	1092.6	0.00
1297.3	…	1299.0	…	1195.4	0.16	1205.5	0.02
1315.0	…	1317.0	…	1289.1	0.62	1302.3	0.07
1319.6	0.74	1322.0	…	1328.6	0.42	1333.4	0.01
1326.7	…	1324.0	…	1381.7	0.17	1390.5	0.01
1349.1	0.47	1344.0	0.24	1410.0	0.32	1407.9	0.04
1393.9	0.48	1402.0	0.14	1457.7	0.18	1475.6	0.01
1446.2	…	1453.0	…	1498.6	0.13	1503.4	0.01
1459.1	0.27	1465.0	0.04	1536.9	0.29	1551.1	0.05
1500.0	0.41	1502.0	0.05	1563.4	0.08	1584.4	0.01
1512.0	…	1514.0	…	1574.4	0.08	1592.2	0.01
1546.9	…	1550.0	…	1632.1	0.28	1640.3	0.05
1560.3	0.35	1567.0	0.13	1670.6	0.33	…	…
1600.7	0.14	1603.0	0.03	1694.5	0.48	1698.2	0.01
1634.7	0.27	1637.0	0.19	1767.0	0.47	…	…
1668.3	0.14	1672.0	0.14	1779.6	…	1784.0	0.01
1689.5	0.19	1692.0	0.15	1809.5	0.21	1831.6	0.03
1720.0	0.10	1717.0	0.05	1885.7	…	…	…
1744.0	0.11	1747.0	0.10	1902.9	0.20	1911.9	0.02
1771.3	…	1776.0	…	1917.0	0.22	1929.1	0.02
1786.2	…	1791.0	…	1947.8	…	1948.7	0.06
1798.0	0.30	1799.0	0.32	1968.6	0.03	…	…
1827.4	0.14	1826.0	0.04				
1845.5	0.07	1847.0	0.09				

Chapter 4

Infrared spectroscopy of jet-cooled ‘grandPAHs’ in the 3-100 μm region

This chapter is published as:
Alexander K. Lemmens, Anouk M. Rijs and Wybren Jan Buma, *The Astrophysical Journal,* 923, 238, 2021

4.1 Abstract

Although large polycyclic aromatic hydrocarbons (PAHs) are likely to be responsible for infrared emission of gaseous and dusty regions, their neutral experimental high-resolution gas-phase infrared spectra -needed to construct accurate astronomical models- have so far remained out of reach because of their nonvolatility. Applying laser desorption to overcome this problem, we report here the first infrared (IR) spectra of the jet-cooled large PAHs coronene ($C_{24}H_{12}$), peropyrene ($C_{26}H_{14}$), ovalene ($C_{32}H_{14}$) and hexa(peri)benzocoronene ($C_{42}H_{18}$) in the 3-100 μm region. Apart from providing experimental spectra that can be compared directly to astronomical data, such IR spectra are crucial for assessing the accuracy of theoretically predicted spectra used to interpret interstellar infrared emission. Here, we use the experimental spectra to evaluate the performance of conventional calculations using the harmonic approximation as well as calculations with an anharmonic (GVPT2) treatment. The harmonic prediction agrees well with the experiment between 100 and 1000 cm^{-1} (100 and 10 μm), but shows significant shortcomings in the combination band (1600-2000 cm^{-1}, 6.25-5 μm) and CH-stretch (2950-3150 cm^{-1}, 3.4-3.17 μm) regions. Especially the CH-stretch region is known to be dominated by the effects of anharmonicity and we find that large PAHs are no exception. However, for the CH out-of-plane region (667-1000 cm^{-1}, 15-10 μm) the anharmonic treatment that significantly improves the predicted spectra for small PAHs leads to large and unrealistic frequency shifts as well as intensity changes for large PAHs, rendering thereby the default results unreliable. A detailed analysis of the results of the anharmonic treatment suggests a possible route for improvement, although the underlying cause for the large deviations remains a challenge for theory.

4.2 Introduction

Polycyclic aromatic hydrocarbons (PAHs) are by now generally accepted to be responsible for the infrared emission referred to as aromatic infrared bands (AIBs) observed from gaseous and dusty regions in the interstellar medium (ISM).[1–3] Much effort has thus been put into analyzing the IR emission spectra and determining the size distribution and structure of the PAHs in the ISM.[4] Although in general IR spectroscopy is an effective tool for structure elucidation[5], when considering the conditions of the ISM combined with that the of the heterogeneity of the mixture, it is challenging -and in fact as yet not possible- to identify specific species in the ISM. A more detailed insight in the infrared spectroscopic properties of directly relevant PAHs is imperative to interpret the interstellar IR emission.

Interstellar PAHs absorb UV radiation from a nearby star resulting in the excitation of rovibronic levels of electronically excited states. Internal conversion to the electronic ground state populates highly excited vibrational levels of the ground state that subsequently relax to the vibrational ground state by emitting IR photons through a vibrational cascade.[6,7] As it is not trivial to produce the UV-pumped IR emission spectra of the PAHs of interest under the relevant conditions[8–10], current state-of-the-art analyses rely on theoretical models.[7,11] Such analyses have led to the conclusion that the astronomically relevant PAHs typically have 50-150 carbon atoms organized in a compact structure.[12] PAHs that meet these characteristics have been designated as grandPAHs.[13] Currently used models are, however, only validated with smaller PAHs and may require optimization for larger molecules.[14]

These theoretical models should include accurate frequency and intensity predictions and be validated by laboratory experiments preferably carried out under cold and gas-phase conditions, e.g. in a molecular beam experiment. Difficulties producing a sufficient amount of gas-phase molecules to seed into a molecular beam by resistively heating the sample have so far restricted cold, gas phase spectroscopy to smaller PAHs.[15–17] To overcome these problems, we make use here of laser desorption[18] to bring a sufficient amount of molecules into the gas phase and subsequently entrain and cool them in a molecular beam. This approach thus enables us to record high-resolution, cold, gas-phase infrared spectra of much larger PAHs than have been reported so far.

In the present study we report on the infrared absorption spectra of the large and compact PAHs coronene ($C_{24}H_{12}$), peropyrene ($C_{26}H_{14}$), ovalene ($C_{32}H_{14}$) and hexa(peri)benzocoronene ($C_{42}H_{18}$). Experimental infrared spectra in the range between 3 and 100 μm are obtained under cold and isolated conditions and compared to, where available, state-of-the-art anharmonic calculations. As a result of its accessibility with ground-based telescopes, the CH-stretch 3 μm region is a well-studied region. Our recent studies on smaller PAHs have shown that this region is dominated by Fermi resonances, which considerably complicate its analysis.[15–17] The CC-stretch region between 5 and 10 μm (1000-2000 cm^{-1}) shows most activity from cationic species, while neutral large PAHs dominate the 15-10 μm (667-1000 cm^{-1}) CH out-of-plane range.[2] This range is most diagnostic for the structure of PAHs. As shifts of only a few wavenumbers are observed for different astronomical objects, a correct interpretation requires accurate reference spectra.[19,20] Longer-wavelength, far-IR regions contain weak bands, but since these bands are associated with unique global modes with molecule-specific infrared frequencies they provide clear fingerprints of the size and global structure of the PAHs from which they originate.[21] Laboratory spectroscopic studies of large PAHs in this region are therefore important to support the interpretation of new observational searches.[12]

4.3 Methods

Experiments were performed using a laser desorption molecular beam apparatus[22] located at the FELIX laboratory in the Netherlands.[23] Coronene (97%) was purchased from Sigma-Aldrich, ovalene (99.6 %) and peropyrene (99.5%) from Kentax, while hexa(peri)benzocoronene was synthesized using the procedure described by Liu et al.[24] The compounds were, without further purification, mixed with carbon black in a 1:1 ratio after which a graphite sample bar was pressed into the mixture. A slightly focused 1064 nm laser beam (10 Hz, Polaris Pulsed Nd:YAG Laser, NewWave Research) with a typical energy of 1 mJ/pulse was used to desorb the molecules while translating the sample bar, thereby providing fresh sample at every shot. The sample bar was placed in front of the nozzle of a pulsed valve (Jordan Co.) covering about half the orifice and the desorbed molecules were picked up by an argon jet (10 Hz, 8 bar backing pressure). The expanding gas pulse was skimmed before being crossed with three laser beams to perform IR-UV ion dip spectroscopy: one IR laser to probe the ground state vibrational frequencies and two UV/VIS lasers perpendicular to the molecular beam to perform 1+1' Resonance Enhanced MultiPhoton Ionization (REMPI). IR light was provided by the free electron laser FELIX for spectroscopy between 100 and 2000 cm^{-1} counterpropagating the molecular beam or by a high-resolution OPO laser (Laser Vision) covering the 2950-3150 cm^{-1} region perpendicular to the molecular beam. The bandwidth of FELIX is 0.5-1% of the IR frequency, while the bandwidth of the OPO is approximately 0.1 cm^{-1}. The idler frequency of the OPO was calibrated continuously during measurements using a HighFinesse WS-7 wavelength meter. Excitation and ionization laser beams were provided by a Nd:YAG laser pumped dye laser (Innolas Spitlight, Lioptec) and a 193 nm ArF excimer laser (Neweks), respectively. The ions were detected in a reflectron time-of-flight mass spectrometer (Jordan Co.). In our experiments we used excitation frequencies of 24187.7 cm^{-1} for coronene (34_0^1)[25], 21455.9 cm^{-1} for ovalene (0_0^0)[26], and 23074.7 cm^{-1} for hexa(peri)benzocoronene (feature *a*, see [27]). The REMPI excitation spectrum of peropyrene has not been measured in previous studies and is reported in the Appendix (Figure 4.5). From this spectrum it can be concluded that the 0_0^0 transition occurs at 23166.2 cm^{-1}, which has been the frequency used for the IR-UV ion dip experiments on this compound. For each of these electronic transitions a typical FWHM of about 1 cm^{-1} was observed. The IR lasers were operated at half the repetition rate of the REMPI lasers in order to collect alternating IR-on/IR-off ion yields.

Results of harmonic calculations on coronene, ovalene and hexa(peri)benzocoronene were retrieved from the NASA Ames PAH IR Spectroscopic Database(PAHdb).[11] The anharmonically calculated spectrum of coronene was taken from the study of Mulas et al.[28] while the anharmonic spectra of ovalene, hexa(peri)benzocoronene and peropyrene were calculated using GVPT2[29] as incorporated into the Gaussian16 suite of programs,

employing the B3LYP/Jun-cc-pVDZ or B3LYP/N07D level of theory with a superfine grid and very tight optimization.[29] For ovalene we found that the standard anharmonic treatment resulted in unrealistic frequency shifts and intensity changes of fundamental bands in the CH out-of-plane region. To resolve this, we recomputed the anharmonic treatment, but skipped modes 55, 58 and 62 and simply applied a scaling factor of 0.96 to these particular modes. This is discussed in more detail in Section 3.7. All displayed calculated spectra have been convoluted with a 1 cm^{-1} FWHM Gaussian in the 3 μm region, and a Gaussian with a FWHM of 1% of the frequency in the 5-100 μm region, roughly corresponding to the FELIX laser bandwidth.

4.4 Results and discussion

The infrared absorption spectra of jet-cooled coronene, ovalene, hexa(peri)benzocoronene and peropyrene in the 3 μm (OPO, 2950-3150 cm^{-1}) and the 5-100 μm (FELIX, 100-2000 cm^{-1}) regions are shown in Figure 4.1. Since the width of the peaks in the FELIX region is determined by the bandwidth of FELIX, narrower linewidths are observed in the far-IR than in the mid-IR region. The bandwidth of the OPO laser, on the other hand, is approximately 0.1 cm^{-1}, meaning that the observed linewidth of about 1 cm^{-1} is a result of the population distribution over rotational states, which is in line with the observed band widths of the electronic transitions. A rough estimate of the rotational temperature leads to a ballpark figure of 2 K, indicating that even with such large molecules effective cooling is possible. A list of the observed transitions is provided in the Appendix (Table 4.1).

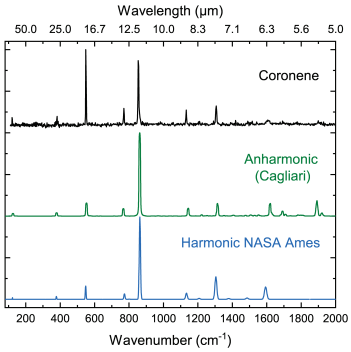
Wavelength (μm)
50.0 25.0 16.7 12.5 10.0 8.3 7.1 6.3 5.6 5.0
Coronene
Anharmonic
(Cagliari)
Harmonic NASA Ames
200 400 600 800 1000 1200 1400 1600 1800 2000
Wavenumber (cm-1)

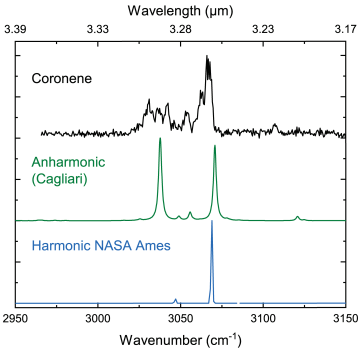
Wavelength (μm)
3.39 3.33 3.28 3.23 3.17
Coronene
Anharmonic
(Cagliari)
Harmonic NASA Ames
2950 3000 3050 3100 3150
Wavenumber (cm-1)

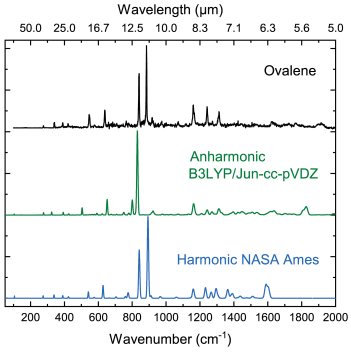
Wavelength (μm)
50.0 25.0 16.7 12.5 10.0 8.3 7.1 6.3 5.6 5.0
Ovalene
Anharmonic
B3LYP/Jun-cc-pVDZ
Harmonic NASA Ames
200 400 600 800 1000 1200 1400 1600 1800 2000
Wavenumber (cm-1)

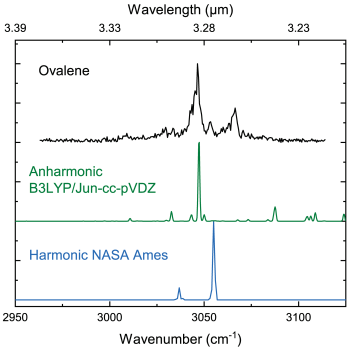
Wavelength (μm)
3.39 3.33 3.28 3.23
Ovalene
Anharmonic
B3LYP/Jun-cc-pVDZ
Harmonic NASA Ames
2950 3000 3050 3100
Wavenumber (cm-1)

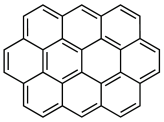

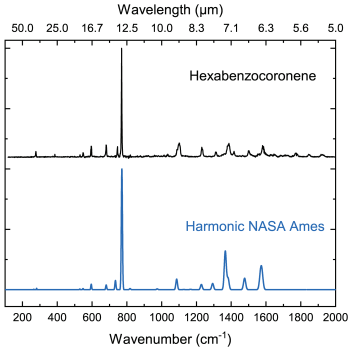
Wavelength (μm)
50.0 25.0 16.7 12.5 10.0 8.3 7.1 6.3 5.6 5.0
Hexabenzocoronene
Harmonic NASA Ames
200 400 600 800 1000 1200 1400 1600 1800 2000
Wavenumber (cm-1)

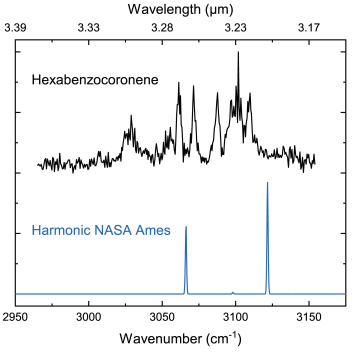
Wavelength (μm)
3.39 3.33 3.28 3.23 3.17
Hexabenzocoronene
Harmonic NASA Ames
2950 3000 3050 3100 3150
Wavenumber (cm-1)

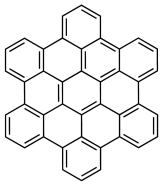

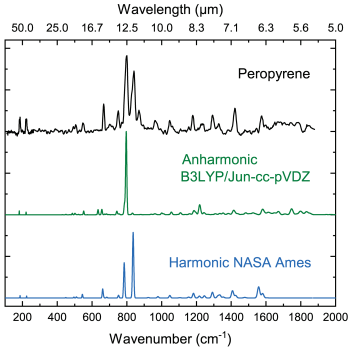
Wavelength (μm)
50.0 25.0 16.7 12.5 10.0 8.3 7.1 6.3 5.6 5.0
Peropyrene
Anharmonic
B3LYP/Jun-cc-pVDZ
Harmonic NASA Ames
200 400 600 800 1000 1200 1400 1600 1800 2000
Wavenumber (cm-1)

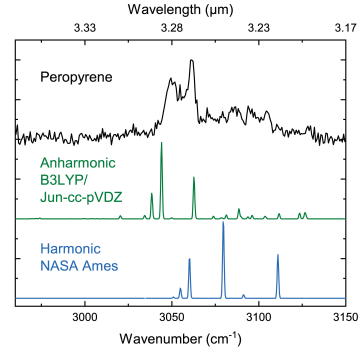
Wavelength (μm)
3.33 3.28 3.23 3.17
Peropyrene
Anharmonic
B3LYP/
Jun-cc-pVDZ
Harmonic
NASA Ames
3000 3050 3100 3150
Wavenumber (cm-1)

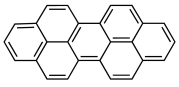

Figure 4.1: Infrared absorption spectra of coronene, ovalene, hexa(peri)benzocoronene and peropyrene in a molecular beam (black), together with predicted spectra using the harmonic approximation (blue) and including anharmonic effects (green). The harmonically calculated spectra have been retrieved from the NASA Ames PAH IR Spectroscopic Database (*PAHdb*)[11], the anharmonic calculation of coronene was taken from the Cagliari database[28], while the (default) anharmonic calculations of ovalene and peropyrene have been performed in the present study. The spectral regions discussed in this article include the CH-stretch (2950-3150 cm^{-1}, 3.4-3.17 μm), combination band (1600-2000 cm^{-1}, 6.25-5 μm), and CH out-of-plane (667-1000 cm^{-1}, 15-10 μm) regions, as well as the far-IR region at lower frequencies (longer wavelengths) than that.

4.4.1 General comparison to harmonic calculations

Figure 4.1 compares experimentally recorded IR spectra with spectra predicted by harmonic and anharmonic calculations. This Figure shows that the most intense bands in the FELIX region associated with the CH out-of-plane modes at approximately 800 cm^{-1} are well predicted using the harmonic approximation. However, as shown in Figure 4.2 the combination bands observed in the experimental spectrum between 1600-2000 cm^{-1} are not reproduced as they are per definition absent at this level of theory. For this reason Boersma et al. analyzed the astronomical PAH emission bands that fall in this region using a combination of laboratory measurements and anharmonic computations.[30] On average, the region below 1000 cm^{-1} is better predicted than the region between 1000 and 1600 cm^{-1} (difference of 0.6 and 1.3%, respectively). Similar to what was observed for smaller PAHs, the 3 μm region of these large PAHs is dominated by Fermi resonances. These lead to the observation of many more bands than predicted by harmonic theory and cause a large discrepancy between experiment and theory. Since the 3 μm and the 5-6 μm region is much more influenced by anharmonicity, it is clear that the interpretation of the IR emission in these regions should be based on models that incorporate resonances and are able to predict combination bands.

4.4.2 General comparison to anharmonic calculations

Anharmonic calculations account for combination bands and resonances and should therefore result in a more accurate prediction of the IR spectra of PAHs. In previous experiments we showed how anharmonic calculations can be used to obtain, for relatively small PAHs, an accurate description (<0.5%) of the FELIX region including the combination bands (1600-2000 cm^{-1}). More extensive research has been performed on the evaluation of anharmonic calculations in the 3 μm region, also for relatively small PAHs, for which the improvement upon anharmonic treatment has led to a significant reappraisal of the interpretation of astronomical observations.[15–17] Here, anharmonic calculations have been performed for ovalene and peropyrene using Gaussian16 GVPT2.[31,32] Such

calculations are not possible for coronene and hexa(peri)benzocoronene since an anharmonic treatment of symmetric top molecules has not **yet** been implemented in Gaussian 16. For coronene we therefore resort to the anharmonic spectrum reported by Mulas et al.[28] but for hexa(peri)benzocoronene anharmonic spectra are for the moment out of our reach. In the following sections we will discuss for each of these compounds in more detail the comparison between experimental and theoretically predicted spectra.

4.4.3 Coronene

Comparison of the anharmonically predicted spectrum of coronene with the experimental spectrum in Figure 4.1 shows good agreement, especially in the combination band region (1600-2000 cm^{-1}) as can be seen more clearly in Figure 4.2. The most intense peak in the spectrum -the CH out-of-plane band at 854.6 cm^{-1} is not shifted significantly upon anharmonic treatment. The same applies to other bands in this region. The band at 549 cm^{-1} is about four times more intense in our experiments than predicted in both the harmonic and anharmonic calculations. Interestingly, we find in the far-IR that the frequency of the band observed in the experimental spectrum at 121 cm^{-1}, which is associated with the drumhead mode, is 4% off in the anharmonic calculation but only 1% in the harmonic. Since the potentials of these low-frequency modes are quite shallow, this difference most probably is the result of inaccurate anharmonic constants.

In the region between 1000 and 2000 cm^{-1} the three largest bands at 1132, 1306 and 1607 cm^{-1} are well described by both harmonic and anharmonic calculations (see Figure 4.2). However, in agreement with the activity in the experimental spectrum the anharmonic analysis gives rise to many small features in this region that are not present in the harmonic approximation, although an unambiguous assignment of each individual feature is challenging. It is gratifying as well to find that the experimentally measured combination bands at 1694, 1774 and 1903 cm^{-1} agree relatively well with the predictions by Mulas et al.[28]

The 3 μm region shows an impressive improvement upon including anharmonicity. Especially notable is the 3030 cm^{-1} band in the anharmonic calculations which accounts for the intensity observed in this region in the experiment, although experimentally this intensity is distributed over three close-lying bands. We tentatively conclude that this discrepancy is caused by Coriolis resonances since coronene possesses degenerate vibrational states but rotation-vibration coupling is not included in the anharmonic approximation made by Mulas et al. Providing further support for the validity of these anharmonic calculations are the smaller bands observed experimentally at 3054 and 3107 cm^{-1} which, albeit slightly shifted, are nicely predicted by these calculations.

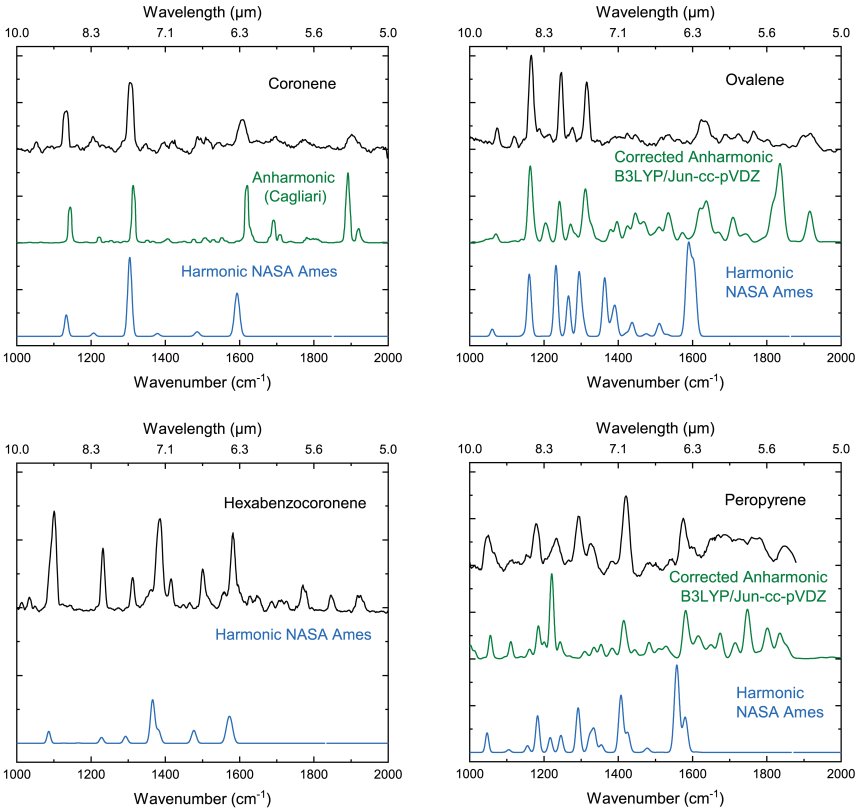

Figure 4.2: Zoom-in of the infrared absorption spectra of coronene, ovalene, hexa(peri)benzocoronene and peropyrene in a molecular beam (black), together with predicted spectra using the harmonic approximation (blue) and including anharmonic effects (green). The harmonically calculated spectra have been retrieved from the NASA Ames PAH IR Spectroscopic Database (PAHdb)[11], the anharmonic calculation of coronene was taken from the Cagliari database[28], while the anharmonic calculations of ovalene and peropyrene have been performed in the present study.

4.4.4 Hexabenzocoronene

The experimental IR spectrum of hexabenzocoronene is compared only to harmonic theory, since the anharmonic treatment of symmetric tops is not implemented in Gaussian16. Reducing the symmetry by a small perturbation of the atomic masses was not sufficient to circumvent this issue. Experimental and theoretical IR spectra are displayed in Figure 4.1. Features that attract interest include the far-IR peak at 276.8 cm^{-1} which is assigned to a mode in which the central ring moves out of the plane. The deviation of the predicted frequency from the experimental one is 1.6%, which is relatively large

compared to other modes below 700 cm^{-1} whose frequencies fall within 0.3% of experimental values.

The most intense band in the spectrum at 770 cm^{-1}, corresponding to the CH out-of-plane bending mode, agrees well with harmonic theory as was the case for coronene. The bands between 1000 and 1600 cm^{-1} are all predicted at a lower frequency than experimentally observed, differences ranging from 4 up to 30 cm^{-1}. The combination bands between 1500 and 2000 cm^{-1} are well resolved for hexabenzocoronene as are most bands in the 3 μm region. Due to the high symmetry of hexabenzocoronene, only three doubly degenerate CH-stretch transitions are IR active in the harmonic approximation. Clearly, this is in contrast with the experiment where at least eight transitions are observed with significantly (red-)shifted frequencies.

4.4.5 Ovalene

In the case of ovalene, the far-IR frequencies are well predicted by the harmonic NASA Ames PAHdb spectra, the average deviation being less than 0.5%. The CH out-of-plane bend region with the most intense bands between 800 and 900 cm^{-1} is somewhat less accurate but still within 1%. Significant deviations from the harmonic predicted spectra occur above 1100 cm^{-1}. Particularly eye-catching are the bands predicted to occur at 1363 and two around 1600 cm^{-1}, which are completely absent in the experimental IR spectrum.

Comparison of the experimental IR spectrum in the FELIX region with the anharmonic spectrum reveals large discrepancies. Upon anharmonic treatment the main fundamental transitions are shifted by an unrealistic large amount and they experience large intensity changes. For example, harmonic calculations predict a band at 879 cm^{-1} with an intensity of 58 km/mol, which is in good agreement with the experiment. In the anharmonic calculation this band shifts to 536 cm^{-1} and is predicted to have an intensity of only 0.1 km/mol. Further inspection of the bands indicates that these unrealistic changes all correspond to C and H out-of-plane bending modes. Since these modes are extensively involved in combination bands and resonances, one would in first instance expect that the combination band region and 3 μm region would also be affected by the incorrect anharmonic description of these modes. Nevertheless, it appears that the position of the main band in the 3 μm region is improved upon including anharmonicity which in general leads to a qualitatively better agreement with the experiment. The large shifts upon anharmonic treatment are discussed further in the section: Anharmonic calculations on large PAHs.

4.4.6 Peropyrene

Comparison of the experimental IR spectrum with the harmonic calculations shows a good agreement of the two most intense bands in the 100-2000 cm^{-1} region although their intensities are reversed (see Figure 4.1). The band observed experimentally at 837 cm^{-1} matches well with harmonic theory, while the second largest band is slightly off (experimentally at 797 cm^{-1} versus harmonic theory at 785 cm^{-1}). The far-IR peaks agree well with theory with an average deviation of 0.6% as was the case for coronene, hexabenzocoronene and ovalene.

Anharmonic treatment of the peropyrene spectrum leads to large discrepancies with the experimental spectrum in the CH out-of-plane bending region. Also, the 1000-1600 cm^{-1} region is not significantly improved by the anharmonic treatment. Although the frequencies of the bands observed experimentally at 1420 and 1576 cm^{-1} are slightly improved, the overall description is better in the harmonic approximation. Due to the bandwidth of FELIX, the 1600-1900 cm^{-1} region is not well resolved. Importantly though, the activity in this region, which is absent in the harmonic calculations but clearly observed in the experimental spectrum, is reproduced by the anharmonic calculations. Similar to ovalene, the 3 μm region in improved qualitatively by including anharmonicity but an assignment of individual bands is not clear-cut. Similar to coronene and ovalene, a significant portion of the intensity is found to the red of the harmonically predicted bands.

4.4.7 Anharmonic calculations of large PAHs

To understand why the anharmonic treatment of the larger PAHs ovalene and peropyrene leads to large and unrealistic changes in their IR absorption spectra, we performed the same procedure on other archetypal small and large PAHs. This study includes naphthalene, anthracene, phenanthrene, acenaphthene, pentacene, benzo[ghi]perylene, isoviolanthrene, anti-dipyrenylene, syn-dipyrenylene as well as the NPAHs quinoline and isoquinoline. Since the fundamental transitions in the 100-1600 cm^{-1} region -and especially the more intense bands- are well predicted using the harmonic approximation, in Figures 4.3a and 4.3b we have plotted the anharmonically calculated frequencies as a function of the harmonic frequencies for smaller PAHs and larger PAHs, respectively, taking 22 carbon atoms as dividing small and large.

For small PAHs we observe a linear relationship between harmonic and anharmonic frequencies, in line with the generally accepted use of a scaling factor to correct harmonic frequencies. No significant (>1%) deviation from the linear relation is observed. Phenanthrene is in this respect an exception, but the affected modes are IR-inactive. In general, the larger PAHs show a similar linear relationship, but large deviations are observed for

modes with frequencies between 750 and 1000 cm^{-1}. We find that the unrealistic large frequency shift that was observed in the anharmonic calculations on ovalene and peropyrene is also present in the calculations on other large PAHs, but absent in anharmonic calculations on smaller PAHs. Concurrently with these large frequency changes also large changes in intensity occur, e.g. the mode at 879 cm^{-1} of ovalene loses almost all of its intensity after the anharmonic treatment. These modes correspond for all investigated PAHs with C and H out-of-plane bending vibrations. Modes in the 3 μm region, on the other hand, behave regularly with almost all fundamental anharmonic frequencies being within a 1% deviation from a linear relationship with the harmonic frequencies.

In order to overcome these clear inadequacies of the anharmonic treatment, we have removed the anharmonic contributions of selected modes, and instead simply scale the frequencies of these modes. In the case of ovalene these concern modes 55, 58 and 62; with modes 55 and 62 corresponding to the bands with the highest intensity in the region up to 2000 cm^{-1}. Mode 58 is the most affected mode in this region in terms of frequency. For peropyrene we similarly find that the modes with the highest intensity (modes 39 and 42) need to be removed from the anharmonic treatment. In the harmonic framework, these modes include out-of-plane displacements of both C and H atoms. The results of this alternative treatment are shown in Figure 4.4. Zoom-ins of the 1000-2000 cm^{-1} region with the corrected anharmonic treatment are displayed in Figure 4.2. For ovalene we observe that -besides the modes that are removed from the anharmonic treatment- also the bands between 1000 and 2000 cm^{-1} are slightly affected. In contrast, the 3 μm region is not affected by removal of the three modes in the anharmonic analysis. The zoom-in of the 1000-2000 cm^{-1} region of ovalene shows a large improvement with respect to the harmonic approximation. In the case of peropyrene, our alternative anharmonic treatment only minimally affects the 1000-2000 cm^{-1} region as well as the 3 μm region (see Figure 4.4). A significant improvement is, however, observed in the bands in the 600-750 cm^{-1} region, directly to the red of modes 39 and 42. Similar to what was found for the 3 μm and mid-IR regions of small PAHs[15–17], we thus conclude that for large PAHs an anharmonic treatment is a suitable and necessary route for improving predicted IR spectra with as an important caveat that one needs to eliminate unrealistic frequency and intensity changes in the 750-1000 cm^{-1} region.

It is interesting to notice that other recent studies[33–36] also report on problems with calculating frequencies of out-of-plane bending modes of systems that include C=C bonds. In these studies, harmonic calculations gave rise to imaginary frequencies for geometries for which these modes should have real frequencies. In our harmonic calculations on large PAHs we do not encounter such imaginary frequencies and also find that the low-frequency peaks in the far-IR are relatively well predicted using harmonic theory. Instead, the unrealistic large intensity changes and frequency shifts of the out-of-plane bending modes only arise after anharmonic analysis. It is nevertheless remarkable

that the modes for which this occurs are the same kind of modes discussed by Lee[35] for benzene-like molecules, namely modes where both C and H atoms move out of the plane, suggesting that there is link between these two issues.

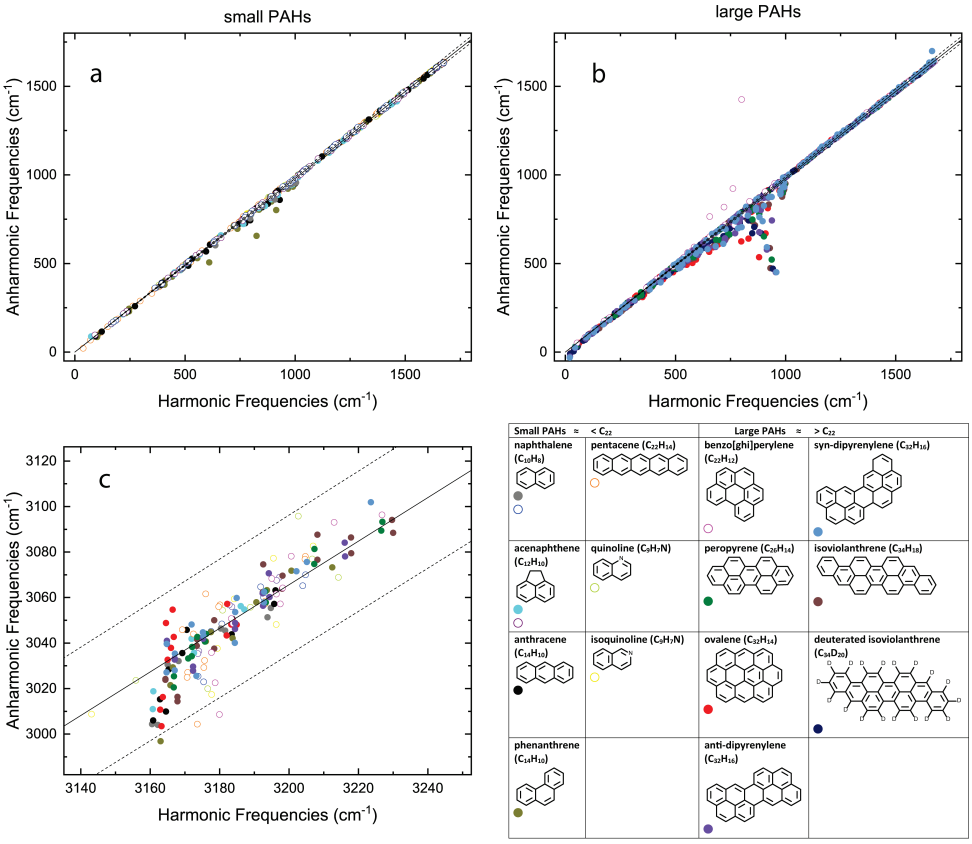

Figure 4.3: Fundamental anharmonic frequencies as a function of harmonic frequencies for small (a) and large (b) PAHs in the far- and mid-IR region, and (c) of small and large PAHs in the 3 μm region. The solid line is a linear fit, the dotted lines indicate a 1% deviation. Closed and open circles correspond to calculations with the Jun-cc-pVDZ and N07D basis sets, respectively.

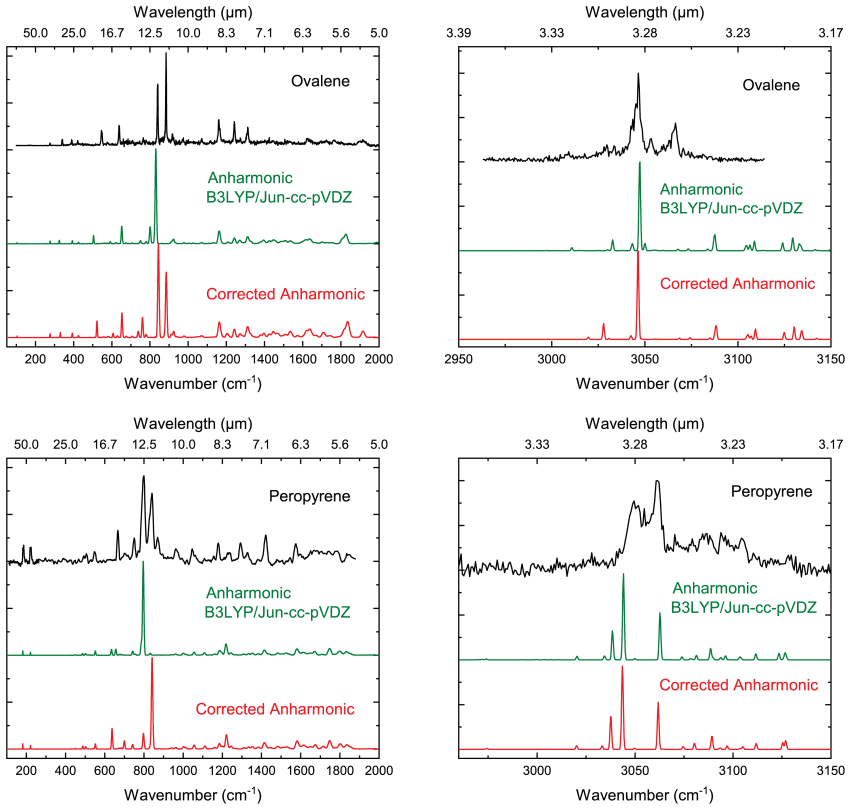

Figure 4.4: Infrared absorption spectrum of ovalene and peropyrene in a molecular beam (black), together with predicted spectra using the anharmonic treatment in Gaussian16 (green). Large, unrealistic frequency shifts and intensity changes are corrected for by taking modes 55, 58 and 62 out of the anharmonic analysis of ovalene and modes 39 and 42 in the case of peropyrene (red).

4.5 Astrophysical implications

The present study has investigated the 3-100 μm (100-3150 cm^{-1}) IR spectra of coronene, ovalene, hexa(peri)benzocoronene and peropyrene under astronomically relevant conditions, that is, at low temperatures and under isolated conditions. These are larger PAHs with different geometries and edge topologies that come close to the size of PAHs concluded to be dominantly responsible for the AIBs.[12,13] Previously, gas-phase high-resolution infrared spectra of small PAHs have been used to validate anharmonic calculations and the incorporation of anharmonicity was proven to be essential. However, larger PAHs have so far remained out of reach both from an experimental point of view as well as from the application of high-end anharmonic theoretical methods. The present study

thus provides the first direct lead to assessing the suitability of theoretical methods to predict IR spectra of large PAHs and their application in astronomical models.

Firstly, we find that the experimental IR spectra of larger PAHs confirm the conclusion drawn from previous experiments on small PAHs that far-IR modes are not by default anharmonic, but can be calculated harmonically with a comparable accuracy as with more expensive anharmonic treatments. In quantitative terms we show that the frequencies of the main CH out-of-plane features in the region below about 1000 cm^{-1} are computed on the harmonic level of theory within 0.6% of their experimental values. This is an important conclusion since this region is also the spectral region in the interstellar infrared emission where most characteristic bands are attributed to neutral PAHs.

Secondly, the bands that are located above about 1000 cm^{-1} are largely affected by anharmonicity. In the combination band region (1600-2000 cm^{-1}), where no intensity is predicted using the harmonic approximation, and especially in the 3 μm region (2950-3150 cm^{-1}) the spectra are dominated by anharmonicity. The combination band region is relatively accurately predicted for coronene by Mulas et al. and also in the 3 μm region a qualitative improvement can be observed for ovalene and peropyrene. For all large PAHs studied here we find that anharmonicity results in an average redshift of the CH-stretch peaks and that its inclusion is necessary to come to a realistic comparison with the experimental spectrum.

Thirdly, the symmetry of coronene and hexabenzocoronene impedes the anharmonic treatment in Gaussian16. Quite unexpectedly, we find that an anharmonic treatment of PAHs with a lower symmetry such as ovalene and peropyrene results in unrealistically large frequency shifts and intensity changes of C and H out-of-plane bending modes between about 700-1000 cm^{-1}. This renders the default GVPT2 calculations in Gaussian16 unreliable. Our studies show that an alternative treatment in which the anharmonic contributions from the most affected modes are not taken into account avoids such problems. Interestingly, we find that removal of these modes leaves the anharmonicity-dominated 3 μm region almost unaffected. Although incorporating anharmonicity is thus key for a proper analysis of AIBs, our studies show that this should be done with much care when considering larger PAHs.

4.6 Conclusions

Laser desorption opens up the possibility to bring large PAHs in the gas phase and study them under cold and isolated conditions. Using IR-UV ion dip spectroscopy, mass-selective IR spectra of neutral PAHs have been obtained that can be used to validate theoretical methods that are crucial for the modeling and subsequent interpretation of astronomical studies of interstellar infrared emission. Previous studies have focused on small

PAHs and mainly on their CH-stretch region. In contrast, the present work gives access to PAHs with astronomically relevant sizes and covering the 3-100 μm region. We have found that the anharmonic treatment that is beneficial for smaller PAHs results in unrealistic, large frequency shifts and intensity changes of C and H out-of-plane bending modes of large PAHs between about 10 and 13 μm. These bands are, on the other hand, relatively well predicted using the harmonic approximation. In the far-IR region global modes are located that are unique for individual PAH species and that may allow for discrimination of specific PAHs. These modes appear to be well described within the harmonic approximation, and their anharmonic treatment does not lead to significant improvements. Anharmonicity remains, however, also for larger PAHs the dominating factor that absolutely needs to be taken into account to come to a proper description of the combination band (5-6 μm) and CH-stretch region (3 μm).

References

1 K. M. Gillett, F. C., Forrest, W. J., & Merrill, *Astrophys. J.*, 1973, **183**, 87–93.
2 A. G. G. M. Tielens, *Annu. Rev. Astron. Astrophys*, 2008, **46**, 289–337.
3 L. J. Allamondola, A. G. G. M. Tielens and J. R. Barker, *Astrophys. J.*, 1985, **290**, L25–L28.
4 A. G. G. M. Tielens, *Rev. Mod. Phys.*, 2013, **85**, 1021–1081.
5 S. Bakels, M. P. Gaigeot and A. M. Rijs, *Chem. Rev.*, 2020, **120**, 3233–3260.
6 L. J. Allamandola, A. G. G. M. Tielens and J. R. Barker, *Astrophys. J. Suppl. Ser.*, 1989, **71**, 733–775.
7 C. J. Mackie, T. Chen, A. Candian, T. J. Lee and A. G. G. M. Tielens, *J. Chem. Phys.*, 2018, 149, 134302.
8 D. J. Cook, S. Schlemmer, N. Balucani, D. R. Wagner, J. A. Harrison, B. Steiner and R. J. Saykally, *J. Phys. Chem. A*, 1998, **102**, 1465–1481.
9 H. S. Kim and R. J. Saykally, *Rev. Sci. Instrum.*, 2003, **74**, 2488–2494.
10 H. Kim and R. J. Saykally, *Astrophys. J. Suppl. Ser.*, 2002, **143**, 455–467.
11 C. W. Bauschlicher, A. Ricca, C. Boersma and L. J. Allamandola, *Astrophys. J. Suppl. Ser.*, 2018, **234**, 32.
12 A. Ricca, C. W. Bauschlicher, C. Boersma, A. G. G. M. Tielens and L. J. Allamandola, *Astrophys. J.*, 2012, **754**, 75.
13 H. Andrews, C. Boersma, M. W. Werner, J. Livingston, L. J. Allamandola and A. G. G. M. Tielens, *Astrophys. J.*, 2015, 807, 24pp.
14 A. Candian and C. J. Mackie, *Int. J. Quantum Chem.*, 2017, **117**, 146–150.
15 E. Maltseva, A. Petrignani, A. Candian, C. J. Mackie, X. Huang, T. J. Lee, A. G. G. M. Tielens, J. Oomens and W. J. Buma, *Astrophys. J.*, 2015, **814**, 6pp.

16 E. Maltseva, A. Petrignani, A. Candian, C. J. Mackie, X. Huang, T. J. Lee, A. G. G. M. Tielens, J. Oomens and W. J. Buma, *Astrophys. J.*, 2016, **831**, 11pp.
17 E. Maltseva, C. J. Mackie, A. Candian, A. Petrignani, X. Huang, T. J. Lee, A. G. G. M. Tielens, J. Oomens and W. J. Buma, *Astron. Astrophys.*, 2018, **610**, 1–13.
18 G. Meijer, M. S. de Vries, H. E. Hunziker and H. R. Wendt, *Appl. Phys. B*, 1990, **51**, 395–403.
19 M. Matsuura, J. Bernard-salas, T. L. Evans, K. M. Volk, B. J. Hrivnak, G. C. Sloan, Y. Chu, R. Gruendl, K. E. Kraemer, E. Peeters, R. Szczerba, P. R. Wood, A. A. Zijlstra, S. Hony, Y. Ita, D. Kamath, E. Lagadec, Q. A. Parker, W. A. Reid, T. Shimonishi, H. Van Winckel, P. M. Woods, F. Kemper, M. Meixner, M. Otsuka, R. Sahai, B. A. Sargent, J. L. Hora and I. Mcdonald, *MNRAS*, 2014, **439**, 1472–1493.
20 S. Hony, C. Van Kerckhoven, E. Peeters and A. G. G. M. Tielens, *Astron. Astrophys.*, 2001, **370**, 1030–1043.
21 G. Mulas, G. Malloci, C. Joblin and D. Toublanc, *Astron. Astrophys.*, 2006, **460**, 93–104.
22 A. M. Rijs and J. Oomens, *Top. Curr. Chem.*, 2015, **364**, 1–42.
23 D. Oepts, A. F. G. Van, D. Meer and P. W. Van Amersfoort, *Infrared Phys. Technol.*, 1995, **36**, 297–308.
24 R. Liu, D. Wu, X. Feng and K. Müllen, *J. Am. Chem. Soc.*, 2011, **133**, 15221–15223.
25 S. Kunishige, A. Kanaoka, T. Katori, M. Kawabata, M. Baba, T. Yamanaka, S. Higashibayashi and H. Sakurai, *J. Chem. Phys.*, 2017, 146, 44309.
26 A. Amirav, *J. Chem. Phys.*, 1981, **74**, 3745.
27 D. L. Kokkin, T. P. Troy, M. Nakajima, K. Nauta, T. D. Varberg, G. F. Metha, N. T. Lucas and T. W. Schmidt, *Astrophys. J.*, 2008, **681**, 49–51.
28 G. Mulas, C. Falvo, P. Cassam-chenaï, C. Joblin, G. Mulas, C. Falvo and P. Cassam-chena, *J. Chem. Phys.*, 2018, **149**, 144102.
29 M. J. Frisch, G. W. Trucks, H. B. Schlegel, G. E. Scuseria, M. A. Robb, J. R. Cheeseman, G. Scalmani, V. Barone, G. A. Petersson, H. Nakatsuji, X. Li, M. Caricato, A. V. Marenich, J. Bloino, B. G. Janesko, R. Gomperts, B. Mennucci, H. P. Hratchian, J. V. Ortiz, A. F. Izmaylov, J. L. Sonnenberg, D. Williams-Young, F. Ding, F. Lipparini, F. Egidi, J. Goings, B. Peng, A. Petrone, T. Henderson, D. Ranasinghe, V. G. Zakrzewski, J. Gao, N. Rega, G. Zheng, W. Liang, M. Hada, M. Ehara, K. Toyota, R. Fukuda, J. Hasegawa, M. Ishida, T. Nakajima, Y. Honda, O. Kitao, H. Nakai, T. Vreven, K. Throssell, J. Montgomery, J. A., J. E. Peralta, F. Ogliaro, M. J. Bearpark, J. J. Heyd, E. N. Brothers, K. N. Kudin, V. N. Staroverov, T. A. Keith, R. Kobayashi, J. Normand, K. Raghavachari, A. P. Rendell, J. C. Burant, S. S. Iyengar, J. Tomasi, M. Cossi, J. M. Millam, M. Klene, C. Adamo, R. Cammi, J. W. Ochterski, R. L. Martin, K. Morokuma, O. Farkas, J. B. Foresman and D. J. Fox, *Gaussian, Inc., Wallingford CT*.

30 C. Boersma, A. L. Mattioda, C. W. Bauschlicher, E. Peeters, A. G. G. M. Tielens and L. J. Allamandola, *Astrophys. J.*, 2009, **690**, 1208–1221.
31 V. Barone, J. Bloino, C. A. Guido and F. Lipparini, *Chem. Phys. Lett.*, 2010, **496**, 157–161.
32 V. Barone, M. Biczysko and J. Bloino, *Phys. Chem. Chem. Phys.*, 2014, **16**, 1759–1787.
33 C. W. Bauschlicher, *Chem. Phys. Lett.*, 2016, **665**, 100–104.
34 P. B. Karadakov, *Chem. Phys. Lett.*, 2016, **646**, 190–196.
35 T. J. Lee and R. C. Fortenberry, *Spectrochim. Acta Part A Mol. Biomol. Spectrosc.*, 2020, **248**, 119148.
36 R. C. Fortenberry, T. J. Lee, J. P. Layfield, R. C. Fortenberry, T. J. Lee and J. P. Layfield, *J. Chem. Phys.*, 2017, **147**, 1–5.

Appendix

Table 4.1: Experimentally measured bands of coronene, ovalene, hexa(peri)benzocoronene and peropyrene compared to the harmonic and anharmonic theoretically predicted bands. Frequencies in (cm^{-1}) and normalized intensities.

Coronene					
Exp (cm^{-1})	**rel. int.**	**Harmonic NASA Ames (cm^{-1})**	**rel. int.**	**Anharmonic (cm^{-1})**	**rel. int.**
121.1	0.004	122.6	0.03	126	0.03
381.1	0.03	377.7	0.04	379	0.04
549.2	0.61	548	0.16	553	0.16
770.1	0.21	773.2	0.07	767	0.09
854.6	1.00	862.8	1.00	862	1.00
1132.1	0.19	1134	0.07	1143	0.10
1208.1	0.08	1207	0.01	1222	0.01
1306.4	0.35	1304	0.16	1315	0.15
1607.1	0.23	1593	0.07	1619	0.19
1694	0.09			1692	0.10
1774.4	0.09			1783	0.04
1902.8	0.12			1889, 1892, 1895, 1918, 1920	0.26
3024.88	0.14				
3030.83	0.52				
3036.62	0.29				
3041.75	0.29				
3053.72	0.28				
3062.84	0.51				
3066.84	1.00				
3107.13	0.11				

Ovalene			
Exp (cm^{-1})	**rel. int.**	**Harmonic NASA Ames (cm^{-1})**	**rel. int.**
276.0	0.03	274.5	0.03
340.4	0.05	338.8	0.04
389.9	0.06	390.0	0.03
421.8	0.05	423.5	0.02
546.6	0.18	541.2	0.08
577.5	0.04	575.4	0.01
638.3	0.21	627.8	0.16
765.2	0.09	759.7	0.02
779.4	0.07	777.2, 773.9	0.07
839.2	0.69	841.4	0.59
884.0	1.00	892.90	1.00
918.7	0.25	910.0	0.03
973.8	0.14	965.4	0.02
1073.4	0.12	1061.0	0.01
1120.5	0.08	1147.0	0.00
1165.4	0.71	1159, 1165	0.12
1245.8	0.53	1232.0	0.13
1277.7	0.13	1294.0	0.11
1315.3	0.56	1363.0	0.11
1421.0	0.49		
1533.5	0.22		
1630.5	0.53	1588, 1604	0.28
1689.0	0.18		
1723.8	0.17		
1765.5	0.18		
1909.9	0.26		
3008.67	0.08		
3029.28	0.16		
3033.62	0.14		
3046.11	1.00		
3053.22	0.20		
3065.77	0.52		
Hexa(peri) benzocoronene			
Exp (cm^{-1})	**rel. int.**	**Harmonic NASA Ames (cm^{-1})**	**rel. int.**
276.8	0.05	281.2	0.01
530.5	0.02	529.2	0.01
548.0	0.05	547.7	0.01
594.4	0.12	595.1	0.05
680.7	0.18	681.2	0.04
746.1	0.11	734.3	0.08
770.1	1.00	771.3	1.00
819.2	0.03	818.3	0.01
1035.4	0.08		
1098.9	0.67	1086	0.04
1232.1	0.26	1228	0.04
1312.0	0.16	1293	0.05
1384.0	0.75	1366	0.32
1414.9	0.17	1382	0.09

1501.7	0.26	1477	0.09
1582.4	0.61	1569 and 1577	0.24
1628.2	0.06		
1647.6	0.10		
1686.3	0.06		
1709.0	0.07		
1726.0	0.05		
1772.4	0.18		
1847.3	0.09		
1923.5	0.12		
3007.2	0.04		
3028.6	0.64		
3046.1	0.06		
3055.3	0.27		
3061.4	0.37		
3071.5	0.36		
3087.5	0.40		
3100.2	1.00		
3109.2	0.50		

Peropyrene

Exp (cm^{-1})	rel. int.	Harmonic NASA Ames (cm^{-1})	rel. int.	Anharmonic	rel. int.
182.40	0.04	181.80	0.01	181.43	0.00878
186.00	0.05	186.00	0.04		
221.80	0.08	223.50	0.03	220.7	0.006829
492.90	0.03	495.40	0.01	486.5	0.007805
506.10	0.05	509.70	0.02	501.6	0.007805
548.50	0.07	544.30	0.06	551.7	0.025366
666.70	0.19	661.00	0.14		
749.80	0.16	751.90	0.04		
772.00	0.06				
797.00	1.00	785.00	0.55		
837.20	0.94	836.10	1.00		
869.20	0.16				
965.40	0.22	978.70	0.02	961.3	0.00878
1018.50	0.02				
1050.50	0.45	1047.00	0.01	1155.8	0.273171
1112.00	0.25	1105.00	0.00	1108.1	0.204878
1155.00	0.11	1156.00	0.01	1161	0.107317
1179.10	0.81	1183.00	0.07	1187.4	0.4
1231.90	0.28			1218.8	1
1267.50	0.07				
1293.60	0.50	1292.00	0.09	1309.6	0.11
1326.90	0.95	1335.00	0.04		
1384.60	0.29		0.00	1383.9	0.15
1420.40	0.93	1407	0.11	1415	0.53
1482.80	0.76	1478	0.01	1484.3	0.263415
1542.60	0.12			1526.1	0.517073
1576.10	1.16	1558	0.17	1581.6	1.073171
1598.50	0.13	1580	0.07	1613.5	0.204878

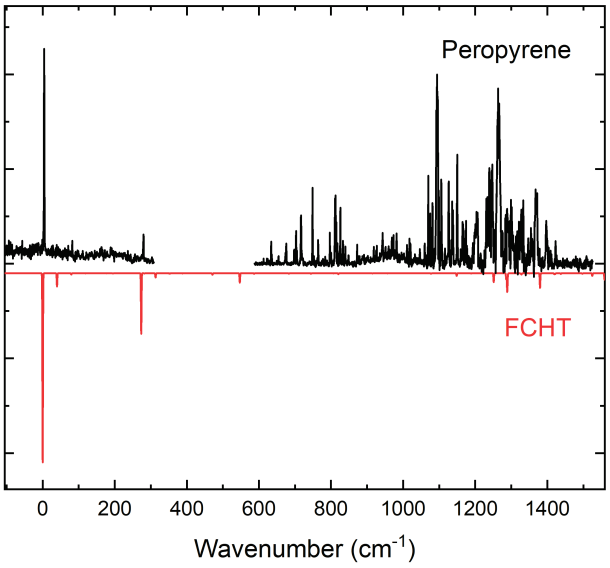

Figure 4.5: 1+1' REMPI excitation spectrum of peropyrene. Energies are given with respect to the 0-0 transition at 23166.2 cm^{-1}.

Chapter 5

Size distribution of polycyclic aromatic hydrocarbons in space: an old new light on the 11.2/3.3 μm intensity ratio

5.1 Abstract

The intensity ratio of the 11.2/3.3 μm emission bands is currently considered to be a reliable tracer to determine the size distribution of polycyclic aromatic hydrocarbons (PAHs) in the interstellar medium. This chapter describes the validation of the calculated intrinsic infrared (IR) spectra of PAHs that underly the interpretation of the observed ratios. The comparison of harmonic calculations from the NASA Ames PAH IR spectroscopic database to gas-phase direct absorption IR spectra reveals a significant, but consistent, underestimation of the 11.2/3.3 μm intensity ratio by 34%. IR spectra based on higher level anharmonic calculations, on the other hand, are in very good agreement with the experiment. Unfortunately, it is not yet possible to reliably calculate spectra at such a level for large PAHs. Therefore, an approximate correction is made to the emission model based on the lower-level calculated IR spectra. This corrected model suggests that typical PAH sizes in the interstellar medium -that previously were concluded to be in the range of 50-70 carbon atoms per PAH- could actually expected to be in the range of 40-55 carbon atoms. The higher limit is quite close to the size of the C_{60} fullerene, which would be in line with the hypothesis that under appropriate conditions large PAHs are converted into the more stable fullerenes in the interstellar medium.

5.2 Introduction

The most widely accepted explanation for the emission of distinct infrared (IR) features, observed towards many different phases of the interstellar medium (ISM) is the PAH hypothesis.[1–3] From different regions of the ISM a small, but clear variation of spectral profiles is observed, which is attributed to a variation in the population of PAHs in terms of size, structure and charge state.[4,5] The variation is thought to be a result of a difference in local physical conditions, which are largely determined by the radiation field.[6,7] Since the introduction of the PAH hypothesis, much effort has gone into modeling the mechanisms of molecular IR emission with the goal of placing more constraints on the molecular inventory of the ISM. Apart from the charge state, abundance and structure, one of the constraints that receives a lot of attention is the size of PAHs in terms of the number of carbon atoms.

The IR emission by isolated PAHs is believed to start with the absorption of a UV photon. Because under the dilute conditions of the ISM the collisional cooling rate is much smaller than the spontaneous emission rate, most energy is lost by vibrational relaxation which is accompanied by the fluorescence of IR photons. The observed IR spectrum is an average of different PAH species relaxing and emitting IR photons via different relaxation

cascades[8]. Interstellar PAHs are exposed to a spectrum of UV photon energies, but in first approximation -and because the UV photon energy does not vary a lot within objects- the UV photon energy is often taken as a single value.[6]

Currently, the commonly accepted approach for deriving the size distribution of PAHs involves the intensity ratio of the 3.3 μm band to that of a band at a longer wavelength, typically the 11.2 μm band.[2,9–16] The 3.3 μm peak corresponds to CH stretch vibrations and the relative intensity of this mode was found to have the strongest (inverse) dependence on the number of carbon atoms within a PAH.[9] The 11.2 μm peak is due to the CH out-of-plane (OOP) mode from solo Hs. The complete CH OOP region, which includes also the duo, trio and quartet H OOP modes, has been nicely decomposed and analyzed by Bauschlicher *et al.* and ranges from about 15.4 to 10.5 μm (650-950 cm^{-1}).[17]

The main reason behind the sensitivity of the 11.2/3.3 μm intensity ratio to molecular size is that smaller PAHs reach a higher temperature upon absorption of the same UV photon due to their smaller heat capacity, and therefore emit more photons at higher frequencies than larger PAHs.[4] The heat capacity, and thereby the cascade starting temperature that results from the absorption of a particular UV photon, can be described in terms of isolated harmonic oscillators or alternatively be calculated using more general PAH properties (approximation by Stein and Dwek et al.).[18–20] Additional advantages of using the 11.2/3.3 μm intensity ratio as a size tracer are that both bands originate mainly from CH bonds in neutral species and that they are spectrally well separated.[6] Moreover, the effect of the number of hydrogen atoms or the effect of PAHs having a particular molecular structure on the ratio is minimal.[12]

The NASA Ames PAH IR spectroscopic database (*PAHdb*) supports a number of analyses of the observed 11.2/3.3 μm ratio.[21] It has been used to determine the PAH sizes in several astrophysical objects[12,22,23] and most recently by Maragkoudakis *et al.* who explored extensively the 11.2/3.3 relation to PAH size with the aim to accurately describe the size distribution.[9] The calculated 0 K absorption intensities (hereafter called intrinsic strengths) that underly the emission models not only affect the emission ratio, but also the band profile. By artificially adjusting the intrinsic ratio it was found that a large 11.2/3.3 μm ratio results in a red-wing at the 11.2 μm feature which fades away at smaller ratios.[24]

The IR intensities in the *PAHdb* that are employed in the emission models are calculated on a relatively low level of theory and based on the harmonic approximation. Because of the significant effect of intrinsic strengths on the outcome of the emission models in terms of ratio and peak profile, it is of key importance to validate these calculations with suitable experiments. Even more so because it was noticed already in the 90s by Langhoff -and later by others- that the intensity ratios derived at different levels of theory can vary significantly.[25–27] First, the use of a smaller basis set results in an overprediction of CH stretch intensities by about 20%.[25] Secondly, it was recently shown that

anharmonicity leading to phenomena such as combination bands and resonances has a dominating effect on the CH stretch region of the IR spectrum in particular. These anharmonic contributions can carry significant intensity.[26,28]

Moreover, also from an experimental perspective it has been concluded that one needs to be cautious. Compared to the gas phase, the CH stretch intensity in IR absorption measurements in the solid phase is about a factor 3 lower. In matrix isolation IR absorption measurements, on the other hand, the CH OOP intensity is about a factor 5 lower. Both experimental conditions will thus have a large effect on the 11.2/3.3 μm ratio.[29]

The main focus of other chapters in this thesis is on the accuracy of peak frequencies and potential energy surfaces using IR-UV ion dip spectroscopy. The aim of this chapter is to compare the anharmonic theory that is used throughout this thesis to experimental data in terms of intensity, utilizing direct absorption techniques for reliable intensities over a wide wavelength range. The theory at a (relatively) low vibrational temperature should be validated before extrapolating the models to describe the emission of highly excited PAHs and using these models to put constraints on the size distribution of PAHs. The gas-phase FTIR technique provides a good benchmark for oscillator strengths, because at the relatively low experimental temperatures there is no significant occupation of higher vibrational levels. In first approximation, the higher temperature will thus only lead to band broadening.[29,30] Moreover, with FTIR spectroscopy data are collected simultaneously from a wide spectral range.

5.3 Methods

We compared (relative) intensities from the IR spectra of PAHs from four different experimental and theoretical sources. The NASA Ames PAH IR spectroscopic database (*PAHdb,* version 3.20)[21], anharmonic calculations extracted from the work by Mackie et al.[31] or performed here by using the Gaussian16[32] software package, experimental gas-phase FT-IR absorption spectra from the NIST database[33] and experimental matrix isolation IR spectra extracted from the *PAHdb*. To study the relation between molecular size and the intrinsic 3.3/11.2 μm ratio, we extracted theoretical PAH spectra from the *PAHdb* of neutral PAHs that do not contain any oxygen or nitrogen atoms (Figure 5.1). The intensity is integrated between 15.4 and 10.5 μm (650-950 cm^{-1}) and will be indicated in the following as 'oop'. The integrated range for the CH stretch region, indicated in the following as 'stretch', spans from 3.6-3.1 μm (2750-3250 cm^{-1}). For the ratio in emission (Figure 5.3) we made the following selection: neutral PAHs that contain more than one hydrogen atom, no aliphatic groups and we did not include Fe, Si, Mg, N, or O substituted species. Lastly, we only considered PAHs with solo (more than 4) and duo hydrogens, as they are generally more compact and thus more stable. One can reasonably expect that

this restriction will only affect to a minor extent the conclusions as the structure of the PAH should not have a large influence on the oop/stretch emission ratio.[25,29] A cascade starting point of 6.5 eV adopted from Croiset *et al.* was used.[12] Calculations referred to as anharmonic are either described previously and extracted from ref.[31], or they have been performed at the anharmonic[34,35] B3LYP[36]/N07D[37,38] level of theory using Gaussian16 as indicated.

5.4 Results and discussion

In order to investigate the intrinsic intensity ratio as a function of PAH size, Figure 5.1a shows the band strength ratio extracted from the (harmonically calculated) PAH database for the complete available size range. The intensity is integrated between 15.4 and 10.5 μm (650-950 cm^{-1}) and is chosen such as to incorporate all significant CH OOP intensity and will be indicated in the following as 'oop'. The integrated range for the CH stretch region, indicated in the following as 'stretch', spans from 3.6-3.1 μm (2750-3250 cm^{-1}). The intrinsic band strength ratio varies by a factor of about 3 between the smallest and largest PAHs considered here. Interestingly, a large variation of the band strength ratio is observed for smaller PAHs that contain up to about 35 carbon atoms, which would result in a larger uncertainty in the calculated emission ratio. The color scale of Figure 5.1a corresponds to the number of trio hydrogens in the PAH. A clear separation of PAHs that contain more than 4 trio hydrogens is visible from PAHs with 4 or less trio hydrogens. The presence of trio hydrogens increases the oop/stretch ratio by suppressing the CH stretch band intensity.

In the most stable PAH species, one does not expect many trio hydrogens as they are in general associated with an irregular rather than a compact shape.[39] To further investigate the relation between the intrinsic ratio and PAH size, PAHs with more than 4 trio hydrogens have therefore been omitted in Figure 5.1b. Moreover, to remove the bias towards the more numerous smaller PAHs an average has been taken. Quite interestingly, we then find that the oop/stretch ratio and the number of carbon atoms in a PAH exhibit a clear correlation that can be well described with an exponential decay function as evidenced by the black trace resulting from a fit to such a function. Although the oop/stretch intensity ratio in emission increases for larger PAHs as a result of their larger heat capacity, the intrinsic ratio decreases exponentially to a value of 0.35.

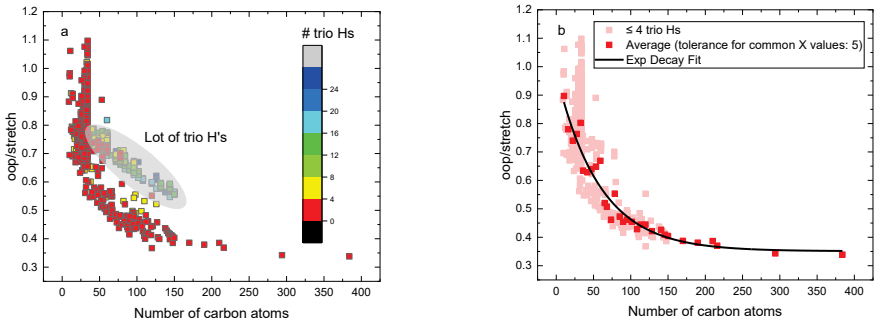

Figure 5.1: (a) The intrinsic oop/stretch 11.2/3.3 μm intensity ratio of neutral PAHs as a function of the number of carbon atoms. The color scale corresponds to the number of trio hydrogens in the PAH. (b) Same plot as (a), but leaving out the PAHs that contain more than 4 trio hydrogens (light red) and the average with an x-value tolerance of 5 (red) taken before fitting to decrease the bias towards smaller PAHs. The fit of these data to an exponential decay relation is shown as the black trace.

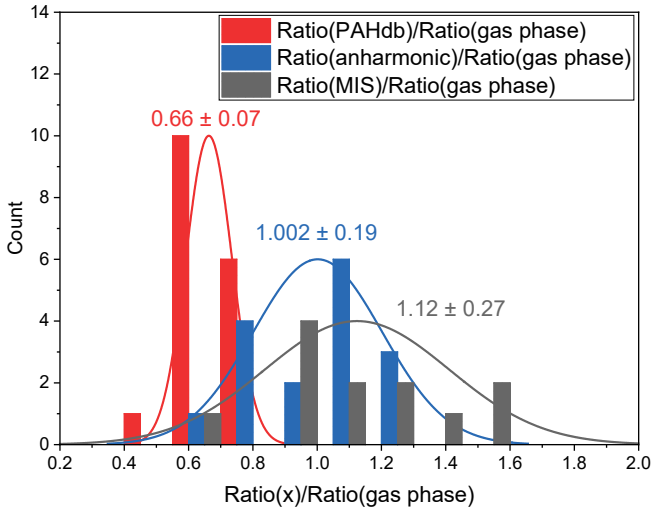

Figure 5.2: Histogram of the 11.2/3.3 μm intensity ratio determined using various theoretical and experimental methods divided by the gas-phase direct absorption measurements. The bin size is 0.15. The intensities were integrated between 15.4-10.5 μm (650-950 cm^{-1}) and 3.6-3.1 μm (2750-3250 cm^{-1}). The PAH species that are taken into consideration are listed in the appendix. The mean and deviation are indicated in the plot.

The large amount of calculations from the *PAHdb* have provided a wealth of insight into the interstellar PAH population and spectroscopic properties of PAHs. However,

considering the intensities, the harmonic, relatively low-level calculations are known to consistently overestimate the CH stretch band intensity.[27] To corroborate these findings, we compare in Figure 5.2 the calculated ratio from the *PAHdb* with the ratio as determined in gas-phase direct absorption measurements. As discussed in the introduction, the anharmonic calculations used throughout this thesis lead to a significant improvement in predicting IR spectra. The improvement mainly lies in the addition of combination bands and resonances that carry a significant amount of intensity, especially in the CH stretch region. Figure 5.2 thus also reports on a comparison in terms of intensities resulting from such calculations. Finally, a comparison is made between the gas-phase absorption measurements to cold, matrix isolation absorption measurements.

The 11.2/3.3 μm ratio determined using the *PAHdb* is smaller than the experimental gas-phase ratio by a factor of 0.66. This corroborates the previous findings that the CH stretch intensities are overestimated, although this overestimation appears to be even larger than previously suspected.[25] Interestingly, the ratio is quite consistently off, which supports the approach to scale the band strengths computed at a relatively inexpensive level to obtain more accurate ratios. This approach was used before to obtain band strengths for methylated PAHs that were as accurate as those calculated at far more expensive levels (MP2/6-311+G(3df,3pd)).[40]

The ratios that result from anharmonic calculations show on average a remarkably good agreement with the gas-phase absorption experiments in terms of accuracy. It should be noted that a larger basis set is used in these anharmonic calculations than has been used for the *PAHdb* and such a larger basis set is expected to lead to a more accurate ratio.[27] Nevertheless, examination of the effects of the inclusion of anharmonicity on the ratio is of great interest as a significant amount of intensity is involved in the combination bands and resonances. The ratio determined from matrix isolation spectroscopy measurements shows the largest spread with respect to gas-phase absorption experiments. The comparison of the ratios of individual PAHs can be found in Figure 5.4 in the appendix.

In view of the above observations it becomes quite interesting to determine how the underestimation of the 11.2/3.3 μm intensity ratio affects conclusions on the PAH size distributions. To this purpose, we used the calculated intrinsic band strengths and applied a full temperature cascade emission model from the *PAHdb* on a large selection of PAHs (for details, see the methods section). The results are shown in Figure 5.3 (grey squares) while a large-scale figure is given in the appendix Figure 5.5. Because the ratio determined from the *PAHdb* is quite consistently off, one possible way of obtaining more accuracy is to scale the ratio. Such an approach was used before for methylated PAHs, where the band strengths of inexpensive calculations were scaled to match the more expensive predictions. The result of a coarse modification to correct for the underestimation of the intrinsic 11.2/3.3 μm intensity ratio by low-level calculations is plotted using

the green squares in the same figure. For this, the emission ratio is simply scaled with the factor by which the low-level theory calculations underestimate the intrinsic ratio. Aiming to facilitate a readout of these plots and serving as a guide to the eye, both data sets have been fitted to an exponential function (red traces).

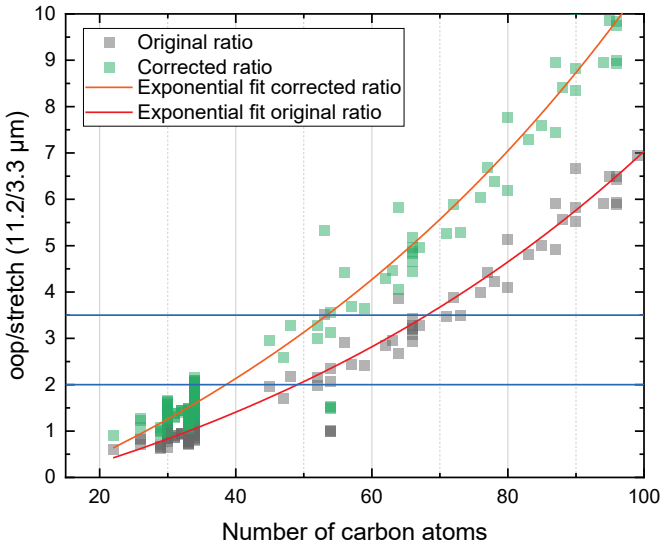

Figure 5.3: (grey squares) The 11.2/3.3 µm intensity ratio as a function of the number of carbon atoms determined using the calculated intrinsic band strengths and a full temperature cascade emission model from the *PAHdb* on a large selection of PAHs (for details, see the methods section). The green squares are scaled by a factor of 1/0.66 (see text) as a coarse correction to get an impression of the implication of the systematic underestimation of the intrinsic 11.2/3.3 µm intensity ratio by low-level calculations. The blue horizontal lines are an example of a lower and higher limit of the observed intensity ratio in a photo-dissociation region.[12] The exponential fits indicated with the red and orange traces are phenomenological and facilitate readout. The intensities were integrated between 12.05-10.15 µm (985-830 cm^{-1}) and 3.4-3.2 µm (2950-3115 cm^{-1}).

The two horizontal blue lines in Figure 5.3 are typical lower and higher limits of observed intensity ratios in a photo-dissociation region.[12] With both the 'original' model and the coarsely corrected model, the 11.2/3.3 µm intensity ratio can now be translated into a PAH size distribution. Using the 'original' model and taking the indicated upper and lower observed ratio limits, one would conclude that typical PAH sizes are in the 50-70 carbon atoms range. Importantly; however, we find that when using the corrected model which takes the systematic underestimation of the intensity ratio into account, this range is reduced to 40-55 carbon atoms.

The results of the present model are quite exciting, but need to be substantiated further with more extensive analyses that incorporate accurate high-level anharmonic

calculations on PAHs with a wide range of sizes in the emission model. Such analyses are now indeed high on our priority list. However, as for larger PAHs these calculations are not available yet, this model awaits completion. Nevertheless, our results do indicate that the underestimation of the 11.2/3.3 μm intensity ratio by low-level calculations translates into a significant overestimation of the PAH size distribution. Equally important is to notice that our results are still in line with the hypothesis that an interconversion between large PAHs and the even more stable C_{60} takes place at a certain level of the UV radiation field.[7] From the higher limit of about 55 carbon atoms that our results imply, it appears that PAHs containing more than 60 carbon atoms should indeed be readily converted into fullerene species.

5.5 Conclusions

By comparing calculations from the NASA Ames PAH IR spectroscopic database (*PAHdb*) and state-of-the-art anharmonic calculations with gas-phase direct absorption IR spectra from the NIST chemistry webbook, this study validates the predicted intrinsic 11.2/3.3 μm intensity ratio of PAHs. Currently, this ratio is recognized as the most reliable tracer for determining the size distribution of PAHs in the interstellar medium. Our studies shows that the intrinsic intensity ratio is consistently underestimated by about 34% by the relatively low-level calculations that have been employed so far to interpret astronomical observations. On the contrary, predictions made with a larger basis-set and taking anharmonic effects such as combination bands and resonances into account, are in good agreement with the experiment. Unfortunately, the high-level anharmonic calculations are not available yet for large PAHs. Nevertheless, the consistency of the underestimation of the intensity ratio allows for making an ad-hoc, course correction to the emission model based on the *PAHdb*. Such a corrected ratio-PAH size relation suggests that the size distribution that up till now has been taken to be in the 50-70 carbon atoms range could very well need to be adjusted to the 40-55 range. It is quite satisfying to notice that the higher limit of the PAH size conforms to the hypothesis that an interconversion takes place between larger sized PAHs and fullerenes in the interstellar medium.

References

1 A. G. G. M. Tielens, *Annu. Rev. Astron. Astrophys*, 2008, **46**, 289–337.

2 L. J. Allamandola, A. G. G. M. Tielens and J. R. Barker, *Astrophys. J. Suppl. Ser.*, 1989, **71**, 733–775.

3 A. Leger and J. L. Puget, *Astron. Astrophys.*, 1984, **137**, L5–L8.
4 E. Peeters, C. Mackie, A. Candian and A. G. G. M. Tielens, *Acc. Chem. Res.*, 2021, **54**, 1921–1933.
5 F. Galliano, S. C. Madden, A. G. G. M. Tielens, E. Peeters and A. Jones, *Astrophys. J.*, 2008, **679**, 310–345.
6 A. G. G. M. Tielens, *Molecular Astrophysics*, Cambridge University Press, Cambridge, 2021.
7 O. Berné and A. G. G. M. Tielens, *Proc. Natl. Acad. Sci. U. S. A.*, 2012, **109**, 401–406.
8 C. J. Mackie, T. Chen, A. Candian, T. J. Lee and A. G. G. M. Tielens, *J. Chem. Phys.*, 2018, 149, 134302.
9 A. Maragkoudakis, E. Peeters and A. Ricca, *MNRAS*, 2020, **494**, 642–664.
10 W. A. Schutte, A. G. G. M. Tielens and L. J. Allamandola, *Astrophys. J.*, 1993, **415**, 397.
11 A. Ricca, C. W. Bauschlicher, C. Boersma, A. G. G. M. Tielens and L. J. Allamandola, *Astrophys. J.*, 2012, **754**, 75.
12 B. A. Croiset, A. Candian, O. Berné and A. G. G. M. Tielens, *Astron. Astrophys.*, 2016, **590**, A26.
13 M. Jourdain de Muizon, P. Cox and J. Lequeux, *Astron. Astrophys. Suppl. Ser.*, 1990, **83**, 337–355.
14 T. I. Mori, I. Sakon, T. Onaka, H. Kaneda, H. Umehata and R. Ohsawa, *Astrophys. J.*, 2012, **744**, 1–15.
15 C. Pech, C. Joblin and P. Boissel, *Astron. Astrophys.*, 2002, **388**, 639–651.
16 H. Andrews, C. Boersma, M. W. Werner, J. Livingston, L. J. Allamandola and A. G. G. M. Tielens, *Astrophys. J.*, 2015, 807, 24pp.
17 C. W. Bauschlicher, E. Peeters and L. J. Allamandola, *Astrophys. J.*, 2009, **697**, 311–327.
18 S. E. Stein, J. N. Spencer, J. R. Seigart, E. Brown, R. L. Sensing and S. E. Stein, *J. Phys. Chem.*, 1978, **82**, 566–571.
19 E. Dwek, R. G. Arendt, D. J. Fixsen, T. J. Sodroski, N. Odegard, J. L. Weiland, W. T. Reach, M. G. Hauser, T. Kelsall, S. H. Moseley, R. F. Silverberg, R. A. Shafer, J. Ballester, D. Bazell and R. Isaacman, *Astrophys. J.*, 1997, **475**, 565–579.
20 C. W. Bauschlicher, C. Boersma, A. Ricca, A. L. Mattioda, J. Cami, E. Peeters, D. Armas, G. P. Saborido, D. M. Hudgins and L. J. Allamandola, *Astrophys. J. Suppl. Ser.*, 2011, **189**, 341–351.
21 C. W. Bauschlicher, A. Ricca, C. Boersma and L. J. Allamandola, *Astrophys. J. Suppl. Ser.*, 2018, **234**, 32.
22 C. Boersma, J. Bregman and L. J. Allamandola, *Astrophys. J.*, 2015, **806**, 121.
23 B. T. Draine, A. Li, B. S. Hensley, L. K. Hunt, K. Sandstrom and J.-D. T. Smith, *Astrophys. J.*, 2021, **917**, 26pp.

24 C. J. Mackie, A. Candian, T. J. Lee and A. G. G. M. Tielens, *Theor. Chem. Acc.*, 2021, **140**, 1–9.
25 S. R. Langhoff, *J. Phys. Chem*, 1996, **100**, 2819–2841.
26 C. J. Mackie, A. Candian, X. Huang, E. Maltseva, A. Petrignani, J. Oomens, W. J. Buma, T. J. Lee and A. G. G. M. Tielens, *J. Chem. Phys.*, 2015, **143**, 1–15.
27 H. Geindre, A. R. Allouche and D. Peláez, *J. Comput. Chem.*, 2021, **42**, 1018–1027.
28 A. K. Lemmens, D. B. Rap, J. M. M. Thunnissen, C. J. Mackie, A. Candian, A. G. G. M. Tielens, A. M. Rijs and W. J. Buma, *Astron. Astrophys.*, 2019, **628**, A130.
29 C. Joblin, L. D'Hendecourt, A. Leger and D. Defourneau, *Astron. Astrophys.*, 1994, **281**, 923–936.
30 C. Joblin, P. Boissel, A. Léger, L. D'Hendecourt and D. Défourneau, *Astron. Astrophys.*, 1995, **299**, 835–846.
31 C. J. Mackie, *The Anharmonic Infrared Spectra of Polycyclic Aromatic Hydrocarbons*, 2018.
32 M. J. Frisch, G. W. Trucks, H. B. Schlegel, G. E. Scuseria, M. A. Robb, J. R. Cheeseman, G. Scalmani, V. Barone, G. A. Petersson, H. Nakatsuji, X. Li, M. Caricato, A. V. Marenich, J. Bloino, B. G. Janesko, R. Gomperts, B. Mennucci, H. P. Hratchian, J. V. Ortiz, A. F. Izmaylov, J. L. Sonnenberg, D. Williams-Young, F. Ding, F. Lipparini, F. Egidi, J. Goings, B. Peng, A. Petrone, T. Henderson, D. Ranasinghe, V. G. Zakrzewski, J. Gao, N. Rega, G. Zheng, W. Liang, M. Hada, M. Ehara, K. Toyota, R. Fukuda, J. Hasegawa, M. Ishida, T. Nakajima, Y. Honda, O. Kitao, H. Nakai, T. Vreven, K. Throssell, J. Montgomery, J. A., J. E. Peralta, F. Ogliaro, M. J. Bearpark, J. J. Heyd, E. N. Brothers, K. N. Kudin, V. N. Staroverov, T. A. Keith, R. Kobayashi, J. Normand, K. Raghavachari, A. P. Rendell, J. C. Burant, S. S. Iyengar, J. Tomasi, M. Cossi, J. M. Millam, M. Klene, C. Adamo, R. Cammi, J. W. Ochterski, R. L. Martin, K. Morokuma, O. Farkas, J. B. Foresman and D. J. Fox, *Gaussian, Inc., Wallingford CT*.
33 NIST Mass Spectrometry Data Center and W. E. Wallace, in *NIST Chemistry WebBook*.
34 V. Barone, *J. Chem. Phys.*, 2005, **1221**, 14108–1007.
35 V. Barone, M. Biczysko and J. Bloino, *Phys. Chem. Chem. Phys.*, 2014, **16**, 1759–1787.
36 A. D. Becke, *J. Chem. Phys.*, 1993, **98**, 5648–5652.
37 V. Barone, P. Cimino and E. Stendardo, *J. Chem. Theory Comput.*, 2008, **4**, 751–764.
38 C. J. Mackie, A. Candian, X. Huang, E. Maltseva, A. Petrignani, J. Oomens, W. J. Buma, T. J. Lee and A. G. G. M. Tielens, *Phys. Chem. Chem. Phys.*, 2018, **20**, 1189–1197.
39 J. Bouwman, P. Castellanos, M. Bulak, J. Terwisscha Van Scheltinga, J. Cami, H. Linnartz and A. G. G. M. Tielens, *Astron. Astrophys.*, 2019, **621**, 1–8.

40 X. J. Yang, A. Li, R. Glaser and J. X. Zhong, *Astrophys. J.*, 2017, **837**, 171.

Appendix

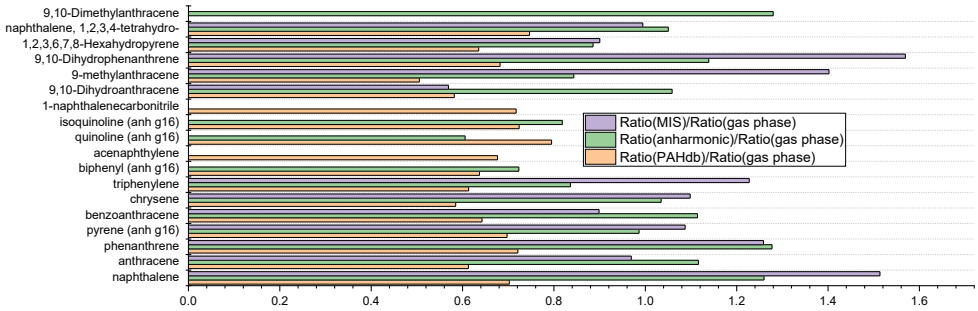

Figure 5.4: The 11.2/3.3 μm intensity ratio for different PAH species determined using various theoretical and experimental methods divided by the gas-phase direct absorption measurements. The intensities were integrated between 15.4-10.5 μm (650-950 cm^{-1}) and 3.6-3.1 μm (2750-3250 cm^{-1}).

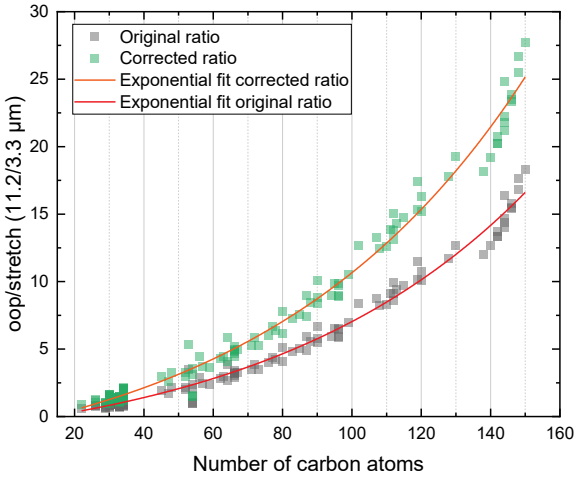

Figure 5.5: Full scale plot of Figure 5.3 (grey squares). The 11.2/3.3 μm intensity ratio as a function of the number of carbon atoms, determined using the calculated intrinsic band strengths and a full temperature cascade emission model from the *PAHdb* on a large selection of PAHs. The green squares are ratios corrected as described in the main text and serve to explore the implications of the systematic underestimation of the intrinsic 11.2/3.3 μm intensity ratio by low-level calculations. The exponential fits are phenomenological and facilitate readout.

Table 5.1: Fit parameters

Figure 5.1b		**Figure 5.3/5 fit original ratio**		**Figure 5.3/5 fit corrected ratio**	
y = A1*exp(-x/t1) + y0		y = A1*exp(x/t1) + y0		y = A1*exp(x/t1) + y0	
y0	0.351 ± 0.018	y0	-3.28 ± 0.29	y0	-4.97 ± 0.44
A1	0.625 ± 0.032	A1	2.77 ± 0.22	A1	4.20 ± 0.33
t1	58.09 ± 6.69	t1	76.14 ± 2.68	t1	76.14 ± 2.68

Chapter 6

Far-infrared and UV spectral signatures of controlled complexation and microhydration of the polycyclic aromatic hydrocarbon acenaphthene

This chapter is published as:
Alexander K. Lemmens, Sébastien Gruet, Amanda L. Steber, Jens Antony, Stefan Grimme, Melanie Schnell and Anouk M. Rijs, *Phys. Chem. Chem. Phys.,* 21, 3414-3422, 2019

6.1 Abstract

In this work we report on the experimental and theoretical investigations of the progressional complexation of the polycyclic aromatic hydrocarbon (PAH) acenaphthene with itself and with water. In the interstellar medium, PAH complexes are an important link between molecular gas and solid state configurations of carbon, and in the form of grains they are postulated to serve as chemical catalysts. However, no direct detection of PAHs or their (microhydrated) complexes in interstellar space has been achieved as of yet. Therefore, we provide UV and far-infrared ion dip spectra of homogeneous PAH multimers and their hydrated clusters. The far-IR region of the IR spectrum is especially interesting since it contains the most spectral features that arise due to complexation or microhydration. We present microhydrated PAH complexes up to the third order, where we show that the water clusters are locked with little perturbation on the different PAH platforms. Density functional theory (DFT) calculations involving hydrogen bond interactions still seem challenging for predicting the far-IR frequency range, although applying anharmonic corrections leads to slight improvements.

6.2 Introduction

Weakly bound complexes of polycyclic aromatic hydrocarbons (PAHs) bridge the gap between molecular gas and solid-state dust configurations of carbon.[1,2] In astrochemistry, PAH complexes are promising candidates as carriers of the unidentified infrared emission bands at wavelengths of 3–20 μm where they might explain the observed but not yet understood broad plateaus.[3–5] Besides the infrared emission, the diffuse interstellar bands (DIBs) are also proposed to (partly) originate from PAHs. However, because of a lack of laboratory data, neither the infrared emission nor the DIBs' origin has been confirmed. Similar to the PAH complexes, heterogeneous PAH–molecule complexes are believed to play an important role in the chemistry of the interstellar medium, in particular in cold molecular clouds.[5] Weakly bound complexes involving water molecules are especially interesting because of the ubiquity of water in the universe. In addition, PAHs have been proposed to exist within interstellar ices, where they influence the structure of water and its reactivity.[6–8] Besides the astrochemical interest, condensation of water molecules on aerosol particles is at the heart of cloud formation and, therefore, of importance in planetary atmospheres. Combustion based emission of carbonaceous particles, such as PAHs, may also contribute to atmospheric chemistry and the climate by forming complexes with water molecules.[9,10] The molecular mechanisms of the formation of such

PAH–water complexes are still not understood at the molecular level,[11] but several experimental and theoretical studies are being undertaken to help elucidate this.

Gas phase high-resolution spectroscopy provides a direct connection between laboratory and astronomical or atmospheric studies.[11,12] In combination with quantum chemical calculations, these experiments supply information on molecular structures and transition frequencies for example in ref. [13] using far-IR and in ref. [14] with microwave spectroscopy. For molecules of astronomical interest, the obtained transition frequencies can be used to elucidate astronomical IR spectra[5,15] or support new searches for molecular species.[16–19] Within high-resolution spectroscopy, the molecular beam technique is a well-established tool to produce the necessary isolated and cold molecular clusters in the gas phase with rovibrational temperatures typically of a few Kelvin,[20,21] thereby simulating the astrophysical environment.

Some gas phase spectroscopic studies have been performed in the UV-VIS and mid-IR range for either benzene–water clusters or pure PAH clusters (*e.g.* in refs. [22–27] for neutrals and refs. [28,29] for cations) but so far, no far-IR studies of microhydrated PAHs have been performed to our knowledge. In addition, several quantum chemical simulations have been carried out on PAH clusters (*e.g.* in refs. [30–34]) that give insight into their preferred geometries. In a parallel spectroscopy study in the microwave range acenaphthene–water (Ace–W)[14] clusters were investigated, which revealed the first steps of PAH–water complex formation. In that study, the structures of the Ace–W_m (m = 1–4) complexes were determined using isotopic substitution, and the cyclic water trimer ($(H_2O)_3$) structure was observed for the first time complexed to a molecule using microwave spectroscopy. Comparison with the structures of the free water clusters and SAPT calculations provided clear indications that the water clusters are loosely bound to the PAH surface. Internal water dynamics were observed in the water clusters, similar to the ones in the corannulene–water[35] complex previously studied. It will be interesting and most insightful to further explore these Ace–water complexes with IR spectroscopy.[36,37] Especially of interest is the far-IR frequency range, where the clusters and other weakly bound complexes involving PAHs can directly contribute to the unidentified infrared emission bands. Moreover, the James Webb infrared space telescope will be equipped with far-IR detection capabilities, making far-IR laboratory studies timely.

In the present work, we investigate clustered-PAH acenaphthene (Ace) molecules and Ace–water complexes (Ace–W) using IR-UV ion dip spectroscopy to obtain spectroscopic signatures in the 100–1800 cm^{-1} region. This spectral region, that includes the far-IR, allows us to probe low energy vibrational modes.[38] The far-IR region, besides being of astrochemical interest, helps to verify calculated structures and vibrational modes. Additionally, we will be able to investigate the extent of perturbation that complex formation or microhydration has on the vibrational frequencies of PAH monomers.

6.3 Methods

6.3.1 Experimental

The experiments were performed at the FELIX laboratory in the Netherlands where the IR spectra were measured *via* IR-UV ion dip spectroscopy using a pulsed supersonic jet expansion extensively discussed in ref. [39]. Acenaphthene (99%) was purchased from Sigma Aldrich and inserted into a molecular beam source consisting of a resistively heated sample compartment and a series 9 pulsed valve from General Valve. The source was operated at 85 °C and 20 Hz with water vapor enriched argon as the carrier gas. A backing pressure of around 2.5 bar was used. The saturation of the molecular beam with water was prohibited by means of regulating the gas flow through an external water container and simultaneously monitoring the mass spectrum. The gas is expanded into vacuum, skimmed and delivered internally cold to the interaction region. In the interaction zone, the molecular beam interacted with a UV laser beam of about 1 mJ per pulse provided by a Nd:YAG-laser pumped UV dye laser (DCM in ethanol) tuned between 31 100–32 300 cm^{-1}. The molecular species were ionized *via* resonance-enhanced multi-photon ionization (REMPI).[40] Subsequently, the ions were mass-separated and detected with a time-of-flight mass spectrometer. In order to acquire an IR spectrum, the UV laser beam was tuned to an electronic transition of the molecular species of interest and preceded by the tunable IR laser beam provided by the free electron laser FELIX, performing IR-UV ion dip spectroscopy.[20] The IR pulses delivered by FELIX are 8–10 μs long with energies ranging from 10–60 mJ and a bandwidth of about 1% of the energy. Whenever the IR laser was tuned to a vibrational transition, the population of the ground state was depleted resulting in a decreased ion signal. The IR beam was set alternating on and off to simultaneously obtain a background signal, directly correcting for fluctuations in the ion signal. In order to convert to absorbance, the logarithm of the on–off signal ratio was taken. A minimum of 90 averages per wavelength was recorded. An IR spectrum is obtained by scanning the IR laser with steps of 1–1.5 cm^{-1} over the complete wavelength range (100–1800 cm^{-1}) and monitoring the ion signal. Every spectrum has been corrected for laser power and the number of photons present in the laser beam.

6.3.2 Theoretical

Using the quantum chemical program package TURBOMOLE,[41] the Ace monomer and its complexes with other Ace molecules or water molecules have been optimized at the PBEh-3c[42] and SCS-MP2[43] (1.1;2/3)[44]/def2-QZVP[45] levels of theory. The resolution-of-identity (RI) approximation for the Coulomb integrals was applied using matching

default auxiliary basis sets.[46] The quantum chemical calculations using the B3LYP functional with dispersion correction D3[47] and SVWN[48,49]/DZ[50] are performed using the program package Gaussian09.[51] The conformation found for the Ace_2–W_1 in the joint parallel microwave study[14] serves as the starting point geometry for the optimization of the Ace_2 structure. The Ace–W_m (m = 1–3) conformations from the same study were used as starting point geometries for the optimization of the Ace–W_m (m = 1–3) complexes. Note that optimization may result in the (slight) modification of a molecular structure. From these optimized structures, IR frequencies were calculated. The calculated spectra of other (non-parallel) Ace_2 conformers overlap in the 100–1800 cm^{-1} infrared range. For Ace_3, both parallel and perpendicular geometries were used as starting point geometries. The simulated infrared spectra are convoluted with a gaussian profile that matches approximately the FELIX bandwidth.

To go beyond scaling, individual anharmonic corrections for each normal mode were computed using vibrational perturbation theory (VPT)[52,53] as implemented in Gaussian09.[51] The SVWN[48,49] local density approximation (LDA) functional was used together with Dunning's double-zeta (DZ) basis set,[50] downloaded from the EMSL basis set exchange database.[54] The anharmonic correction was obtained by adding the difference between the anharmonic and the harmonic frequencies at the SVWN/DZ level of theory to the harmonic PBEh-3c result. The SVWN/DZ level has been used previously with good success for the anharmonic correction of computed rotational constants of medium sized organic molecules.[55] For this purpose, the normal modes computed with the two methods were related to each other in a one-to-one fashion by evaluating the matrix of their overlaps, which was calculated after having oriented the molecules in the principal axis system. The latter was done with the help of the molden visualisation software.[56] The harmonic intensities were not modified.

6.4 Results and discussion

6.4.1 UV spectra of Ace and Ace–water complexes

The time-of-flight mass spectra of the Ace_n–W_m (n = 1–4, m = 1–4) and Ace_n (n = 1–7) clusters are presented in Figure 6.1a and b respectively. Ace clusters up to the heptamer were detected. Clusters of the Ace monomer complexed with up to three water molecules were readily formed, together with a significant number of higher order clusters. Following the identification of clusters in our beam by mass spectrometry, UV one color Resonance Enhanced Multi Photon Ionization (REMPI) spectra of the desired complexes were obtained (Figure 6.2).

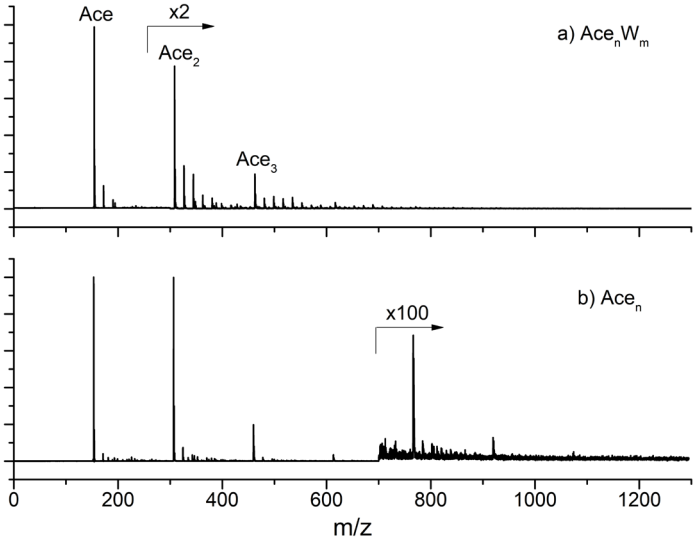

Figure 6.1: Calibrated TOF mass spectra of (a) acenaphthene (Ace) complexes with water and (b) solely Ace. Microhydration of the PAH(-clusters) with up to three water molecules is readily achieved. Acenaphthene complexes up to the heptamer are detected. Trace (a) is recorded using a UV wavelength of 31250.0 cm^{-1}, trace (b) using 31474.1 cm^{-1}. The Ace monomer signal in trace (b) is saturated.

The Ace monomer origin was found to be at 31 474.1 cm^{-1}, close to the previously reported value.[57] Complexation of Ace with a second or third Ace monomer to form Ace_2 or Ace_3 results in a redshift of the origin to 31 329.5 and 31 289.0 cm^{-1}, respectively. Comparing the UV spectrum of Ace_2 in Figure 6.2b with Ace in Figure 6.2a reveals an increase in vibronic transitions for Ace_2. The narrow linewidths in the Ace_2 spectrum indicate a molecular excitation;[58,59] the two monomer units in Ace_2 have a slightly different electronic environment and therefore two slightly different UV spectra of the monomer units comprise the UV spectrum of Ace_2. Astronomically the splitting of the bands is interesting in the framework of DIBs, where clusters of PAHs have only been rarely considered as possible carriers.[60] This spectrum in particular is interesting since it contains very narrow bands, whereas the dimers of other small PAHs show significantly more broadening.[24,61] The broad features in the UV excitation spectrum of Ace_3 in Figure 6.2c are typical for excitonic excitations[59] in oligomers, and distinct lines are not observed anymore. A similar red shift upon complexation has been observed previously in the PAH clusters of anthracene and was also ascribed to an excitonic nature of the excited state.[24]

With respect to the observed line splitting and broadening upon complexation we speculate that some variations in the line positions or linewidths of the DIBs could be due to the formation of clusters. However, it must be noted that the broadening of the spectral features can also be a result of less efficient cooling of the larger clusters.

Dissociation of higher order clusters that end up in the smaller sized cluster mass detection channels and thereby introduce dynamics may also contribute to broadening.

Similarly, as for the higher order Ace_n complexes, broader absorption features are observed in the UV REMPI spectra of the Ace–W_m (m = 1–4) complexes (Figure 6.2e–h). However, in contrast to the Ace_n complexes, higher order Ace–W_n (n > 2) clusters exhibit a blue shift of the electronic origin. The three main features in the Ace spectrum (overlaid in grey in Figure 6.2e–h) are still recognizable in the Ace–W_n complexes unlike in the Ace_n spectra in Figure 6.2a–d where the UV spectra change drastically upon complex formation.

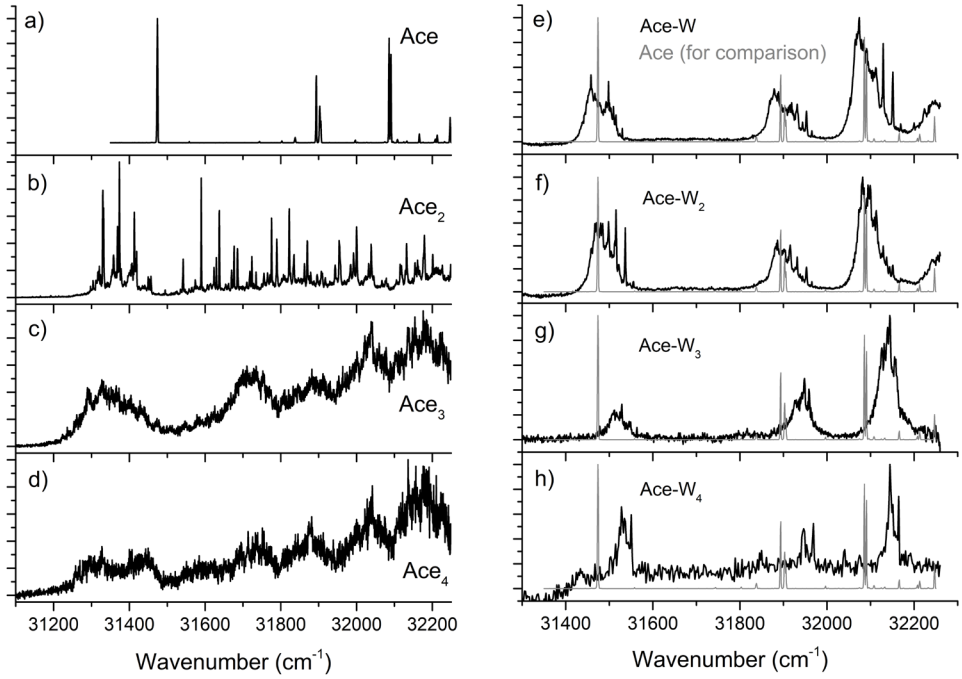

Figure 6.2: 1 + 1 REMPI spectra of (a–d) Ace_n (n = 1–4) complexes and (e–h) Ace–W_m (m = 1–4) complexes. The origin of Ace is found to be at 31474 cm^{-1}. The Ace spectrum (a) is added in gray in the (e–h) Ace–W_m (m = 1–4) spectra for comparison.

6.4.2 Infrared spectra of pure Ace complexes

Following the determination of the resonant two photon ionization wavelengths, IR action spectra in the 100–1800 cm^{-1} range were obtained for the Ace_n (n = 1–3) complexes and are displayed in Figure 6.3a–c. The various UV frequencies used in the IR-UV ion dip experiments are listed in Table 6.1. Multiple UV frequencies were selected in order to

determine whether different conformers possibly existed in the molecular beam. They would be expected to have a different IR spectrum. This was not the case for any of the clusters, and the spectra were assigned to single conformations. In addition, IR-UV hole burning experiments, where the IR laser was fixed on a unique transition, also did not indicate the presence of more than one conformer.

Table 6.1: UV frequencies used in the IR-UV ion dip spectra reported throughout this chapter.

Ace_1	31474 cm^{-1}
Ace_2	31374; 31637.5 and 31358 cm^{-1}
Ace_3	31374; 31637.5 and 31358 cm^{-1}
Ace_1-W_1	32074 cm^{-1}
Ace_1-W_2	31536 cm^{-1}
Ace_1-W_3	32157 and 32126 cm^{-1}
Ace_2-W_3	31367 cm^{-1}

By selecting the UV probe wavelengths carefully, we managed to minimize infrared ion gain effects[62] in the spectra of Ace and Ace_2. Infrared ion gain can be a result of intramolecular vibrational energy redistribution that causes a broadening and redshift in the UV absorption (as shown in ref. [62]), or it occurs due to an increase of UV dissociation of higher order clusters after IR absorption. As the gain signals distort the IR spectra and possibly mask or disturb weaker IR absorption peaks, they are undesired. The Ace_3 spectrum (Figure 6.3c) shows some gain features at 251 cm^{-1} where it indeed prevented us from acquiring a 'clean' IR absorption spectrum *via* the intended IR-UV ion dip scheme.

Depicted in blue in Figure 6.3a–c are theoretically calculated spectra (DFT), using the PBEh-3c level of theory. The corresponding optimized molecular structures are shown in Figure 6.4a–c. The stacked structure found for Ace_2–W_1 in the joint parallel microwave study[14] is used as a starting point for Ace_2. The stacked Ace_3 conformation led to an optimized geometry with lower energy than structures containing perpendicular (T-shaped) Ace molecules. This result matches previous computational studies which found that for relatively small PAH complexes the stacked configuration is most stable.[30]

The PBEh-3c calculations and the experimental spectra are in good agreement with respect to peak positions: a standard deviation of 6.2, 4.9 and 4.6 cm^{-1} is determined for Ace, Ace_2 and Ace_3, respectively. The good agreement allows for the assignment of the measured peaks in the spectra even in the far-IR region, where generally more elaborate computational techniques have to be applied.[13] Solely global normal modes are found below 700 cm^{-1}, including the bending, stretching and folding modes of the carbon rings. The more local C–C and C–H vibrations are present above 1000 cm^{-1}. The relatively stronger lines at 780 and 1602 cm^{-1} correspond to the CH and CH_2 out of plane motion and the concerted C–C stretch vibration, respectively. It must, however, be noted that the

transition observed in all Ace_n complexes at 1759 cm^{-1} is absent in the calculations. We believe that this transition is a combination mode similar to the transitions in PAHs above 1700 cm^{-1} as calculated in ref. [63].

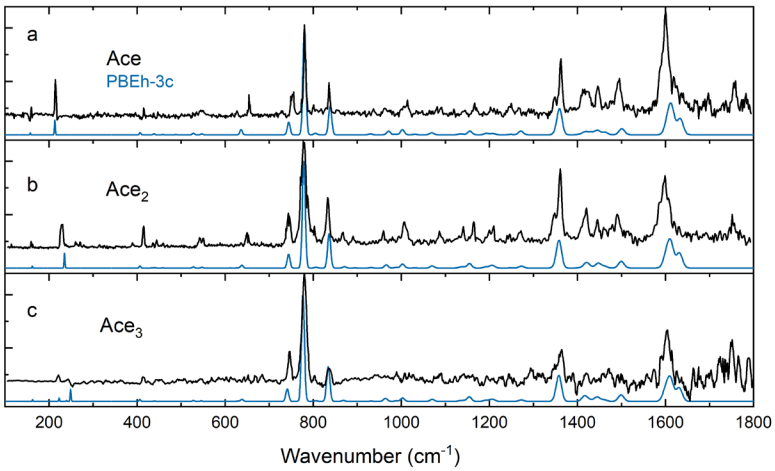

Figure 6.3: Mid- to far-infrared gas phase action spectra of jet cooled Ace_n (n = 1–3) complexes in black. Displayed in blue are the corresponding calculated spectra at the PBEh-3c level of theory (uncorrected, but scaled with 0.95).

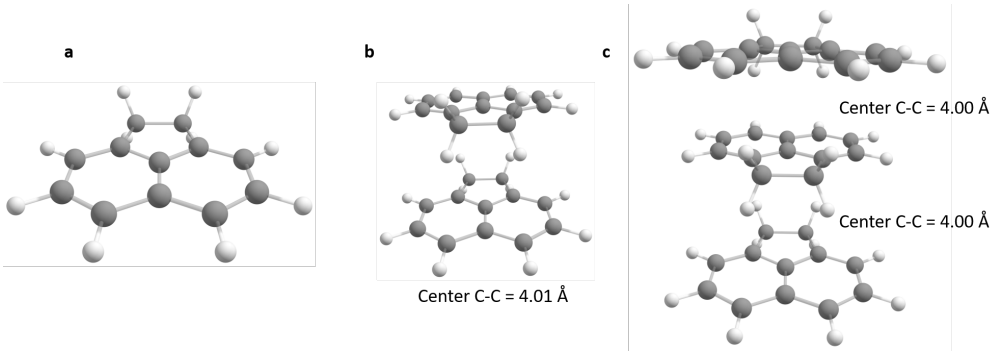

Figure 6.4: The calculated structures of Ace_n (n = 1–3) complexes at the PBEh-3c level of theory.

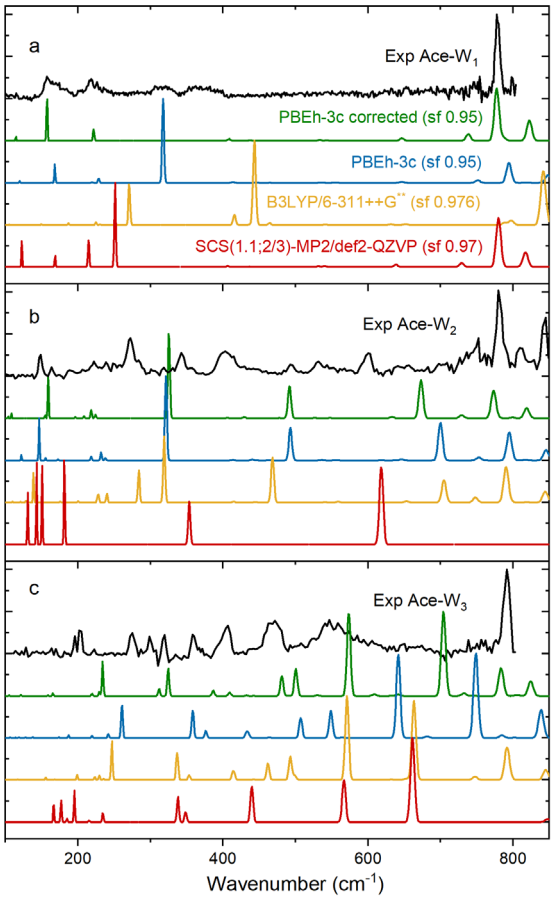

Figure 6.5: Experimental (black) infrared spectra of the (a) Ace–W_1 complex, the (b) Ace–W_2 complex and the (c) Ace–W_3 complex. The corrected (green) and uncorrected (blue) PBEh-3c calculated infrared spectra are added as well as the B3LYP-D3/6-311++G** (yellow) and SCS(1.1;2/3)-MP2/def2-QZVP (red) calculated spectra.

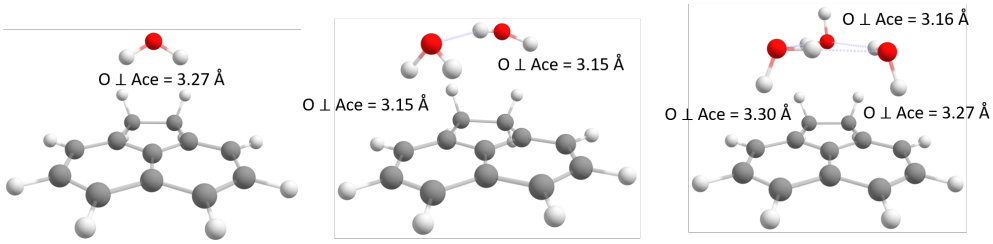

Figure 6.6: Calculated structures of Ace–W_n (n = 1–3) complexes corresponding to the predicted infrared spectra displayed in Figure 6.5. The molecular structures are based on the microwave spectroscopy determined structures and re-optimized at the PBEh-3c level of theory.

At first sight, the IR signatures of the monomer do not change upon complexation. In other words, the addition of another Ace molecule does not alter most IR vibrations of the Ace it is complexed to. It appears that the stacking interaction does not shift many of the normal modes in the mid-IR range. Most spectroscopic features of complexation seem to manifest themselves in the spectrum below about 300 cm^{-1}, in the far-IR region. The global bending mode is observed at 214 and 231 cm^{-1}, respectively, for Ace and Ace_2. This normal mode is concerted for Ace_2 and it results in a single peak. However, the same bending mode in Ace_3 is split into at least two frequencies, both of which were observed experimentally as predicted in our calculations. The mode is now decoupled due to the increased size of the complex. It is an interesting speculation that, in the astronomically observed infrared emission bands and in the limit of larger complexes, the slightly shifted decoupled global bending modes cumulatively result in a broad feature in the far-IR region before significant broadening is observed in the higher infrared region.[26,64] A second spectroscopic feature of PAH clustering manifests in the relative intensity of the transitions at 780, 1363 and 1602 cm^{-1}, which seems to change significantly. The transition at 780 cm^{-1} grows in relative intensity upon further PAH complexation.

6.4.3 Infrared spectra of Ace water complexes

Adding a controlled amount of water vapor to the backing gas allowed us to complex the Ace_n (n = 1–3) complexes with one or more water molecules, see Figure 6.1. The experimental IR spectra of the Ace–W_m (m = 1–3) complexes are presented in Figure 6.5a–c (plotted in black) along with theoretical spectra at various levels of theory in color. The experimental IR spectra show multiple isolated peaks together with some broad bands. The broad IR signatures might indicate the presence of dynamic hydrogen bond interactions. This could be expected since in the microwave study,[14] internal dynamics and tunneling were also observed for the Ace–W_1 complex. The assigned structures that were found in our microwave study in ref. [14] have been used as starting point geometries for the calculations presented here. In both experiments, the molecular beam technique was used to measure the microwave spectra or the infrared spectra (although it must be mentioned that argon was used as the carrier gas in this study instead of neon as in the microwave spectroscopic study). The structures that were optimized at the PBEh-3c level of theory are presented in Figure 6.6. Since the structures of the Ace–water complexes were experimentally determined in the microwave study, we can use these Ace–W_m (m = 1–3) clusters to evaluate the preciseness of our computational methods to describe IR signatures and present intermolecular interactions, which are extremely hard to predict.[65] Note that the optimization of the clusters has led to the modification of the molecular structure with respect to the experimental ones. The $(H_2O)_2$ in the Ace–W_2 complex resides in its lowest energy configuration where it is skewed with respect to the plane of

symmetry of the Ace platform, unlike in the microwave study where the $(H_2O)_2$ sat on the plane of symmetry. In the Ace–W_3 complex, the free protons of $(H_2O)_3$ are oriented more towards the Ace platform after optimization. As described in the methods section, the PBEh-3c calculations of vibrational frequencies are corrected for anharmonicity and most emphasis will be on the performance of this method. However, the widely used B3LYP and SCS-MP2 as well as the uncorrected PBEh-3c infrared spectra are also shown for comparison. The infrared range below 800 cm^{-1} is selected, since we expect to see most spectral changes here upon complexation with water molecules based on the DFT calculations.

PBEh-3c (with and without anharmonic correction)

Both the experimental as well as the theoretical IR spectra of the Ace–W_1 complex (Figure 6.5a) show the most intense transition at 777 cm^{-1}. This peak and the smaller peaks on both sides of this strong transition are assigned to the CH and CH_2 out of plane motion and are well represented by the PBEh-3c calculations. The anharmonic correction induces a small red shift resulting in an improved agreement with the experimental signatures. The remaining transitions are observed deep into the far-IR and have significantly weaker intensities. The main difference between the uncorrected PBEh-3c and corrected calculations (green corrected and blue uncorrected trace, resp.) is the presence of an intense peak in the uncorrected calculation at 318 cm^{-1}, which is not observed in the experiment. Moreover, a similar red shift in the far-IR region upon anharmonic correction using the SVWN/DZ level of theory is seen, which also improves the match with the experimental spectrum for the Ace–W_1 cluster in the far-IR region significantly. This holds especially for the smaller transitions in the far-IR region at around 157 and 218 cm^{-1}.

Similar shifts, mostly to the red, are observed between the harmonically and anharmonically calculated spectra of the Ace–W_2 and Ace–W_3 clusters (Figure 6.5b and c), where the shifts upon anharmonic correction slightly improves the agreement. The anharmonically corrected PBEh-3c calculations and experimental infrared spectrum of the Ace–W_2 complex show good agreement for the largest experimental transitions around 800 cm^{-1} originating from CH out of plane and CC stretch modes. However, the transitions observed in the far-infrared region, below 700 cm^{-1}, cannot be assigned based on either the PBEh-3c calculations or the B3LYP and SCS-MP2 (see below) calculations. Most remarkable is the fact that the intensities are predicted to be relatively high, however, we do not observe this in our experiments. The anharmonic corrections seem to be small, and in the region above 650 cm^{-1} they lead to an improved agreement with the experimental spectrum.

As was observed for the Ace–W_1 and Ace–W_2 complexes, the largest transition for Ace–W_3 is found at 791 cm^{-1} and originates from CH wagging. The band at 552 cm^{-1} is very broad, but at lower energies the line widths decrease. Therefore, the broadening is

most probably due to the dynamics of the Ace–W_3 complex. Since no good agreement can be found between any level of calculations and the experiment, no conclusive assignment based on the calculated infrared spectra has been made.

B3LYP-D3/6-311++G**

The B3LYP-D3 calculations show a good agreement for the homogeneous Ace_n clusters (see ref [66]). However, they perform poorly at predicting the vibrational frequencies of complexes involving water molecules; Ace_n–W_m. For the Ace–W_1 complex (Figure 6.5a), B3LYP-D3 has a poorer agreement than the PBEh-3c method in both peak positions as well as in intensities. In contrast, for the Ace–W_2 complex (Figure 6.5b), the B3LYP-D3 method results in an almost identical spectrum to the uncorrected PBEh-3c calculated spectrum. The only difference between the two is the appearance of a peak at 284 cm^{-1} that was not predicted in the PBEh-3c calculations. This transition is associated with the water twisting mode. When comparing the B3LYP-D3 and PBEh-3c calculated spectra of the Ace–W_3 complex, all peaks are significantly red-shifted.

SCS(1.1;2/3)-MP2/def2-QZVP

The SCS-MP2 calculations (red spectra in Figure 6.5a–c) predict for all measured Ace–W_m (m = 1–3) complexes a large number of peaks in the region below 300 cm^{-1}. These are not observed experimentally nor predicted by the DFT methods and they are associated with modes involving both the water molecule(s) and the Ace molecule simultaneously. This is contrary to what the previously described DFT methods predict, where the modes of the water molecule(s) and the Ace molecule were mostly decoupled (see also the discussion below).

6.4.4 PAH–water interactions

Figure 6.7a–c compares the experimental Ace–W_3, Ace_2–W_3 and Ace_2 spectra, respectively. This comparison will help us to understand the spectral signatures resulting from Ace, water and their interactions. It also helps elucidate the extent of the perturbation that the Ace molecules have on the structure of the water complexes. The vertical dotted lines are added to the spectra presented in Figure 6.7 to highlight the similarities between different spectra; the green dotted lines correspond to transitions that originate from the pure water cluster signatures, while the red dotted lines correspond to modes from the Ace "platform".

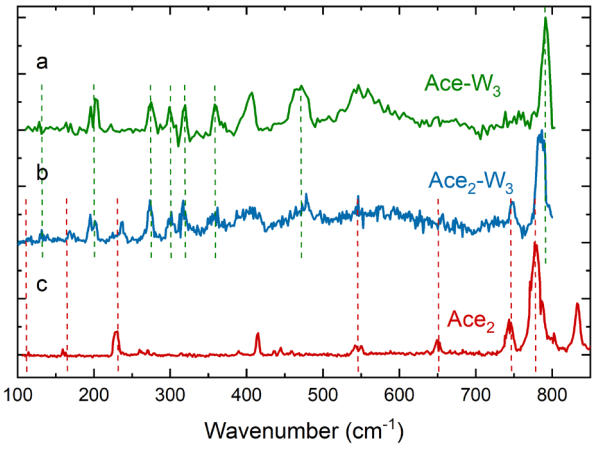

Figure 6.7: Far-infrared jet cooled gas phase action spectra of (a) Ace complexed with a water trimer Ace–W_3, (b) Ace_2 complexed with a water trimer: Ace_2–W_3 and (c) Ace_2. Vertical red lines indicate vibrational bands originating from Ace_2. The green vertical lines mark vibrational bands involving $(H_2O)_3$ complexed to either Ace or Ace_2.

Following the red dotted lines from Ace_2 (Figure 6.7c) to the Ace_2–W_3 (Figure 6.7b) cluster, we can directly assign which signatures in the IR spectrum of the Ace_2–W_3 cluster originate from the Ace_2 platform. The peaks resulting from the Ace_2 platform appear in both spectra at similar or slightly shifted frequencies. The peak at 413 cm^{-1} might either be blue-shifted or buried underneath the broad peak of the Ace_n–W_3 complex from 387 to 418 cm^{-1}. The peak at 785 cm^{-1} in the Ace_2–W_3 spectrum is thought to be composed of the peaks at 791 and 779 cm^{-1} for Ace_2 and Ace–W_3, respectively, and is therefore broader. By excluding the IR transitions of Ace_2 and by comparing the IR spectra of Ace–W_3 and Ace_2–W_3, we are able to identify the IR signatures arising from the (W_3)-part of the Ace_2–W_3 cluster as indicated by the green lines in the Ace_n–W_3 spectra in the 100–700 cm^{-1} region. We have also made an attempt to find a correlation between the Ace_n–W_3 spectra and the calculated spectra of the pure $(H_2O)_3$. However, large variations (of more than 25%) in frequencies between the SCS-MP2 and PBEh-3c and other[65] levels of theory prohibit us from correlating the calculated W_3 to the experimental Ace_n–W_3 spectra. The present spectral analysis indicates that an additional Ace molecule does not affect the W_3-infrared bands in our Ace_n–W_3 complexes. Even in the far-IR region, where the weaker interactions in the structure are probed, the modes involving water are similar when either complexed to Ace or Ace_2. The perturbative effect of the Ace platform, be it Ace or Ace_2, seems therefore to be small leading to uncoupled vibrations in the water and Ace units. The non-directional dispersion force locking the water complexes to

Ace is estimated to be insignificant compared to the hydrogen bonding interactions between the water molecules since the complexation of a second Ace molecule to the Ace–W_3 cluster does not perturb the modes originating from the W_3 (green dotted lines). The interaction seems to have a very limited perturbative effect even though this particular PAH contains two out-of-plane hydrogens. It can be expected that this effect is even smaller for the more common types of PAHs that possess only in-plane hydrogen atoms. Regarding the small perturbative effect and with respect to the poor agreement with theory discussed in Figure 6.5, we conclude that the hydrogen bonding in the W_3 might be the main reason for the large discrepancy between theory and experiment in that region.

The finding that the PAH has a very limited perturbative effect on the water complexes is in agreement with the parallel study in the microwave range where it is shown that the O–O bond distance in the water complexes is only minimally distorted.[14] We confirm this non-perturbative effect of the PAH platform and elucidate the implications on infrared spectroscopic signatures.

6.5 Conclusions

Infrared ion dip and UV excitation spectra of neutral acenaphthene, acenaphthene clusters, and microhydrated acenaphthene complexes are presented in this chapter and discussed using various levels of theory. Homogenous clusters with up to seven monomer units of acenaphthene are detected and UV and IR absorption spectra are measured up to the trimer. It is shown where spectral changes upon complexation of PAHs manifest in the IR range, and it is discussed how complexation of PAHs may impact the position and spectral features seen in diffuse interstellar bands (DIBs). The UV and infrared spectra of microhydrated PAH complexes with up to three water molecules are presented. The far-infrared spectra of Ace_n–W_m (n = 1–3, m = 1–3) show distinct features originating either from the pure Ace-cluster or from the pure water-clusters, rather than strong shifts from PAH–water interactions. Hence, the water clusters seem to be locked with negligible perturbation to the PAH structures, which is in line with the findings in the parallel study in the broadband microwave range.[14] DFT calculations of vibrational frequencies on molecular systems with competing dispersive interactions and hydrogen bonds are still challenging, though anharmonic corrections lead to slight improvements, especially in the CH out of plane bending and C–C stretch region.

References

1 F. Salama, *Proc. Int. Astron. Union*, 2008, **4**, 357.

2 C. Jäger, F. Huisken, H. Mutschke, I. L. Jansa and T. Henning, *Astrophys. J.*, 2009, **696**, 706–712.

3 H. Andrews, C. Boersma, M. W. Werner, J. Livingston, L. J. Allamandola and A. G. G. M. Tielens, *Astrophys. J.*, 2015, 807, 24pp.

4 S. Kwok and Y. Zhang, *Nature*, 2011, **479**, 80–83.

5 A. G. G. M. Tielens, *Annu. Rev. Astron. Astrophys*, 2008, **46**, 289–337.

6 J. Bouwman, H. M. Cuppen, M. Steglich, L. J. Allamandola and H. Linnartz, *Astron. Astrophys.*, 2011, **525**, A93.

7 Z. Guennoun, C. Aupetit and J. Mascetti, *J. Phys. Chem. A*, 2011, **115**, 1844–1852.

8 A. L. F. de Barros, A. L. Mattioda, A. Ricca, G. A. Cruz-Diaz and L. J. Allamandola, *Astrophys. J.*, 2017, **848**, 112.

9 W. Klemperer and V. Vaida, *Proc. Natl. Acad. Sci. U. S. A.*, 2006, **103**, 10584–10588.

10 V. Vaida and J. E. Headrick, *J. Phys. Chem. A*, 2000, **104**, 5401–5412.

11 E. Herbst, *Chem. Soc. Rev.*, 2001, **30**, 168–176.

12 A. Belloche, R. T. Garrod, H. S. P. Müller and K. M. Menten, *Science*, 2014, **345**, 1584–7.

13 D. J. Bakker, A. Dey, D. P. Tabor, Q. Ong, J. Mahé, M.-P. Gaigeot, E. L. Sibert III and A. M. Rijs, *Phys. Chem. Chem. Phys.*, 2017, **19**, 20343–20356.

14 A. L. Steber, C. Pérez, B. Temelso, G. C. Shields, A. M. Rijs, B. H. Pate, Z. Kisiel and M. Schnell, *J. Phys. Chem. Lett.*, 2017, **8**, 5744–5750.

15 E. Maltseva, C. J. Mackie, A. Candian, A. Petrignani, X. Huang, T. J. Lee, A. G. G. M. Tielens, J. Oomens and W. J. Buma, *Astron. Astrophys.*, 2018, **610**, 1–13.

16 B. A. Mcguire, A. M. Burkhardt, S. Kalenskii, C. N. Shingledecker, A. J. Remijan, E. Herbst and M. C. Mccarthy, *Science*, 2018, **359**, 202–205.

17 D. P. Zaleski, N. A. Seifert, A. L. Steber, M. T. Muckle, R. A. Loomis, J. F. Corby, O. Martinez, K. N. Crabtree, P. R. Jewell, J. M. Hollis, F. J. Lovas, D. Vasquez, J. Nyiramahirwe, N. Sciortino, K. Johnson, M. C. McCarthy, A. J. Remijan and B. H. Pate, *Astrophys. J.*, 2013, **765**, L10.

18 R. A. Loomis, D. P. Zaleski, A. L. Steber, J. L. Neill, M. T. Muckle, B. J. Harris, J. M. Hollis, P. R. Jewell, V. Lattanzi, F. J. Lovas, O. Martinez, M. C. McCarthy, A. J. Remijan, B. H. Pate and J. F. Corby, *Astrophys. J.*, 2013, **765**, L9.

19 M. Elyajouri, R. Lallement, N. L. J. Cox, J. Cami, M. A. Cordiner, J. V Smoker, A. Fahrang, P. J. Sarre and H. Linnartz, *Astron. Astrophys.*, 2018, **616**, A143.

20 A. M. Rijs and J. Oomens, *Gas-Phase IR Spectroscopy and Structure of Biological Molecules*, Springer, 2015.

21 G. Scoles, *Atomic and Molecular Beam Methods: Vol. 1*, Oxford University Press, 1988.
22 C. J. Gruenloh, J. R. Carney, C. A. Arrington, T. S. Zwier, S. Y. Fredericks and K. D. Jordan, *Science*, 1997, **276**, 1678–1681.
23 Ö. Birer and E. Yurtsever, *J. Mol. Struct.*, 2015, **1097**, 29–36.
24 F. Piuzzi, I. Dimicoli, M. Mons, P. Millié, V. Brenner, Q. Zhao, B. Soep and A. Tramer, *Chem. Phys.*, 2002, **275**, 123–147.
25 J. Antony, B. Alameddine, T. A. Jenny and S. Grimme, *J. Phys. Chem. A*, 2013, **117**, 616–625.
26 J. E. Roser, A. Ricca and L. J. Allamandola, *Astrophys. J.*, 2014, **783**, 97.
27 C. Joblin, L. Dontot, G. A. Garcia, F. Spiegelman, M. Rapacioli, L. Nahon, P. Parneix, T. Pino and P. Bréchignac, *J. Phys. Chem. Lett.*, 2017, **8**, 3697–3702.
28 K. Chatterjee and O. Dopfer, *Chem. Sci.*, 2018, **9**, 2301–2318.
29 K. Chatterjee and O. Dopfer, *Phys. Chem. Chem. Phys.*, 2017, **19**, 32262–32271.
30 M. Rapacioli, F. Calvo, F. Spiegelman, C. Joblin and D. J. Wales, *J. Phys. Chem. A*, 2005, **109**, 2487–2497.
31 N. K. Lee, S. Park and S. K. Kim, *J. Chem. Phys.*, 2002, **116**, 7910–7917.
32 H. Takeuchi, *J. Phys. Chem. A*, 2012, **116**, 10172–10181.
33 C. Gonzalez and E. C. Lim, *J. Phys. Chem. A*, 2000, **104**, 2953–2957.
34 M. Rapacioli, C. Joblin and P. Boissel, *Astron. Astrophys.*, 2005, **429**, 193–204.
35 C. Pérez, A. L. Steber, A. M. Rijs, B. Temelso, G. C. Shields, J. C. Lopez, Z. Kisiel and M. Schnell, *Phys. Chem. Chem. Phys.*, 2017, **19**, 14214–14223.
36 A. Potapov, *Mol. Astrophys.*, 2017, **6**, 16–21.
37 A. Potapov and P. Asselin, *Int. Rev. Phys. Chem.*, 2014, **33**, 275–300.
38 S. Jaeqx, J. Oomens, A. Cimas, M. P. Gaigeot and A. M. Rijs, *Angew. Chemie Int. Ed.*, 2014, **53**, 3663–3666.
39 A. M. Rijs, E. R. Kay, D. A. Leigh and W. J. Buma, *J. Phys. Chem. A*, 2011, **115**, 9669–9675.
40 P. M. Johnson and C. E. Otis, *Ann. Rev. Phys. Chem*, 1981, **32**, 139–157.
41 F. Furche, R. Ahlrichs, C. Hättig, W. Klopper, M. Sierka and F. Weigend, *Wiley Interdiscip. Rev. Comput. Mol. Sci.*, 2014, **4**, 91–100.
42 S. Grimme, J. G. Brandenburg, C. Bannwarth and A. Hansen, *J. Chem. Phys.*, 2015, **143**, 54107.
43 S. Grimme, *J. Chem. Phys.*, 2003, **118**, 9095–9102.
44 T. Risthaus, M. Steinmetz and S. Grimme, *J. Comput. Chem.*, 2014, **35**, 1509–1516.
45 F. Weigend and R. Ahlrichs, *Phys. Chem. Chem. Phys.*, 2005, **7**, 3297.
46 F. Weigend, A. Köhn and C. Hättig, *J. Chem. Phys.*, 2002, **116**, 3175–3183.
47 S. Grimme, J. Antony, S. Ehrlich and H. Krieg, *J. Chem. Phys.*, 2010, **132**, 154104.
48 J. C. Slater, *Phys. Rev.*, 1951, **81**, 385–390.

49 S. H. Vosko, L. Wilk and M. Nusair, *Can. J. Phys.*, 1980, **58**, 1200–1211.
50 T. H. Dunning, *J. Chem. Phys.*, 1970, **53**, 2823–2833.
51 M. J. Frisch, G. W. Trucks, H. B. Schlegel, G. E. Scuseria, M. A. Robb, J. R. Cheeseman, G. Scalmani, V. Barone, B. Mennucci, G. A. Petersson, H. Nakatsuji, M. Caricato, X. Li, H. P. Hratchian, A. F. Izmaylov, J. Bloino, G. Zheng, J. L. Sonnenberg, M. Hada, M. Ehara, K. Toyota, R. Fukuda, J. Hasegawa, M. Ishida, T. Nakajima, Y. Honda, O. Kitao, H. Nakai, T. Vreven, J. A. Montgomery, J. E. Peralta, F. Ogliaro, M. Bearpark, J. J. Heyd, E. Brothers, K. N. Kudin, V. N. Staroverov, R. Kobayashi, J. Normand, K. Raghavachari, A. Rendell, J. C. Burant, S. S. Iyengar, J. Tomasi, M. Cossi, N. Rega, J. M. Millam, M. Klene, J. E. Knox, J. B. Cross, V. Bakken, C. Adamo, J. Jaramillo, R. Gomperts, R. E. Stratmann, O. Yazyev, A. J. Austin, R. Cammi, C. Pomelli, J. W. Ochterski, R. L. Martin, K. Morokuma, V. G. Zakrzewski, G. A. Voth, P. Salvador, J. J. Dannenberg, S. Dapprich, A. D. Daniels, Ö. Farkas, J. B. Foresman, J. V. Ortiz, J. Cioslowski and D. J. Fox, *Gaussian 09*, 2009.
52 V. Barone, *J. Chem. Phys.*, 2005, **1221**, 14108–1007.
53 V. Barone, *J. Chem. Phys.*, 2004, **120**, 3059–3065.
54 K. L. Schuchardt, B. T. Didier, T. Elsethagen, L. Sun, V. Gurumoorthi, J. Chase, J. Li and T. L. Windus, 2007, **47**, 1045–1052.
55 S. Grimme and M. Steinmetz, *Phys. Chem. Chem. Phys.*, 2013, **15**, 16031.
56 G. Schaftenaar and J. H. Noordik, *J. Comput. Aided. Mol. Des.*, 2000, **14**, 123–134.
57 T. Chakraborty and M. Chowdhury, *Chem. Phys. Lett.*, 1991, **177**, 223–228.
58 J. Roden, A. Eisfeld, M. Dvorak, O. Bünermann and F. Stienkemeier, *J. Chem. Phys.*, 2011, **134**, 54907.
59 M. Wewer and F. Stienkemeier, *Phys. Rev. B*, 2003, **67**, 125201.
60 P. J. Sarre, *Mon. Not. R. Astron. Soc.*, 2000, **313**, L14–L16.
61 C. Gilliéron, N. Sharma, K. Nauta and T. W. Schmidt, *J. Phys. Chem. A*, 2007, **111**, 4211–4214.
62 M. Schmitt, F. Spiering, V. Zhaunerchyk, R. T. Jongma, S. Jaeqx, A. M. Rijs and W. J. van der Zande, *Phys. Chem. Chem. Phys.*, 2016, **18**, 32116–32124.
63 C. J. Mackie, A. Candian, X. Huang, E. Maltseva, A. Petrignani, J. Oomens, W. J. Buma, T. J. Lee and A. G. G. M. Tielens, *Phys. Chem. Chem. Phys.*, 2018, **20**, 1189–1197.
64 D. Uridat, V. Brenner, I. Dimicoli, J. Le Calve, P. Millie, M. Mons and F. Piuzzi, *Chem. Phys.*, 1998, **239**, 151–175.
65 M. J. Gillan, D. Alfè and A. Michaelides, *J. Chem. Phys.*, 2016, **144**, 130901.
66 A. K. Lemmens, S. Gruet, A. L. Steber, J. Antony, S. Grimme, M. Schnell and A. M. Rijs, *Phys. Chem. Chem. Phys.*, 2019, **21**, 3414–3422.

Chapter 7

High-resolution infrared spectroscopy of naphthalene and acenaphthene dimers

This chapter is published as:
Alexander K. Lemmens, Pragya Chopra, Diksha Garg, Amanda L. Steber, Melanie Schnell, Wybren Jan Buma, Anouk M. Rijs, *Molecular Physics,* 119, e1811908, 2021

7.1 Abstract

Non-covalent interactions are rapidly gaining interest as they are often crucial in determining the properties of materials, and key to supramolecular chemistry and to biochemistry. Non-covalent Polycyclic Aromatic Hydrocarbon (PAH) complexes are in particular relevant to astrochemistry and combustion chemistry where they are involved in the initial steps of condensation and soot formation, respectively. Here, we investigated non-covalent π-π stacking and CH-π interactions in naphthalene and acenaphthene clusters using high-resolution IR-UV spectroscopy in combination with quantum chemical calculations. We identified spectral shifts that occur upon complexation and thereby evaluated predicted potential energy surfaces. Although theory predicts a blueshift, a redshift is observed for the aliphatic CH-π interactions in the experimental spectrum of acenaphthene upon dimerization, indicating that CH-π interaction indeed affects the aliphatic bonds, while a blueshift is predicted, consequently theory deserves attention here. The results provide strong indications for a prevalent parallel naphthalene dimer, showing that π-π stacking interactions become significant for bicyclic and larger PAHs.

7.2 Introduction

The interactions governing cluster formation of small PAH molecules are receiving significant interest from both theoreticians and experimentalists.[1–7] The *π-π* stacking and/or CH-π interactions that may be present in these archetypal complexes can have important contributions to the structure of molecules or molecular complexes of interest in astrochemistry[8–13], biochemistry[14–16] as well as in material sciences[17,18]. Understanding and modelling these interactions is therefore crucial to get a grip on the structure of such molecular complexes, and thereby understand their function in biology and how they determine the characteristics of materials. Moreover, the PAH clusters studied here are of considerable interest to the combustion community[19,20] since they are key players in the initial steps of soot formation, and to the astrochemistry community because they form a link between isolated molecules and carbonaceous grains.[8–13]

The geometry of PAH dimers shows two different structural preferences depending on their size. Large PAHs and even graphene favour a parallel geometry.[3] Alternatively, the significant body of experimental and theoretical work on the benzene dimer and its derivatives indicate a T-shaped geometry as the global minimum[21–23] with the parallel-displaced isomer being slightly higher in energy. Grimme[24], and later Martinez and Iverson[14], concluded that *π-π* stacking interactions are strongly size-dependent and become

significant only for parallel complexes containing more than 10–15 carbon atoms, i.e. from naphthalene or anthracene onwards. At a certain PAH size, a turning point from a T-shaped geometry, as observed in the benzene dimer, to a parallel geometry is expected, which is accompanied by a smooth change in character of the noncovalent interactions.[25] Insight into the geometry of naphthalene(-like) dimers would contribute to finding this turning point and validate the existing theory of interactions between aromatic moieties.

A number of studies have been performed on the structure of the naphthalene dimer. In most theoretical studies the (C_2 crossed) parallel geometry was found to be more stable than the T-shaped geometry (see Figure 7.1).[26–33] Interestingly, in larger clusters such as the trimer[34] or the crystal structure of smaller PAHs [8,25] a non-parallel structure, clearly differing from the parallel geometry of PAH dimers, is found. Experimental studies using electronic spectroscopy or IR matrix isolation spectroscopy have so far not provided a conclusive picture. Fluorescence spectroscopy suggests a parallel geometry as it is favoured by the singlet excimers.[35] The excimer formation appears to be a barrierless process, from which it has been concluded that the change in geometry from the ground to the excited state is minimal. Further support for a parallel geometry is provided by the Resonance Enhanced MultiPhoton Ionisation (REMPI) excitation spectrum of the non-parallel trimer -for which excimer formation is less expected- which is much sharper than that of the dimer.[36] In contrast, Gilliéron et al. concluded using REMPI spectroscopy that the naphthalene dimer-argon$_n$ complex contained a T-shaped configuration.[37] A similar geometry was deduced from matrix isolation IR spectroscopy.[38] However, in a later theoretical evaluation by Bauschlicher and Ricca it was shown that argon stabilises the T-shaped geometry relative to the parallel geometries.[39] A definitive conclusion on the geometry of the pure naphthalene dimer can therefore still not be drawn.

In the same theoretical study, the authors suggested that IR vibrational spectroscopy in the CH out-of-plane and CH stretch regions could be a useful diagnostic tool to come to a conclusive determination of the ground-state structure of the naphthalene dimer. In this work, we therefore present IR absorption spectra of mass-selected naphthalene clusters obtained by ion-dip spectroscopy and discuss the implications of these spectra for the geometry of the naphthalene dimer. Besides the naphthalene dimer, IR ion-dip spectra of acenaphthene monomer and dimer in the 3 μm region are presented. In contrast to the naphthalene dimer, the structural preference of the acenaphthene dimer appears to be more straightforward due to the influence of the aliphatic groups as is supported by the theoretical calculations (see Figure 7.1). It can, therefore, serve as a reference system in this study. At the same time, it should be remarked that experimentally it has not been possible to come to a definite conclusion. Nevertheless, it is noteworthy that in microwave spectroscopy studies by Steber et al. the dimer was not observed, which suggests that this dimer preferably adopts a parallel structure.[40] An

additional interesting aspect of this dimer is that it not only displays π-π interactions but also CH-π interactions, which are evaluated here as well.

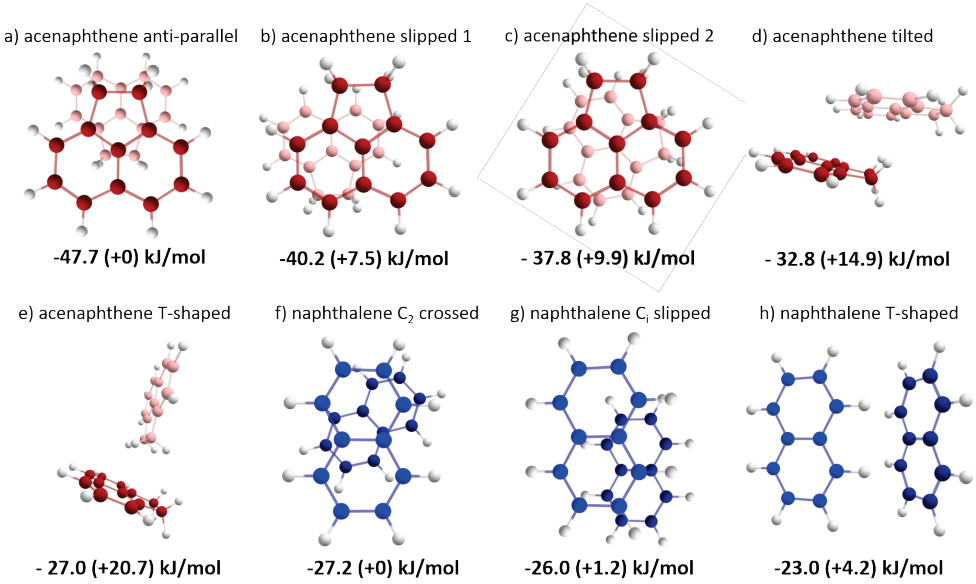

Figure 7.1: (a–e) Five lowest energy-minimized structures of the acenaphthene dimer and (f–h) three lowest energy-minimized structures of the naphthalene dimer. The corresponding interaction energies are given below the structures.

7.3 Methods

7.3.1 Experimental

Experiments on acenaphthene and naphthalene were performed on samples that were heated to 80 °C in a glass sample compartment located just upstream of a Series 9 pulsed valve from General Valve. The valve was operated at 20 Hz using a backing pressure of 2.5 bar of argon. The mixed gas was expanded into a vacuum chamber, after which it passed through a skimmer. The molecular beam was excited by an IR beam in the 3 µm region, provided by a Nd:YAG laser pumped OPO laser (Laser Vision) with a bandwidth of about 0.1 cm^{-1} and operating at 10 Hz. Mid-IR experiments were performed using radiation provided by the Free Electron Laser FELIX operating at 10 Hz.[41] After a delay of 200 ns the molecular beam was probed via REMPI with a counterpropagating UV laser beam produced by a Nd:YAG laser pumped dye laser (LiopTec) running at 20 Hz to

acquire alternating IR-on and IR-off shots. The UV photon energy was set to 31,175 cm^{-1} for acenaphthene and 32,299 cm^{-1} for the naphthalene dimer corresponding to the maximised infrared ion gain signal and the $8^{-}108^{-}01$ transition, respectively. The ionised molecules were detected in a reflectron time-of-flight mass spectrometer (R. M. Jordan Co.). The idler frequency of the OPO laser was calibrated continuously during measurements using a High Finesse WS-7 wavelength meter.

7.3.2 Theoretical

DFT calculations were performed with the Gaussian16 suite of programs[42] using a superfine grid and very tight optimisation criteria. The energy minima of the naphthalene and acenaphthene dimer structures depicted in Figure 7.1 were calculated at the B3LYP-D3/Jun-cc-pVDZ level of theory, interaction energies being calculated by subtracting two times the ZPE-corrected monomer energy from the ZPE-corrected energy of the dimer. A small survey using the lowest-energy, antiparallel structure was carried out to validate predicted spectra with the experimental spectra of the acenaphthene dimer employing the B3LYP-D3BJ, B97-D3BJ, APFD, wB97XD, M062X-D3, LC-wPBE-D3BJ functional in combination with the Jun-cc-pVDZ basis set. The B3LYP functional was used with and without dispersion (and damping) corrections to evaluate the effects of these corrections. To check the effect of a larger or slightly different basis set, the B3LYP-D3 functional was also tested with the 6-311++G** basis set. Since the survey did not produce qualitatively different results (see Figures 7.5 and 7.6), the calculations used for analysis of both the acenaphthene and naphthalene spectra were performed at the B3LYP/Jun-cc-pVDZ level of theory. To account for the dispersion interactions, the D3 empirical dispersion correction was applied.[3] Frequency calculations have been performed in the harmonic approximation as well as anharmonically using GVPT2.[43] For a better comparison with the experiment, predicted spectra have been convoluted with a 1 cm^{-1} FWHM Gaussian unless stated otherwise.

7.4 Results and discussion

In the following, we will first evaluate the experimental and theoretical IR spectra of acenaphthene as the structure of the dimer is more straightforward and its non-observation with microwave spectroscopy would suggest a parallel geometry. Spectral characteristics in the aromatic CH stretch region that reflect the geometry of the complex can subsequently be used in the second part of the results section where the infrared spectrum of the naphthalene dimer is discussed.

7.4.1 Acenaphthene

The acenaphthene monomer contains four out-of-plane hydrogens and two aromatic rings. Intuitively, one expects complexes that enable both CH-π and *π-π* stacking interactions to show the largest stabilisation energies. This is indeed reflected by the DFT energy-minimised structures in Figure 7.1(a–e). In structures a–c, both of these interactions can be present, whereas in the higher-energy structures, d and e, only CH-π interactions are present. Microwave spectroscopic studies, which provide an accurate structure of the monomer, have as yet not been able to observe signals from the acenaphthene dimer, which would be in line with the computational prediction that the non-polar anti-parallel structure is the lowest-energy structure. In this anti-parallel configuration, the out-of-plane hydrogen atoms are oriented towards the aromatic rings of the opposite but equivalent monomer unit (see Figure 7.1(a)). Additionally, in a broadband microwave spectroscopic study, the parallel conformation was also found for the fluorene dimer, a PAH of comparable size as acenaphthene and naphthalene.[7] Compared to the naphthalene dimer structures, the acenaphthene dimer shows a significantly higher interaction energy for acenaphthene (47.7 kJ/mol) compared to a maximum of 27.2 kJ/mol for naphthalene (Figure 7.1(f)). We ascribe the higher binding energy of the acenaphthene dimer to the presence of CH-π interactions that are lacking in the parallel structure of the naphthalene dimer. The T-shaped naphthalene dimer could potentially have CH-π interactions, but in such geometries, the *π-π* stacking interactions would be absent and they would thus be at much higher energies.

The experimental 3 μm IR spectra of the acenaphthene monomer and dimer are shown in Figure 7.2 together with the calculated IR spectra of the anti-parallel geometry. The trimer spectrum is presented in Figure 7.7 and calculated IR spectra of slipped and T-shaped dimers are displayed in Figure 7.8.

At first sight, the experimental spectra of the monomer, dimer and trimer are quite similar. The effect of complexation is very subtle and manifests itself mostly in the aliphatic region (2800–3000 cm^{-1}) as a redshift of typically 5–6 cm^{-1} going from the monomer to the dimer. Compared to the dimer, the trimer peak positions do not change significantly (see Figure 7.7). The aromatic region (3000–3150 cm^{-1}) also shows a redshift, although the difference here is smaller (about 2 cm^{-1}) than in the aliphatic region. Considering the lowest-energy structure of the dimer in Figure 7.1(a), the larger redshift in the aliphatic region compared to shift in the aromatic region is in line with a priori expectations since the aliphatic region is more susceptible to CH-π interactions. The observed redshift thus shows that such interactions are non-negligible and important for assessing the driving forces of complex formation. A similar conclusion is drawn from the observation that the strong band at 2944 cm^{-1} of the monomer is split in the dimer

and trimer spectrum, which is consistent with an induced non-equivalence of the aliphatic CH groups upon complex formation.

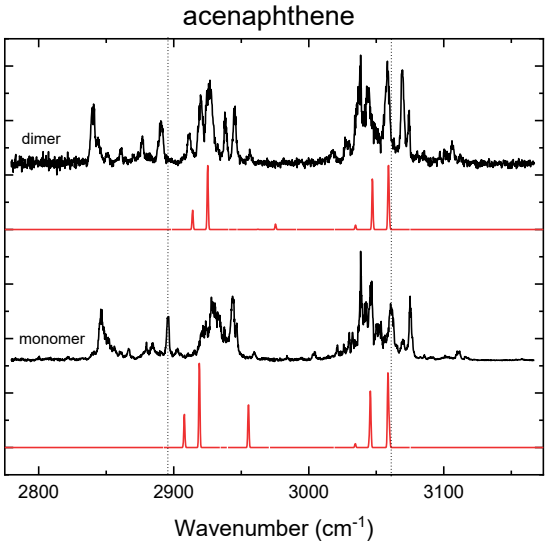

Figure 7.2: High-resolution experimental IR spectra of the acenaphthene monomer and dimer (black) in the 3 μm region in combination with calculated IR spectra (red) at the B3LYP-D3/Jun-cc-pVDZ level using a scaling factor for the harmonic frequencies of 0.96.

The harmonic theory does not include combination bands and resonances and, as a result, it does not predict the appropriate number of bands in the monomer or dimer spectrum.[44] Although anharmonic theory includes these effects, the prediction is not sufficiently accurate to come to a definitive assignment. In addition, the experimental, small change is not predicted at the anharmonic level (see Figure 7.7). A poorly predicted intermolecular potential can be the cause of the incorrectly calculated additional bands and resonances. For this reason, the harmonic calculations, which do show a small change upon complexation, are used in the structural analysis.

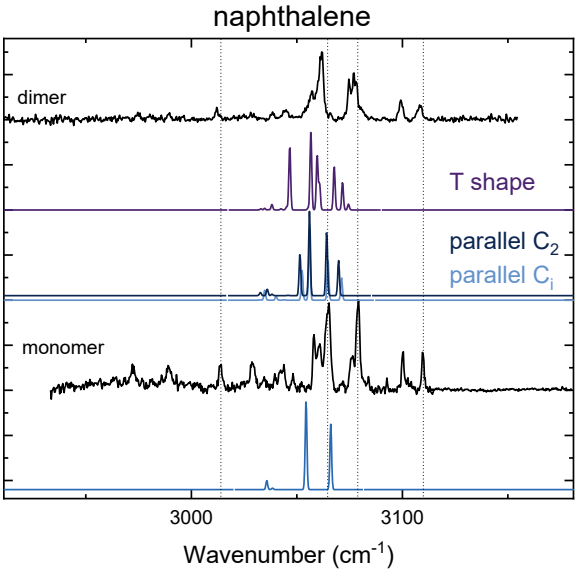

Figure 7.3: High-resolution IR spectra of the naphthalene monomer (obtained by Maltseva et al.[45]) and dimer (black) in combination with predicted spectra of the configurations presented in Figure 7.1 (T-shaped (purple), C_2 crossed parallel (dark blue) and C_i slipped parallel (light blue)) at the B3LYP-D3/Jun-cc-pVDZ level of theory using the harmonic approximation and a frequency scaling factor of 0.96.

The harmonic calculated IR spectra of the monomer and anti-parallel dimer are qualitatively very similar. An analogous analysis for the anharmonic calculations is reported in Figure 7.7. In the aromatic region, a very small blueshift is predicted, whereas the experiment shows a redshift of about 2 cm^{-1}. In the aliphatic region, the calculations predict a significant blueshift upon complexation with the most intense band being shifted by 6 cm^{-1} upon complexation. This blueshift is predicted in almost all the calculations that we performed in a survey with a broad range of functionals (see theoretical section and Figure 7.5), the M062X-D3 functional being the only one that shows a small redshift. Such a blueshift is at odds with the experimentally observed redshift, but might be related to the so-called improper hydrogen bonds[46,47] that are not properly described at the employed levels of theory. Although not of direct importance for the present study, the predicted blueshift nevertheless requires further attention from theoretical studies, not only because of the present observations but also because similar observations were made in studies by Erlekam et al. on the benzene dimer.[22] In the aromatic region, the intermolecular interactions in the (displaced) parallel configuration cause a small decrease in the bond strength of the aromatic CHs resulting in the observed redshift of about 2 cm^{-1}.

7.4.2 Naphthalene

Since the different configurations of the naphthalene dimer are close in energy, its geometry is still under heavy debate. IR spectroscopy can contribute to the elucidation of its structure[39] since both the CH stretch and CH out-of-plane modes are expected to be affected differently in the possible configurations of the naphthalene dimer. Figure 7.3 shows the experimental infrared spectrum in the 3 μm region of the naphthalene dimer presented with the IR spectrum of the naphthalene monomer recorded by Maltseva et al.[45] The experimental spectrum of the monomer and dimer are again qualitatively very similar but with a redshift of about 3 cm^{-1} upon dimerisation, similar to what was observed in the aromatic region of acenaphthene. The two main bands in the dimer spectrum at 3061 and 3077 cm^{-1} most likely correspond to the two strong bands in the monomer spectrum at 3065 and 3079 cm^{-1}, their shape appearing to be slightly changed with a shoulder on the red and blue side, respectively. Figure 7.3 also displays calculated IR spectra in the 3 μm region for the monomer, the T-shaped dimer, the C_2 crossed parallel dimer and the C_i slipped parallel dimer at the B3LYP-D3/Jun-cc-pVDZlevel of theory (see Figure 7.1(f–h) for geometries and relative energies). The IR spectrum of the monomer calculated at the harmonic level of theory matches qualitatively with the experimental spectrum, i.e. two strong bands are predicted to be separated by approximately the experimentally observed energy. Even though anharmonic calculations are necessary to make a full prediction of the spectrum (see Figure 7.9), we will use these harmonic spectra in the further discussion as a main guide to interpret the effects of complexation in order to avoid unnecessary complications of such a discussion.

The calculated harmonic IR spectra of the dimer can be divided into two groups. The two parallel geometries, C_2 crossed and C_i slipped, contain equivalent monomer units and lead to infrared spectra that are similar to the monomer spectrum with the main peaks being split as a result of the dimer formation. In contrast, the T-shaped geometry exhibits two non-equivalent monomer units of which one is significantly affected by dimer formation. This results in the activation of previously IR-inactive modes and leads to an IR spectrum that is quite different from the spectra of the parallel geometries and that shows a larger number of bands. The similarity between the experimentally observed IR spectra of the monomer and dimer thus strongly suggests that the dimer adopts a parallel structure and not a T-shaped geometry. Further support for this conclusion is found in the shoulders on the main bands in the experimental spectrum, which can be explained by the splitting of the two main peaks as predicted by theory for the parallel geometries.

The main features in the harmonic calculations of the naphthalene monomer coincide with the features that are predicted in the aromatic region of the acenaphthene monomer. This is not surprising since the aromatic parts of the two molecules are similar.

From our studies on acenaphthene we concluded that the dimer predominantly adopts a parallel conformation, and we concluded above for naphthalene that the 3 μm region also suggests a parallel dimer. One might, therefore, expect both molecules to show similar spectral shifts upon dimerisation. Since such shifts are small, the effect of dimerisation is better visualised in difference spectra constructed by subtracting the IR spectrum of the dimer from that of the monomer, which are depicted in Figure 7.4. Figure 7.4(a) shows that for both molecules overall a similar redshift is observed in the main features, which manifests itself in the difference spectrum as a negative going to positive signal from low to high wavenumbers. The features observed for acenaphthene between 3020 and 3040 cm^{-1}, which are not present in the difference spectrum of naphthalene, result from the coupling between aliphatic and aromatic groups.[44,48] Our calculations indicate that the two main bands pointed out by an asterisk in both the spectrum of acenaphthene (3060 and 3072 cm^{-1} at highest slope) and naphthalene (3063 and 3078 cm^{-1} at highest slope) are associated with normal modes that are very similar in the two molecules. Our experiments show that both modes undergo a similar shift upon complex formation. This is in line with what would be expected if both molecules would have a similar (parallel) geometric arrangement of the monomer units.

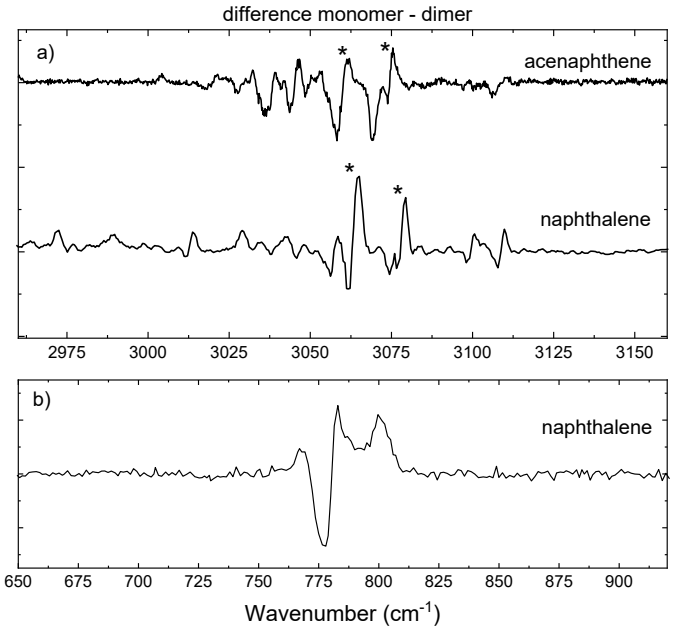

Figure 7.4: (a) Difference spectra (monomer-dimer) of acenaphthene and naphthalene in the aromatic CH stretch region and (b) of naphthalene in the aromatic CH out-of-plane region. In the monomer-dimer difference plot, a redshift manifests itself as a negative going to positive signal from low to high wavenumbers. The CH stretch and the CH out-of-plane region show a redshift of 2–3 and 4 cm^{-1}, respectively, as a result of complex formation.

Stronger support for the conclusion that the naphthalene dimer adopts a parallel geometry comes from the difference spectrum in the mid-IR region (Figure 7.4(b)) where an overall redshift is observed upon complexation. The major advantage of this region is that it is much less affected by Fermi-resonances, since the density of vibrational states is lower and resonances are thus less likely to occur. Therefore, the harmonic calculations here are more reliable than in the 3 μm region.[49] Theoretical studies of Bauschlicher and coworkers have shown that a parallel configuration of the monomer units would lead to a redshift.[39] Our calculations (Figure 7.6) also predict a redshift of 5 cm^{-1} for a parallel orientation, which compares well with the experimentally observed redshift of 4 cm^{-1}. For the T-shaped orientation, in contrast, a nonsignificant blueshift is predicted. We recall that for the aliphatic region of the acenaphthene dimer only the M062X-D3 functional correctly predicted the experimentally observed redshift. In order to ensure that the signs and magnitudes of the shifts calculated here at the B3LYP level for the mid-IR region are not dependent on the level of theory, we have performed similar calculations with the M062X-D3 functional. These calculations qualitatively give the same results as the B3LYP-D3 calculations (see Figure 7.6) and do not lead to different conclusions.

7.5 Conclusions

We have presented high-resolution mass-selected IR ion-dip spectra of monomers and clusters of acenaphthene and naphthalene. In combination with quantum chemical calculations, these studies have allowed us to elucidate and evaluate the effects of cluster formation on the infrared signatures and vibrational modes of these molecules. In the case of acenaphthene we have found that the aliphatic CH-π interactions result in a redshift and possible splitting of the corresponding vibrational bands upon dimerisation. Such a redshift in general indicates a weaker bond, and we can thus conclude that the CH-π interaction affects the aliphatic bonds as expected. Interestingly, DFT calculations predict a blueshift, and this is certainly an aspect that deserves further theoretical attention. In the aromatic region of both naphthalene and acenaphthene dimers a similar, small redshift is observed.

Together with the diagnostic features for a particular geometry that the studies on acenaphthene provided, the experimental and theoretical results obtained for the naphthalene dimer provide strong indications that this dimer predominantly adopts a parallel configuration. Firstly, the naphthalene dimer high-resolution IR spectrum shows a large resemblance with the parallel acenaphthene dimer IR spectrum in the aromatic CH stretch region. Secondly, the CH out-of-plane band is redshifted, which is a strong diagnostic feature of a parallel configuration. Our experiments thus support the theoretical

prediction of a prevalent parallel configuration of the naphthalene dimer in which π-π stacking interactions are enabled. This is in line with the general idea that π-π stacking interactions become significant for stacked monomers with more than 10–15 carbon atoms.

References

1 P. M. Felker, P. M. Maxton and M. W. Schaeffer, *Chem. Rev.*, 1994, **94**, 1787–1805.
2 S. Speiser, *Chem. Rev.*, 1996, **96**, 1953–1976.
3 S. Grimme, J. Antony, S. Ehrlich and H. Krieg, *J. Chem. Phys.*, 2010, **132**, 154104.
4 J. Moellmann and S. Grimme, *J. Phys. Chem. C*, 2014, **118**, 7615–7621.
5 S. Grimme, C. Mück-Lichtenfeld and J. Antony, *J. Phys. Chem. C*, 2007, **111**, 11199–11207.
6 A. Potapov, *Mol. Astrophys.*, 2017, **6**, 16–21.
7 M. Fatima, A. L. Steber, A. Poblotzki, C. Pérez, S. Zinn and M. Schnell, *Angew. Chemie - Int. Ed.*, 2019, **58**, 3108–3113.
8 M. Rapacioli, F. Calvo, F. Spiegelman, C. Joblin and D. J. Wales, *J. Phys. Chem. A*, 2005, **109**, 2487–2497.
9 F. Salama, *Proc. Int. Astron. Union*, 2008, **4**, 357.
10 C. Jäger, F. Huisken, H. Mutschke, I. L. Jansa and T. Henning, *Astrophys. J.*, 2009, **696**, 706–712.
11 A. G. G. M. Tielens, *Annu. Rev. Astron. Astrophys*, 2008, **46**, 289–337.
12 A. K. Lemmens, D. B. Rap, J. M. M. Thunnissen, B. Willemsen and A. M. Rijs, *Nat. Commun.*, 2020, **11**, 1–7.
13 A. K. Lemmens, S. Gruet, A. L. Steber, J. Antony, S. Grimme, M. Schnell and A. M. Rijs, *Phys. Chem. Chem. Phys.*, 2019, **21**, 3414–3422.
14 C. R. Martinez and B. L. Iverson, *Chem. Sci.*, 2012, **3**, 2191–2201.
15 K. Schwing and M. Gerhards, *Int. Rev. Phys. Chem.*, 2016, **35**, 569–677.
16 S. Bakels, E. M. Meijer, M. Greuell, S. B. A. Porskamp, G. Rouwhorst, J. Mahé, M. P. Gaigeot and A. M. Rijs, *Faraday Discuss.*, 2019, **217**, 322–341.
17 X. Feng, M. Liu, W. Pisula, M. Takase, J. Li and K. Müllen, *Adv. Mater.*, 2008, **20**, 2684–2689.
18 R. Fitzner, C. Elschner, M. Weil, C. Uhrich, C. Körner, M. Riede, K. Leo, M. Pfeiffer, E. Reinold, E. Mena-Osteritz and P. Bäuerle, *Adv. Mater.*, 2012, **24**, 675–680.
19 K. O. Johansson, M. P. Head-Gordon, P. E. Schrader, K. R. Wilson and H. A. Michelsen, *Science*, 2018, **361**, 997–1000.
20 M. Thomson and T. Mitra, *Science*, 2018, **361**, 978–979.
21 R. H. Page, Y. R. Shen and Y. T. Lee, *J. Chem. Phys.*, 1988, **88**, 4621–4636.

22 U. Erlekam, M. Frankowski, G. Meijer and G. Von Helden, *J. Chem. Phys.*, 2006, 124.
23 M. Schnell, U. Erlekam, P. R. Bunker, G. Vonhelden, J. U. Grabow, G. Meijer and A. Van der Avoird, *Angew. Chemie - Int. Ed.*, 2013, **52**, 5180–5183.
24 S. Grimme, *Angew. Chemie - Int. Ed.*, 2008, **47**, 3430–3434.
25 S. M. Ryno, C. Risko and J. L. Brédas, *Chem. Mater.*, 2016, **28**, 3990–4000.
26 C. Gonzalez and E. C. Lim, *J. Phys. Chem. A*, 2000, **104**, 2953–2957.
27 S. Tsuzuki, K. Honda, T. Uchimaru and M. Mikami, *J. Chem. Phys.*, 2004, **120**, 647–659.
28 T. R. Walsh, *Chem. Phys. Lett.*, 2002, **363**, 45–51.
29 N. K. Lee, S. Park and S. K. Kim, *J. Chem. Phys.*, 2002, **116**, 7910–7917.
30 M. Saeki, H. Akagi and M. Fujii, *J. Chem. Theory Comput.*, 2006, **2**, 1176–1183.
31 C. Gonzalez and E. C. Lim, *J. Phys. Chem. A*, 2003, **107**, 10105–10110.
32 T. Sato, T. Tsuneda and K. Hirao, *J. Chem. Phys.*, 2005, 123, 104307.
33 R. Podeszwa and K. Szalewicz, *Phys. Chem. Chem. Phys.*, 2008, **10**, 2581–2583.
34 P. Benharash, M. J. Gleason and P. M. Felker, *J. Phys. Chem. A*, 1999, **103**, 1442–1446.
35 H. Saigusa and E. C. Lim, *Acc. Chem. Res.*, 1996, **29**, 171–178.
36 T. Fujiwara and E. C. Lim, *J. Phys. Chem. A*, 2003, **107**, 4381–4386.
37 C. Gilliéron, N. Sharma, K. Nauta and T. W. Schmidt, *J. Phys. Chem. A*, 2007, **111**, 4211–4214.
38 J. E. Roser and L. J. Allamandola, *Astrophys. J.*, 2010, **722**, 1932–1938.
39 C. W. Bauschlicher and A. Ricca, *Theor. Chem. Acc.*, 2013, **132**, 1–8.
40 A. L. Steber, C. Pérez, B. Temelso, G. C. Shields, A. M. Rijs, B. H. Pate, Z. Kisiel and M. Schnell, *J. Phys. Chem. Lett.*, 2017, **8**, 5744–5750.
41 D. Oepts, A. F. G. Van, D. Meer and P. W. Van Amersfoort, *Infrared Phys. Technol.*, 1995, **36**, 297–308.
42 M. J. Frisch, G. W. Trucks, H. B. Schlegel, G. E. Scuseria, M. A. Robb, J. R. Cheeseman, G. Scalmani, V. Barone, G. A. Petersson, H. Nakatsuji, X. Li, M. Caricato, A. V. Marenich, J. Bloino, B. G. Janesko, R. Gomperts, B. Mennucci, H. P. Hratchian, J. V. Ortiz, A. F. Izmaylov, J. L. Sonnenberg, D. Williams-Young, F. Ding, F. Lipparini, F. Egidi, J. Goings, B. Peng, A. Petrone, T. Henderson, D. Ranasinghe, V. G. Zakrzewski, J. Gao, N. Rega, G. Zheng, W. Liang, M. Hada, M. Ehara, K. Toyota, R. Fukuda, J. Hasegawa, M. Ishida, T. Nakajima, Y. Honda, O. Kitao, H. Nakai, T. Vreven, K. Throssell, J. Montgomery, J. A., J. E. Peralta, F. Ogliaro, M. J. Bearpark, J. J. Heyd, E. N. Brothers, K. N. Kudin, V. N. Staroverov, T. A. Keith, R. Kobayashi, J. Normand, K. Raghavachari, A. P. Rendell, J. C. Burant, S. S. Iyengar, J. Tomasi, M. Cossi, J. M. Millam, M. Klene, C. Adamo, R. Cammi, J. W. Ochterski, R. L. Martin, K. Morokuma, O. Farkas, J. B. Foresman and D. J. Fox, *Gaussian, Inc., Wallingford CT*.

43 J. Bloino, *J. Phys. Chem. A*, 2015, **119**, 5269–5287.
44 E. Maltseva, C. J. Mackie, A. Candian, A. Petrignani, X. Huang, T. J. Lee, A. G. G. M. Tielens, J. Oomens and W. J. Buma, *Astron. Astrophys.*, 2018, **610**, 1–13.
45 E. Maltseva, A. Petrignani, A. Candian, C. J. Mackie, X. Huang, T. J. Lee, A. G. G. M. Tielens, J. Oomens and W. J. Buma, *Astrophys. J.*, 2016, **831**, 11pp.
46 J. Joseph and E. D. Jemmis, *J. Am. Chem. Soc.*, 2007, **129**, 4620–4632.
47 P. Hobza and Z. Havlas, *Theor. Chem. Acc.*, 2002, **108**, 325–334.
48 P. R. Franke, D. P. Tabor, C. P. Moradi, G. E. Douberly, J. Agarwal, H. F. Schaefer and E. L. Sibert, *J. Chem. Phys.*, 2016, **145**, 224304.
49 A. K. Lemmens, D. B. Rap, J. M. M. Thunnissen, C. J. Mackie, A. Candian, A. G. G. M. Tielens, A. M. Rijs and W. J. Buma, *Astron. Astrophys.*, 2019, **628**, A130.

Appendix

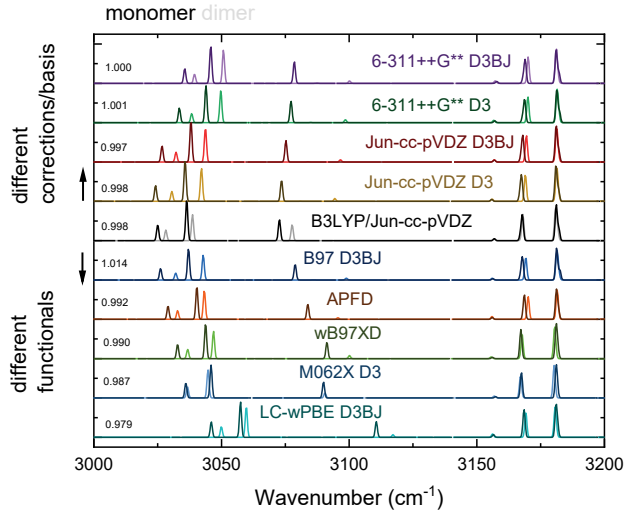

Figure 7.5: The effect of different functionals on the shift in the aliphatic and aromatic CH stretch region of acenaphthene upon complexation. All dispersion corrections result in a blueshift upon complexation. The same holds for slightly different, larger basis sets. Using different functionals only shows a qualitative difference in the case of M062X-D3, for which a small redshift is observed in the aliphatic region as well as in the aromatic region. In order to verify whether this would lead to different conclusions in the case of the naphthalene dimer, we also compare these functionals for both the naphthalene monomer and two configurations of the dimer. This comparison reveals no qualitative differences (see Figure 7.6) and we thus conclude that the poor performance of describing the aliphatic region in the acenaphthene case does not influence our conclusions for naphthalene.

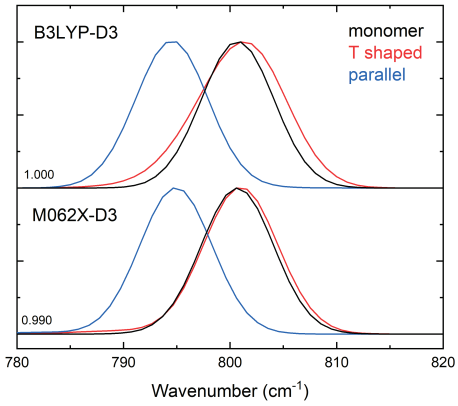

Figure 7.6: The effect of two different functionals on the IR peak of the CH out-of-plane mode of naphthalene and naphthalene dimer. The calculated peaks are convoluted with an 8 cm^{-1} FWHM gaussian, corresponding to the FELIX bandwidth. The black line corresponds to the monomer, the red line to the T-shaped dimer and the black line to the C2 crossed parallel dimer. Calculations have been performed at the B3LYP-D3 and M062X-D3 level of theory, both with the Jun-cc-pVDZ basis set using a superfine grid and very tight optimization. Both levels of theory show the same trend, i.e. almost no shift upon complexation in the case of the T-shaped dimer and a significant blueshift upon complexation in the case of a parallel dimer.

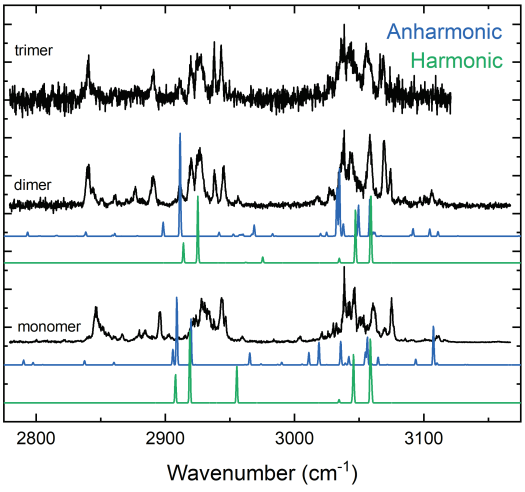

Figure 7.7: High-resolution IR spectra of the acenaphthene monomer, dimer and trimer (black) in combination with predicted spectra at the harmonic (green, using a scaling factor of 0.96) and anharmonic (blue) level of theory (B3LYP-D3/Jun-cc-pVDZ).

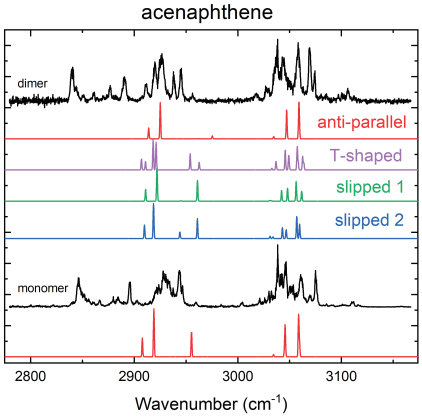

Figure 7.8: High-resolution IR spectra of the acenaphthene monomer and dimer (black) in combination with predicted spectra at the harmonic level of theory (color, using a scaling factor of 0.96 (B3LYP-D3/Jun-cc-pVDZ)). The experimental spectra of the monomer and dimer are very similar. The IR spectrum of the dimer that changes least upon complexation is the anti-parallel spectrum, confirming the expectation of a (anti-)parallel dimer configuration.

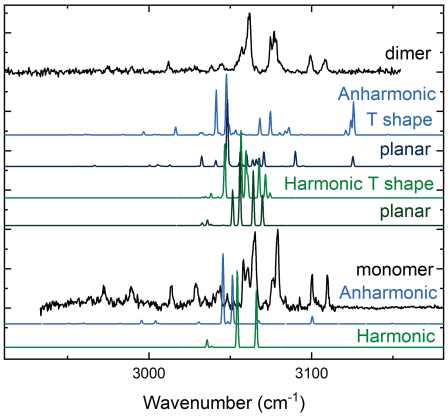

Figure 7.9: High resolution IR spectra of the naphthalene monomer (obtained by Maltseva et al.[45]) and dimer (black) in combination with predicted spectra on the harmonic (green, using a scaling factor of 0.96) and anharmonic (blue) level of theory (B3LYP-D3/Jun-cc-pVDZ). Although the anharmonic theory predicts a more appropriate number of bands in both the spectrum of the monomer and the dimer, the prediction is not sufficiently accurate to come to a definite assignment. Moreover, the predicted change upon complexation in the anharmonic spectra does not correspond to the small change observed experimentally. It may very well be that a poorly predicted intermolecular potential is the cause of many additional bands and band shifts since intermolecular modes also contribute to resonances. For this reason, the structural analysis has been based on purely harmonic calculations. Although the harmonic calculations are lacking a large number of bands, the change upon complexation is minimal and can be well compared with the experiment.

Chapter 8

Polycyclic aromatic hydrocarbon formation chemistry in a plasma revealed: naphthalene

This chapter is published as:
Alexander K. Lemmens, Daniël B. Rap, Johannes M. M. Thunnissen, Bryan Willemsen & Anouk M. Rijs, *Nature Communications,* 11, 269, 2020

8.1 Abstract

Large polycyclic aromatic hydrocarbons (PAHs) are the most abundant complex molecules in the interstellar medium; however, their possible formation pathways from small molecular species are still elusive. In the present work, we follow and characterize the formation of PAHs in an electrical discharge, specifically the PAH naphthalene in a molecular beam of argon. The fragments, products and reaction intermediates are unambiguously structurally identified by mass-selective IR-UV spectroscopy combined with quantum chemical calculations. This experiment provides evidence of the formation of larger PAHs containing up to four cyclic rings in the gas phase originating from a non-radical PAH molecule as a precursor. In addition to PAH formation, key resonance stabilized radical intermediates and intermediates containing di-acetylenic side groups are unambiguously identified in our experiment. We thereby not only reveal competing formation pathways to larger PAHs, but also identify intermediate species to PAH formation that are candidates for detection in radio-astronomy.

8.2 Introduction

Polycyclic aromatic hydrocarbons (PAHs) are considered ubiquitous carriers of carbonaceous material in the interstellar medium (ISM). They are responsible for the infrared emission features called the aromatic infrared bands[1] in the 3–20 μm region and considered promising candidates for the diffuse interstellar bands[2] that are present between about 400 and 1200 nm. In some astrophysical objects up to about 20% of carbon is estimated to be locked up by PAHs with a typical size of more than 50 carbon atoms.[3] PAHs also participate in the complex network of reactions that occurs in stellar ejecta as constituent or even catalysts, thereby affecting the overall chemical composition of star- and planet-forming regions.[3,4] If the chemistry of PAHs in relevant environments is thoroughly understood, then the PAH molecules could also act as a probe for the physical environment that surrounds them.

The exact formation mechanisms and chemistry of large PAHs in the ISM, however, are still under debate and ask for laboratory experiments under controlled conditions.[3–5] Currently, it is especially of interest to elucidate these formation mechanisms now that both large aromatic systems and a small aromatic molecule have been identified by astronomical observations in combination with laboratory spectroscopy[6–8] and it is expected that more molecule identifications will follow.

Bottom-up and top-down gas phase reaction mechanisms that lead to the formation of PAHs are both considered[1] and as of yet, the formation of larger PAHs from smaller PAHs has not been thoroughly explored in controlled conditions in a laboratory.

Therefore, exact intermediates and possible reaction steps are still unknown. The current knowledge on PAH growth is mostly based on combustion and flame experiments, where PAH growth is explained mainly by the hydrogen abstraction–acetylene addition (HACA) mechanism. However, these studies start from reactive precursors at elevated temperatures[9] and are limited to the formation of bi- and tricyclic PAHs.[10–13] In the HACA mechanism described by Frenklach et al.[14] PAHs grow in a multi-step reaction that involves acetylene. First, an aromatic radical reacts with an acetylene radical, which is followed by abstraction of molecular hydrogen. Subsequently, a second acetylene molecule is added to the ring structure followed by ring closure. Apart from the HACA mechanism, PAH growth reactions including vinylacetylene are also found to occur with extremely low activation barrier, illustrating the efficiency of two-body instead of multi-body reactions[10]. While the HACA mechanism has remained central in explaining the formation of small PAHs, both the necessary complementary reaction pathways to tricyclic PAHs and larger PAHs created under controlled conditions are still elusive.[10,12–18] In relation to astrochemistry, plasma sources have often been used to create a suitable chemically reactive environment, i.e. gas phase and cold.[19–25] For example, it was shown that polyyne and small (transient) cyclic compounds can be formed in a discharge source. These were identified using high-resolution techniques such as cavity ring-down or microwave spectroscopy and still belong to the largest carbon species detected in the ISM with the exception of fullerenes.[26]

In stellar outflows or the ISM energetic particles and photons ionize atoms and molecules, thereby inducing gas phase synthesis of larger molecules.[27,28] In our experiment, we perform ionization/radicalization and subsequently induce gas phase reactions by means of an electrical discharge. Although conditions are not analogs, reaction routes that occur in this discharge are of interest for astrochemistry as possible growth pathways for PAHs. Much is still unclear on the growth mechanisms of PAHs in these plasma environments, mainly because one has had to rely solely on mass spectrometry.[29–32] Here, we identify reaction products and intermediates through mass-selective IR-UV ion dip spectroscopy and study the reactions of PAH growth at a deeper level. This versatile approach enables us to unambiguously assign reaction products using the obtained mass-selective IR-fingerprint spectra in combination with quantum chemical calculations.[33–35] Together with the reaction products, we also identify key intermediate species that are crucial for understanding interstellar chemistry. Not only does the observation of intermediates in the reaction process aid in elucidation of the main mechanism, it also provides chemical species with a dipole moment suited for astronomical searches in radio-astronomy. This region of the electromagnetic spectrum complements the infrared regime and allows for direct comparison with telescope observations.[36,37]

8.3 Methods

All experiments were performed at the FELIX laboratory[38] in the Netherlands using a molecular beam apparatus.[39] A gas pulse consisting of naphthalene in argon (80 °C, 0.25%) is discharged at 0.55 kV and 50 mA before being expanded into a vacuum chamber using the approach of McCarthy et al.[19,20] In this approach, an isolating spacer of 6 mm is used to confine the plasma directly after discharge in order to increase the number of collisions before the expansion to create a longer reaction time. The subsequent expansion "freezes" the reaction after which the reaction mixture is probed. A current of 50 mA was found to be optimal for the formation of products. Using the Paschen curve (for γ between 0.1 and 0.2 (ref. [40]) which corresponds to a pressure between 0.37 and 0.51 mbar) and the relation between electron energy and pressure from Engel[41], the electron energy is estimated to be 3.15–3.45 eV. The rovibrational cooling was increased by changing the geometry of the discharge nozzle with respect to the design of McCarthy as shown in Figure 8.1: a compression after the discharge but before expansion in vacuum ensures a colder molecular beam (SCOOTER nozzle).

In order to achieve sufficient cooling in our molecular beam, the widely used linear discharge nozzle has been adapted. The geometry in Figure 8.1 contains the new design discharge nozzle used in our experiments: a compression zone after discharge but before expansion (Supersonic Compression Outstanding OuTflow Electrical Reactor: SCOOTER nozzle). The new design ensures better rovibrational cooling of the molecular beam. Geometry a is used to show that not having compression after discharge results in less efficient cooling (linear nozzle). The compression after discharge results in a better expansion into the vacuum chamber with respect to no compression after discharge. The compression enables a larger pressure difference upon expansion. Figure 8.2 shows the REMPI spectra resulting from using 3 different nozzle types (2 linear, 1 SCOOTER nozzle) with both the high voltage applied (red) and without the high voltage applied (orange). They are compared to the REMPI spectrum obtained using only our General Valve. The two broad features correspond to leakage of dissociation of dimer leaking into the monomer mass channel. Upon addition of any discharge nozzle, the REMPI is broadened (corresponding to less efficient cooling), where in the case of the 3 mm linear nozzle, the effect is worst. In case the discharge is turned on, only the SCOOTER nozzle shows resolvable bands at the position where originally two sharp peaks are present. This shows the SCOOTER nozzle ensures better rovibrational cooling and is therefore beneficial to our IR-UV ion dip experiments.

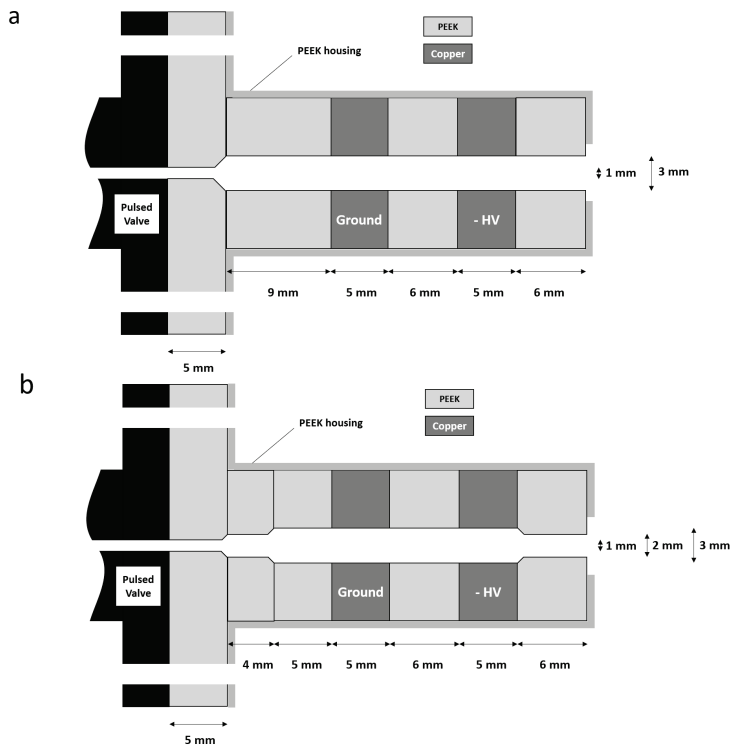

Figure 8.1: Geometry of two different discharge nozzle. The linear nozzle (a) and the SCOOTER nozzle (b).

The formed fragments, intermediates, and products in the molecular beam are probed using either [1 + 1′] resonant enhanced multiphoton ionization (REMPI) at 270 nm or non-resonant ionization by an ArF laser (193 nm) or via direct ionization using the VUV (118 nm) source.[42] Infrared spectra are recorded with IR-UV ion dip spectroscopy using the free electron laser FELIX. Ionized species are detected using a reflectron time-of-flight mass spectrometer equipped with a multichannel plate ion detector.

Initial computations for assignment are performed using the Gaussian 16 program[43] on the B3LYP/6-31+G* level of theory.[44,45] Second, in order to simulate the anharmonic 1210 cm^{-1} band in spectra of the molecules in Figure 8.4 the option anharmonic is used with the Jun-cc-pVDZ basis set[46] (i.e. for the spectra of buta-1,3-diyn-1-ylbenzene; 1-(buta-1,3-diyn-1-yl)-2-ethynylbenzene, 1-(buta-1,3-diyn-1-yl)-3-ethynylbenzene, and 1,2,3-triethynylbenzene; 1- and 2-ethynylnaphthalene and 1- and 2-(buta-1,3-diyn-1-yl)naphthalene). However, since the perturbation treatment leads to large and unwanted shifts in the fundamental frequencies of bands especially between 500 and 1000 cm^{-1}, the derivatives with respect to these normal modes are selectively removed. All IR spectra are scaled with an appropriate scaling factor (0.96 for the Jun-

cc-pVDZ and 0.976 for 6–31+G*) and convoluted with 1% of the photon energy to match the FELIX bandwidth.

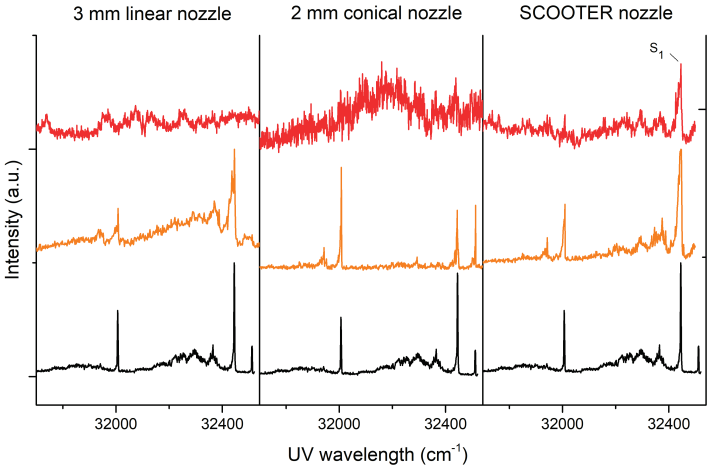

Figure 8.2: UV spectra of naphthalene showing approximate temperature of molecular beam for three nozzle geometries. The black trace is made without nozzle, the orange trace with nozzle but no discharge, the red trace is with running discharge nozzle. The SCOOTER nozzle yields the lowest rovibrational temperature of our molecular beam after discharge compared to the 2 and 3 mm linear nozzles. 2.5 bar He backing pressure is used for all three REMPI spectra.

8.4 Results

8.4.1 Detection of products

Figure 8.3a displays a typical mass spectrum of the discharge of naphthalene probed via $1 + 1'$ REMPI spectroscopy, where the first photon is resonant with an unresolved vibronic band of an electronic state of the formed molecules. The parent signal ($m/z = 128$) is truncated to visualize the lower intensity signals. Fragmentation of the parent (naphthalene) results in fragments with $m/z < 128$, whereas reaction products are observed with $m/z > 128$. The REMPI scheme is required to probe IR absorption which leads to depopulation of molecules that are prepared in the ground state, thereby recording mass-selective IR-UV ion dip spectra.[47] The high-intensity mass channels in the $1 + 1'$ REMPI mass spectrum are probed using the IR-UV ion dip technique. Note that the observed intensity does not directly reflect relative abundance since excitation and ionization cross-sections vary between different species. Figure 8.3b shows the mass spectrum recorded via non-resonant ionization with either 193 nm (produced with ArF excimer laser) or ionization with higher energy photons of 118 nm VUV (produced using an Xe

HHG cell). In general, larger molecules are ionized more readily using 193 nm UV light while smaller species are more prone to ionization by the 118 nm VUV light.[42] By monitoring relative ion signals of products, photodissociation using the non-resonant ionization techniques is avoided. The non-resonant ionization allows for the ionization of species with up to $m/z = 326$. Doubly ionized species are not expected with photoionization, thus the m/z value reflects the mass of species created. In addition to the photoionization mass spectra we have obtained a mass spectrum of the cations produced in the electrical discharge (see ref [48]). The cationic mass spectrum provides a good reference for relative abundancies of the different products that are produced with no chance of photofragmentation.

The lower mass fragments from naphthalene ($m/z < 128$) after discharge consist mostly of carbon atoms with only a few hydrogen atoms. Similar masses are previously observed by Linnartz and co-workers over the years.[21–23,49,50] Typical examples of formed fragments and low mass products are C_3 ($m/z = 36$), C_4H_2 ($m/z = 50$), C_5H ($m/z = 61$), C_6H_2 ($m/z = 74$), and C_8H_2 ($m/z = 98$). These result typically from the discharge of a mixture containing acetylene (C_2H_2, $m/z = 26$) and argon. However, the main neutral small fragment that is produced in our experiment is observed at $m/z = 50$, which most probably corresponds to diacetylene (C_4H_2). As will be shown in this work, the formation of diacetylene seems to be a key ingredient and an important contributor to PAH formation. This is in contrast to what was previously considered, as the current HACA mechanism describes the addition of mono-acetylene units. Diacetylene is already proposed to be a potential competitor for radical pathways to form large hydrocarbons[51] and C_4H_2 has been detected in Titan's atmosphere[52] and the ISM[7]. For the molecules with masses larger than the parent molecule naphthalene ($m/z > 128$), only the chemical composition may be determined from the m/z values. The chemical structures cannot be deduced from the m/z value alone and spectroscopic information is required to ascertain the molecular formulae and/or structures. For example, the addition of two mono-acetylene functional groups to the precursor naphthalene would result in the same mass as if one diacetylene unit would be attached. In a similar fashion, the formation of acenaphthylene cannot be distinguished from ethynylnaphthalene as both reaction products would have an m/z of 152.

8.4.2 Structure identification of substituted PAHs

Where the chemical formula of small species can be deduced from their mass, spectroscopic experiments are necessary in order to elucidate the chemical formulae and structures of the products of naphthalene ($m/z > 128$). Using non-resonant ionization we are able to observe PAH formation up to $m/z = 326$, which would correspond to PAHs

containing seven cyclic rings. In order to assign the molecular structures of the masses indicated in green in Figure 8.3a, we rely on the combination of mass-selective IR spectroscopy in the fingerprint region (600–1800 cm^{-1}) and quantum chemical calculations to assign the experimental IR spectra.[53]

By comparison of theoretically calculated IR spectra of multiple possible isomers to experimental spectra we are able to assign the reaction products with $m/z = 126$ to (a) buta-1,3-diyn-1-ylbenzene (diacetylenebenzene); $m/z = 150$ to (b) 1-(buta-1,3-diyn-1-yl)-2-ethynylbenzene, 1-(buta-1,3-diyn-1-yl)-3-ethynylbenzene, and 1,2,3-triethynylbenzene; $m/z = 152$ to (c) 1- and 2-ethynylnaphthalene (1EN and 2EN); $m/z = 154$ to (d) 1- and 2-ethenylnaphthalene; and $m/z = 176$ to (e) 1- and 2-(buta-1,3-diyn-1-yl)naphthalene as displayed in Figure 8.4. In order to assign these observed masses, we have calculated a variety of IR spectra originating from possible isomers that coincide with the observed mass. The unambiguous structural identification shows both the accuracy as well as suitability of mass-selective IR spectroscopy in determining discharge reaction products. Certainly as important as assigning reaction products, some species can be discarded based on a mismatch between the experimental and calculated IR spectra. For several product mass channels, multiple constitutional (structural) isomers are computed and their IR spectra are combined in order to match the observed IR spectra. For example, the calculated IR spectra of 1-ethynylnaphthalene and 2-ethynylnaphthalene (1EN and 2EN respectively) are summed in a ratio that will match the intensities observed in the experimental spectra as shown in Figure 8.4c. Spectral dissimilarity indicates that acenaphthylene can be discarded based on the mismatch between the calculated and experimental IR spectrum.

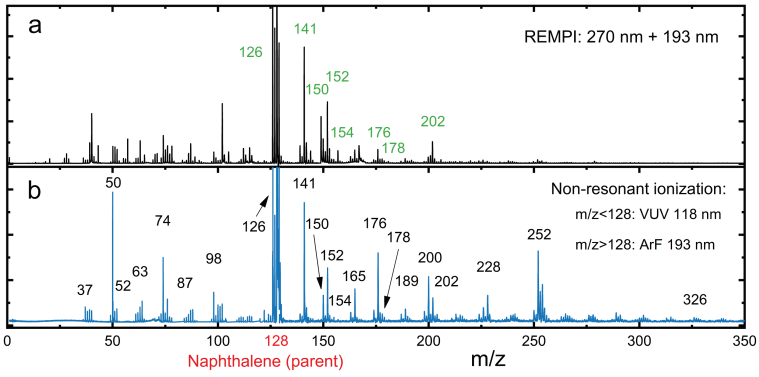

Figure 8.3: Mass spectra of products and fragments from naphthalene formed in electrical discharge. Trace **a** is recorded with two-color REMPI during our IR-UV ion dip measurements. Products that are assigned to a molecular structure are labeled with their masses in green, see Figs. 8.4 and 8.5. Trace **b** is taken using 118 nm VUV for the region below $m/z = 128$ and 193 nm UV for the region above $m/z = 128$. The $m/z = 326$ would correspond to a formed cyclic structure containing seven aromatic rings.

Overall, an excellent agreement between theoretical and experimental IR spectra is found. The IR region between 550 and 1000 cm^{-1} of the vibrational spectrum is most important, since both the highest intensity and most diagnostic bands can be found here. This region is often sufficient to assign a calculated spectrum of a particular molecular structure to the experimental spectrum. The bands around 600 cm^{-1} arise from ≡CH deformation, present in Figure 8.4a–c, e. Around 800 cm^{-1} the CH out-of-plane of aromatic rings are found. The small deviations between experimental frequencies and theoretical frequencies as shown in the inset of Figure 8.4a below about 700 cm^{-1} are common and usually corrected for by using multiple scaling factors.[54] A notable feature in the remaining part of the experimental IR spectra arises from reaction products that contain a ≡CH group. For these molecules an intense band at 1210 cm^{-1} is observed, which is predicted using anharmonic theory (e.g. in Figure 8.4a). This peak is the result of an overtone arising from the ≡CH deformation as is known in literature[55–57] and shown by anharmonic calculations and by gas phase FT-IR spectra of reference compounds by ourselves and Constantinidis et al.[58] In order to cement the assignment of structures presented in Figure 8.4, we have compared the reference gas phase FT-IR spectra of 1EN and 2EN, i.e. the assigned compounds presented in Figure 8.4c, with $m/z = 152$ (see blue trace in Figure 8.4c). Excellent agreement between the reference compound FT-IR spectra of 1EN and 2EN and the IR-UV ion dip spectrum of $m/z = 152$ recorded after the discharge of naphthalene is observed for the diagnostic region between 550 and 1000 cm^{-1} as well as the anharmonic band at 1210 cm^{-1}. The peak at 1210 cm^{-1} appears in all experimental spectra where, based on the 550–1000 cm^{-1} region, ethynyl functional groups are expected (Figure 8.4a–c, e). In contrast, the experimental IR spectrum presented in Figure 8.4d assigned to ethenylnaphthalene does not show this peak at 1210 cm^{-1}. The intense band at 1210 cm^{-1} can act as a diagnostic tool for the identification of ≡CH containing structures. Moreover, this is a clear demonstration of how anharmonicity influences not only the mid-IR spectra of PAHs[59] but also the IR spectra of PAH substituents and PAH growth intermediates.

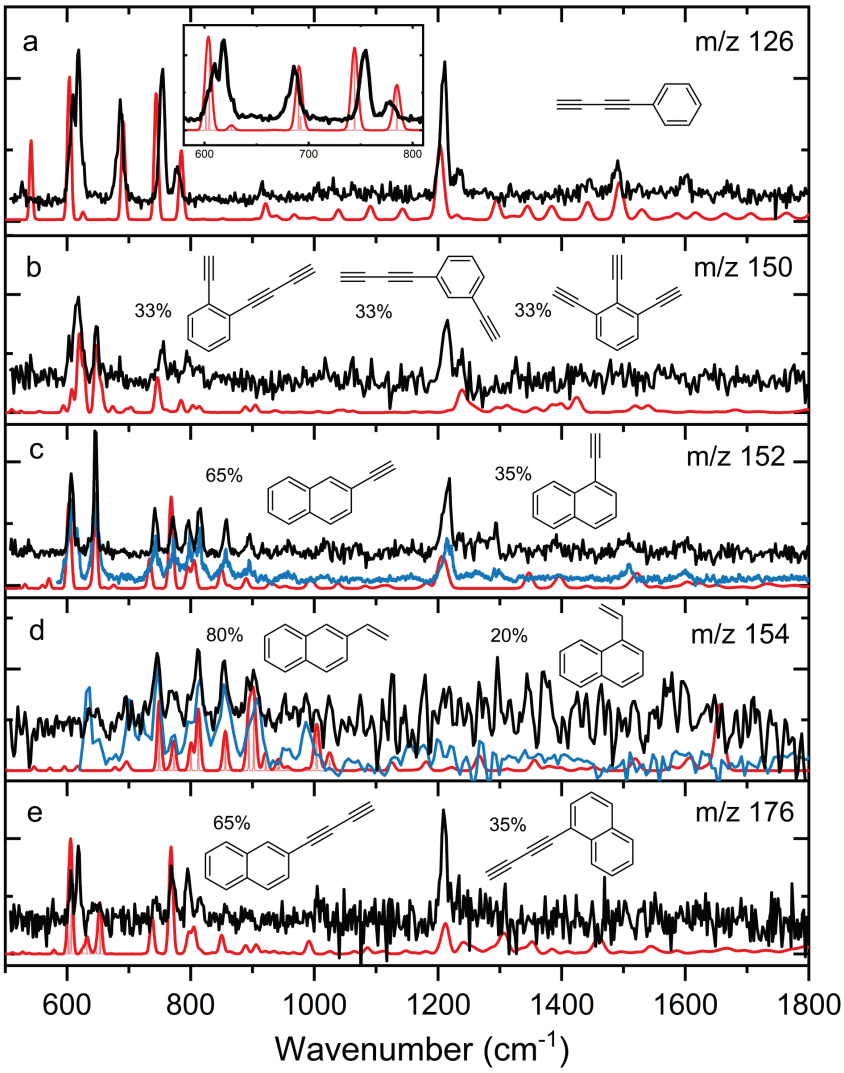

Figure 8.4: Mass selected IR spectra (black) of discharge products with the assigned theoretical IR spectra (red). The mass channels shown are m/z= **a** 126, **b** 150, **c** 152, **d** 154, and **e** 176 and are recorded using 36616 cm^{-1} UV photon energy. The molecules assigned are **a** buta-1,3-diyn-1-ylbenzene (diacetylenebenzene); **b** 1-(buta-1,3-diyn-1-yl)-2-ethynylbenzene, 1-(buta-1,3-diyn-1-yl)-3-ethynylbenzene, and 1,2,3-triethynylbenzene; **c** 1- and 2-ethynylnaphthalene (1EN and 2EN); **d** 1- and 2-ethenylnaphthalene; and **e** 1- and 2-(buta-1,3-diyn-1-yl)naphthalene. For **b**–**e**, two or more theoretical IR spectra of structural isomers are used to fit the experiment allowing for the determination of the ratio between the formed isomers. The blue trace in the m/z 152 box corresponds to an FT-IR reference spectrum taken from 1EN and 2EN combined with a 1:2 ratio, respectively. The blue trace in the m/z 154 box corresponds to an FT-IR reference spectrum taken from 1- and 2-vinylnaphthalene combined with a 1:4 ratio, respectively. The light red traces correspond to stick spectra to display adjacent peaks.

8.4.3 Identification of larger PAHs

Besides the substituted PAHs, we are also able to identify fully cyclic structures that are larger than the original PAH naphthalene, see Figure 8.5. The top panel of Figure 8.5 shows the two color [1 + 1′] UV excitation spectrum obtained for $m/z = 178$, which can be assigned to phenanthrene by comparing this REMPI UV spectrum to a previously reported spectrum of phenanthrene.[60] Similarly to our IR spectra, high-resolution REMPI spectra also provide a unique fingerprint of a molecule and especially together with the mass of an unknown species, a few transitions are sufficient for spectroscopic assignment. The obtained UV spectrum after discharge is somewhat broader than the literature spectrum[60] due to thermal-broadening; however, the S_2 origin as well as the first few vibronic bands are clearly observed. We hereby simultaneously show that we can use UV ion spectroscopy to identify molecules created in a discharge and that larger PAHs are formed in an electrical discharge.

Two additional fully cyclic compounds are identified using mass-selective IR-UV ion dip spectroscopy, namely the benzo[7]annulene radical and pyrene (with $m/z = 141$ and 202, respectively), see Figure 8.5b,c. For both the assignment of benzo[7]annulene and pyrene, the 550–1000 cm^{-1} IR region is most diagnostic and excellent agreement between theoretical and experimental spectra is observed. Methyl-radical addition to the parent naphthalene leading to species with $m/z = 141$ is excluded based on the comparison between the experimental spectrum and calculated spectra (not shown here). The anti-symmetric CH out-of plane mode with a frequency of 670 cm^{-1} is the most diagnostic mode, which is clearly present in the calculated IR spectrum of benzo[7]annulene, but absent in the calculated spectra of methyl-radical containing compounds.

8.5 Discussion

In general, two types of PAHs are formed from the discharge of naphthalene, namely larger PAHs and polyyne substituted PAHs. From the latter, the most remarkable of the identified structures presented in Figure 8.4 are the diacetylene side chains. The HACA mechanism described by Frenklach et al.[14] and Visser et al.[61], which is currently considered the main reaction pathway, does involve the addition of acetylenic side chains to PAH but lacks intermediates with diacetylene side groups. Here we show that using only naphthalene as a precursor, PAHs grow via the addition of radical diacetylenic side chains, see Figure 8.6. Based on the observed IR signatures in combination with the calculated IR spectra, single acetylene side group addition was excluded for the $m/z = 126$ and 176 channels (not shown here). Instead, diacetylene

moieties are attached to the PAH ring. The formation mechanism of radical diacetylene is not precisely known, although we propose that it originates from the most abundant fragment, diacetylenebenzene (m/z = 126). As shown in Figure 8.6a, opening of one of the naphthalene rings upon electrical discharge forms buta-1,3-diyn-1-ylbenzene (diacetylenebenzene) (m/z = 126), and subsequent dissociation of the diacetylene side group of the naphthalene precursor results in free diacetylene radicals. Radical diacetylene can attach to the naphthalene parent molecule, as shown in Figure 8.6b, forming the diacetylene–naphthalene isomeric structures (m/z = 176). In the reaction region of our discharge nozzle, the created radicals have ample opportunity to react with the abundant parent molecules that are not fragmented in the plasma zone. We do expect radical-neutral reaction pathways involving the diacetylene radical, since these are more favorable as shown by calculations.

Besides acetylenic moieties, the addition of a vinyl side group is observed in lower quantities. This corresponds well with the minor reaction pathway to PAHs as described by Brittner and Howard.[62] Butadiynyl-ethynylbenzene, the product with m/z = 150, is thought to be the result of ring opening of 1EN and 2EN (m/z = 152). This confirms our assignment of m/z = 152 to ethynylnapthalene, as ring opening would indeed result in m/z = 150. The formation of acenaphthylene (m/z = 152) can be excluded, this is notably different to pyrolysis experiments where acenaphthylene is one of the most ubiquitous combustion effluents.[61] The reaction mechanisms presented here and illustrated in Figure 8.6a, b show key intermediates and their reaction pathways to the formation of larger PAHs in a plasma containing only naphthalene as a precursor.

The larger, three-membered ring PAH, phenanthrene, is most likely formed by ring closure of the identified compound diacetylene–naphthalene (m/z = 176) after hydrogenation as shown in Figure 8.6c. The four-membered ring PAH pyrene (m/z = 202), which is identified and characterized as well, is believed to be formed by a similar mechanism from phenanthrene via acetylene addition followed by ring closing as the formation of phenanthrene itself. Although we did not find intermediates (e.g. phenanthrene with acetylene side-chain) in our experiment, pyrolysis experiments do point in this direction.[61,63] Unfortunately, ethynyl phenanthrene (phenanthrene with an acetylene side-chain) has the same m/z = as pyrene itself. However, one would expect to observe the anharmonic peak at 1210 cm^{-1} if traces of this intermediate species would be still present after supersonic cooling of the discharged mixture, thus on this basis of the absence of the 1210 cm^{-1} peak we exclude the ethynyl phenanthrene species.

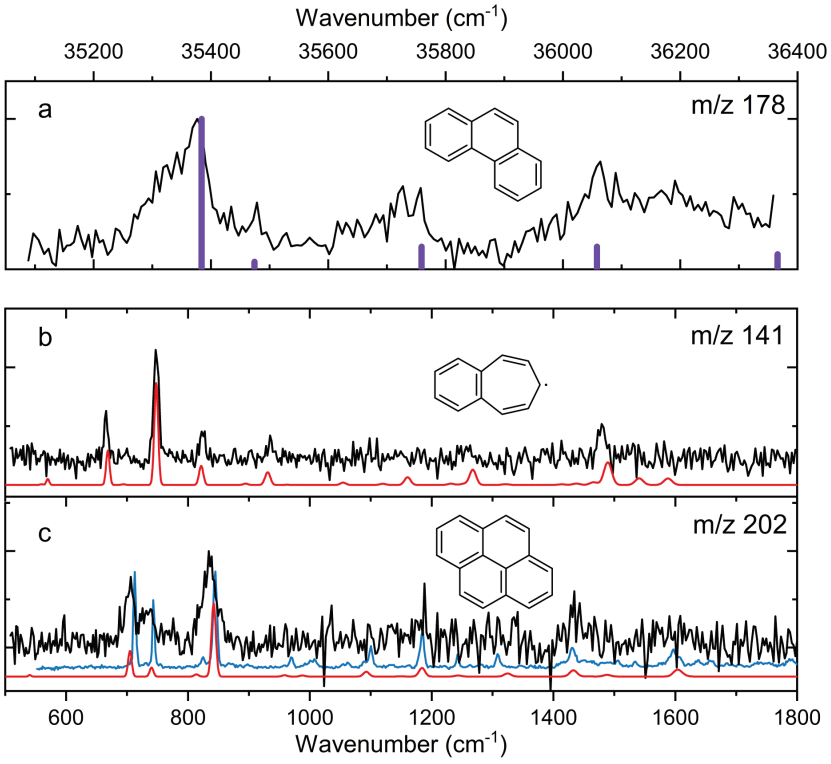

Figure 8.5: Assignment of larger PAHs formed in the discharge using REMPI and IR ion dip spectroscopy. **a** Experimental REMPI spectrum of the $m/z = 178$ channel (black) with literature values of the spectrum of phenanthrene[28] (mass 178 amu) as reference (violet). **b**, **c** Experimental IR-UV ion dip spectra recorded using 36616 cm^{-1} UV photon energy (black). Theoretical spectra of the assigned molecular structures displayed in red: benzo[7]annulene radical for $m/z = 141$ and pyrene for $m/z = 202$. The IR-UV ion dip spectrum of reference compound pyrene is in blue and was recorded using the methods described in ref. [64].

The peak at $m/z = 141$ has been unambiguously assigned to the resonance stabilized radical benzo[7]annulene. However, no measurable intermediates are identified in our experiment, hence its formation pathways remain uncertain. Possibly the benzo[7]annulene radical is formed via cyclopropanaphthalene, which is known to be able to react to annulene species.[65–67] Johansson et al.[68] stress the importance of resonance stabilized radicals in the growth process of PAHs and soot particles in combustion. Our observation and characterization of the benzo[7]annulene radical substantiates these conclusions. All the intermediate species presented in Figure 8.4 and the benzo[7]annulene have significant dipole moments of up to about 2 Debye and are therefore potential candidates for microwave studies such as the one performed by Lee and co-workers[69] and radio-astronomy searches. Up to now, no RSRs have been observed in the ISM and the benzo[7]annulene radical would a promising candidate.[70]

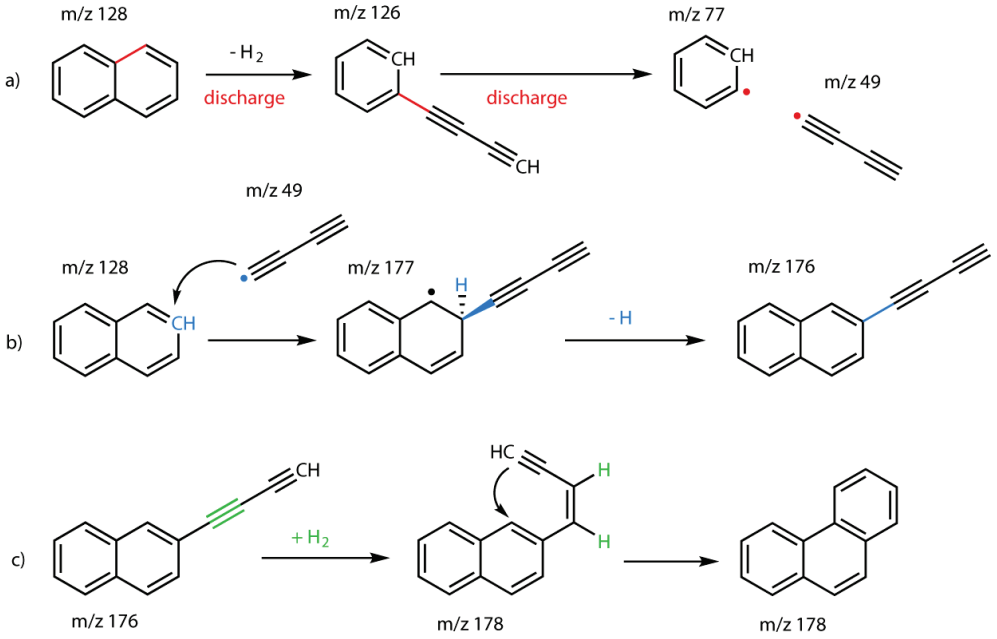

Figure 8.6: Proposed reaction mechanism of the formation of phenanthrene and intermediates. **a** Reaction mechanism of the formation and subsequent fragmentation of diacetylenebenzene ($m/z = 126$). **b** The diacetylene that is created in step **a** can further react to form diacetylene–naphthalene ($m/z = 176$) which is a likely precursor for the formation of phenanthrene (**c**).

8.6 Conclusions

In summary, our experiments identify additional reaction pathways for the interstellar chemistry of PAHs. In particular, the chemistry of one of the smallest PAHs, naphthalene, in an electrical discharge, is elucidated by unambiguously assigning reaction products by mass-selective IR-UV ion dip spectroscopy. Growth of naphthalene is observed resulting in the formation of phenanthrene and pyrene, compact 3- and 4-ring PAHs, respectively. Most of the identified intermediates contain acetylene and diacetylene side chains, thereby providing alternatives to the HACA mechanism by Frenklach in which up to now, the growth of PAHs was described via the addition of mono-acetylenic side chains. Our experiments demonstrate that (radical) diacetylene addition has to be taken into account in PAH growth models. Moreover, the identified intermediates also include a resonance stabilized radical which has only recently been put forward as crucial intermediate to promote low barrier reactions.[68] Finally, the identified substituted PAHs and PAH

radicals have significant dipole moments and are ideal candidates for radio-astronomy searches.

References

1 A. G. G. M. Tielens, *Astrochem. Astrobiol.*, 2013, **85**, 35–72.
2 W. W. Duley, *Faraday Discuss.*, 2006, **133**, 415–425.
3 A. G. G. M. Tielens, *Annu. Rev. Astron. Astrophys*, 2008, **46**, 289–337.
4 E. Herbst, *Astrochemistry and Star Formation : Successes and Challenges 1 Introduction: The Science of Astrochemistry*, WILEY-VCH, Weinheim, 2006.
5 H. Andrews, C. Boersma, M. W. Werner, J. Livingston, L. J. Allamandola and A. G. G. M. Tielens, *Astrophys. J.*, 2015, 807, 24pp.
6 E. K. Campbell, M. Holz, D. Gerlich and J. P. Maier, *Nature*, 2015, **523**, 322–323.
7 J. Cernicharo, A. M. Heras, A. G. G. M. Tielens, J. R. Pardo, F. Herpin, M. Guélin and L. B. F. M. Waters, *Astrophys. J.*, 2001, **546**, L123:L126.
8 B. A. Mcguire, A. M. Burkhardt, S. Kalenskii, C. N. Shingledecker, A. J. Remijan, E. Herbst and M. C. Mccarthy, *Science*, 2018, **359**, 202–205.
9 L. Zhao, R. I. Kaiser, B. Xu, U. Ablikim, W. Lu, M. Ahmed, M. M. Evseev, E. K. Bashkirov, V. N. Azyazov, M. V. Zagidullin, A. N. Morozov, A. H. Howlader, S. F. Wnuk, A. M. Mebel, D. Joshi, G. Veber and F. R. Fischer, *Nat. Commun.*, 2019, **10**, 1510.
10 L. Zhao, R. I. Kaiser, B. Xu, U. Ablikim, M. Ahmed, M. M. Evseev, E. K. Bashkirov, V. N. Azyazov and A. M. Mebel, *Nat. Astron.*, 2018, **2**, 973–979.
11 D. S. N. Parker, R. I. Kaiser, T. P. Troy and M. Ahmed, *Angew. Chemie - Int. Ed.*, 2014, **53**, 7740–7744.
12 T. Yang, R. I. Kaiser, T. P. Troy, B. Xu, O. Kostko, M. Ahmed, A. M. Mebel, M. V. Zagidullin and V. N. Azyazov, *Angew. Chemie - Int. Ed.*, 2017, **56**, 4515–4519.
13 T. Yang, T. P. Troy, B. Xu, O. Kostko, M. Ahmed, A. M. Mebel and R. I. Kaiser, *Angew. Chemie - Int. Ed.*, 2016, **55**, 14983–14987.
14 M. Frenklach, A. D. D. W. Clary and S. E. Stein, in *Twentieth Symposium (International) on Combustion/The Combustion Institute*, 1984, pp. 887–901.
15 I. Cherchneff, J. R. Barker and A. G. G. M. Tielens, *Astrophys. J.*, 1992, **401**, 269–287.
16 P. Constantinidis, H.-C. Schmitt, I. Fischer, B. Yan and A. M. Rijs, *Phys. Chem. Chem. Phys.*, 2015, **17**, 29064–29071.
17 Y. Carpentier, T. Pino and P. Bréchignac, *J. Phys. Chem. A*, 2013, **117**, 10092–10104.
18 N. Hansen, M. Schenk, K. Moshammer and K. Kohse-Höinghaus, *Combust. Flame*, 2017, **180**, 250–261.

19 M. C. McCarthy, M. J. Travers, A. Kovacs, C. A. Gottlieb and P. Thaddeus, *Astrophys. J. Suppl. Ser.*, 1997, **113**, 105–120.
20 M. C. McCarthy, W. Chen, M. J. Travers and P. Thaddeus, *Astrophys. J. Suppl. Ser.*, 2000, **129**, 611–623.
21 T. Motylewski and H. Linnartz, *Rev. Sci. Instrum.*, 1999, **70**, 1305–1312.
22 H. Linnartz, T. Motylewski and J. P. Maier, *J. Chem. Phys.*, 1998, **109**, 3819–3823.
23 T. Motylewski, O. Vaizert, T. F. Giesen, H. Linnartz and J. P. Maier, *J. Chem. Phys.*, 1999, **111**, 6161–6163.
24 P. Ehrenfreund and M. A. Sephton, *Faraday Discuss.*, 2006, **133**, 277–288.
25 C. S. Contreras and F. Salama, *Astrophys. Journal, Suppl. Ser.*, 2013, 208, 17pp.
26 H. S. P. Müller, S. Thorwirth, D. A. Roth and W. S. Winnewisser, *Astron. Astrophys.*, 2001, **370**, L49–L52.
27 N. Indriolo and B. J. Mc Call, *Chem. Soc. Rev.*, 2013, **42**, 7763–7773.
28 A. G. G. M. Tielens, M. M. Meixner, P. P. van der Werf, J. Bregman, J. A. Tauber, J. Stutzki and D. Rank, *Science*, 1993, **262**, 86–89.
29 M. Alliati, D. Donaghy, X. Tu and J. W. Bradley, *J. Phys. Chem. A*, 2019, **123**, 2107–2113.
30 D. L. Hobrock and R. W. Kiser, *J. Phys. Chem.*, 1964, **68**, 575–579.
31 X. Gillon and L. Houssiau, *Plasma Sources Sci. Technol.*, 2014, 23, 45010.
32 B. West, C. Joblin, V. Blanchet, A. Bodi, B. Sztáray and P. M. Mayer, *J. Phys. Chem. A*, 2012, **116**, 10999–11007.
33 J. Martens, J. Grzetic, G. Berden and J. Oomens, *Nat. Commun.*, 2016, **7**, 11754.
34 J. Martens, G. Berden, R. E. Van Outersterp, L. A. J. Kluijtmans, F. Udo, C. D. M. Van Karnebeek, R. A. Wevers and J. Oomens, *Sci. Rep.*, 2017, **7**, 3363.
35 J. Bouwman, A. J. De Haas and J. Oomens, *Chem. Commun.*, 2016, **52**, 2636–2638.
36 L. J. Allamandola, A. G. G. M. Tielens and J. R. Barker, *Astrophys. J. Suppl. Ser.*, 1989, **71**, 733–775.
37 K. Sellgren, *Astrophys. J.*, 1984, **277**, 623–633.
38 D. Oepts, A. F. G. Van, D. Meer and P. W. Van Amersfoort, *Infrared Phys. Technol.*, 1995, **36**, 297–308.
39 A. M. Rijs, M. Kabeláč, A. Abo-Riziq, P. Hobza and M. S. De Vries, *ChemPhysChem*, 2011, **12**, 1816–1821.
40 M. A. Lieberman and A. J. Lichtenberg, *Principles of Plasma Discharges and Materials Processing*, John Wiley & Sons, Inc., Hoboken, NJ, USA, 2005.
41 A. Von Engel, *Ionized gases*, American Institute of Physics, New York, 1994.
42 V. Yatsyna, D. J. Bakker, P. Salén, R. Feifel, A. M. Rijs and V. Zhaunerchyk, *Phys. Rev. Lett.*, 2016, **117**, 118101.
43 M. J. Frisch, G. W. Trucks, H. B. Schlegel, G. E. Scuseria, M. A. Robb, J. R. Cheeseman, G. Scalmani, V. Barone, G. A. Petersson, H. Nakatsuji, X. Li, M.

Caricato, A. V. Marenich, J. Bloino, B. G. Janesko, R. Gomperts, B. Mennucci, H. P. Hratchian, J. V. Ortiz, A. F. Izmaylov, J. L. Sonnenberg, D. Williams-Young, F. Ding, F. Lipparini, F. Egidi, J. Goings, B. Peng, A. Petrone, T. Henderson, D. Ranasinghe, V. G. Zakrzewski, J. Gao, N. Rega, G. Zheng, W. Liang, M. Hada, M. Ehara, K. Toyota, R. Fukuda, J. Hasegawa, M. Ishida, T. Nakajima, Y. Honda, O. Kitao, H. Nakai, T. Vreven, K. Throssell, J. Montgomery, J. A., J. E. Peralta, F. Ogliaro, M. J. Bearpark, J. J. Heyd, E. N. Brothers, K. N. Kudin, V. N. Staroverov, T. A. Keith, R. Kobayashi, J. Normand, K. Raghavachari, A. P. Rendell, J. C. Burant, S. S. Iyengar, J. Tomasi, M. Cossi, J. M. Millam, M. Klene, C. Adamo, R. Cammi, J. W. Ochterski, R. L. Martin, K. Morokuma, O. Farkas, J. B. Foresman and D. J. Fox, *Gaussian, Inc., Wallingford CT*.

44 A. D. Becke, *J. Chem. Phys.*, 1993, **98**, 5648–5652.

45 C. Lee, W. Yang and R. G. Parr, *Phys. Rev. B*, 1988, **37**, 785–789.

46 E. G. Hohenstein and C. D. Sherrill, *J. Chem. Phys*, 2010, **132**, 184111.

47 A. M. Rijs and J. Oomens, *Top. Curr. Chem.*, 2015, **364**, 1–42.

48 A. K. Lemmens, D. B. Rap, J. M. M. Thunnissen, B. Willemsen and A. M. Rijs, *Nat. Commun.*, 2020, **11**, 1–7.

49 H. Linnartz, T. Motylewski, F. Maiwald, D. a. Roth, F. Lewen, I. Pak and G. Winnewisser, *Chem. Phys. Lett.*, 1998, **292**, 188–192.

50 M. A. Haddad, D. Zhao, H. Linnartz and W. Ubachs, *Chinese J. Chem. Phys.*, 2012, **25**, 129–134.

51 T. S. Zwier and M. Allen, *Icarus*, 1996, **123**, 578–583.

52 V. G. Kunde, A. C. Aikin, R. A. Hanel, D. E. Jennings, W. C. Maguire and R. E. Samuelson, *Nature*, 1981, 292, 686–688.

53 F. Hirsch, P. Constantinidis, I. Fischer, S. Bakels and A. M. Rijs, *Chem. A Eur. J.*, 2018, **24**, 7647–7652.

54 C. W. Bauschlicher, A. Ricca, C. Boersma and L. J. Allamandola, *Astrophys. J. Suppl. Ser.*, 2018, **234**, 32.

55 L. J. Bellamy, *The Infra-red Spectra of Complex Molecules*, Chapman and Hall, London, 1975.

56 J. C. Evans and R. A. Nyquist, *Spectrochim. Acta*, 1963, **19**, 1153–1163.

57 R. A. Nyquist and W. J. Potts, *Spectrochim. Acta*, 1960, **16**, 419–427.

58 P. Constantinidis, F. Hirsch, I. Fischer, A. Dey and A. M. Rijs, *J. Phys. Chem. A*, 2017, **121**, 181–191.

59 A. Candian and C. J. Mackie, *Int. J. Quantum Chem.*, 2017, **117**, 146–150.

60 A. Amirav, M. Sonnenschein and J. Jortner, *J. Phys. Chem.*, 1984, **88**, 5593–5596.

61 T. Visser, M. Sarobe, L. W. Jenneskens and J. W. Wesseling, *Fuel*, 1998, **77**, 913–920.

62 J. D. Bittner and J. B. Howard, in *Eighteenth Symposium (International) on Combustion*, 1981, pp. 1105–1116.

63 B. Shukla and M. Koshi, *Phys. Chem. Chem. Phys.*, 2010, **12**, 2427–2437.
64 A. K. Lemmens, D. B. Rap, J. M. M. Thunnissen, C. J. Mackie, A. Candian, A. G. G. M. Tielens, A. M. Rijs and W. J. Buma, *Astron. Astrophys.*, 2019, **628**, A130.
65 B. Halton, C. S. Jones, A. J. Kay, D. Margetic and S. Sretenovic, *J. Chem. Soc., Perkin Trans*, 2000, **1**, 2205–2210.
66 L. He, W. Shen and M. Sulkes, *Chem. Phys. Lett.*, 2009, **471**, 210–215.
67 C. Lifshitz, *Acc. Chem. Res.*, 1994, **27**, 138–144.
68 K. O. Johansson, M. P. Head-Gordon, P. E. Schrader, K. R. Wilson and H. A. Michelsen, *Science*, 2018, **361**, 997–1000.
69 K. L. K. Lee and M. McCarthy, *J. Phys. Chem. Lett.*, 2019, **10**, 2408–2413.
70 T. W. Schmidt, *Int. Rev. Phys. Chem.*, 2016, **35**, 209–242.

Chapter 9

The complex network of PAH formation pathways revealed in a benzene discharge

9.1 Abstract

Infrared signatures of polycyclic aromatic hydrocarbons (PAHs) are detected towards planet-forming disks, dark molecular clouds and the general diffuse interstellar medium (ISM). Due to their stability, PAHs are expected to be a major player in the carbon chemistry of the ISM, forming the connection between small hydrocarbons and large fullerenes. However, as details on the formation and dissociation of PAHs in these environments are still unclear, modeling their abundance and chemistry has remained far from trivial. Here, we study and determine in unprecedented detail the complex chemistry of the aromatic molecule benzene under isolated conditions in an electrical discharge. By combining molecular beam techniques with mass-selective IR spectroscopy in the fingerprint region and quantum chemically predicted IR absorption spectra, we assign the most prominent products formed in the discharge to specific molecular structures, including larger PAHs, radicals and intermediates. This allow us to identify multiple reactions leading to PAH growth that occur simultaneously and competitively, revealing the complex and interconnected network of PAH formation pathways. Supported by quantum chemical calculations, the results of this study point towards key exothermic reaction schemes that need to be included in astrochemical models describing the carbon chemistry in our universe.

9.2 Introduction

The interstellar medium (ISM) can be considered as the repository of stellar and planetary matter. It contains the remains of previous stars and molecules that are continuously processed under widely varying conditions, such as temperature, density and external radiation (photons and cosmic rays) from stars and supernovae. More dense regions of the ISM can become gravitationally instable and collapse to form new stars and planets[1]. Within all these phases of the ISM (including planet-forming disks, surfaces of dark clouds and the diffuse ISM), infrared and microwave signatures of polycyclic aromatic hydrocarbons (PAHs) have been detected.[2–11] The stability of the aromatic forms of hydrocarbons makes PAHs important carriers of organic matter. The evolution of PAHs in the ISM and their contribution to interstellar chemistry as constituents or catalysts is an important aspect of astrochemistry. They are expected to form a connection between small (aromatic) molecules such as benzene and benzonitrile and larger molecules such as fullerenes, both classes having been detected in the ISM.[12,13]

Pyrolysis and crossed molecular beam studies have made major contributions towards understanding gas-phase formation pathways of PAHs.[14–16] However, the

complexity of the interconnected chemical pathways resulting in PAH formation and dissociation is still difficult to account for in astrochemical models.[17–19] This generally leads to an underestimation of aromatic species in the ISM[20,21] or in pyrolysis experiments.[22] Identifying and mapping the bottom-up and top-down pathways of interstellar PAH formation and processing under the influence of UV photons[23], cosmic rays[24], or secondary electrons[25] is key to improve our understanding of interstellar chemistry.[26]

Individual PAH growth reaction pathways that have been identified in crossed molecular beam or pyrolysis experiments (Figure 9.1), generally start with the formation of a radical by hydrogen abstraction. In contrast to hotter environments such as circumstellar envelopes (CSE), UV radiation is expected to be responsible for the hydrogen abstraction in the cold ISM.[27–29] A phenyl radical (possibly as a part of a larger PAH) then reacts with a neutral hydrocarbon, which can be a small unsaturated hydrocarbon such as (mono-/di-/tri-/vinyl-)acetylene. This addition is followed by a cyclization step and together generally classified as the hydrogen-abstraction acetylene-addition (HACA, Figure 9.1a) mechanism.[30–40] The phenyl radical can also form a covalent bond with another aromatic ring resulting in biphenyl-type molecules, which is described by the phenyl addition cyclization (PAC, Figure 9.1b) mechanism.[36,38,41,42] Other mechanisms that have been identified and suggested as possible routes in the complex network of PAH formation pathways involve small radical hydrocarbons. These include the ethynyl ($\bullet C_2H$) addition mechanism (EAM, Figure 9.1e)[43], the ring expansion mechanism with methylidyne ($\bullet CH$)[44–48], (Figure 9.1c), and the methylidyne addition–cyclization–aromatization (MACA, Figure 9.1d) mechanism.[16] Fast and successive radical-radical reactions have recently been added to the collection of possible reaction mechanisms.[49–51]

In the ISM, energetic particles or photons initiate gas phase chemistry by hydrogen abstraction.[23–25,52] In our experiment, radicalization and fragmentation is realized by free electrons in an electrical discharge.[53] Using this approach, a number of new species of astrochemical interest have been formed and identified by mass spectrometry[54–57] or spectroscopy.[58–60] Lee et al. have identified a wealth of chemical species resulting from the discharge of benzene using microwave spectroscopy.[61] Although experimental conditions in such experiments differ from those found in cold regions of the ISM, identifying intermediates and products of discharge experiments is very useful as it can bring possible formation reactions to light that otherwise would remain elusive. With the support of quantum chemical calculations, exothermic and barrier-free reaction pathways can be revealed and the relevance of particular pathways under the cold and isolated conditions in the ISM can be evaluated.[27,53]

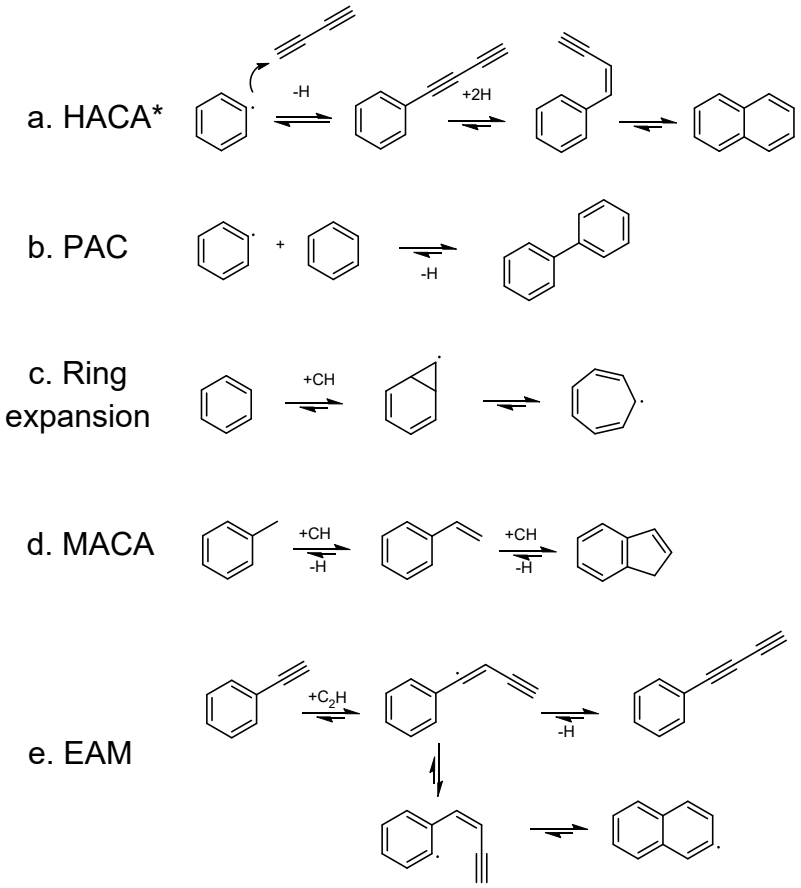

Figure 9.1: Reaction mechanisms leading to the formation of larger PAHs. The HACA en PAC mechanisms are initiated with the formation of a phenyl radical. The ring expansion, MACA and EAM mechanisms involve a methylidyne or an ethynyl radical. *The conventional HACA mechanism involves acetylene, but we classify mono-, di- and tri-acetylene addition in this mechanism. For more details see text.

Microwave (MW) spectroscopy allows for determining relative abundances, thereby providing vital information for benchmarking kinetic PAH growth studies.[17] In the electrical discharge MW studies of benzene reported by Lee and coworkers[61], many products heavier in mass than the precursor have been identified. Since rotational spectroscopy relies on molecules possessing a permanent dipole moment, MW studies on hydrocarbon discharges in general reveal product species that contain chains or ring-chain combinations with a large dipole moment.[61,62] Stable hydrocarbons, such as fully benzenoid PAHs, on the other hand, often only have a small or no dipole moment. To uncover the full complex network of PAH formation pathways -for which knowledge on such species is crucial-complementary analysis techniques are required. In our studies, we use IR-UV action

spectroscopy to record IR spectra in the fingerprint region of mass-selected products in situ[63]. The UV laser used to ionize the molecules in the molecular beam is set to a wavelength where PAHs generally have large absorption cross sections, making our approach particularly sensitive to PAHs. Structural information is obtained by matching the measured IR absorption spectra to calculated spectra of candidate compounds.[64–67] As will become clear in the following, this approach enables us to identify many new species resulting from the complex network of PAH formation pathways starting with benzene that were, as of yet, not observable.

9.3 Methods

Experiments have been performed at the FELIX laboratory[68] using the molecular beam technique discussed in more detail in ref.[69]. Argon (1.5 bar) was passed through a glass container containing benzene at room temperature. A gas pulse was created using a General Valve, which was discharged at 0.75 kV for about 100 μs between two ring electrodes with an opening of 3 mm and separated by 6 mm, traveling through a confined region for 6 mm before being expanded into a vacuum chamber. The design of the discharge nozzle was adapted from McCarthy et al. [59,60] and described in more detail in ref.[53]. A current of ~20 mA was found to be optimal for the formation of the products of interest. The electron energy was estimated to be about 3 eV using the Paschen curve (with γ between 0.1 and 0.2[70]) and the relation between electron energy and pressure.[71] The expanding gas pulse was skimmed before being crossed with three laser beams to perform IR-UV ion dip spectroscopy: one IR laser to probe the ground state vibrational levels and two UV lasers to perform 1+1' REMPI. The IR light was provided by the free electron laser FELIX for spectroscopy between 400 and 1650 cm^{-1} with a bandwidth of 0.5-1% of the IR frequency. The UV excitation laser beam of 270 nm was provided by a Nd:YAG laser pumped dye laser (Spectra Physics, Lioptec) and the UV ionization laser beam of 193 nm by an ArF excimer laser (Neweks). The ions were detected in a reflectron time-of-flight mass spectrometer (Jordan Co.) equipped with a multichannel plate ion detector. The IR laser was run at half the repetition rate of the rest of the experiment in order to acquire alternating IR on and IR off shots, thereby compensating for shot-to-shot ion signal fluctuations. IR spectra are displayed as the logarithm of the ion signal depletion and are composed of an average of 90 shots per wavenumber, further averaged with a 5-point running average.

Density function theory calculations have been performed using the Gaussian 16 program[72]. The B3LYP functional and N07D basis set[64,73–75], a combination that has been shown to perform well for predicting IR absorption spectra, has been used for structure optimization and harmonic vibrational frequency calculations. For comparison with the

experimental spectra, theoretical spectra have been convoluted with a Gaussian function with a full width at half maximum of 1% of the photon frequency, corresponding to the FEL bandwidth. The minima and transition state structures have been optimized at the B3LYP/6-311G(d,p) level of theory. The transition states have been evaluated by intrinsic reaction coordinate (IRC) calculations to connect the minima on the potential energy surface.

9.4 Results

9.4.1 Mass spectrometric overview

Figure 9.2 shows the mass spectrum of the discharge products of benzene (m/z 78). Products are ionized using 1 + 1' REMPI, where the excitation laser is resonant with unresolved vibronic transitions of the formed molecules. The m/z 126 channel shows the strongest signal: twice the height of the m/z 128 peak (the y-axis is truncated for visibility of the lower intensity signals). Note that the signal strength does not need to reflect the abundance of species as UV absorption cross sections can vary for the different products and fragments in our experiment. We detect fragments of benzene down to a m/z of 50, including hydrogen abstracted species of benzene, as well as reaction products up to m/z 230. Because the UV excitation cross section at 270 nm is expected to be significantly lower for the smaller molecules, they are not observed in our mass spectrum. MW spectroscopy is more sensitive to such species and they are identified in the complementary study that was performed previously by Lee et al.[61]. Typically, 1 + 1' resonant ionization does not result in doubly ionized species, i.e. the m/z value corresponds to the mass of the products. The m/z 50 channel is assigned to C_4H_2, a common fragmentation product of PAHs, and is likely to play a role in the formation of products with a higher mass than the parent species. Considering only its mass, the species with m/z 230 could correspond to a PAH consisting of multiple rings, showing that hydrocarbon growth occurs easily under discharge conditions. The exact chemical structures of the products can; however, not be deduced from merely their mass as multiple structural isomers exist for each mass. Here, we have used mass-selective IR spectroscopy[53,64] to obtain such structural information.

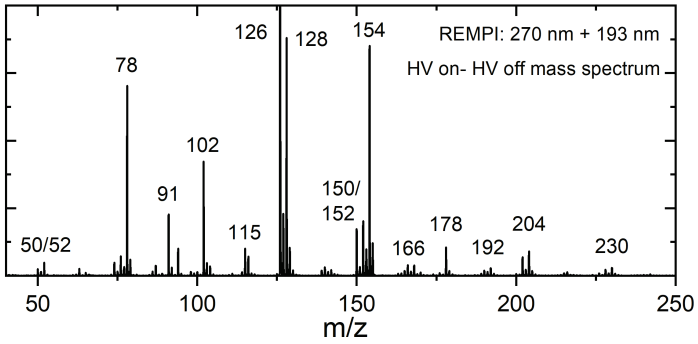

Figure 9.2: Mass spectra of fragments and products from the electrical discharge of benzene in argon. Neutral species are (singly) ionized using two-color REMPI with 270 and 193 nm. The spectrum displayed is obtained by subtracting the mass spectrum with the discharge off from the mass spectrum with the discharge source in operation. For visibility of lower intensity signals the y-axis is truncated, the m/z 126 peak being twice as intense as the m/z 128 peak.

9.4.2 IR spectroscopic assignments

Figure 9.3 displays the experimentally obtained mass-selective IR spectra in the 400-1650 cm^{-1} range for all the significant products of the benzene discharge. For each of these masses we have calculated IR absorption spectra for structural isomers that reasonably can be expected and compared them with the experimentally obtained spectra. We find that the spectral region below 1000 cm^{-1} in combination with the mass of a species provides in general sufficiently unique fingerprints to identify a molecular structure or combination of structural isomers to be present in a particular m/z channel. As such, we come to the conclusion that m/z 91 must be assigned to the tropyl radical, m/z 102 to phenylacetylene, m/z 115 to the tropylacetylene radical, m/z 126 to phenyldiacetylene, m/z 128 to naphthalene, m/z 150 to phenyltriacetylene, m/z 152 to 1- and 2-ethynylnaphthalene (1:2), m/z 154 to biphenyl, m/z 166 to fluorene, m/z 178 to diphenylacetylene and phenanthrene (2:1), m/z 192 to 1- and 2-phenyl-H-indene (2:1) m/z 204 to 1- and 2-phenylnaphthalene and m/z 230 to p-terphenyl.

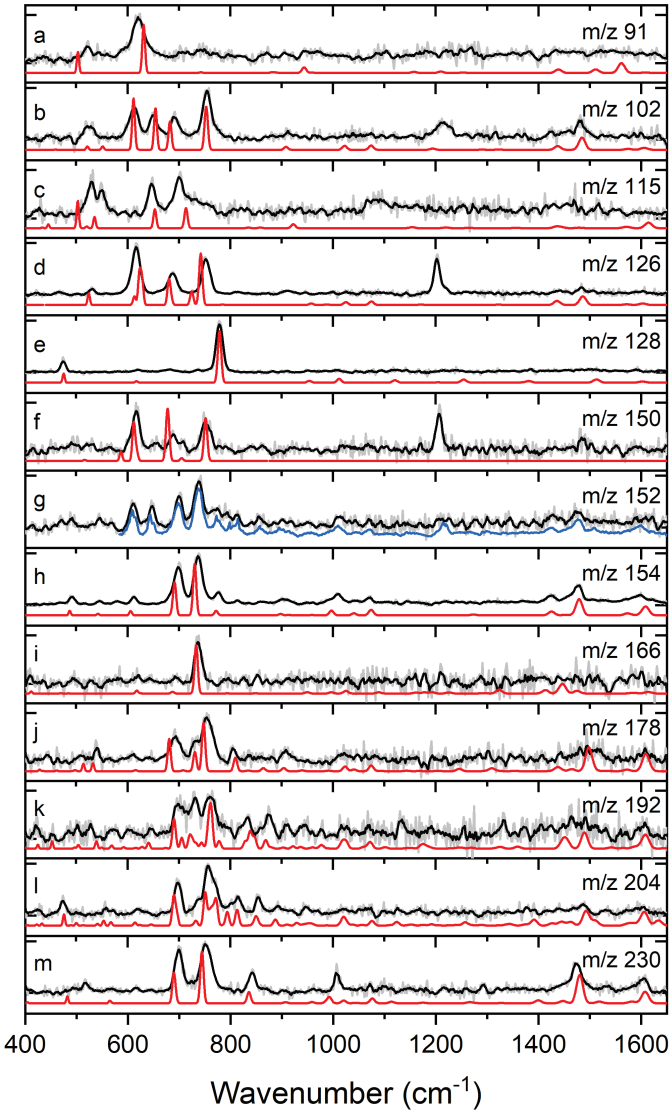

Figure 9.3: Assignment of molecular species formed in the discharge of benzene to the structures presented in Figure 9.4a-m using mass-selective IR spectroscopy (black) with calculated IR absorption spectra (red). The mass channels shown are m/z= a 91, b 102, c 115, d 126, e 128, f 150, g 152, h 154, i 166, j 178, k 192, l 204 and m 230. The molecules assigned to each mass are a tropyl radical, b phenylacetylene, c tropylacetylene radical, d phenyldiacetylene, e naphthalene, f phenyltriacetylene, g 1- and 2-ethynylnaphthalene (1:2), h biphenyl, i fluorene, j diphenylacetylene and phenanthrene (2:1), k 1- and 2-phenyl-H-indene (2:1), l 1- and 2-phenylnaphthalene (1:1) and m p-terphenyl. For m/z 152, the blue trace consists 50% of the FT-IR reference spectra of 1- and 2-ethynylnaphthalene (1:2) and 50% of the experimental spectrum of m/z=154 (see text for further information).

Although in general there is an excellent agreement between experimentally observed and theoretically predicted spectra, the peak at 1210 cm^{-1} in m/z channels 102, 126, 150 and to a lesser extent 152 is not well predicted. However, this can be well understood as this feature is an overtone of the triple bond ≡CH deformation mode that appears around 616 cm^{-1} as was demonstrated in previous studies.[53,76,77] Since our calculations are based on the harmonic approximation, the overtone is not present in the predicted spectra. Although not predicted by the calculations, the peak at 1210 cm^{-1} serves as quite a useful diagnostic feature for ≡CH terminal groups. Similarly, the feature at 1090 cm^{-1} in the IR spectrum of the m/z 115 channel is expected to be an overtone of the same functional group (≡CH) with the fundamental ≡CH out-of-plane transition of the seven-membered ring being red-shifted to 550 cm^{-1} compared with a six-membered ring structure.

For several m/z channels (m/z 152, 178, 192 and 204) the IR spectrum could not be the reproduced by a single isomer as not all IR signatures were accounted for by the predicted spectrum of a single species. In those cases, the spectra of more than one constitutional isomer were summed to achieve the best agreement between theory and experiment. The calculated spectra of diphenylacetylene and phenanthrene added in a ratio of 2:1 result in the best agreement with the experimental IR spectrum of m/z channel 178. For m/z 204, adding the calculated spectra of 1- and 2-ethynylnaphthalene in a 1:2 ratio leads to a nice agreement with the experimental spectrum. The m/z 152, the (black) experimental spectrum is compared to a sum of experimental reference spectra that include 50% of the FT-IR reference spectra of 1- and 2-ethynylnaphthalene (1:2) and 50% of the experimental spectrum of m/z=154. The much more prominent m/z 154 species (with respect to m/z 152) can loose molecular hydrogen upon photoionization. IR absorption reduces the UV absorption (and dissociation) efficiency and as a result, the IR spectrum of the m/z 154 channel appears also in the m/z 152 channel.

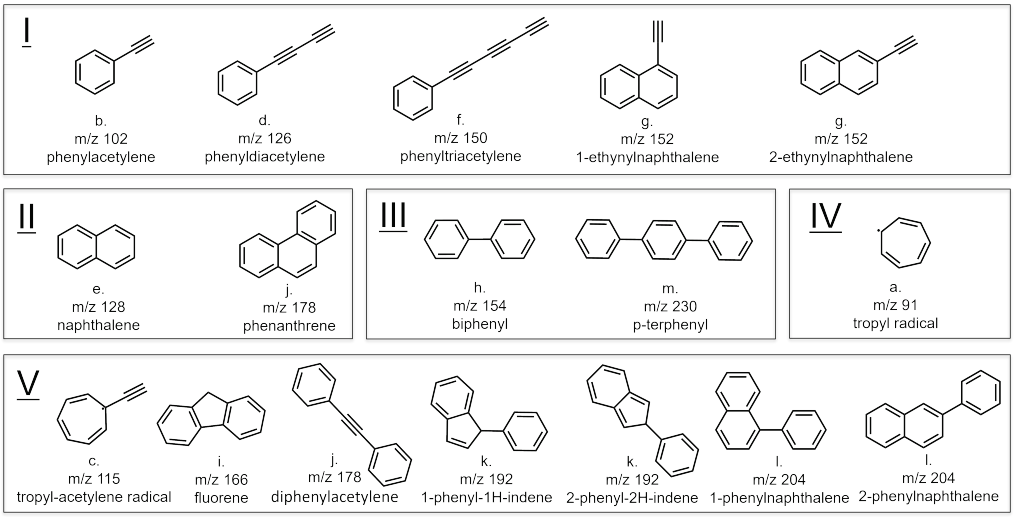

Figure 9.4: Molecular structures assigned to the mass selected IR spectra in Figure 9.3 with their respective m/z value. The letters a-m correspond to the IR spectra in Figure 9.3.

9.5 Discussion

9.5.1 Classification of identified products in light of previous analyses

The molecular structures assigned on the basis of their mass selective IR spectra can be divided into 5 classes and are displayed in Figure 9.4. We confirm the identification of polyyne-substituted benzene molecules, so called ring-chain molecules by Lee and coworkers[61]: phenylacetylene, phenyldiacetylene and phenyltriacetylene (class I). These species are expected to be detectable by both MW and IR-UV spectroscopy as they are highly polar and at the same time have a large UV cross section at around 270 nm. The overlap in these identified species provides support for the reliability of both spectroscopic methods and confirms that the conditions in our discharge are comparable. Besides the polyyne-substituted phenyl species, two ethynylnaphthalene isomers (m/z 152) are newly identified ring-chain molecules in the product mixture of the benzene discharge. It is interesting to notice that two structurally related PAHs, e.g. cyano-naphthalenes, have recently been detected via their rotational spectrum in TMC-1.[9] In view of the similarities of the ethynyl and nitrile functional groups one might speculate that these compounds are formed along similar routes as the ethynylnaphtalenes. It would thus be highly interesting to perform similar experiments as done here with benzonitrile

as precursor. Class II comprises the unsubstituted PAH species naphthalene and phenanthrene, illustrating that fully benzenoid PAH growth readily occurs under our discharge conditions with only benzene as precursor. Class III is characterized by covalently bound benzene moieties, such as biphenyl and p-terphenyl.

Products with more than six carbon atoms in one ring, such as the seven-membered tropyl radical, form an interesting class of hydrocarbons (class IV). The identification of reactive radicals indicates that the discharge chemistry is stopped as the mixture is cooled and isolated in the adiabatic expansion of the molecular beam. Owing to the isolation of molecules in the molecular beam, the reaction mixture can be probed in situ without first collecting the reactants. The observation of these radical involved reactions corroborates the conclusions about the importance of radicals by Johansson et al.[78] Class V contains hydrocarbons that are formed by a combination of the mechanisms summarized in Figure 9.1. For example, the phenyl-naphthalene isomers are likely to be formed by the combination of the PAC and HACA reaction mechanisms, phenyl-indene via MACA and PAC reactions, tropylacetylene via ring expansion and HACA, and diphenylacetylene via HACA and PAC. The involvement of multiple pathways illustrates the complexity that needs to be considered in constructing astrochemical PAH formation models.

The formation of some of the products is surprising. For example, the diphenylacetylene signal is significantly more prominent than that of phenanthrene, yet diphenylacetylene is considerably higher in energy than phenanthrene (+194 kJ/mol, zero-point vibrational energy corrected) as determined by DFT calculations (B3LYP/6-311G(d,p)[79]). Also other biphenyl species are generally higher in energy than their more compact counterparts, e.g. biphenyl with respect to acenaphthene (+17 kJ/mol). The observation of species with a higher formation energy suggests that the reactions are kinetically controlled, similar to how pure gas-phase chemistry occurs in the ISM.

The observation of the tropyl radical, the assignment of the PAHs naphthalene and phenanthrene (Class II), bi- and terphenyl (Class III), and the phenyl-substituted naphthalenes are excellent examples of the conclusion that microwave spectroscopy and mass-selective IR spectroscopy act as complementary techniques in the analysis of these complex mixtures. Combining these two techniques is thus an attractive means to fully reveal the composition of products and decrease the observational bias for particular species. Additionally, the two techniques each have their own merits in providing input for constructing chemical models. Microwave analysis, on the one hand, allows for the indirect determination of relative abundancies of highly polar ring-chain molecules, thereby providing the possibility to put quantified constraints on (astro)chemical models. Mass-selective IR-UV spectroscopy, on the other hand, is ideally suited for identifying (fully benzenoid) PAH molecules because of their large UV absorption cross section which are of primary interest in PAH growth studies.

9.5.2 Comparison to other gas-phase hydrocarbon chemistry experiments

The presence of 7-membered carbon rings was already suggested by Lee et al. because of the MW spectroscopic identification of tropone (C_7H_6O) in the discharge of benzene and oxygen.[61] However, because it does not have permanent electric dipole moment, the pure hydrocarbon analogue tropyl radical (C_7H_7) was not detected in their survey. The identification of the tropyl radical in this work, and the benzo[7]annulene radical in our previous work[53] involving the discharge of naphthalene, raises carbon insertion (Figure 9.1c) as a possible hydrocarbon growth route. However, as was the case for the benzo[7]annulene formation in the naphthalene discharge, no intermediate for the tropyl radical was found in the benzene discharge. We expect that for larger PAHs, ring growth intermediates could very well be stabilized and. The role of methylidyne in the ring expansion mechanism confirms that besides the larger diacetylene and phenyl radicals also small radical hydrocarbons play an important role in PAH formation in our experiments.

In our previous study of the growth of naphthalene in a discharge, no biphenyl-type products were identified[53]. Instead, the main products consisted of ring-chain hydrocarbons and larger PAHs. In the present study; however, a number of identified molecules contain covalently linked phenyl groups. This suggests that in the current experiments phenyl radicals – which react with benzene to form biphenyl structures – are formed abundantly. The presence of phenylacetylene and ethynyl-naphthalene implies at the same time that also (mono-/di-/tri-)acetylene and their radical forms are readily available, and not only phenyl radicals.

Similar to the discharge of naphthalene, a prominent species is phenyldiacetylene, which suggests a favorable route to PAH formation via diacetylene addition. Another similarity with the naphthalene discharge experiments is that no acenaphthylene is detected, a common product in pyrolysis experiments.[80] A large resemblance exists between our product mixture and the pyrolysis of azobenzene, as can be expected because in our mass spectrum we also detect phenyl radicals.[41] However, the considerable fragmentation and subsequent recombination reactions in the discharge experiments result in an overall richer chemistry. The species that are formed include substituted PAHs with a large dipole moment, and these would be promising candidates for radio astronomy searches.

9.5.3 The tropylacetylene radical case

The large variety of products -including phenyl or acetylene substituted, 7-membered ring and 'pure' PAH species that are highlighted in the previous sections- indicates that various formation pathways are proceeding simultaneously in the discharge of benzene. In order to investigate how and where multiple formation mechanisms are connected, and lead to more complex hydrocarbons such as the ones in class V, we have constructed the potential energy surface of the formation of a typical product, the tropylacetylene radical. A combination of the ring expansion (see Figure 9.1c) and acetylene addition mechanism (EAM, Figure 9.1e)) forms a logical pathway for this formation reaction. Both reaction sequences in which benzene reacts first with either the methylidyne radical (red pathways) or with the ethynyl radical (black pathway) are shown in Figure 9.5.

The (**B1**, black) pathway starts with ethynyl radical addition to form a benzene-ethynyl intermediate (**B1-1**)**.** Hydrogen removal proceeds via (**TS-B1-1**) to yield the observed phenylacetylene (**B1-2**). In the next step, insertion of the methylidyne radical produces three similar bicyclic cyclopropa-phenylacetylene isomeric structures. The transition states (**TS-P-2**) have almost the same energy as the bicyclic minima (**P-3**, within ~ 1-2 kJ/mol). The formation of such bicyclic intermediate structures has been observed for the bimolecular reaction of methylidyne radical with styrene, where the corresponding transition states were also determined to be only 8 kJ/mol higher in energy.[16]

The (**B2**, red) pathway -starting with the addition of the methylidyne radical to form the tropyl radical (**B2-2**)- goes via a bicyclic cyclopropa-benzene radical (**B2-1**) and a transition state (**TS-B2-1**). The latter is calculated to be only 2 kJ/mol higher in energy than **B2-1**, which is below the channel entrance energy.[48] The subsequent addition of an ethynyl radical leads to an isomeric product distribution denoted by structures (**d**) and (**e**) as the seven-membered ring does not retain planarity. Both species proceed differently to the tropylacetylene product (**B-4**): the pathway via (**e**) shows hydrogen migration (**TS-B2-2**) on top of the aromatic surface prior to a barrier-less removal of the hydrogen atom. The pathway via (**d**) to (**B-4**) occurs directly. As these different tropylacetylene adducts are both relatively low in energy and have a closed shell electron configuration, they may be stable and important reaction intermediates for ring growth and acetylene addition mechanisms.

Both pathways of the combined EAM and ring expansion pathways are exothermic in nature. Here, we have investigated possible routes towards a single isomer product, but in general the order of the reaction steps in the benzene discharge mixture will dictate the chemical complexity. Different sequences can form distinct conformers and isomers, such as the observed phenylacetylene intermediate (Figure 9.3b) in the tropylacetylene example in Figure 9.5. Each of the stable intermediate structures may act as a new precursor to extend the chemical complexity even more.

Many of the observed intermediates possess a permanent dipole moment and are promising candidates for searches in the ISM by radio astronomy, especially the ring-chain molecules. For some species, rotational data is already available or could otherwise be obtained. Their observation would shed light on the relevance of particular formation routes such as the ones presented in this study. Additionally, the determination of the relative abundance in astronomical objects would provide quantified observational constraints to chemical models.

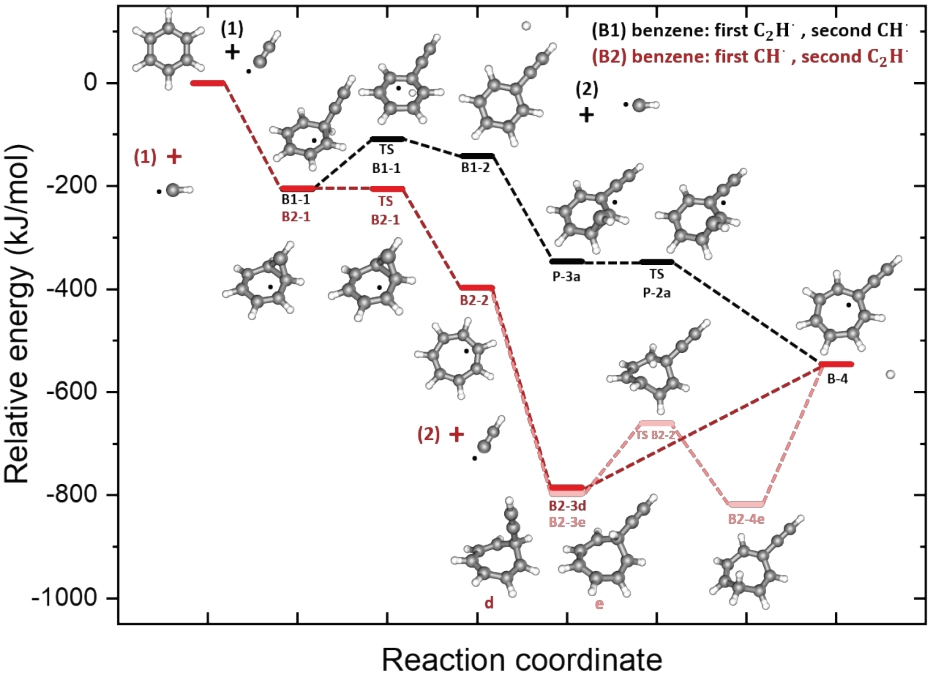

Figure 9.5: Potential energy surfaces of the benzene + ethynyl radical + methylidyne radical reaction pathways to tropylacetylene radical. The B1 pathway (black) involves first a reaction with the ethynyl radical to form B1-2 phenylacetylene and is followed by a reaction with a methylidyne radical. In the B2 pathway (red) the order is reversed and this pathway occurs via the B2-2 tropyl radical. The energies include the zero point vibrational energy correction and are calculated with respect to the entrance energy.

9.6 Conclusions

To conclude, using mass selective IR spectroscopy in the fingerprint region and quantum chemical calculations we have identified a large number of products in the benzene discharge, thereby revealing the complex and unexpectedly rich chemistry of benzene. By

observing products in combination with (radical) intermediates, our experiments reveal multiple pathways to PAH growth to occur simultaneously and competitively. These pathways include the more commonly considered HACA and PAC mechanisms involving acetylene and phenyl radicals, respectively, but also the ring expansion mechanism that requires yet smaller radical hydrocarbons. Without laboratory input of possible structures and pathways such as provided in the present studies, important contributions to PAH chemistry may be overlooked. Our studies demonstrate that multiple routes to PAH formation explicitly need to be considered in order to account for the observed interstellar abundancies of PAHs. Quantum chemical calculations of the combined pathways to one of the reaction products provide a first insight into the energetic landscapes along different sequences of mechanisms that result in the same product. Many of these pathways show only submerged energy barriers, and are thus expected to proceed at low temperatures in the interstellar medium as well.

Our experiments have also identified intermediates and products that so far had not been observed. A number of them -including the ring-chain hydrocarbons ethynyl-naphthalene and tropylacetylene- are of direct interest as they are quite polar and thus key targets for radio astronomy searches. Structurally similar to the recently detected cyanonaphthalenes, the astronomical observation and determination of the relative abundancies of these compounds would put constraints on specific structures for constructing quantitative PAH chemistry models. Laboratory experiments such as the one reported here -in which it is brought to light how the complex network of PAH formation pathways is interconnected- in combination with observational constraints are the way forward to disentangle the complex carbon chemistry in the universe.

References

1 A. G. G. M. Tielens, *Astrochem. Astrobiol.*, 2013, **85**, 35–72.

2 S. Hony, C. Van Kerckhoven, E. Peeters and A. G. G. M. Tielens, *Astron. Astrophys.*, 2001, **370**, 1030–1043.

3 E. Peeters, S. Hony, C. Van Kerckhoven, A. G. G. M. Tielens and L. J. Allamandola, *Astron. Astrophys.*, 2002, **390**, 1089–1113.

4 E. Peeters, A. G. G. M. Tielens, L. J. Allamandola and M. G. Wolfire, *Astrophys. J.*, 2012, **747**, 44.

5 B. R. Brandl, H. W. W. Spoon, D. Devost, G. C. Sloan, S. Guilles, Y. Wu, J. R. Houck, D. W. Weedman, L. Armus, P. N. Appleton, B. T. Soifer, L. Hao, J. A. Marshall, S. J. Higdon and T. L. Herter, *Astrophys. J.*, 2006, **653**, 1129–1144.

6 L. Armus, V. Charmandaris, H. W. W. Spoon, J. A. Marshall, S. J. U. Higdon, V. Desai, H. I. Teplitz, L. Hao, D. Devost, B. R. Brandl, Y. Wu, G. C. Sloan, B. T. Soifer, J. R. Houck and T. L. Herter, *Astrophys. J.*, 2007, **656**, 148.
7 F. Galliano, S. C. Madden, A. G. G. M. Tielens, E. Peeters and A. Jones, *Astrophys. J.*, 2008, **679**, 310–345.
8 A. M. Burkhardt, K. Long, K. Lee, P. B. Changala, C. N. Shingledecker, I. R. Cooke, R. A. Loomis, H. Wei, S. B. Charnley, E. Herbst, M. C. Mccarthy and B. A. Mcguire, *Astrophys. J. Lett.*, 2021, **913**, L18.
9 B. A. Mcguire, R. A. Loomis, A. M. Burkhardt, K. Long, K. Lee, C. N. Shingledecker, S. B. Charnley, I. R. Cooke, M. A. Cordiner, E. Herbst, S. Kalenskii, M. Siebert, E. R. Willis, C. Xue, A. J. Remijan and M. C. McCarthy, *Science*, 2021, **371**, 1265–1269.
10 M. C. Mccarthy, K. Long, K. Lee, R. A. Loomis, A. M. Burkhardt, C. N. Shingledecker, S. B. Charnley, M. A. Cordiner, E. Herbst, S. Kalenskii, E. R. Willis, C. Xue, A. J. Remijan and B. A. Mcguire, *Nat. Astron.*, 2021, **5**, 176–180.
11 J. Cernicharo, C. Cabezas, B. Tercero, N. Marcelino, J. R. Pardo and P. De Vicente, *Astron. Astrophys.*, 2021, **649**, L15.
12 J. Cernicharo, A. M. Heras, A. G. G. M. Tielens, J. R. Pardo, F. Herpin, M. Guélin and L. B. F. M. Waters, *Astrophys. J.*, 2001, **546**, L123:L126.
13 B. A. Mcguire, A. M. Burkhardt, S. Kalenskii, C. N. Shingledecker, A. J. Remijan, E. Herbst and M. C. Mccarthy, *Science*, 2018, **359**, 202–205.
14 L. N. X. Mercier, A. Faccinetto, S. Batut, G. Vanhove, D. K. Bozanic, H. R. Hrodmarsson, G. A. Garcia, *Phys. Chem. Chem. Phys.*, 2020, **22**, 15926–15944.
15 Y. Carpentier, T. Pino and P. Bréchignac, *J. Phys. Chem. A*, 2013, **117**, 10092–10104.
16 S. Doddipatla, G. R. Galimova, H. Wei, A. M. Thomas, C. He, Z. Yang, A. N. Morozov, C. N. Shingledecker, A. M. Mebel and R. I. Kaiser, *Sci. Adv.*, 2021, **7**, 1–12.
17 H. Richter, O. A. Mazyar, R. Sumathi, W. H. Green, J. B. Howard and J. W. Bozzelli, *J. Phys. Chem. A*, 2001, **105**, 1561–1573.
18 A. Violi, *Combust. Flame*, 2004, **139**, 279–287.
19 Y. Bentarcurt, F. Ruette and M. Sanchez, *Int. J. Quantum Chem.*, 2010, **110**, 2560–2572.
20 A. M. Burkhardt, R. A. Loomis, C. N. Shingledecker, K. Long, K. Lee, A. J. Remijan, M. C. Mccarthy and B. A. Mcguire, *Nat. Astron.*, 2021, **5**, 181–187.
21 I. Cherchneff, J. R. Barker and A. G. G. M. Tielens, *Astrophys. J.*, 1992, **401**, 269–287.
22 H. Richter, T. G. Benish, O. A. Mazyar, W. H. Green and J. B. Howard, *Proc. Combust. Inst.*, 2000, **28**, 2609–2618.
23 T. S. Zwier and M. Allen, *Icarus*, 1996, **123**, 578–583.
24 N. Indriolo and B. J. Mc Call, *Chem. Soc. Rev.*, 2013, **42**, 7763–7773.

25 N. J. Mason, B. Nair, S. Jheeta and E. Szymańska, *Faraday Discuss.*, 2014, **168**, 235–247.
26 M. Gatchell, *Nat. Astron.*, 2020, **4**, 21–22.
27 R. I. Kaiser, D. S. N. Parker and A. M. Mebel, *Annu. Rev. Phys. Chem*, 2015, **66**, 43–67.
28 D. S. N. Parker, F. Zhang, Y. S. Kim, R. I. Kaiser, A. Landera, V. V Kislov, A. M. Mebel and A. G. G. M. Tielens, *PNAS*, 2012, **109**, 53–58.
29 T. Allain, S. Leach and E. Sedlmayr, *Astron. Astrophys.*, 1996, **305**, 602–615.
30 M. Frenklach, A. D. D. W. Clary and S. E. Stein, in *Twentieth Symposium (International) on Combustion/The Combustion Institute*, 1984, pp. 887–901.
31 L. Zhao, R. I. Kaiser, B. Xu, U. Ablikim, M. Ahmed, D. Joshi, G. Veber, F. R. Fischer and A. M. Mebel, *Nat. Astron.*, 2018, **2**, 413–419.
32 L. Zhao, R. I. Kaiser, B. Xu, U. Ablikim, M. Ahmed, M. M. Evseev, E. K. Bashkirov, V. N. Azyazov and A. M. Mebel, *Nat. Astron.*, 2018, **2**, 973–979.
33 T. Yang, R. I. Kaiser, T. P. Troy, B. Xu, O. Kostko, M. Ahmed, A. M. Mebel, M. V. Zagidullin and V. N. Azyazov, *Angew. Chemie - Int. Ed.*, 2017, **56**, 4515–4519.
34 L. Zhao, R. I. Kaiser, B. Xu, U. Ablikim, M. Ahmed, M. M. Evseev, E. K. Bashkirov, V. N. Azyazov and A. M. Mebel, *Angew. Chemie - Int. Ed.*, 2020, **59**, 4051–4058.
35 D. S. N. Parker, R. I. Kaiser, T. P. Troy and M. Ahmed, *Angew. Chemie - Int. Ed.*, 2014, **53**, 7740–7744.
36 B. Shukla and M. Koshi, *Phys. Chem. Chem. Phys.*, 2010, **12**, 2427–2437.
37 H. Bohm, H. Jander and D. Tanke, *Twenty-Seventh Symp. Combust.*, 1998, 1605–1612.
38 P. Constantinidis, F. Hirsch, I. Fischer, A. Dey and A. M. Rijs, *J. Phys. Chem. A*, 2017, **121**, 181–191.
39 N. D. Marsh and M. J. Wornat, *Proc. Combust. Inst.*, 2000, **28**, 2585–2592.
40 L. Zhao, M. Prendergast, R. I. Kaiser, B. Xu, U. Ablikim, W. Lu, M. Ahmed and A. D. Oleinikov, *Phys. Chem. Chem. Phys.*, 2019, **21**, 16737–16750.
41 P. Constantinidis, H. C. Schmitt, I. Fischer, B. Yan and A. M. Rijs, *Phys. Chem. Chem. Phys.*, 2015, **17**, 29064–29071.
42 L. Zhao, M. B. Prendergast, R. I. Kaiser, B. Xu, U. Ablikim, M. Ahmed, B. J. Sun, Y. L. Chen, A. H. H. Chang, R. K. Mohamed and F. R. Fischer, *Angew. Chemie - Int. Ed.*, 2019, **58**, 17442–17450.
43 A. M. Mebel, V. V Kislov and R. I. Kaiser, *J. Am. Chem. Soc.*, 2008, **130**, 13618–13629.
44 L. Zhao, R. I. Kaiser, W. Lu, B. Xu, M. Ahmed, A. N. Morozov, A. M. Mebel, A. H. Howlader and S. F. Wnuk, *Nat. Commun.*, 2019, **10**, 3689.
45 S. Soorkia, C. A. Taatjes, D. L. Osborn, T. M. Selby, A. J. Trevitt, R. Wilson and S. R. Leone, *Phys. Chem. Chem. Phys.*, 2010, **12**, 8750–8758.

46 J. Bouwman, A. J. De Haas and J. Oomens, *Chem. Commun.*, 2016, **52**, 2636–2638.
47 L. T. Scott and N. H. Roelofs, *J. Am. Chem. Soc.*, 1987, **109**, 5461–5465.
48 C. He, A. M. Thomas, G. R. Galimova, A. N. Morozov, A. M. Mebel and R. I. Kaiser, *J. Am. Chem. Soc.*, 2020, **142**, 3205–3213.
49 K. O. Johansson, M. P. Head-Gordon, P. E. Schrader, K. R. Wilson and H. A. Michelsen, *Science*, 2018, **361**, 997–1000.
50 M. Thomson and T. Mitra, *Science*, 2018, **361**, 978–979.
51 M. N. Mccabe, P. Hemberger, E. Reusch, A. Bodi and J. Bouwman, *J. Phys. Chem. Lett.*, 2020, **11**, 2859–2863.
52 A. G. G. M. Tielens, M. M. Meixner, P. P. van der Werf, J. Bregman, J. A. Tauber, J. Stutzki and D. Rank, *Science*, 1993, **262**, 86–89.
53 A. K. Lemmens, D. B. Rap, J. M. M. Thunnissen, B. Willemsen and A. M. Rijs, *Nat. Commun.*, 2020, **11**, 1–7.
54 M. Alliati, D. Donaghy, X. Tu and J. W. Bradley, *J. Phys. Chem. A*, 2019, **123**, 2107–2113.
55 C. S. Contreras and F. Salama, *Astrophys. Journal, Suppl. Ser.*, 2013, 208, 17pp.
56 L. He, W. Shen and M. Sulkes, *Chem. Phys. Lett.*, 2009, **471**, 210–215.
57 X. Gillon and L. Houssiau, *Plasma Sources Sci. Technol.*, 2014, 23, 45010.
58 H. Linnartz, *Cavity Ring-Down Spectroscopy of Molecular Transients of Astrophysical Interest*, Blackwell Publishing Ltd., 2009.
59 M. C. McCarthy, W. Chen, M. J. Travers and P. Thaddeus, *Astrophys. J. Suppl. Ser.*, 2000, **129**, 611–623.
60 M. C. McCarthy, M. J. Travers, A. Kovacs, C. A. Gottlieb and P. Thaddeus, *Astrophys. J. Suppl. Ser.*, 1997, **113**, 105–120.
61 M. C. McCarthy, K. L. K. Lee, P. B. Carroll, J. P. Porterfield, P. B. Changala, J. H. Thorpe and J. F. Stanton, *J. Phys. Chem. A*, 2020, **124**, 5170–5181.
62 M. C. Mccarthy and P. Thaddeus, *Chem Soc Rev*, 2001, **30**, 177–185.
63 A. M. Rijs and J. Oomens, *Top. Curr. Chem.*, 2015, **364**, 1–42.
64 A. K. Lemmens, D. B. Rap, J. M. M. Thunnissen, C. J. Mackie, A. Candian, A. G. G. M. Tielens, A. M. Rijs and W. J. Buma, *Astron. Astrophys.*, 2019, **628**, A130.
65 A. K. Lemmens, S. Gruet, A. L. Steber, J. Antony, S. Grimme, M. Schnell and A. M. Rijs, *Phys. Chem. Chem. Phys.*, 2019, **21**, 3414–3422.
66 A. K. Lemmens, P. Chopra, D. Garg, A. L. Steber, M. Schnell, W. J. Buma and A. M. Rijs, *Mol. Phys.*, 2021, **119**, e1811908.
67 A. K. Lemmens, D. B. Rap, J. M. M. Thunnissen, S. Gruet, A. L. Steber, S. Panchagnula, A. G. G. M. Tielens, M. Schnell, W. J. Buma and A. M. Rijs, *J. Phys. Chem. Lett.*, 2020, **11**, 8997–9002.
68 D. Oepts, A. F. G. Van, D. Meer and P. W. Van Amersfoort, *Infrared Phys. Technol.*, 1995, **36**, 297–308.

69 A. M. Rijs, M. Kabeláč, A. Abo-Riziq, P. Hobza and M. S. De Vries, *ChemPhysChem*, 2011, **12**, 1816–1821.
70 M. A. Lieberman and A. J. Lichtenberg, *Principles of Plasma Discharges and Materials Processing*, John Wiley & Sons, Inc., Hoboken, NJ, USA, 2005.
71 A. Von Engel, *Ionized gases*, American Institute of Physics, New York, 1994.
72 M. J. Frisch, G. W. Trucks, H. B. Schlegel, G. E. Scuseria, M. A. Robb, J. R. Cheeseman, G. Scalmani, V. Barone, G. A. Petersson, H. Nakatsuji, X. Li, M. Caricato, A. V. Marenich, J. Bloino, B. G. Janesko, R. Gomperts, B. Mennucci, H. P. Hratchian, J. V. Ortiz, A. F. Izmaylov, J. L. Sonnenberg, D. Williams-Young, F. Ding, F. Lipparini, F. Egidi, J. Goings, B. Peng, A. Petrone, T. Henderson, D. Ranasinghe, V. G. Zakrzewski, J. Gao, N. Rega, G. Zheng, W. Liang, M. Hada, M. Ehara, K. Toyota, R. Fukuda, J. Hasegawa, M. Ishida, T. Nakajima, Y. Honda, O. Kitao, H. Nakai, T. Vreven, K. Throssell, J. Montgomery, J. A., J. E. Peralta, F. Ogliaro, M. J. Bearpark, J. J. Heyd, E. N. Brothers, K. N. Kudin, V. N. Staroverov, T. A. Keith, R. Kobayashi, J. Normand, K. Raghavachari, A. P. Rendell, J. C. Burant, S. S. Iyengar, J. Tomasi, M. Cossi, J. M. Millam, M. Klene, C. Adamo, R. Cammi, J. W. Ochterski, R. L. Martin, K. Morokuma, O. Farkas, J. B. Foresman and D. J. Fox, *Gaussian, Inc., Wallingford CT*.
73 C. Puzzarini, M. Biczysko and V. Barone, *J. Chem. Theory Comput.*, 2010, **6**, 828–838.
74 V. Barone, M. Biczysko and J. Bloino, *Phys. Chem. Chem. Phys.*, 2014, **16**, 1759–1787.
75 S. Panchagnula, J. Bouwman, D. B. Rap, P. Castellanos, A. Candian, C. MacKie, S. Banhatti, S. Brünken, H. Linnartz and A. G. G. M. Tielens, *Phys. Chem. Chem. Phys.*, 2020, **22**, 21651–21663.
76 L. J. Bellamy, *The Infra-red Spectra of Complex Molecules*, Chapman and Hall, London, 1975.
77 R. A. Nyquist and W. J. Potts, *Spectrochim. Acta*, 1960, **16**, 419–427.
78 K. O. Johansson, M. P. Head-Gordon, P. E. Schrader, K. R. Wilson and H. A. Michelsen, *Science*, 2018, **361**, 997–1000.
79 A. D. Becke, *J. Chem. Phys.*, 1993, **98**, 5648–5652.
80 T. Visser, M. Sarobe, L. W. Jenneskens and J. W. Wesseling, *Fuel*, 1998, **77**, 913–920.

Chapter 10

Perspective

10.1 Discussion

In this chapter several insights and implications from this thesis are highlighted with the aim to encourage discussion and stimulate scientific advancement. In particular, it is in my opinion important to share experiences and thoughts on the experiment from the perspective of the experimentalist. This will clarify what the strengths and limitations of a particular technique are and point out improvable aspects.

Infrared spectroscopy in molecular beams

The principal technique used in this thesis to look at molecules is IR-UV ion dip spectroscopy.[1] The preparation of isolated and cold molecules, a requirement for performing IR-UV ion dip spectroscopy, is very elegantly done by using molecular beam techniques. However elegant and adequate these techniques are to study small molecules with a high vapor pressure, for large molecules the method encounters difficulties on two counts. Firstly, large molecules are typically less volatile and high temperatures or laser desorption is required to bring the molecules in the gas phase. The higher starting temperature and more downstream entrainment of molecules in the expansion makes cooling them more difficult. Secondly and more importantly, larger molecules require more collisions with the carrier gas to cool down. At some point, practical constraints on the pressure of the carrier gas or on the gas pulse length limit the size of the molecule that can be cooled effectively.[2] Curiously, it is found by experience, however, that for a large molecule a higher backing pressure (with more collisions) does not necessarily lead to better cooling. From that point of view there is still a lot of room for research and development in order to achieve more effective cooling of large molecules to their vibrational ground state.

In the chapters 2-4, 6 and 7 IR-UV ion dip spectroscopy is employed to obtain detailed information on the vibrational potential energy surfaces of PAHs. What makes these studies so special is that they combine the advantages of the IR-UV ion dip technique with IR radiation that is provided by the free electron laser FELIX.[3] This laser covers a wide range of wavelengths well into the far-IR region, but is moreover fully tunable over the entire wavelength range. Whereas in the low-energy far-IR region multiphoton dissociation techniques would struggle to put sufficient energy for dissociation into a molecule, IR-UV ion dip is –in theory at least– a one-photon process, making it relatively sensitive at longer wavelengths. The high fluence of the far-IR light from FELIX even allowed us to investigate not only the 'bottom' of the vibrational potential energy surface along low-frequency modes, but climb the vibrational ladder and get a detailed view on the potential at higher energies.

Although IR-UV ion dip spectroscopy appears to be a rather clean and straightforward method to record IR absorption spectra, the studies presented in this thesis show

that one should be cautious with the interpretation of such spectra. In the IR-UV ion dip scheme, the IR wavelength is scanned and the effect of IR absorption on the UV probe step is monitored. The IR absorption changes the UV spectrum which leads, more often than not, to a decrease of the ion signal at vibronic transitions (hence ion dip). Such changes are normally interpreted as being in a one-on-one correspondence with the IR absorption spectrum, and providing an unambiguous probe of the structure of the electronic ground state.

That this does not necessarily need to be the case is shown in chapter 2 where IR-UV hole-burning experiments are described. In such experiments the IR laser is fixed at a vibrational transition and the UV probe laser wavelength is scanned. Hole-burning is typically used to distinguish different conformers that may be present in the molecular beam. In chapter 2, however, the IR laser is indeed fixed at a vibrational transition, but the goal is not to distinguish conformers as rigid PAHs are expected to have only one conformation. Instead, the transfer of population to higher-lying vibrational levels upon IR excitation is probed by monitoring the increase of UV absorption intensity upon IR pre-excitation. As stated previously, one normally expects a decrease of the ion signal at vibronic transitions, but chapter 2 shows -and uncovers the full details underlying this phenomenon- that also IR-induced gain can occur at particular vibronic transition frequencies. Such interplay between loss and gain of probe signal makes the technique not the perfectly clean form of IR spectroscopy in the way it is often regarded. Yes, the molecules are studied under conditions in which there are no interactions with the environment and, yes, the molecules are under cold conditions, but is should not be forgotten that it is an indirect method for studying IR absorption. Moreover, as opposed to for example FTIR spectroscopy, recording an infrared spectrum with IR-UV spectroscopy over a wide frequency range requires scanning the spectrum in parts. Such spectra are joined by trying to have sufficient overlap between different parts of the spectrum, but nevertheless, the whole process introduces uncertainties in the intensities of bands, in particular when comparing bands that are spectrally far apart.

Spectroscopy of weakly bound complexes

The far-IR, which has received special attention in this thesis, is a particularly diagnostic region to probe long-range, weaker interactions. More and more, one is becoming aware of the importance of such interactions and how utilizing knowledge of these interactions could help to address challenges society currently faces. Considering interstellar PAHs, these complexes form the connection between the gas and solid phase configurations of carbon. A thorough knowledge of this connection will help us to understand the processes on a molecular scale that govern the first stages of star and planetary formation. Back on earth in combustion processes, non-covalent interactions underly soot formation. Emission of such soot particles in the atmosphere influence cloud formation by

providing nucleation sites for water. In turn, non-covalent interactions govern such nucleation processes. Recently, for example, it was shown that emission of soot by airplanes causing condensation trails may actually have a larger greenhouse effect than the emission of CO_2.[4] Weak interactions should thus not be underestimated! In this thesis, a section is devoted to weakly bound complexes. As I see it these experiments are just scratching the surface, which is illustrated mainly in chapter 6 that reports on theory and experiment that comprise long-range interactions. The interactions between water molecules and the resulting far-IR spectra appear computationally challenging. Since interactions involving water are so widespread in biology, but also in astrochemical ices, improving our theoretical understanding is imperative and more experimental data will support that. The UV(/VIS) spectroscopic part will also bring to light the effects of complexation to the electronic configuration of the systems. Especially for PAHs, the experimental details on the electronic configuration is of importance both from a theoretical point of view (see section 10.2), but also from the perspective of using them as functional organic electronics.[5,6]

Challenges in theory

Another issue coming prominently forward from the present thesis is provided by chapter 4 in which the theoretical limits for predicting infrared spectra in terms of size and structure of PAHs come into play. One key aspect here is the role of anharmonicity. As commonly referred to, anharmonicity is a collective noun that can be interpreted as all deviations from the harmonic approximation. Considering that the harmonic approximation is rather crude -though extremely useful- there are many aspects of anharmonicity and how it works through that can be considered. This thesis is mainly focused on overtones, combination bands and resonances between vibrational states that can influence to a large extent the IR spectrum, especially in regions with a higher density of states.[7] The application of anharmonic analyses has proven to be key for a proper interpretation of IR spectra, especially when considering a complex mixture as needs to be done in chapters 8 and 9. In these chapters, we use a correction on harmonic theory that enables us to assign all prominent experimentally observed IR features and improve the reliability of the assignment of molecular structures. The molecular inventory of the interstellar medium is an extremely complex mixture and in analyzing it, such accurate theoretical predictions are crucial. One could ask weather using a correction on a crude (harmonic) approximation, which in turn is based on a semi-empirical method is the way forward. Especially since the correction is, relative to the harmonic approximation, computationally very demanding. For astrochemistry, if the goal is an accurate model of the infrared spectrum of PAHs, one could consider letting go of first principle calculations and employ machine learning methods.

10.2 Outlook (and some gems)

Far-IR future

Isomer-selective IR-UV ion dip spectroscopy together with the far-IR capabilities of FELIX is a unique combination that calls for many more experiments to be performed. Think, for example, of extending more spectroscopic studies to the low-frequency region, which contains vibrations that are highly sensitive to long-range, weaker interactions and that are typically much more difficult to calculate. It is therefore an interesting region to test theory. The PAH-water complexes that are presented in chapter 6 are just a few of the many complexes of astrochemical interest to study with IR-UV spectroscopy, including ones with ammonia, molecular hydrogen or oxygen or other small astrochemical molecules.[8] Low-frequency modes are also important from other points of view. Vibrational levels of such modes can be occupied at room temperature which make them important for the thermodynamics of chemical reactions. Probing a molecule's potential energy surface at higher energies is also of considerable interest; this is where IR-induced isomerization reactions can occur, which allows for studying conformational changes as occurring in biology. Even more, ps probe lasers would allow for studying IVR processes and help elucidating the interaction between vibrational modes, a consequence of anharmonicity that was not focused on extensively in this thesis.

Absorption intensities

While this thesis mainly focuses on the mechanical vibrational potential, developing a reliable way of measuring the absolute IR intensities using IR-UV ion dip spectroscopy is for spectroscopists highly desired. Such measurements would provide accurate cross-sections -of tremendous importance from an astronomical point of view-, help in the assignment of (bio)molecular structures in the gas-phase, and, as always, provide theoreticians with laboratory standards. However, such experiments are challenging and require a well-defined, well-characterized IR beam with a homogeneous beam profile and tunability over the desired range. Moreover, for the molecule of interest, there should be a full picture of the exact IR-UV ion dip mechanism. FELIX has all the characteristics to reach those goals as it is able to provide a widely tunable IR laser beam, but one important aspect that needs further studies is the influence of its characteristic micro pulse structure.

Preview

In order to record an IR spectrum of a molecule using IR-UV ion dip spectroscopy one first needs to record its Resonance Enhanced Multiphoton Ionization (REMPI) spectrum under jet-cooled conditions. These REMPI spectra have been reported for only a little more than 20 fully benzenoid PAHs. Adiabatic excitation energies of the lower-lying

electronic states of PAHs with their highly delocalized electrons are notoriously hard to calculate.[9] These transitions and transitions to vibrationally excited levels in these states are not only of interest to astronomers as candidates for the diffuse interstellar bands, but also for physical chemists a thorough description of such systems is desired. An extension of the REMPI spectrum database would allow for a broader comparison between experiment and theory and thereby instigate theoretical progress. In this thesis, large PAHs are studied that were mostly compact. Also, for most of them, the REMPI spectrum was reported before except for the case of peropyrene. Here, I will briefly discuss as yet unpublished results obtained for the non-compact PAHs [4]-helicene, picene and pentacene (Figure 10.1). They are examples from classes of PAHs of which REMPI spectra are highly desired. The [4]-helicene and picene REMPI spectra are new additions to the small database of REMPI spectra of PAHs. Their IR-UV ion dip spectra are also reported and shortly discussed. The helicenes are an interesting class of PAHs because they are non-planar as a result of the steric hindrance of the cove hydrogens. Picene (part of the phenancene class) recently attracted more interest because of its electronic properties and higher stability with respect to pentacene.[10]

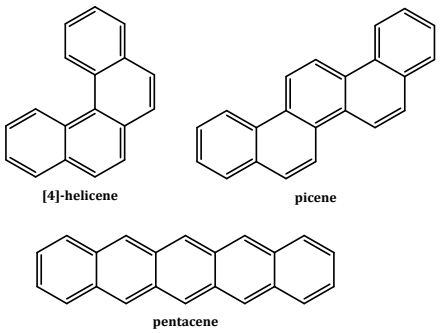

Figure 10.1: Molecular structures of [4]-helicene, picene and pentacene

The jet-cooled electronic spectra of [4]-helicene and picene are shown in Figure 10.2. The origin transitions to the lowest excited singlet state are found at 27090 cm^{-1} and 27231 cm^{-1} for [4]-helicene and picene, respectively. The [4]-helicene spectrum is highly dense, with vibronic transitions having more intensity than the origin transition. It shows a progression from the origin spaced by 114 cm^{-1}. TDDFT calculations indicate that this progression can be attributed to the fact that in the lowest electronically excited singlet state the molecule adopts a slightly different, more planar geometry than in the electronic ground state. The REMPI spectrum of picene is much less dense and a comparison to the 'linear' sister-PAH pentacene would be interesting to make.

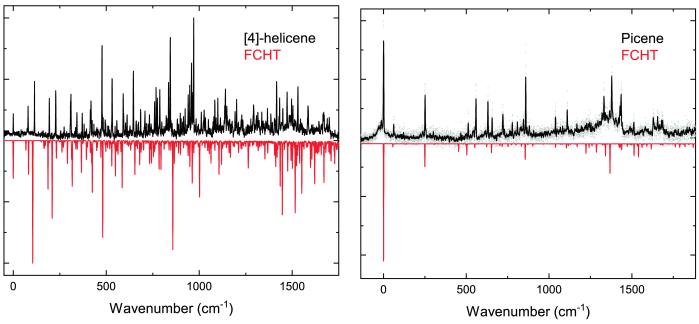

Figure 10.2: The (1+1') $S_1 \leftarrow S_0$ REMPI spectra of jet-cooled [4]-helicene and picene (black). The spectra have been shifted to set the origin transitions at 27090 cm^{-1} and 27231 cm^{-1} for [4]-helicene and picene, respectively to be zero. Spectra predicted taking Herzberg-Teller coupling into account are shown in red. These spectra have been calculated at the wB97XD/aug-cc-pVDZ and B3LYP/6-31+G* levels of theory for [4]-helicene and picene, respectively.

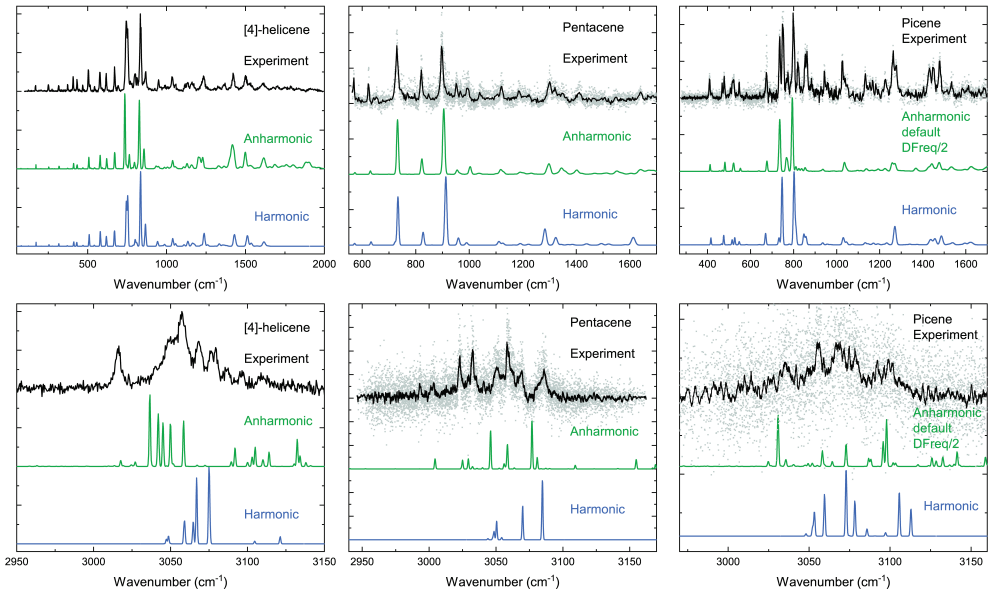

Figure 10.3: Infrared absorption spectra of [4]-helicene, pentacene and picene in a molecular beam (black), together with spectra predicted using the harmonic approximation (blue) and including anharmonic effects (green). The harmonically calculated spectra are retrieved from the NASA Ames database for [4]-helicene and pentacene. For picene spectra were calculated by ourselves at the B3LYP/6-31+G* level using a scaling factor of 0.96. The anharmonic calculations were calculated using Gaussian16 with GVPT2 at the B3LYP/Jun-cc-pVDZ or B3LYP/N07D level of theory with a superfine grid and very tight optimization.

The infrared absorption spectra of jet-cooled [4]-helicene, pentacene and picene in the 3 μm (OPO, 2950-3150 cm^{-1}) and the 5-100 μm (FELIX, 100 and 2000 cm^{-1}) regions are shown in Figure 10.3. The experimental spectra are compared to predictions using both the standard harmonic approximation and to anharmonic calculations. The 3 μm, CH-stretch, region shows the major role of anharmonicity. Although DFT VPT2 calculations improve the comparison with the experimental spectra, it is clear that there is still considerable room for improvement. In the mid-IR, the harmonic calculations agree well with the experiment for [4]-helicene and pentacene with the exception of the region between 5-6 μm (2000-1600 cm^{-1}). The CH out-of-plane bands of picene, however, are not well predicted at all, in particular the doublet at about 750 cm^{-1}. The IR spectra illustrate once more that there is still much to learn when it comes to accurately predicting the IR spectra of PAHs and correctly incorporating the effects of anharmonicity. Who knows what the quantum computing revolution will bring for the chemistry community and for the prediction of photophysical properties of PAHs in particular.

All we know is that we have to keep testing theories with empirical data, and that we have to continue to perform fundamental research to discover the rules of the universe. Not only will this help us to improve our understanding of all that happens around us, but it will also lead to the development of human technologies that benefit our lives *and* surroundings. To be able to put the large universe in the proper perspective, one has to remember to look closely at (and understand) smaller things such as molecules: no detail is too small.

References

1 A. M. Rijs and J. Oomens, *Top. Curr. Chem.*, 2015, **364**, 1–42.
2 G. Scoles, *Atomic and Molecular Beam Methods: Vol. 1*, Oxford University Press, 1988.
3 D. Oepts, A. F. G. Van, D. Meer and P. W. Van Amersfoort, *Infrared Phys. Technol.*, 1995, **36**, 297–308.
4 L. Bock and U. Burkhardt, *Atmos. Chem. Phys.*, 2019, **19**, 8163–8174.
5 P. M. Zimmerman, Z. Zhang and C. B. Musgrave, *Nat. Chem.*, 2010, **2**, 648–652.
6 M. Watanabe, Y. J. Chang, S.-W. Liu, T.-H. Chao, K. Goto, M. M. Islam, C.-H. Yuan, Y.-T. Tao, T. Shinmyozu and T. J. Chow, *Nat. Chem.*, 2012, **4**, 574–578.
7 A. Candian and C. J. Mackie, *Int. J. Quantum Chem.*, 2017, **117**, 146–150.
8 A. Potapov, *Mol. Astrophys.*, 2017, **6**, 16–21.
9 M. Parac and S. Grimme, *Chem. Phys.*, 2003, **292**, 11–21.
10 R. Mitsuhashi, Y. Suzuki, Y. Yamanari, H. Mitamura, T. Kambe, N. Ikeda, H. Okamoto, A. Fujiwara, M. Yamaji, N. Kawasaki, Y. Maniwa and Y. Kubozono, *Nature*, 2010, **464**, 76–79.

Summary

Wonder

noun
A feeling of amazement and admiration, caused by something beautiful, remarkable, or unfamiliar.

verb
Desire to know something; feel curious.

Oxford Languages

We are surrounded by carbon, we are even made of it. Close to half of all dry biomass is represented by carbon. Many consider it a key ingredient for life on Earth, or anywhere else for that matter. Its ability to form multiple bonds in saturated and unsaturated form allows carbon to have a rich chemistry unlike any other element. Complete research departments are devoted to organic chemistry, where chemists study carbon-containing compounds. While organic chemistry on earth is often considered unique and different from that in space, in recent years one has come to realize that carbon also plays a central role in the chemistry and physical conditions in the universe.

The wonder of telescopes and carbon in the universe

The biggest wonders are witnessed only by a small amount of people. Allow me to share some of the wonderments I have had the privilege to have in my work over the past four years, which resulted in this thesis. Beginning with how light originating from space, caught by ground- and space-based telescopes, is responsible for our perspective of (and on) the universe.

Telescopes have uncovered the vastness of the universe, but also provided us with detailed insights that have led to the paradigm of the presence and role of carbonaceous molecules in space. The fruitful combination of the disciplines of astronomy and (laboratory) spectroscopy enabled us to see distant matter that cannot be observed with our naked eyes. Using telescopes and spectrometers, we can zoom in and discover distant astrophysical objects in a color pallet that is much richer than "only" visible light. As of today, spectroscopy has detected over 200 molecules in space, most of which contain carbon. We are getting to know more and more about the chemical evolution and inventory of interstellar space and it is justified to say: we are surrounded by carbon.

Quite remarkable is that towards all phases of stellar evolution, telescopes observe distinct emission features in the infrared region of the spectrum, referred to as the aromatic infrared bands (AIBs). Aromatic, because vibrational transitions of Polycyclic Aromatic Hydrocarbons (PAHs) are hypothesized to be responsible for the emission. PAHs consist of adjoined rings of carbon that are stabilized by aromaticity and surrounded by hydrogen atoms. AIBs are detected in star-forming regions, proto-planetary disks, surfaces of dark clouds, around carbon rich stars in their last stage and the general diffuse interstellar medium. PAHs are thus not without reason considered as being one of the major lockers of carbon in the universe.

Interpreting the infrared features that we see with our surrogate eyes, the telescopes, requires a detailed understanding of the fundamentals that govern how light interacts with matter. This is where spectroscopy comes into play, together with the quantum chemistry that we use to explain and understand the properties of molecules. The spectroscopic knowledge is key for astronomers to assign absorption or emission features detected by telescopes to specific molecules, thereby ultimately enabling them to

determine the chemical composition and evolution of astrophysical objects. Especially the upcoming James Webb Space telescope which features an unprecedented spectral and spatial resolution will deliver a wealth of spectroscopic data that requires a more detailed understanding of the infrared spectra of PAHs than ever before.

The wonder of laser spectroscopy in molecular beams

Already in the 19th century, organic chemists were interested in the structure of carbon and also the stable, aromatic compounds caught their interest. Van 't Hoff, after which the Van 't Hoff Institute for Molecular Sciences at the University of Amsterdam is named, made an important connection in this respect. As obvious as it may seem nowadays, he used the three-dimensional structure of atoms in a molecule to explain the photophysical properties of a molecule. Now, after the quantum theory revolution, light still offers the most direct probe of the structure and quantum mechanical nature of molecules. Quantum theory tells us that a molecule can only occupy very specific energy levels, be it electronic, vibrational or rotational. Electromagnetic radiation, light, can be used to change the state of a molecule, making transitions between these distinct energy levels. Hence, the uniqueness of a molecule is imprinted into its electromagnetic spectrum. Spectroscopists typically scan the wavelength of the light, i.e., the energy of the photons, and obtain the unique spectrum associated with a molecule. The unique spectrum is of high value to astronomers who try to assign spectral features observed by telescopes.

The conditions and surroundings of molecules in a spectrometer can influence the resulting spectrum to a large extent. Higher temperatures and collisions with surrounding matter obscures the intrinsic spectrum of a molecule and impedes direct comparison with theory. In the end, the repetitive comparison between experiment and theory leads to new insights and improved models. To obtain a detailed understanding of the intrinsic spectral properties of PAHs, one ideally wants to study molecules of interest at very low temperatures and under conditions in which they are not influenced by other molecules. The molecular beam technique offers these conditions in a very wonderful, elegant way. It still amazes me that using only a valve and a vacuum, one can make a pulse of noble gas that is able to cool the entrained molecules to effective temperatures of only a few degrees above absolute zero. The entrained molecules are cooled down to their vibrational ground state and reach rotational temperatures of only a few Kelvin. Combining this technique with narrowband lasers results in highly resolved spectra of isolated molecules that can be used directly to evaluate theory, as described in Chapter 2 and 3. However, there is a caveat. Importantly, there are indications that a small set of large PAHs dominate the PAH population in the universe, described in more detail in Chapter 5. These so-called grandPAHs are more stable and thus best suited to survive the intense radiation that permeates the interstellar medium. Subtle variations in their composition could explain all observed spectral variations. Bringing sufficient amounts of grandPAHs

into the gas phase to study their intrinsic properties is difficult using conventional heating techniques due to their low vapor pressure. To circumvent this problem, laser desorption has been applied to bring large PAHs into the gas phase before entraining them into a molecular beam. As Chapter 4 of this thesis convincingly shows, this has opened a new door for studying grandPAHs under isolated and cold conditions and has allowed us to record laboratory infrared spectra of PAHs with sizes that are directly relevant for assessing the grandPAH hypothesis.

This thesis comprises the complete relevant infrared range of PAHs from the far-infrared to the mid-infrared. In these different parts of the infrared spectrum, the vibrational motions of PAHs have quite different characteristics. On the one hand, to probe the global structure of a PAH, i.e. to excite delocalized vibrations, one needs to resort to the far-IR. Such modes are dependent on the complete structure of a PAH, thereby making them promising diagnostic features for individual PAH species. A common assumption was that these delocalized vibrations have a very anharmonic potential, which would make interpreting the far-IR bands difficult and unreliable. However, the results of Chapter 2 in this thesis show, quite unexpectedly, that this assumption is not necessarily the case for the delocalized far-IR modes of PAHs, which is good news for astronomers.

On the other hand, localized vibrational modes are located in the mid-IR and, because of the structural similarity of the edge structure of PAHs, overlap to a large extent. The spectral overlap makes distinguishing individual PAH species using only local vibrations rather difficult. Moreover, the experimental IR spectra in this region in Chapter 4 show that anharmonicity, the interaction between vibrational modes that is hard to calculate, has a dominating effect. Nevertheless, so far, as a result of limits from the observational side not the delocalized, but the local vibrations have been used extensively by astronomers to draw far-reaching conclusions from subtle spectral features. About time to move to longer wavelengths!

The wonder of chemistry in space

There are indications that even in the dilute and cold conditions of the interstellar medium, chemical reactions take place. Instinctively, one would certainly not expect that under these conditions large carbonaceous molecules such as PAHs or fullerenes are formed. It is one thing to know *what* we 'see' with the telescopes, but another to *explain* what we 'see'. In particular the growth of PAHs and their high abundance has so far been troublesome to account for. To understand the presence of PAHs, we have to map the network of chemical reactions that lead to their formation and find out how PAHs influence, and are influenced by, their environment. It is known that the PAHs present in interstellar space have a profound effect on the chemistry and physical conditions of molecular clouds and star forming regions. They influence temperature, shield the interior of clouds, regulate charge balance and many more aspects. Elucidating the evolution of

molecules can therefore be considered key to understanding the evolution of the universe.

As explained in the above, spectroscopy can be applied to determine the composition of mixtures of molecules in space, but also in a laboratory on earth the combination of mass spectrometry and spectroscopy is very powerful for analyzing the content of a gas-phase mixture. That strength has been used in Chapter 8 and 9 of this thesis to understand the chemistry of PAHs in controlled and suitable environments. To this purpose gas-phase chemical reactions of benzene and naphthalene, simple aromatic molecules, have been initiated by an electrical discharge. The supplied energy results in the dissociation of parent molecules, after which the fragments can recombine with each other or the parent. The chemical dance of fragmentation and reconstruction that we create in this way is much like the chemistry in interstellar space where photons typically induce the reactions. The mixture that results is analyzed by matching mass-selective IR spectra to quantum chemically predicted spectra. Such a systematic identification of molecular structures is a unique and powerful tool for constructing reliable models that describe the carbon chemistry in our universe and help us to understand in full detail why PAHs are so ubiquitous.

Physical chemistry

In both *getting to know* and *explaining* what we see in the universe, the molecular physics fundamentals are crucial. The properties of molecules, their chemical bonds and molecular dynamics govern the evolution of carbon in the universe. Besides of being of direct relevance to astronomy, fundamental research aimed at describing these properties is of major importance to society. To contribute to expanding the fundamental knowledge about the interactions of carbon, the Chapters 6 and 7 of this work focus on non-covalent interactions between PAHs (and water). In recent years, these long-distance interactions attract steeply increasing interest, because of their importance in self-assembly, molecular recognition in biology, materials science and much more. In Chapter 6, a PAH has been used as a platform to which water clusters of different sizes are non-covalently bound. That enabled us to expose the far-infrared features resulting from complexation, which are particularly diagnostic for the interactions between the water molecules. Non-covalent interactions between aromatic hydrocarbons themselves are interesting to molecular physicists due to the special interactions between the delocalized electrons. For larger aromatic systems, these interactions are theoretically not well understood. Experimental information on the structure of non-covalent PAH complexes that exist as a result of these interactions is therefore highly desired. Chapter 7 presents structural information of isolated PAH complexes obtained with infrared spectroscopy by identifying spectral features that transpire from complexation. New evidence is provided in the very long-standing discussion from both the theoretical and experimental perspective about

the structure of the naphthalene dimer. The results strongly suggest that the naphthalene dimer attains a parallel configuration, indicating that π-π stacking interactions become significant already for small PAHs.

In short, this thesis aims at contributing to answering three questions about carbon in our universe. What is the organic inventory in the universe, how do molecules form in the interstellar medium and lastly, how do they interact? The results in this thesis suggest that the answer to the first question lies in the far-infrared. In answering the second question, we really uncovered the full complexity of that question and provided initial handles to construct reliable models describing the formation of PAHs. While investigating the third question, we provided new evidence in a long-standing discussion about the structure of PAH complexes.

However small the details that were uncovered in this thesis, one has to remember: no detail is too small. After all, the rules that govern the behavior of small matter on earth are the same that rule the rest of the universe. To discover these rules, we will have to keep testing theory with (laboratory) experiments and continue doing fundamental research, but above all: keep wondering.

Samenvatting

Verwondering

Het gevoel tegenover iets te staan dat, eer het er was, niet geheel te voorzien viel of, nu het er is, niet geheel te doorzien valt

Nederlandse encyclopedie

We zijn omgeven door koolstof, we zijn er zelfs van gemaakt. Bijna de helft van alle droge biomassa bestaat uit koolstof. Velen beschouwen het fundamenteel voor het leven op aarde, of waar ook in het universum. Het vermogen van koolstof om verschillende bindingen te vormen, in verzadigde en onverzadigde vorm, zorgt voor een ontzettend rijke chemie. Gehele vakgroepen zijn toegewijd aan het bestuderen van koolstofverbindingen: de organische chemie. Hoewel organische chemie hier op aarde vaak wordt beschouwd als uniek, is men de laatste jaren tot het inzicht gekomen dat koolstof ook een centrale rol speelt in de chemische reacties en fysieke omstandigheden in het hele universum.

De verwondering over telescopen en koolstof in het universum

De grootste wonderen worden soms aanschouwd door maar een klein gezelschap. Laat me een paar van de verwonderingen met jullie delen, welke ik het voorrecht heb gehad in de laatste vier jaar te ondervinden en die hebben geleid tot dit proefschrift. Beginnend bij hoe licht afkomstig uit de ruimte wordt opgevangen door grondgebonden en ruimtetelescopen en hoe dat ons perspectief van (en op) ons universum bepaalt.

Telescopen hebben niet alleen een glimp van de onmetelijkheid van het universum laten zien, ze hebben ook details blootgelegd van ruimteobjecten op honderden lichtjaren afstand. Die details hebben, onder andere, gezorgd voor een paradigmaverschuiving over de aanwezigheid en rol van moleculen in de ruimte. Aan de grondslag daarvan ligt de vruchtbare combinatie van de disciplines astronomie en spectroscopie, die ons ruimteobjecten laat zien in een kleurenpallet dat ons menselijk zicht ver ontstijgt. Vandaag de dag hebben we door middel van spectroscopie meer dan 200 verschillende moleculen geïdentificeerd in de ruimte tussen sterren, de interstellaire ruimte. Het zal je misschien al niet meer verbazen dat de meesten van deze moleculen koolstof bevatten. Door deze aandacht voor de ruimte komen we steeds meer te weten over de chemische evolutie en inventaris van de interstellaire ruimte. Het is gerechtvaardigd om te stellen: we zijn omgeven door koolstof.

Opvallend is dat we met onze telescopen vanuit bijna elke levensfase van een ster zeer onderscheidende kenmerken in infrarood licht waarnemen. Deze kenmerken worden aromatische infrarood banden (AIB) genoemd. Aromatisch, omdat wordt verondersteld dat vibrationele overgangen in polycyclische *aromatische* koolwaterstoffen (PAK's) verantwoordelijk zijn voor de infrarood emissie. PAK's, zoals de naam al aangeeft, zijn moleculen die bestaan uit meerdere ringen van koolstof omgeven door waterstof, en bijzonder stabiel door wat chemici *aromaticiteit* noemen. AIB's, de verklikkers van de PAK's, worden waargenomen in de geboorteplaatsen van sterren, protoplanetaire schijven, oppervlakten van donkere nevels, in de omgeving van koolstofrijke sterren in hun laatste levensfase, en in de algemene interstellaire ruimte. Niet zonder reden worden PAK's gezien als een zeer belangrijke klasse van koolstofhoudende moleculen.

Voor de interpretatie van het kenmerkende infraroodlicht, dat we met onze surrogaat-ogen, de telescopen, zien hebben we een nauwkeurig en gedegen beeld nodig van de wisselwerking tussen licht en materie. Hier komen spectroscopisten om de hoek kijken, want ondersteund door kwantumchemie proberen spectroscopisten namelijk precies deze wisselwerking te begrijpen. De spectroscopische kennis die zij vergaren speelt vaak een sleutelrol voor astronomen die absorptie of emissiekenmerken, gedetecteerd met telescopen, proberen te verklaren. Met de juiste kennis zijn zij in staat om de details over de chemische compositie en evolutie van ruimteobjecten te bepalen die honderden lichtjaren van ons zijn verwijderd. Het duurde even voordat het tot me doordrong hoe wonderbaarlijk het is dat we zulke gedetailleerde informatie kunnen verkrijgen van objecten die zich op een afstand bevinden die we als mens nu onmogelijk kunnen bereizen. De nieuwe James Webb ruimtetelescoop zal hier nog een schepje bovenop doen, met een ongeëvenaarde ruimtelijke en spectrale resolutie. Het interpreteren van zijn waarnemingen zullen een nog diepgaander inzicht in de infrarood spectra van PAK's vereisen dan voorheen.

De verwondering over laserspectroscopie en molecuulbundels

Organisch chemici waren in de 19de eeuw al geïnteresseerd in de structuur van koolstofverbindingen en ook de gestabiliseerde, aromatische moleculen vielen hen op. Jacobus Henricus van 't Hoff, naamgever van het Van 't Hoff Institute for Molecular Sciences aan de Universiteit van Amsterdam, legde een zeer belangrijk verband. Het lijkt nu triviaal, maar hij gebruikte de driedimensionale structuur van atomen in een molecuul om fotofysische eigenschappen te verklaren. Nu, ook na de kwantumtheorie-revolutie, biedt licht nog steeds het beste portaal naar de structuur en kwantumwereld van moleculen. De term kwantum komt voort uit de bevinding dat een molecuul zich alleen maar in zeer specifieke energieniveaus kan bevinden, afhankelijk van zijn structuur. En ook dat de opname of uitzending van alleen een specifieke hoeveelheid energie (een bepaald kwantum aan energie), bijvoorbeeld in de vorm van licht, een transitie kan veroorzaken tussen twee van zulke energieniveaus. Deze koppeling zorgt ervoor dat de structuur van een molecuul af te lezen is aan de golflengten (energieën) van het licht dat het opneemt of uitzendt. Spectroscopisten scannen de golflengte van het licht en nemen zo een spectrum op dat hoort bij een bepaalde molecuulstructuur. Dit unieke spectrum is van groot belang voor astronomen die proberen te verklaren welke moleculen verantwoordelijk zijn voor bepaalde kenmerken in het (infrarood) spectrum.

De omstandigheden waarin moleculen zich bevinden in een spectrometer zijn van grote invloed op het spectrum dat wordt gemeten. Hoge temperaturen en botsingen met andere moleculen of materialen kunnen het intrinsieke spectrum van een molecuul verhullen. Een spectrum van een molecuul dat is beïnvloed door zijn omgeving kan niet meteen vergeleken worden met een gemodelleerd intrinsiek spectrum. Dat is nadelig, want

juist die directe vergelijking en ijking van theorie aan een experiment leidt tot verbeterde modellen, en misschien wel belangrijker, tot nieuwe inzichten. Om een diepgaand begrip te verkrijgen in de intrinsieke spectrale eigenschappen van PAK's, zou je de moleculen willen bestuderen bij zeer lage temperaturen en zonder dat ze botsen met hun omgeving.

De molecuulbundeltechniek is een bijzonder elegante manier om moleculen precies in zulke condities te brengen. Het verbaast me nog steeds dat je met enkel een ventiel en een vacuüm een gaspuls kunt maken dat moleculen meeneemt en ze (effectief) dichtbij het absolute nulpunt brengt. De meegesleepte moleculen komen in hun vibrationele grondtoestand en bereiken rotationele temperaturen van een paar Kelvin. Combineer deze elegante techniek met nauwbandige lasers en je hebt een manier om zeer hoge-resolutie spectra van geïsoleerde moleculen op te nemen, die direct te vergelijken zijn met theorie. Precies dit is beschreven in Hoofdstuk 2 en 3 van dit proefschrift. Maar dan zijn we er nog niet. Belangrijk is om te weten dat er aanwijzingen zijn dat een kleine set van grote PAK's de populatie in het universum domineren. Deze zogenoemde *"grandPAHs"* zijn stabieler en beter bestand tegen de straling waarmee de interstellaire ruimte is doordrongen. Maar omdat ze een zeer lage dampdruk hebben, is het lastig om door verhitting genoeg *"grandPAHs"* in de gasfase te brengen. Daar zouden zeer hoge, onpraktische temperaturen voor nodig zijn. Om dit probleem te omzeilen wordt in dit proefschrift laserdesorptie gebruikt om grote PAK's te verdampen alvorens ze op te nemen in de molecuulbundel. Hoofdstuk 4 laat zien hoe laserdesorptie de weg effent om *"grandPAHs"* te bestuderen bij lage temperatuur en vrij van interacties met de omgeving. Daarmee brengen we de limieten van de gebruikte theoretische modellen aan het licht.

Dit proefschrift bevat experimenten aan PAK's die het complete relevante infraroodbereik beslaan, van het ver-infrarood tot het midden-infrarood. In deze verschillende infraroodregio's worden molecuulvibraties aangeslagen van een nogal verschillend karakter. Enerzijds, om een beeld te krijgen van de complete structuur van een PAK, is het ver-infrarood bijzonder interessant. Bij vibraties in het ver-infrarood is de hele structuur van een molecuul betrokken. Dat maakt het ver-infrarood een potentieel interessant gebied om diagnostische kenmerken te vinden voor specifieke PAK's. Een algemene aanname is dat ver-infrarood vibraties sterk afwijken van de veelgemaakte harmonische benadering voor de beschrijving van vibraties. Elke afwijking van deze harmonische benadering scharen we onder anharmoniciteit. Een sterk anharmonisch karakter zou de interpretatie van het ver-infrarood bereik lastig en onbetrouwbaar maken. Niettemin, tegen verwachtingen in, laat Hoofdstuk 2 zien dat deze aanname niet noodzakelijkerwijs het geval hoeft te zijn voor de ver-infrarood vibraties van PAK's, Hetgeen goed nieuws is voor astronomen.

In het midden-infrarood gebied vindt men, anderzijds, vibraties van PAK's waarbij enkel een klein deel van het molecuul in beweging is. Bij deze lokale vibraties zijn de koolwaterstofbindingen betrokken aan de rand van het molecuul. Omdat de randen van

PAK's op elkaar kunnen lijken, overlappen deze vibraties vaak, wat het lastig maakt om individuele structuren van elkaar te onderscheiden. Daarbovenop laten Hoofdstuk 3 en 4 ook zien dat anharmoniciteit hier wél een dominante invloed heeft. Desalniettemin gebruiken astronomen de midden-infrarood regio veel, omdat de infrarood emissie hier duidelijker wordt waargenomen en niet wordt verdoezeld door de infrarood emissie van stof, zoals in het ver-infrarood. Van kleine verschillen in het midden-infrarood worden vergaande conclusies getrokken. Hoogtijd om de focus te verleggen naar het ver-infrarood!

De verwondering over chemie in de ruimte

De interstellaire ruimte bevat een zeer lage dichtheid aan deeltjes en het is er ook nog eens extreem koud. Op het eerste gezicht zou je niet verwachten dat onder zulke omstandigheden chemische reacties plaatsvinden. Hier op aarde gebruiken chemici namelijk vaak verhitting om chemische reacties te laten verlopen, waarbij de precursoren ook bij elkaar in een bekerglas zitten. Toch vinden er in de interstellaire ruimte reacties plaats waarbij zelfs grote PAK's en fullerenen (koolstofkooien van wel 60 atomen) worden gevormd. Stap één is om te weten te komen *wat* we zien met telescopen en je daarover te verwonderen. Stap twee is om te *verklaren* en begrip te krijgen voor wat we waarnemen. Tot vandaag de dag is het verre van triviaal om de formatie van grote PAK's en hun hoge aantallen te verklaren. Om hun aanwezigheid te begrijpen, moeten we op zoek naar het netwerk aan chemische reacties dat tot hun vorming leidt. We moeten erachter komen hoe moleculen in het universum worden gevormd door bepaalde omstandigheden, maar tegelijkertijd ook hoe de moleculen precies deze omstandigheden zelf beïnvloeden. Ze hebben namelijk een ingrijpend effect op hun omgeving, op moleculaire nevels en de geboorteplaatsen van sterren en planeten. De PAK's beïnvloeden bijvoorbeeld de temperatuur, ze schermen af voor straling en reguleren het ladingssaldo. Een begrip van de evolutie van sterren en het universum gaat daarom hand in hand met het verklaren van de evolutie van moleculen en PAK's in het bijzonder.

Zoals beschreven in de vorige paragraaf kunnen we spectroscopie gebruiken om de inventaris van moleculen in de ruimte te bepalen, maar ook in een laboratorium is spectroscopie al jaren een veelgebruikt instrument voor het ophelderen van chemische structuren. In combinatie met massaspectrometrie wordt het een krachtige techniek om de samenstelling van complexe mengsels te bepalen. Hoofdstuk 8 en 9 laten zien hoe die kracht ingezet kan worden om de chemie van PAK's in relevante condities bloot te leggen. Van relatief eenvoudige aromatische koolwaterstoffen in de gasfase worden reacties opgewekt door middel van een elektrische ontlading. De elektrische ontlading breekt de moleculen op, van welke de fragmenten weer kunnen recombineren tot nieuwe, exotische producten. Deze chemische dans van fragmentatie en reconstructie lijkt op de chemie van PAK's in de ruimte die wordt geïnitieerd door fotonen en welke zorgt voor de

chemische rijkdom die we observeren. De combinatie van massa-selectieve infraroodspectroscopie met kwantumchemisch berekende spectra maakt het mogelijk de afzonderlijke componenten van het complexe mengsel te identificeren. Het in kaart brengen van de producten stelt ons in staat om meer betrouwbare modellen te ontwikkelen die de koolstofevolutie in onze ruimte beschrijven en waarmee we in detail de wijdverbreide aanwezigheid van PAK's kunnen verklaren.

Fysische chemie

Voor zowel het ontdekken als het verklaren van alles in ons universum zijn de fundamenten van fysische chemie cruciaal. De eigenschappen van moleculen, hun bindingen en dynamiek bepalen de evolutie van koolstof in het universum. En naast het feit dat een beter begrip van deze fundamenten van direct belang is voor astronomie, is het ook van grote waarde in allerlei andere hoeken van de samenleving. De Hoofdstukken 6 en 7 van dit proefschrift zijn gericht op de zwakke aantrekkingskracht die bestaat tussen PAK's en tussen PAK's en water. De laatste jaren krijgen deze langeafstand-interacties steeds meer aandacht, omdat ze een belangrijke rol spelen in moleculaire zelfassemblage, in moleculaire herkenning in biologie, materiaalwetenschappen enzovoort. In Hoofdstuk 6 dient een PAK als platform waaraan één, twee of drie watermoleculen kunnen hechten. Dat platform bracht de ver-infrarood kenmerken, die diagnostisch zijn voor de langeafstand-interacties tussen watermoleculen, aan het licht. De interactie tussen PAK's zelf is al veel bestudeerd vanwege de bijzondere aantrekking tussen gedelokaliseerde elektronenwolken die zich aan beide vlakke zijden van een PAK bevinden, zogenaamde π-wolken. Theoretisch is deze π-π stapel-interactie zeer lastig te beschrijven, en vandaar dat experimentele informatie over de structuur van complexen die bestaan dankzij de π-π stapel-interacties zeer gewaardeerd is. Door kenmerken in het ver-infraroodspectrum te identificeren die voortkomen uit de interactie tussen moleculen levert Hoofdstuk 7 nieuw bewijs in de langdurende discussie over de structuur van de dimeer van de tweering aromaat naftaleen. De resultaten zijn een sterke aanwijzing voor een voornamelijk parallelle configuratie van de dimeer. Op zijn beurt wijst dat erop dat de π-π stapel-interacties ook al significant zijn voor kleine PAK's.

Al met al biedt dit proefschrift nieuwe aanwijzingen voor het beantwoorden van drie vragen over koolstof in ons universum. Wat is de chemische inventaris van de interstellaire ruimte? Hoe vormen (grote) aromatische koolstofmoleculen aldaar? En, wat is de interactie tussen polycyclische aromatische koolwaterstoffen? Dit proefschrift laat zien dat het antwoord op de eerste vraag wellicht in het ver-infrarood te vinden is. In het beantwoorden van de tweede vraag hebben we de complexiteit van die vraag blootgelegd en eerste handvaten aangereikt voor het maken van meer complete modellen die de vorming van PAK's kunnen beschrijven. Bij het onderzoeken van de derde vraag levert

dit proefschrift nieuw bewijs in een langdurende discussie over de structuur van PAK-complexen.

Hoe klein de details ook mogen zijn die aan het licht zijn gekomen, herinner je dat geen detail te klein is. Tenslotte zijn de natuurwetten waaraan de kleinste deeltjes op aarde onderhevig zijn, dezelfde als de natuurwetten die over het hele universum regeren. Om deze regels te ontdekken zullen we onze theorieën moeten blijven testen met experimenten en fundamenteel onderzoek blijven doen, maar bovenal, want daar begint het mee, ons blijven verwonderen.

Publications

This thesis is based on the following publications:

Far-IR and UV spectral signatures of controlled complexation and microhydration of the polycyclic aromatic hydrocarbon acenaphthene
Alexander K. Lemmens, Sébastien Gruet, Amanda L. Steber, Jens Antony, Stefan Grimme, Melanie Schnell and Anouk M. Rijs.
Phys. Chem. Chem. Phys., 21, 3414-3422, 2019

Anharmonicity in the mid-infrared spectra of polycyclic aromatic hydrocarbons: molecular beam spectroscopy and calculations
Alexander K. Lemmens, Daniël B. Rap, Johannes M. M. Thunnissen, Cameron J. Mackie, Alessandra Candian, Alexander G. G. M. Tielens, Anouk M. Rijs and Wybren Jan Buma.
Astronomy & Astrophysics, 628, A130, 2019

Polycyclic aromatic hydrocarbon formation chemistry in a plasma jet revealed by IR-UV action spectroscopy
Alexander K. Lemmens, Daniël B. Rap, Johannes M. M. Thunnissen, Bryan Willemsen and Anouk M. Rijs.
Nature Communications, 11, 269, 2020

Far-IR absorption of neutral polycyclic aromatic hydrocarbons (PAHs): light on the mechanism of IR–UV ion dip spectroscopy
Alexander K. Lemmens, Daniël B. Rap, Johannes M. M. Thunnissen, Sébastien Gruet, Amanda L. Steber, Sanjana Panchagnula, Alexander G. G. M. Tielens, Melanie Schnell, Wybren Jan Buma, and Anouk M. Rijs.
The Journal of Physical Chemistry Letters, **11**, 21, 2020.

High-resolution infrared spectroscopy of naphthalene and acenaphthene dimers
Alexander K. Lemmens, Pragya Chopra, Diksha Garg, Amanda L. Steber, Melanie Schnell, Wybren Jan Buma and Anouk M. Rijs.
Molecular Physics, 119, e1811908, 2021

Infrared Spectroscopy of Jet-cooled "GrandPAHs" in the 3–100 μm Region
Alexander K. Lemmens, Anouk M. Rijs and Wybren Jan Buma.
The Astrophysical Journal, 923, 238, 2021

The complex network of PAH formation pathways revealed in a benzene discharge
Alexander K. Lemmens, Daniël B. Rap, Sandra Brünken, Wybren Jan Buma and Anouk M. Rijs.
Submitted, 2022

Size distribution of polycyclic aromatic hydrocarbons in space: an old new light on the 11.2/3.3 μm intensity ratio
Alexander K. Lemmens, Cameron J. Mackie, Alexander G. G. M. Tielens, Anouk M. Rijs and Wybren Jan Buma.
In preparation

Other publications:

Muscovite mica as a growth template of $PC_{61}BM$ crystallites for organic photovoltaics
Jon Feenstra, Maarten Van Eerden, Alexander K. Lemmens, Wester De Poel, Paul H.J. Kouwer, Alan E. Rowan and John J. Schermer.
CrystEngComm, 19, 30, 2017

Revealing the correlation between real-space structure and chiral magnetic order at the atomic scale
Nadine Hauptmann, Melanie Dupé, Tzu-Chao Hung, Alexander K. Lemmens, Daniel Wegner, Bertrand Dupé and Alexander A. Khajetoorians.
Physical Review B, 97, 10, 2018

Time-resolved relaxation and fragmentation of polycyclic aromatic hydrocarbons investigated in the ultrafast XUV-IR regime
J.W.L. Lee, D.S. Tikhonov, P. Chopra, S. Maclot, A.L. Steber, S. Gruet, F. Allum, R. Boll, X. Cheng, S. Düsterer, B. Erk, D. Garg, L. He, D. Heathcote, M. Johny, M.M. Kazemi, H. Köckert, J. Lahl, A.K. Lemmens, D. Loru, R. Mason, E. Müller, T. Mullins, P. Olshin, C. Passow, J. Peschel, D. Ramm, D. Rompotis, N. Schirmel, S. Trippel, J. Wiese, F. Ziaee, S. Bari, M. Burt, J. Küpper, A.M. Rijs, D. Rolles, S. Techert, P. Eng-Johnsson, M. Brouard, C. Vallance, B. Manschwetus and M. Schnell
Nature Communications, 12, 1, 2021

Acknowledgements

I look back on the past four years with the greatest pleasure. Already from a young age curiosity and adventure have driven me and in the past 4 years I have the feeling I was fully able to express myself as a curious scientist and adventurous person. Anouk, I think that we are on the same wavelength when it comes to work, but also about enjoying life. After my masters in 2015, I was therefore very happy that I could stay in your group at FELIX and learn even more about molecular beams and infrared spectroscopy from you. You introduced me to Wybren Jan and in a collaboration within the Dutch Astrochemistry Network, I would shuttle between Nijmegen and Amsterdam. We all knew that I would mostly work in Nijmegen. Wybren Jan, thank you for having the enthusiasm and energy of a highly vibrationally excited molecule and for sharing some of your impressive knowledge about physical chemistry. I feel very lucky to have had you both as my supervisors, giving me the perfect balance between guidance and freedom. Who knows what will come next!

With my closest colleagues and friends, Sjors and Iuliia, I was happy to share many coffee breaks, gossip, frustrations, but also joy from the lab. Discussions with both of you have kept me sharp and your humor in high spirits.

I would also like to mention the students I have had the honor to work with. Especially the work on discharge experiments with astro-photographer and Instagram-influencer Daniël, who is now conducting his own research as my neighbor, is still very motivating and fruitful. Not to forget Jan, Sjoerd, Sophie and Bernard. Thank you for your hard work, new insights and sharing the passion for my research.

Equally I am grateful for the collaborations with Hamburg, Leiden and Würzburg: Amanda, Sébastien, Pragya, Diksha, Donatella, Melanie, Jens, Stefan, Sanjana, Cameron,

Alessandra, Alexander, Florian, Tobi, Floriane and Ingo. Science is best when shared! Also, I should mention the molecular laser physics people in the Huygens building, thank you for the help and my apologies again for the moisture in your lab.

The discharge experiments would not have been successful without the help of Harold Linnartz and Bryan Willemsen and the discussions with Michael Schmitt were very helpful to understand the strange spectral features in the UV after far-IR excitation.

Michel, you have taught me a lot about FELIX and the physics of sailing. For mechanical work and shared admiration of round-the-world sailors, I need to thank Aryan. Without Giel I would not have any working laser to do research with and without Joost I would have no-one to borrow (or steal) equipment from. René has been crucial in providing me either with enough gas pressure or helping me to get rid of it. I have also received a lot of help from the very competent technicians Victor, Wouter and Guus. More recently, Marije, Bas, Paul and Jose joined the amazing team of technicians at FELIX. Thank you Erna for your support and for providing such amusing lunch break topics. Buurman en buurman Wim and Michiel from Amsterdam have made me feel at home the days I spent at the UvA. Thanks a lot to all of you!

From day one I shared my office with Julianna and I have the feeling that we will stay colleagues and friends for many days to come. Nils, thank you for all the much-enjoyed squash games! To all my colleagues and friends at FELIX and Molecular Photonics and I hope I do not forget anyone: Andrei, Angela Annemieke Aravindh, Begum, Ben, Carl, Chao, Daire, Daniel, David, Deepak, Dian, Dina, Dongdong, Frank, Fred, Frederico, Giulia, Hannah, Hans, Hernan, Hong, Ivan, Jarich, Jelle, Jiayun, Joen, Jonathan, Jos, Jun, Kamyar, Kas, Kefan, Kim, Laura, Lex, Lianjia, Lisa, Lisanne, Maan, Maarten, Mark, Mart, Marloes, Martin, Martine, Matthias, Max, Maxime, Miriam, Musleh, Olga I, Olga II, Orr, Paola, Pavel, Pieter, Quentin, René, Rianne, Robert, Roberto, Sander, Sebastiaan, Sandra, Sonja, Thera, Thom, Vasyl, Viktoria, Wasqas, Yanni, Yansong, Yu, Zoi: you create an environment where people feel good and that bears good people and good science. I should also thank Britta, for her large contribution in this respect.

I have always said in some form or other: “Pauze is de basis van elke vooruitgang”. We all know that breaks are meant to share and for that I need to thank my friends, especially Irene, Annika, Jorryt, Ilva, Marleen, Jolanda and Anne.

“The answer, my friend, is blowin’ in the wind.” My time catching the wind, windsurfing and sailing, with such positive and interested people at Aeolus, has truly helped me find the answers I was looking for.

Lastly and most importantly, my family, Titus, Myrte and Mieke, form the basis from which I can spread my wings. Mieke, although we busy ourselves with seemingly opposite subjects, I think we both agree that they are not so different after all. You have immersed me in adventure and somehow given me the curiosity that drives me forward.
Le voyage est en route!